

THE UNIVERSITY OF CHICAGO

VIOLATING BELL'S INEQUALITY WITH REMOTELY-CONNECTED
SUPERCONDUCTING QUBITS

A DISSERTATION SUBMITTED TO
THE FACULTY OF THE INSTITUTE FOR MOLECULAR ENGINEERING
IN CANDIDACY FOR THE DEGREE OF
DOCTOR OF PHILOSOPHY

BY
YOUPENG ZHONG

CHICAGO, ILLINOIS

MARCH 2019

Copyright © 2019 by Youpeng Zhong
All Rights Reserved

To my family

CONTENTS

LIST OF FIGURES	vi
LIST OF TABLES	viii
ACKNOWLEDGMENTS	ix
ABSTRACT	xiv
1 INTRODUCTION	1
2 SUPERCONDUCTING QUANTUM CIRCUITS	5
2.1 LC resonator	5
2.1.1 Classical model	5
2.1.2 Quantum model	8
2.2 Transmission line	10
2.2.1 Classical model	11
2.2.2 Quantum model	13
2.2.3 Transmission line resonators	16
2.2.4 Coplanar waveguide	22
2.3 Superconducting qubit	24
2.3.1 Josephson junction	25
2.3.2 Transmon qubit	26
2.3.3 Qubit control and readout	29
2.4 Coupling	32
2.4.1 Capacitive and inductive coupling	33
2.4.2 Tunable coupling	34
2.4.3 Input-output theory	34
3 CIRCUIT DESIGN	37
3.1 Xmon qubit	40
3.2 Gmon tunable coupler	44
3.3 Coplanar waveguide delay line	45
4 FABRICATION	50
4.1 Base layer	50
4.1.1 Deposition	51
4.1.2 Lithography	51
4.1.3 Etching	52
4.2 Airbridge	53
4.2.1 Lithography and deposition	53
4.2.2 Release the SiO_2 scaffold	55
4.3 Josephson junction	56
4.3.1 Dolan bridge	57

4.3.2	Bandage	59
4.3.3	Room temperature test	61
5	EXPERIMENTAL SETUP	64
5.1	Dilution refrigerator	65
5.2	Electronics	65
5.2.1	GHz DAC board	66
5.2.2	Gaussian filter and differential amplifier	71
5.2.3	IQ mixer	80
5.2.4	GHz ADC board	86
5.2.5	Fastbias card	87
5.2.6	Synchronization	88
5.3	LabRAD	89
6	EXPERIMENTAL RESULTS	96
6.1	Room temperature characterization	96
6.2	Cryogenic temperature characterization	98
6.3	Relay method	107
6.4	Quantum ping-pong	109
6.5	Itinerant photon method	115
7	CONCLUSION	120
7.1	Summary	120
7.2	Outlook	121
A	BELL'S INEQUALITY	122
B	PLAYOUT	126
C	<i>ABCD</i> MATRIX	136
D	ELECTRONICS DOCUMENTS	138
D.1	GHz DAC board	138
D.2	Gaussian filter and differential amplifier	150
D.3	Signal generator	154
D.4	IQ mixer	158
D.5	GHz ADC board	160
	BIBLIOGRAPHY	174

LIST OF FIGURES

2.1	series RLC resonator.	5
2.2	parallel RLC resonator.	7
2.3	LC resonator quantum model.	8
2.4	Transmission line schematic.	11
2.5	Short-circuited transmission line resonator.	17
2.6	Open-circuited transmission line resonator.	19
2.7	Transmission line multimode resonances.	21
2.8	Coplanar waveguide transmission line.	23
2.9	CPW line characteristic impedance.	24
2.10	Josephson junction schematic.	25
2.11	Transmon schematic.	26
2.12	Transmon control and readout.	30
2.13	Image of a practical transmon.	32
2.14	Capacitive and inductive coupling.	33
2.15	A resonator coupled to a long transmission line.	34
2.16	Interaction spectrum.	35
3.1	Quantum state transfer using time-reversal symmetry.	37
3.2	Gmon tunable coupler.	38
3.3	Circuit architecture for quantum state transfer and entanglement generation.	39
3.4	Sonnet simulation of the XY drive line.	42
3.5	Z bias line Sonnet simulation.	43
3.6	Calculating the Z line loading.	43
3.7	Sonnet simulation of the tunable coupler.	44
3.8	CPW delay line cross coupling.	45
3.9	Crossover shunting capacitance impact on delay line transmission.	47
4.1	Negative photoresist nLOF2020 dose test.	53
4.2	Schematic for SiO_2 layer lithography and deposition.	54
4.3	Vapor HF etch.	55
4.4	Schematic for junction fabrication.	58
4.5	SEM image of a Josephson junction.	59
4.6	SEM image of the bandage layer.	60
4.7	Qubit SQUID DC resistance measurement.	61
4.8	Coupler junction DC resistance measurement.	62
5.1	Schematic for electronics and wiring setup.	64
5.2	Custom made DAC board.	66
5.3	Block diagram of the DAC board.	67
5.4	Low-pass filters comparison.	71
5.5	Suppressing the DAC clock feedthrough.	72
5.6	Lumped-element model of a lossy transmission line with Gaussian response.	73
5.7	7-section lumped-element Gaussian filter.	75
5.8	Optimizing the 7-section Gaussian filter parameters.	76

5.9	Suppress the DAC low frequency noise with differential amplifier.	77
5.10	Four Gaussian filters and two differential amplifiers integrated on one board. . .	78
5.11	Rectangle pulses with 10 ps step resolution.	80
5.12	Schematic of a mixer.	80
5.13	Schematic of an IQ mixer.	82
5.14	Custom IQ mixer based on HMC8193.	85
5.15	The impulse response of the custom IQ mixer.	86
5.16	ADC board and IQ mixer configuration.	87
5.17	Multiple GHz DAC/ADC boards synchronization protocol.	89
5.18	Screenshot of the LabRAD manager.	90
5.19	Screenshot of the Registry Editor.	91
5.20	Screenshot of the Grapher.	92
6.1	Device image and schematic.	97
6.2	Qubit single-shot readout.	99
6.3	Multimode feature of the long transmission line.	100
6.4	Transmission line characterization.	102
6.5	Coupling strength versus coupler junction phase δ	104
6.6	Quantum state transfer with relay method.	107
6.7	Quantum state transfer with relay method.	108
6.8	Single qubit “ping-pong” with itinerant photons.	110
6.9	Modeling the quantum “ping-pong” dynamics.	111
6.10	Optimizing photon catch by adjusting control pulse envelope.	114
6.11	Quantum state transfer with itinerant photons.	116
6.12	Remote entanglement generation with itinerant photons.	118
6.13	Traveling photon envelope estimated from simulations.	119
B.1	PLayout in Jupyter notebook environment.	128
B.2	Re-entrant hole (keyhole).	130
B.3	Offset a polygon.	131
B.4	CPW line creation using PLayout.	131
B.5	Add an arc to the CPW line.	132
B.6	Serpentine shape CPW line creation.	133
B.7	Adapt a CPW line to another CPW line with different size.	133
B.8	Serpentine CPW line with evenly distributed crossovers.	135
C.1	Schematic of a two-port device.	136
C.2	A cascade connection of two-port devices.	136

LIST OF TABLES

4.1	ICP etch parameters.	52
4.2	Vapor HF etch parameters.	56
4.3	Ar-ion mill parameters.	60
6.1	Device room temperature tests.	97
6.2	Device parameters.	106
7.1	Summary of experimental results.	120
A.1	CHSH Bell’s inequality.	124

ACKNOWLEDGMENTS

It has been a long and fruitful journey since I became a graduate student at Zhejiang University in 2013 and moved to UChicago in 2015. The meaning of “long” is not measured in time but in experience. In the end, I came out much stronger and I am grateful for the help of many people who have contributed to this journey directly or indirectly.

First, I would like to thank my supervisor, Andrew Cleland, without whom this thesis would not have been possible. I still remember the moment when I first met Andrew in Denver during the 2014 March meeting. After a short conversation in the lobby of the convention center, he kindly invited me to join his group at UChicago. And here I am. One month after I came to Chicago in 2015, he showed me around the laboratory space in the brand new Eckhardt Research Center, where there were nothing but some empty tables and chairs. I am so thankful I had the great opportunity to build a new lab from scratch with a talented group. I learned a lot from Andrew by serving as a teaching assistant in his Quantum Computing class and Microwave Engineering class. I learned more from his guidance/comments in the group meetings and our one-on-one discussions, they have reshaped my way of thinking when approaching difficult problems. Before I came to Chicago, I knew nothing about electronics. Without Andrew’s support and encouragement, I would not have been able to set up the data acquisition system and develop our custom electronics here. The idea of transferring quantum state using gmon tunable coupler was originally conceived by him. I had doubts at the beginning, but after overcoming many obstacles, it turns out that we really can transfer quantum states between two remotely-connected qubits with unprecedented fidelity, allowing for the demonstration of Bell’s inequality violation, the benchmarking result in this thesis. Andrew has, as always, shed light on the right direction. You have been and will continue to be a lighthouse in my life.

Hung-Shen Chang is my first buddy since I came to Chicago. I still remember the early days when we worked on Thermodynamics homework and tested the custom DAC boards from UCSB together. Later we decided to tackle different aspects of the superconducting

circuits, where he started to develop the qubit fabrication recipe, and I continued to test and improve the data acquisition system. As a result of this collaboration, the first working qubit in the UChicago Cleland group was fabricated by him and measured by me. Later we switched roles, Hung-Shen showed me how to fabricate qubits, and I showed him how to use our custom data acquisition system to do qubit experiment. Hung-Shen, thanks for always willing to offer help, and thanks for being my buddy from the beginning to the end. I hope your experiment would turn out excellent.

Kevin Satzinger is the first Ph.D student who graduated from the UChicago Cleland group, after finishing an incredibly excellent experiment with surface acoustic wave (SAW) phonons. Kevin pioneered the SAW experiment and developed a lot of standard cleanroom recipes including the flip-chip technique in our group. I have benefited from his exploration of the gmon tunable coupler. Kevin, we are all proud of you, and your nice device pictures that pop up in all the media. I'm glad that you joined your dream team at Google and are having a happy life in Santa Barbara. Dreams do come true!

Ming-Han Chou is the constant VIP of the cleanroom bill. Almost every time I stayed late in the cleanroom, he's ready to buddy me. My first airbridge vapor HF recipe was created by him. Thank you for your countless help in the cleanroom, and your delicious snacks in the office.

Audrey Bienfait joined the group as a post-doc in 2017, but she soon played an important role in every aspect of the lab with her intelligence and diligence. She kindly offered to help me solder forty eight 0.86 mm cryogenic coaxial cables, which could not have been finished so quickly without her. She's an expert in engineering and has designed almost all the machining parts for the custom electronics. She's also an expert in amplifiers and set up the TWPA from MIT Lincoln Laboratory. Besides the help in the infrastructure, Audrey also helped me a lot in my project such as the input-output theory and fitting the tunable coupling. I'm glad that your quantum transfer experiment with SAW phonon has just come out.

Chris Conner is the youngest member in the group so far, but he learned everything quickly. I'm glad that as I'm writing my thesis, your flip-chip experiment already has some nice result.

Étienne Dumur is our great post-doc. I still remember the early days when we worked together on the dilution refrigerator, and he suddenly sang some metal music, which quite impressed me. I am thankful for all his effort in setting up the fridge. He constantly pushes us to clean the stuff on the table or in the cleanroom. Without him, the lab could have been more unorganized. He proposed and hosted the journal club bi-weekly, and invited everyone to downtown to see a movie now and then. It was a pleasure to work with you Étienne, and I will miss your French style joke after years.

Joel Grebel is the JPA guy in the group. I can't remember how many failures he has encountered when trying to make a JPA work, but none has changed his optimism. I'm glad that you just got a JPA working, and I wish your next ambitious experiment will come out excellent. I wish I have a chance to see your orchestra performance before I leave.

Greg Peairs is a computer geek in the group who finds fun in autoLISP and Julia. He maintains the computing infrastructure in the lab. Good luck with your optomechanical experiment.

Rhys Povey is an expert in Mathematica and Comsol and he's a leader in the graduate community. It's amazing to see how he uses Mathematica to extract features from the SEM pictures. Good luck with your beautiful snowflake.

Ivan Gutierrez helped me assemble a power supply box for the custom electronics during the 2017 summer, after spending a lot of time in the machine shop. Thank you very much for your help.

Dave Schuster kindly received me in his lab for two months when I first arrived in Chicago. Dave is always willing to offer help. He kindly served on my graduate candidacy committee and my dissertation committee. I also thank Yao Lu, Nelson Leung and S. Srivatsan from the Schuster group for helps and discussions in the past few years.

David Awschalom's lab is just next to our lab and is always willing to lend a piece of equipment to us when needed. I still remember the funny story that the first day I came to the campus, I was led to David's lab by mistake (I was supposed to visit Dave's lab), where I stayed for two hours without realizing it because a few students in David's lab were also co-advised by Dave. It is my honor to have David on my graduate candidacy committee and my dissertation committee.

Aashish Clerk is an enthusiastic theorist who joined the Institute for Molecular Engineering in 2017. His famous review paper on quantum noise and amplification was one of the enlightening papers I read when I just entered the superconducting circuits field. Thank you for serving on my dissertation committee.

Mary Pat McCullough has always kindly and promptly helped me deal with all kinds of financial and administrative business. She was never bothered when I asked her to help me to order a small piece of stuff or send out a box. I sincerely thank you for your endless help in the past years.

Peter Duda III is the technical director (superhero) of the cleanroom who is always ready to rescue people out of trouble. I would not have been able to figure out the airbridge fabrication without his help. And thank you for your enthusiasm for the flexible substrate.

Besides the UChicago big family, I would like to thank Prof. Haohua Wang from Zhejiang University, who introduced me to the superconducting circuits community, supervised me for three years since my senior year in college, and kindly recommended me to Andrew. I'd like to also thank Longjun He for babysitting me in the lab when I was still a rookie. Prof. Fuchun Zhang, a highly respected physicist, has kindly advised me since my undergraduate. Your encouragement and expectation has always lighten me up when I feel down. I wish I can be as strong as you one day.

I would like to thank Amit Vainsencher for providing me the Gerber files of the Gaussian filters and the differential amplifiers, following which I have developed a more integrated version. I also thank Daniel Sank, Matthew Neeley and Evan Jeffrey for kindly answering

my questions about LabRAD.

Although I have never had a chance to interact with John Martinis so far, I have learned a lot about electronics from his open source documents. The GHz DAC board, the Gaussian filter and the differential amplifier I developed in UChicago all followed his original design. Developing these custom electronics is not just to save money; the DIY spirit inherent in these custom electronics has greatly inspired me.

Finally, I want to sincerely thank my family for always encouraging and supporting me. I couldn't have gone so far without your love.

ABSTRACT

Quantum communication relies on the efficient generation of entanglement between remote quantum nodes, due to entanglement's key role in achieving and verifying secure communications. Remote entanglement has been realized using a number of different probabilistic schemes, but deterministic remote entanglement has only recently been demonstrated, using a variety of superconducting circuit approaches. However, the deterministic violation of a Bell inequality, a strong measure of quantum correlation, has not to date been demonstrated in a superconducting quantum communication architecture, in part because achieving sufficiently strong correlation requires fast and accurate control of the emission and capture of the entangling photons. Here we present a simple and robust architecture for achieving this benchmark result in a superconducting system.

CHAPTER 1

INTRODUCTION

Quantum computing holds the promise of solving some computationally hard problems that are otherwise intractable with conventional computers, for example factorizing large numbers [1] and simulating complex quantum systems [2]. The fundamental unit of a quantum computer is a two-level quantum system called a *qubit*, which is the quantum analogy of a binary system in conventional computers. A practical quantum computer requires thousands or even millions of qubits.

There are different ways to make qubits, for example using trapped ions [3], defects in diamond/silicon carbide [4, 5], and superconducting quantum circuits [6, 7]. An important advantage of superconducting circuits over other quantum systems are their potential scalability. Superconducting qubits are built and coupled together with standard circuit components, e.g., capacitors, inductors, Josephson junctions and transmission lines etc. Their fabrication, as will be discussed in detail in chapter 4, is similar to that of conventional integrated circuits (IC), which is extremely well developed for easy integration. The use of optical and electron-beam lithography for circuit patterning directly enables scaling to larger system sizes.

Superconducting qubits have made significant progress over the past two decades, demonstrating improved qubit lifetimes, gate fidelities, and increasing circuit complexity [6, 7]. Superconducting qubits also offer highly flexible quantum control over other systems, including electromagnetic [8, 9] and mechanical resonators [10, 11, 12, 13]. More recently, the research efforts on superconducting qubits have grown significantly, after tech giants like Google and IBM entered the quantum race to build a commercial quantum computer using superconducting qubits [14, 15].

To date, however, the state-of-the-art superconducting quantum processors have less than 100 qubits on one chip [14, 15]. Although it has been predicted that “quantum supremacy” (a quantum device without error correction can perform a well-defined computational task

beyond the capabilities of supercomputers) can be demonstrated with this scale of quantum processors [16, 17], they are still very far away from being practically useful. On the other hand, D-wave’s quantum annealer system, which has less stringent requirements on qubit performance, already has 2000 qubits on one chip [18]. In fact, scaling the number of qubits while maintaining the performance of each qubit is still experimentally challenging.

An alternative approach for scaling, similar to the classical supercomputer cluster, is to coherently link multiple high performance quantum processors together to form a more powerful quantum computing cluster using a “quantum network” [19, 20]. Classical networks in modern communication routinely use propagating microwave fields. However, quantum communication with quantized propagating microwave fields, e.g., itinerant photons, is still at an elementary level: recent demonstrations showed deterministic remote state transfer and entanglement generation between two superconducting chips connected by a superconducting coaxial cable [21, 22, 23].

Quantum communication with microwave photons is fundamentally different from classical microwave communication. In classical microwave communication, the channel loss can be compensated by a low noise amplifier at the receiver end without losing the encoded information. In quantum communication, the information is carried by each microwave photon, so that once the photon is lost in the channel, the information is lost. While heralding can help to improve fidelity by discarding photon loss events, it comes at the price of low efficiency [24]. When the photon successfully travels through the channel and reaches the destination, it faces another challenge. In classical microwave communication, the continuous microwave field can be perfectly absorbed by the receiver if the impedance is matched. However, in quantum communication, the perfect absorption of an itinerant microwave photon has been a long-standing challenge. Indeed, itinerant photons emitted by natural qubit state decay has a sharp rising and exponentially decaying envelope, for which a receiver with fixed coupling can have at most 54% absorption efficiency even if it is identical and perfectly matched to the emitter [25, 26].

To achieve high fidelity quantum communication with microwave photons, these two challenges must be addressed by providing: (1) a low-loss communication channel, and (2) a time-symmetric photon release and capture process [27, 28]. In the recent demonstrations in Refs.[21, 22, 23], the coupling is not strong enough that the state transfer duration is orders of magnitude larger than the photon transit time in the channel, making reflections and their interference nearly unmanageable. To avoid the interference from reflections, they used a circulator interrupting the channel to tune up the time symmetric release and capture process, which inevitably introduces significant loss to the channel. Although the normal-metal SMA connectors (each contributes about 2.5% loss [21]) used to connect the cable to the device package can be replaced by direct soldering or wirebonding to reduce loss, the circulator (contributes about 13% loss [21]) is indispensable, limiting the overall fidelity in these experiments.

In this thesis, we have addressed both challenges with the following improvements:

1. Large coupling tuning range and fast tuning speed. The maximum coupling we can achieve is about one or two orders of magnitude larger than that in Refs.[21, 22, 23] because we use an electrically-controlled coupler instead of using microwave parametric driving to control the coupling. The coupling can be effectively turned off, minimizing the impact on the qubit coherence. With the ability to turn the coupling from off to maximum in just a few nanoseconds, we can release and capture a photon faster than the photon round-trip time in the channel. This eliminates the interference from reflections, therefore the circulator can be removed, significantly reducing the channel loss. The fast transfer time also significantly reduces photon dissipation in the channel.
2. Simple and robust control pulse. In Refs.[21, 22, 23], the control pulses are carefully calibrated with the help of the circulator to achieve high fidelity state transfer. Without a circulator interrupting the channel in this experiment, it is difficult to monitor the itinerant photon wave-packet in situ and calibrate the control pulse. Furthermore, fine tuning the nanosecond-scale control pulse requires extraordinary high bandwidth

control electronics, which is impractical. Instead, we experimentally demonstrate that applying a simple control pulse (the convolution of a Gaussian and a rectangle pulse) with a few tuning parameters is sufficient to achieve a very high transfer fidelity due to the robustness of our protocol.

With these improvements, we are able to transfer quantum states and generate remote entanglement over a 78 cm long transmission line with unprecedented fidelities, allowing for the violation of a Bell's inequality (see Appendix A) in a quantum communication architecture, the benchmarking result of this thesis.

This thesis is structured as followings: In chapter 2, we introduce the building blocks of superconducting circuits: the LC resonator, the transmission line and the transmon qubit, then discuss the coupling mechanism between these components. In chapter 3, we discuss the design details of each circuit component in our device. We use a custom Python package called *PLayout* to generate the circuit pattern, and use a commercial electromagnetic simulation software called *Sonnet* extensively to test and verify the design. In chapter 4, we discuss the fabrication details of the device. In chapter 5, we discuss the wiring setup inside the dilution refrigerator and the data acquisition system. The features of the custom electronics are presented in detail. In chapter 6, we show the main result of this thesis: transferring quantum states and generating remote entanglement with unprecedented fidelities, allowing for the violation of Bell's inequality. In chapter 7, we conclude the thesis with outlook for scaling up the channels with superconducting cables.

CHAPTER 2

SUPERCONDUCTING QUANTUM CIRCUITS

This chapter discusses the physics of some basic circuit components commonly used in both classical and quantum circuits. We start with the simple and profound LC resonant circuit, then introduce the transmission line model and show that a transmission line can be approximated as an LC resonator in certain cases. By replacing the lumped element inductor in the LC resonator with the nondissipative, nonlinear inductor—the Josephson junction, we show how to make an artificial atom out of superconducting circuits, the transmon qubit. With these building blocks introduced, we finally discuss the coupling between different circuit components.

2.1 LC resonator

An LC resonator is a simple and profound circuit model comprising a lumped inductor L and a lumped capacitor C . A resistor R is sometimes included to account for dissipation in the system, forming an RLC circuit. At frequencies near resonance, a microwave resonator can usually be modeled by either a series or a parallel RLC equivalent circuit. Here let us review the basic properties of these circuits, following Ref. [29].

2.1.1 Classical model

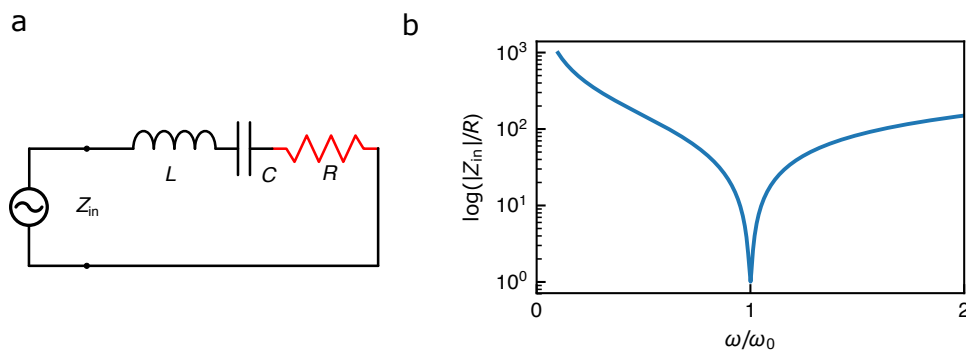


Figure 2.1: (a) Schematic of a series RLC resonator. (b) The input impedance Z_{in} (normalized by R) of the series RLC resonator is minimized at $\omega = \omega_0$, where $Z_{in} = R$.

The schematic of a series RLC circuit is shown in Fig. 2.1(a), with an input impedance

$$Z_{\text{in}} = i\omega L + \frac{1}{i\omega C} + R = i\omega L \frac{\omega^2 - \omega_0^2}{\omega^2} + R \approx i2L\Delta\omega + R, \quad (2.1)$$

where $\omega_0 = 1/\sqrt{LC}$ is the resonant frequency of the circuit, and $\Delta\omega = \omega - \omega_0$. One important feature of series resonance is that the input impedance is minimized at the resonant frequency, where $Z_{\text{in}} = R$, see Fig. 2.1(b).

To quantize the impact of the dissipation on the resonance, we introduce the quality factor Q_0 of this circuit, defined as

$$Q_0 = \omega_0 \frac{\text{energy stored}}{\text{power loss}}. \quad (2.2)$$

For the series resonant circuit in Fig. 2.1, Q_0 is given by

$$Q_0 = \frac{\omega_0 L}{R} = \frac{1}{\omega_0 RC}. \quad (2.3)$$

An alternative approach to modeling dissipation in the circuit is to introduce a complex resonant frequency instead of a resistor. In Eq. 2.1, if we replace ω_0 by

$$\omega'_0 = \omega_0 \left(1 + \frac{i}{2Q_0}\right), \quad (2.4)$$

then the input impedance can be written without the resistor R :

$$Z_{\text{in}} = i2L(\omega - \omega'_0). \quad (2.5)$$

This is useful because for most practical resonators the loss is very small, so that we can begin with a lossless solution, then the effect of the loss can be introduced by replacing ω_0 with the complex resonant frequency ω'_0 .

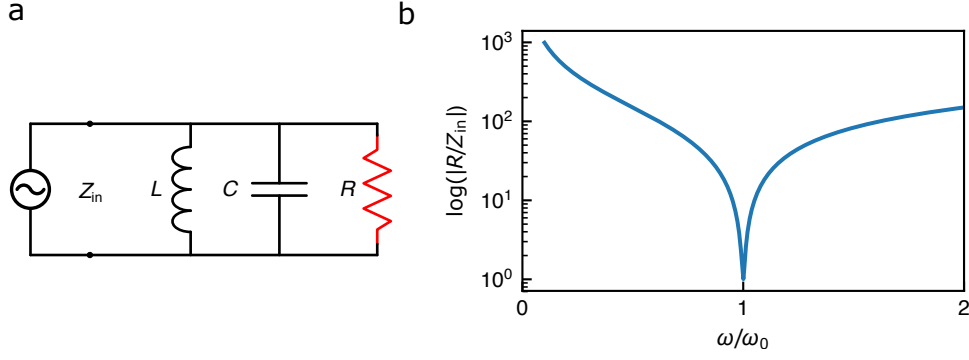


Figure 2.2: (a) Schematic of a parallel RLC resonator. (b) The input admittance $1/Z_{\text{in}}$ (normalized by $1/R$) of the parallel RLC resonator is minimized at $\omega = \omega_0$, where $Z_{\text{in}} = R$.

The parallel RLC circuit shown in Fig. 2.2(a) is the dual of the series RLC circuit, with the input admittance given by

$$Y_{\text{in}} = \frac{1}{Z_{\text{in}}} = \frac{1}{i\omega L} + i\omega C + \frac{1}{R}. \quad (2.6)$$

Similar to a series resonance, a parallel resonance has a minimum admittance (maximum impedance) at the resonant frequency $\omega_0 = 1/\sqrt{LC}$, see Fig. 2.2(b). Near resonance, the input impedance can be simplified as

$$Z_{\text{in}} \approx (2i\Delta\omega C + \frac{1}{R})^{-1} = \frac{R}{1 + 2i\Delta\omega RC}. \quad (2.7)$$

The quality factor Q_0 for parallel resonance is

$$Q_0 = \frac{R}{\omega_0 L} = \omega_0 RC. \quad (2.8)$$

2.1.2 Quantum model

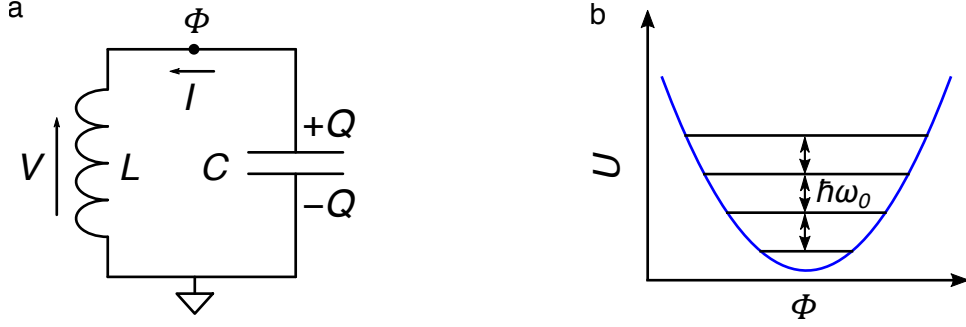


Figure 2.3: LC resonator quantum model. (a) Schematic of the LC resonator. (b) The parabolic potential and the energy levels equally-spaced by $\hbar\omega_0$.

To establish a quantum model for the LC resonator, let us consider the stand-alone LC circuit in Fig. 2.3(a), and define the node flux Φ as

$$\Phi(t) = \int^t d\tau V(\tau), \quad (2.9)$$

so that $V(t) = \dot{\Phi}$. According to Faraday's law, this flux variable is just the physical magnetic flux threaded through the inductor L . Therefore the magnetic energy stored in the inductor is

$$U = \frac{1}{2L}\Phi^2, \quad (2.10)$$

and the electrical energy stored in the capacitor is

$$T = \frac{1}{2}C\dot{\Phi}^2. \quad (2.11)$$

The Lagrangian, choosing Φ as the coordinate, becomes

$$\mathcal{L} = \frac{1}{2}C\dot{\Phi}^2 - \frac{1}{2L}\Phi^2, \quad (2.12)$$

and the momentum conjugate of Φ is the charge Q stored in the capacitor C :

$$Q = \frac{\partial \mathcal{L}}{\partial \dot{\Phi}} = C\dot{\Phi}. \quad (2.13)$$

The Hamiltonian is then given by

$$H = Q\dot{\Phi} - \mathcal{L} = \frac{1}{2C}Q^2 + \frac{\Phi^2}{2L}. \quad (2.14)$$

A quantum description of the LC resonator is obtained by promoting the flux and charge quantities to quantum operators obeying the canonical commutation relation

$$[\hat{\Phi}, \hat{Q}] = i\hbar, \quad (2.15)$$

allowing the Hamiltonian to be rewritten in a standard quantum harmonic oscillator form:

$$H = \hbar\omega_0(a^\dagger a + \frac{1}{2}). \quad (2.16)$$

In this expression $\omega_0 = 1/\sqrt{LC}$ is the resonant frequency of the circuit, a and a^\dagger are the lowering and raising operators defined as

$$a = \frac{i}{\sqrt{2\hbar\omega_0 L}}\hat{\Phi} + \frac{1}{\sqrt{2\hbar\omega_0 C}}\hat{Q}, \quad (2.17)$$

$$a^\dagger = \frac{-i}{\sqrt{2\hbar\omega_0 L}}\hat{\Phi} + \frac{1}{\sqrt{2\hbar\omega_0 C}}\hat{Q}, \quad (2.18)$$

they obey the commutation relation

$$[a, a^\dagger] = 1. \quad (2.19)$$

The eigenstates of this Hamiltonian are called Fock states $|n\rangle$ and satisfy

$$H|n\rangle = \hbar\omega_0(n + 1/2)|n\rangle. \quad (2.20)$$

Their corresponding energy levels are equally spaced by $\hbar\omega_0$, see Fig. 2.3(b).

The flux and charge operators can be expressed in terms of a and a^\dagger as

$$\hat{\Phi} = \Phi_{\text{ZPF}}(a + a^\dagger) \quad (2.21)$$

$$\hat{Q} = -iQ_{\text{ZPF}}(a - a^\dagger), \quad (2.22)$$

where

$$\Phi_{\text{ZPF}} = \sqrt{\frac{\hbar\omega_0 L}{2}} = \sqrt{\frac{\hbar Z}{2}} \quad (2.23)$$

$$Q_{\text{ZPF}} = \sqrt{\frac{\hbar\omega_0 C}{2}} = \sqrt{\frac{\hbar}{2Z}}, \quad (2.24)$$

are the quantum zero-point fluctuations of the flux and charge:

$$\langle 0|\hat{\Phi}^2|0\rangle = \Phi_{\text{ZPF}}^2 \quad (2.25)$$

$$\langle 0|\hat{Q}^2|0\rangle = Q_{\text{ZPF}}^2, \quad (2.26)$$

and $Z = \sqrt{L/C}$ is the characteristic impedance of the resonator. Notice the Heisenberg uncertainty principle is obeyed:

$$\Phi_{\text{ZPF}}Q_{\text{ZPF}} = \frac{\hbar}{2}. \quad (2.27)$$

2.2 Transmission line

A lumped circuit element, such as the inductor and capacitor in the LC circuit, has physical dimensions much smaller than the electrical wavelength, so that the voltage and current do

not vary appreciably over its physical dimensions. A distributed circuit element, on the other hand, may be a considerable fraction of a wavelength, or many wavelengths in size, where the voltage and current can vary in magnitude and phase over its physical dimensions. A transmission line is a simple distributed circuit model widely used in microwave circuits.

2.2.1 Classical model

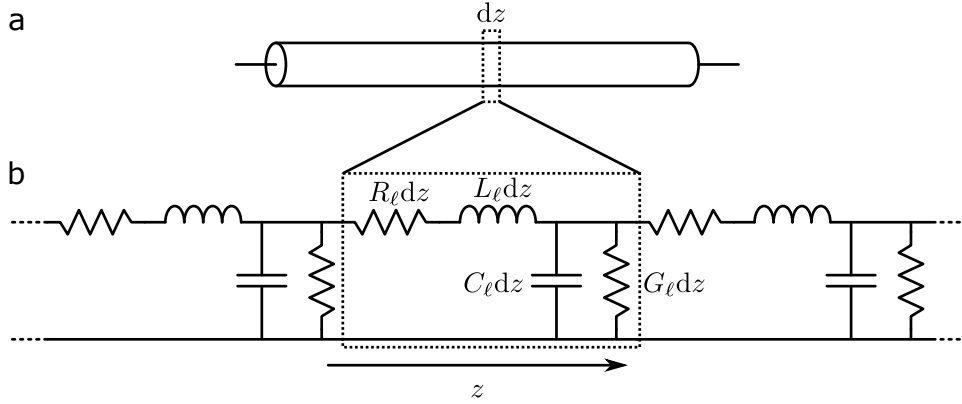


Figure 2.4: (a) Circuit diagram for a transmission line. (b) Transmission line lumped element model. R_ℓ , L_ℓ , G_ℓ and C_ℓ are the resistance, inductance, conductance, and capacitance per unit length of the transmission line.

While transmission lines have various physical implementations, e.g., coaxial cables, microstrip lines, and coplanar waveguides, a transmission line can always be modeled as an infinite series of lumped element circuits that have the same impedance per unit length as the transmission line itself, see Fig. 2.4, where R_ℓ , L_ℓ , G_ℓ and C_ℓ are the resistance, inductance, conductance, and capacitance per unit length of the transmission line. The R_ℓ can usually be associated with conductor loss, while the G_ℓ can be thought of as leakage in the dielectric.

The evolution of the voltage $v(z, t)$ and current $i(z, t)$ of the transmission line follows the

telegrapher equations [29]:

$$\frac{\partial v(z, t)}{\partial z} = -R_\ell i(z, t) - L_\ell \frac{\partial i(z, t)}{\partial t}, \quad (2.28)$$

$$\frac{\partial i(z, t)}{\partial z} = -G_\ell v(z, t) - C_\ell \frac{\partial v(z, t)}{\partial t}. \quad (2.29)$$

For steady-state solutions with $v(z, t) = V(z) \cos(\omega t)$, $i(z, t) = I(z) \cos(\omega t)$, the telegrapher equations simplify to

$$\frac{dV(z)}{dz} = -(R_\ell + j\omega L_\ell)I(z), \quad (2.30)$$

$$\frac{dI(z)}{dz} = -(G_\ell + j\omega C_\ell)V(z). \quad (2.31)$$

Solving these two equations simultaneously, we obtain the wave equations

$$\frac{d^2 V(z)}{dz^2} - \gamma^2 V(z) = 0, \quad (2.32)$$

$$\frac{d^2 I(z)}{dz^2} - \gamma^2 I(z) = 0, \quad (2.33)$$

where

$$\gamma = \alpha + j\beta = \sqrt{(R_\ell + j\omega L_\ell)(G_\ell + j\omega C_\ell)} \quad (2.34)$$

is the complex propagation constant. Traveling wave solutions to these wave equations are

$$V(z) = V_0^+ e^{-\gamma z} + V_0^- e^{\gamma z}, \quad (2.35)$$

$$I(z) = \frac{V_0^+}{Z_0} e^{-\gamma z} - \frac{V_0^-}{Z_0} e^{\gamma z}, \quad (2.36)$$

where

$$Z_0 = \sqrt{\frac{R_\ell + j\omega L_\ell}{G_\ell + j\omega C_\ell}} \quad (2.37)$$

is the characteristic impedance of the transmission line.

When a transmission line of length ℓ is terminated by a load impedance Z_L , its equivalent

impedance is:

$$Z_{\text{in}} = Z_0 \frac{Z_L + Z_0 \tanh \gamma \ell}{Z_0 + Z_L \tanh \gamma \ell}. \quad (2.38)$$

In many practical cases, the loss of the transmission line is negligible: the transmission line model can be simplified by setting $R_\ell = G_\ell = 0$. The propagation constant then becomes

$$\gamma = j\beta = j\omega\sqrt{L_\ell C_\ell}, \quad (2.39)$$

and the characteristic impedance reduces to

$$Z_0 = \sqrt{L_\ell/C_\ell}. \quad (2.40)$$

Its equivalent impedance when terminated by an impedance Z_L becomes:

$$Z_{\text{in}} = Z_0 \frac{Z_L + jZ_0 \tan \beta \ell}{Z_0 + jZ_L \tan \beta \ell}. \quad (2.41)$$

2.2.2 Quantum model

Similar to the quantization procedure for an LC resonator, to obtain a quantum description of a transmission line, it is convenient to define a local flux variable associated to the local voltage variable $v(z, t)$ introduced in Eq. 2.28:

$$\phi(z, t) = \int_{-\infty}^t v(z, \tau) d\tau. \quad (2.42)$$

Integrating both sides of Eq. 2.28 over t with $R_\ell = G_\ell = 0$, we have

$$i(z, t) = -\frac{\partial_z \phi(z, t)}{L_\ell}. \quad (2.43)$$

The Lagrangian of the whole transmission line is the integration of the Lagrangian density \mathcal{L}_z over the line:

$$\mathcal{L}_{TL} = \int \mathcal{L}_z dz,$$

where

$$\mathcal{L}_z = \frac{C_\ell}{2}(\partial_t \phi)^2 - \frac{1}{2L_\ell}(\partial_z \phi)^2. \quad (2.44)$$

The momentum conjugate to ϕ is the charge density

$$q(z, t) = \frac{\delta \mathcal{L}}{\delta \partial_t \phi} = C_\ell \partial_t \phi = C_\ell v(z, t), \quad (2.45)$$

therefore the Hamiltonian is

$$\mathcal{H}_{TL} = \int dz \left[\frac{1}{2C_\ell} q^2 + \frac{1}{2L_\ell} (\partial_z \phi)^2 \right]. \quad (2.46)$$

The quantization of the transmission line can be obtained by promoting the local flux and charge density variables to quantum operators $\hat{\phi}$ and \hat{q} obeying the commutation relation

$$[\hat{\phi}(z'), \hat{q}(z)] = i\hbar \delta(z - z'). \quad (2.47)$$

The Heisenberg equation of motion

$$i\hbar \dot{\hat{\phi}} = [\hat{\phi}, \mathcal{H}_{TL}] \quad (2.48)$$

results in the wave equation

$$\frac{\partial^2 \hat{\phi}}{\partial t^2} - v_p^2 \frac{\partial^2 \hat{\phi}}{\partial z^2} = 0, \quad (2.49)$$

where $v_p = 1/\sqrt{L_\ell/C_\ell}$ is the phase velocity. The general solution has the form

$$\hat{\phi}(z, t) = \hat{\phi}^L\left(\frac{z}{v_p} + t\right) + \hat{\phi}^R\left(-\frac{z}{v_p} + t\right), \quad (2.50)$$

where L and R here denote the left and right propagating waves along the z axis respectively.

Here we introduce the Fourier transform of $\hat{\phi}$:

$$\hat{\phi}(z, t) = \frac{1}{\sqrt{2\pi}} \int_{-\infty}^{\infty} \hat{\phi}(k, t) e^{ikz} dk, \quad (2.51)$$

then the wave equation Eq. 2.49 reduces to

$$\ddot{\hat{\phi}}(k, t) + v_p^2 |k|^2 \hat{\phi}(k, t) = 0, \quad (2.52)$$

which is essentially the equation of motion for a classical harmonic oscillator with resonant frequency $\omega = v_p |k|$. In analogy to the LC resonator, we can express $\phi(k, t)$ in terms of the creation and annihilation operators of photons:

$$\hat{\phi}(k, t) = \sqrt{\frac{\hbar}{2C_\ell \omega_k}} \left[a_k(t) + a_{-k}^\dagger(t) \right],$$

where a and a^\dagger obey the canonical commutation relations:

$$[a_k, a_{k'}^\dagger] = \delta(k - k').$$

The left and right propagating wave can be expressed in terms of a_k and a_k^\dagger :

$$\hat{\phi}^L(z, t) = \sqrt{\frac{\hbar}{4\pi C_\ell}} \int_0^\infty \frac{dk}{\sqrt{\omega_k}} \left[a_k^L e^{-i(\omega_k t + kz)} + h.c. \right], \quad (2.53)$$

$$\hat{\phi}^R(z, t) = \sqrt{\frac{\hbar}{4\pi C_\ell}} \int_0^\infty \frac{dk}{\sqrt{\omega_k}} \left[a_k^R e^{-i(\omega_k t - kz)} + h.c. \right], \quad (2.54)$$

where $h.c.$ denotes the Hermitian conjugate.

With the dispersion relation $\omega_k = v_p k$, we can also use frequency instead of wavenumber:

$$\hat{\phi}^L(z, t) = \sqrt{\frac{\hbar Z_0}{4\pi}} \int_0^\infty \frac{d\omega}{\sqrt{\omega}} \left[a_\omega^L e^{-i(\omega t + k_\omega z)} + h.c. \right], \quad (2.55)$$

$$\hat{\phi}^R(z, t) = \sqrt{\frac{\hbar Z_0}{4\pi}} \int_0^\infty \frac{d\omega}{\sqrt{\omega}} \left[a_\omega^R e^{-i(\omega t - k_\omega z)} + h.c. \right], \quad (2.56)$$

where $k_\omega = \omega/v_p$, and $[a_\omega, a_{\omega'}^\dagger] = \delta(\omega - \omega')$. With this formalism, the transmission line Hamiltonian has the following form:

$$\mathcal{H}_{TL} = \int_{-\infty}^\infty \frac{d\omega}{2\pi} \hbar \omega (a_\omega^\dagger a_\omega + 1/2). \quad (2.57)$$

2.2.3 Transmission line resonators

The microwave frequency of interest in this thesis (a few GHz) has a wavelength of the scale of 1 cm. Making a high quality lumped element LC resonator at such a frequency range is challenging as the dimension of the capacitor or inductor becomes comparable to the wavelength. On the other hand, a transmission line of the length of half-wavelength or quarter-wavelength can be easily used to create an effective LC resonator. This simple approach has been widely adopted in superconducting circuits [30, 31]. Here we give a quick review of transmission line resonators following Ref. [29].

Short-circuited transmission line

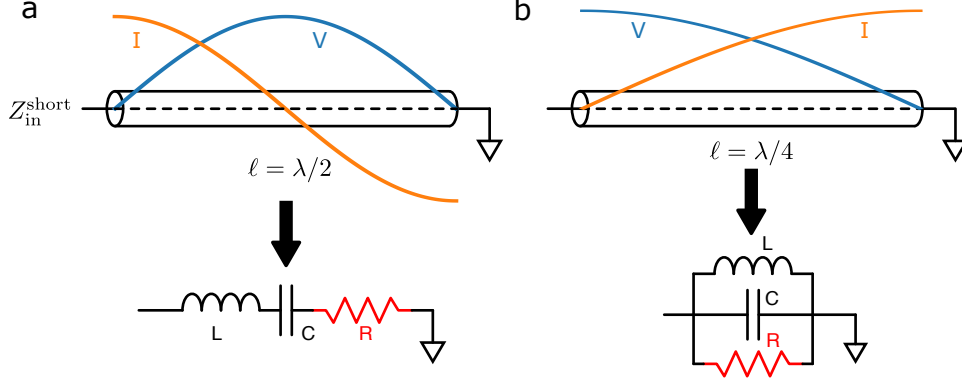


Figure 2.5: Short-circuited transmission line resonator. (a) $\lambda/2$ resonator where ℓ is equal to half the wavelength at resonance. Near resonance, this line can be modeled as a series RLC resonator. (b) $\lambda/4$ resonator where ℓ is equal to a quarter of the wavelength at resonance. Near resonance, this line can be modeled as a parallel RLC resonator. The blue and orange lines indicate the voltage and current distribution along the line at resonance.

Consider a lossy transmission line of characteristic impedance Z_0 , propagation constant β and attenuation constant α . The transmission line has a length of ℓ and is short circuited at one end, see Fig. 2.5. The input impedance is given by Eq. 2.41 by setting $Z_L = 0$:

$$Z_{\text{in}}^{\text{short}} = Z_0 \tanh(\alpha + i\beta)\ell = Z_0 \frac{\tanh \alpha \ell + i \tan \beta \ell}{1 + i \tan \beta \ell \tanh \alpha \ell}. \quad (2.58)$$

In practice a low-loss transmission line is desirable, so we assume $\alpha \ell \ll 1$, and then $\tanh \alpha \ell \approx \alpha \ell$. This line is on resonant when the line length is equal to half the wavelength $\ell = \lambda/2$ at frequency $\omega = \omega_{\lambda/2}$, see Fig. 2.5(a). Near this frequency, we have

$$\beta \ell = \pi + \frac{\pi \Delta \omega}{\omega_{\lambda/2}}, \quad (2.59)$$

then

$$\tan \beta \ell = \tan \left(\pi + \frac{\pi \Delta \omega}{\omega_{\lambda/2}} \right) = \tan \frac{\pi \Delta \omega}{\omega_{\lambda/2}} \approx \frac{\pi \Delta \omega}{\omega_{\lambda/2}}. \quad (2.60)$$

Inserting this into Eq. 2.58, we have

$$Z_{\text{in}}^{\text{short}} = Z_0 \frac{\alpha \ell + i(\pi \Delta \omega / \omega_{\lambda/2})}{1 + i(\pi \Delta \omega / \omega_{\lambda/2}) \alpha \ell} \approx Z_0 (\alpha \ell + i \frac{\pi \Delta \omega}{\omega_{\lambda/2}}). \quad (2.61)$$

Compared with Eq. 2.1, we find that the two equations have the same form, and this shorted $\lambda/2$ resonator is equivalent to a series RLC resonator with

$$R = Z_0 \alpha \ell, \quad (2.62)$$

$$L = \frac{\pi Z_0}{2\omega_{\lambda/2}} = \frac{1}{2} L_\ell \ell, \quad (2.63)$$

$$C = \frac{1}{\omega_{\lambda/2}^2 L} = \frac{2}{\pi^2} C_\ell \ell, \quad (2.64)$$

$$Q_0 = \frac{\omega_{\lambda/2} L}{R} = \frac{\beta}{2\alpha}. \quad (2.65)$$

Another resonant condition for this shorted line is that the line length is equal to a quarter of the wavelength $\ell = \lambda/4$ at frequency $\omega = \omega_{\lambda/4}$, see Fig. 2.5(b). Near this frequency, we have

$$\beta \ell = \frac{\pi}{2} + \frac{\pi \Delta \omega}{2\omega_{\lambda/4}}, \quad (2.66)$$

and

$$\cot \beta \ell \approx -\frac{\pi \Delta \omega}{2\omega_{\lambda/4}}. \quad (2.67)$$

Inserting this into Eq. 2.58, we have

$$Z_{\text{in}}^{\text{short}} \approx \frac{Z_0}{\alpha \ell + i \frac{\pi \Delta \omega}{2\omega_{\lambda/4}}}. \quad (2.68)$$

Compared with Eq. 2.7, we find that they have the same form, and this shorted $\lambda/4$ resonator

is equivalent to a parallel RLC resonator with

$$R = \frac{Z_0}{\alpha \ell}, \quad (2.69)$$

$$C = \frac{\pi}{4Z_0\omega_{\lambda/4}} = \frac{1}{2}C_\ell\ell, \quad (2.70)$$

$$L = \frac{1}{\omega_{\lambda/4}^2 C} = \frac{8}{\pi^2}L_\ell\ell, \quad (2.71)$$

$$Q_0 = \omega_{\lambda/4}RC = \frac{\beta}{2\alpha}. \quad (2.72)$$

Open-circuited transmission line

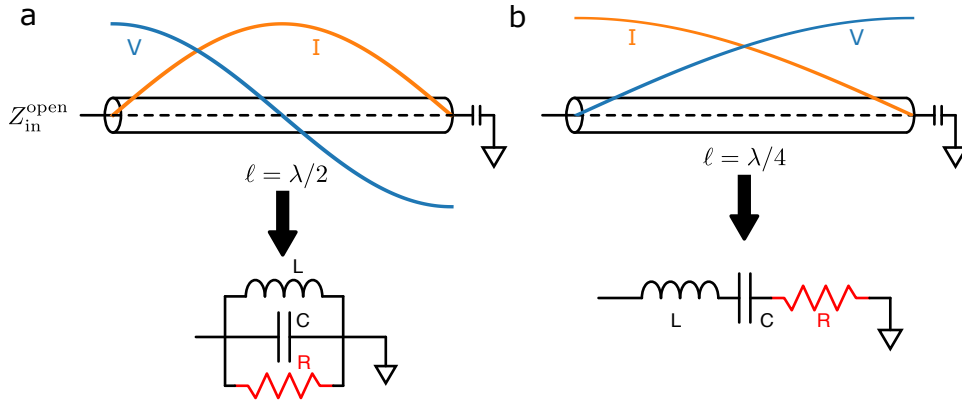


Figure 2.6: Open-circuited transmission line resonator. The right end of the line is connected to the ground through a negligibly small capacitance. (a) $\lambda/2$ resonator where ℓ is equal to half the wavelength at resonance. Near resonance, this line can be modeled as a parallel RLC resonator. (b) $\lambda/4$ resonator where ℓ is equal to a quarter of the wavelength at resonance. Near resonance, this line can be modeled as a series RLC resonator. The blue and orange lines indicate the voltage and current distribution along the line at resonance.

Similarly, we can create a $\lambda/2$ or $\lambda/4$ resonator using an open-circuited transmission line. The input impedance of the open-circuited transmission line shown in Fig. 2.6 is given by Eq. 2.41 by setting $Z_L = \infty$:

$$Z_{\text{in}}^{\text{open}} = Z_0 \coth(\alpha + i\beta)\ell = Z_0 \frac{1 + i \tan \beta \ell \tanh \alpha \ell}{\tanh \alpha \ell + i \tan \beta \ell}. \quad (2.73)$$

As before, $\ell = \lambda/2$ at $\omega = \omega_{\lambda/2}$. Near this frequency, we have

$$\beta\ell = \pi + \frac{\pi\Delta\omega}{\omega_{\lambda/2}}, \quad (2.74)$$

and so

$$\tan \beta\ell \approx \frac{\pi\Delta\omega}{\omega_{\lambda/2}}. \quad (2.75)$$

With the low-loss assumption, we have $\tanh \alpha\ell \approx \alpha\ell$, inserting these results in Eq. 2.73, we have

$$Z_{\text{in}}^{\text{open}} \approx \frac{Z_0}{\alpha\ell + i(\pi\Delta\omega/\omega_{\lambda/2})}. \quad (2.76)$$

Comparing with Eq. 2.7, we find that they have the same form, and this open $\lambda/2$ resonator is equivalent to a parallel RLC resonator with

$$R = \frac{Z_0}{\alpha\ell}, \quad (2.77)$$

$$C = \frac{\pi}{2\omega_{\lambda/2}Z_0} = \frac{1}{2}C_\ell\ell, \quad (2.78)$$

$$L = \frac{1}{\omega_{\lambda/2}^2 C} = \frac{2}{\pi^2}L_\ell\ell, \quad (2.79)$$

$$Q_0 = \omega_{\lambda/2}RC = \frac{\beta}{2\alpha}. \quad (2.80)$$

For $\lambda/4$ resonator, we insert Eq. 2.66 into Eq. 2.73 and get the following approximation:

$$Z_{\text{in}}^{\text{open}} \approx Z_0 \left(\alpha\ell + i \frac{\pi\Delta\omega}{2\omega_{\lambda/4}} \right), \quad (2.81)$$

which can be modeled as a series RLC resonator with

$$R = Z_0 \alpha \ell, \quad (2.82)$$

$$L = \frac{\pi Z_0}{4\omega_{\lambda/4}} = \frac{1}{2} L_{\ell} \ell, \quad (2.83)$$

$$C = \frac{1}{\omega_{\lambda/4}^2 L} = \frac{8}{\pi^2} C_{\ell} \ell, \quad (2.84)$$

$$Q_0 = \frac{\omega_{\lambda/4} L}{R} = \frac{\beta}{2\alpha}. \quad (2.85)$$

Transmission line multimode resonator

Different from the lumped element LC resonator which supports a single resonant mode only, a transmission line resonator can naturally support a sequence of standing wave modes equally spaced in frequency, see Fig. 2.7 as an example. This short-circuited transmission line supports modes with wavelength $\lambda_n = 2\ell/n$.

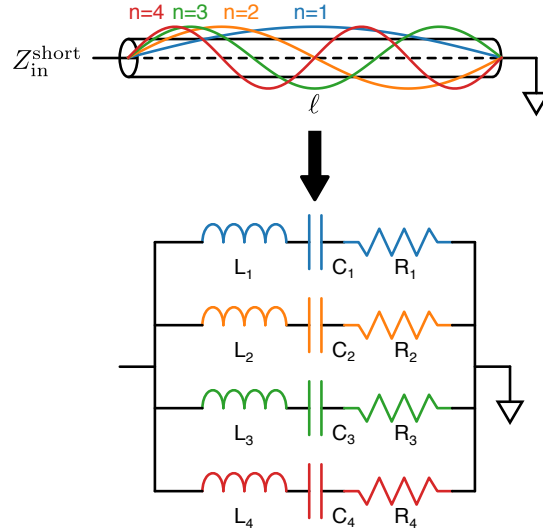


Figure 2.7: Transmission line multimode resonances. This short-circuited transmission line naturally supports modes with wavelength $\lambda_n = 2\ell/n$. The voltage distribution of the $n = 1$ to $n = 4$ resonant modes are shown. It can be modeled as a parallel combination of series LC resonators.

Near the n th mode resonance, we have

$$\beta\ell = n\pi + \frac{\pi\Delta\omega}{\omega_{\lambda/2}}. \quad (2.86)$$

Near this frequency we have the input impedance

$$Z_{\text{in}} \approx Z_0 \left(\alpha\ell + i \frac{\pi\Delta\omega}{\omega_{\lambda/2}} \right). \quad (2.87)$$

This impedance is equivalent to a series RLC resonant circuit with equivalent lumped-element parameters

$$\omega_n = n\omega_{\lambda/2}, \quad (2.88)$$

$$R_n = Z_0\alpha\ell, \quad (2.89)$$

$$L_n = \frac{\pi Z_0}{2\omega_{\lambda/2}} = \frac{1}{2}L_\ell\ell, \quad (2.90)$$

$$C_n = \frac{1}{n^2\omega_{\lambda/2}^2 L_n}, \quad (2.91)$$

$$Q_n = \frac{\omega_n L_n}{R_n} = \frac{\beta}{2\alpha}. \quad (2.92)$$

This transmission line can be modeled as a parallel combination of these series RLC circuits.

The continuous mode Hamiltonian for an infinite transmission line in Eq. 2.57 then reduces to a discrete form:

$$\mathcal{H} = \sum_{n=1}^{\infty} \hbar n \omega_{\lambda/2} (a_n^\dagger a_n + 1/2). \quad (2.93)$$

2.2.4 Coplanar waveguide

So far we have discussed the general properties of transmission line independent of its physical implementation. Here we consider one particular form of transmission line, the coplanar waveguide (CPW), which is widely used in superconducting circuits.

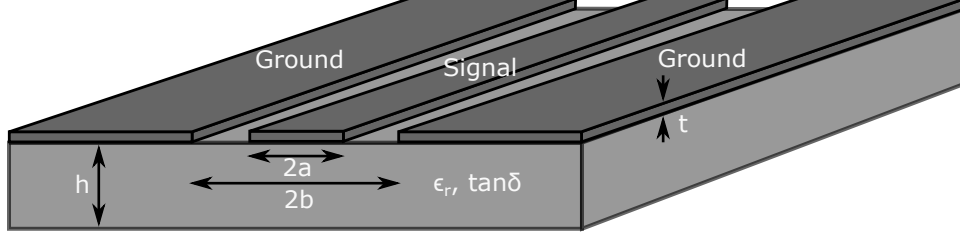


Figure 2.8: Coplanar waveguide transmission line.

A typical CPW line is shown in Fig. 2.8, where the center signal trace of width $2a$ is surrounded by two ground planes separated by $2b$. The conducting layer is a low-loss thin film with thickness $t \ll a, b$. The dielectric thickness $h \gg a, b$ is assumed to be infinite. The substrate has a relative permittivity of ϵ_r and a loss tangent of $\tan \delta$. With these assumptions, the electromagnetic properties of the CPW line can be analytically solved using a conformal transformation [32]:

$$L_\ell = \frac{\mu_0}{4} \frac{K(k'_0)}{K(k_0)}, \quad (2.94)$$

$$C_\ell = 4\epsilon_0\epsilon_{\text{eff}} \frac{K(k_0)}{K(k'_0)}, \quad (2.95)$$

where K is the complete elliptic integral of the first kind with the following arguments:

$$k_0 = \frac{a}{b}, \quad (2.96)$$

$$k'_0 = \sqrt{1 - k_0^2}, \quad (2.97)$$

and

$$\epsilon_{\text{eff}} = \frac{1 + \epsilon_r}{2}$$

is the effective permittivity of the transmission line. Note the L_ℓ here is the geometric inductance. For high frequency applications, there is in addition a kinetic inductance L_K originating from the inertial mass of the charge carriers. This contribution of inductance can be considerable in some cases, depending on the material and its thickness [33]. But for the

thesis here, we use aluminum of about 100 nm thickness, in which case $L_K \ll L_\ell$, and thus the kinetic inductance can be safely ignored. The characteristic impedance is then given by

$$Z_0 = \sqrt{\frac{Z_\ell}{C_\ell}} = \frac{1}{4} \sqrt{\frac{\mu_0}{\epsilon_0 \epsilon_{\text{eff}}}} \frac{K(k'_0)}{K(k_0)}. \quad (2.98)$$

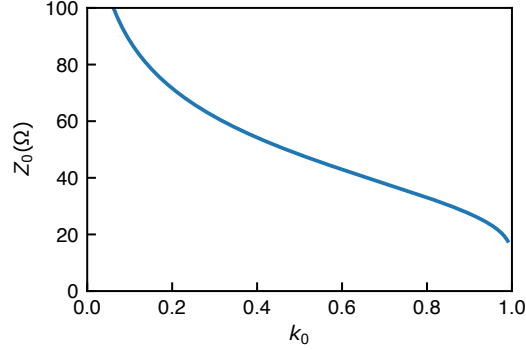


Figure 2.9: CPW line characteristic impedance versus k_0 on c-plane sapphire wafer. $Z_0 \approx 50 \Omega$ when $k_0 = 0.5$.

Sapphire is an extremely low loss substrate widely used for superconducting circuits. The relative permittivity of c-plane sapphire is $\epsilon_r = 11.5$. The CPW characteristic impedance versus k_0 on sapphire is shown in Fig. 2.9. We see that the impedance lies in the range of 20 Ω to 100 Ω for reasonable CPW geometries. When $k_0 = 0.5$, $Z_0 \approx 50 \Omega$ is impedance-matched with external wirings, which is favorable for microwave transmission [29].

The dielectric attenuation coefficient of a CPW line is given by [32]

$$\alpha_d = \frac{\epsilon_{\text{eff}} - 1}{\epsilon_r - 1} \frac{\epsilon_r}{\sqrt{\epsilon_{\text{eff}}}} \frac{\omega \tan \delta}{2c} \text{ Np/m} \propto \omega, \quad (2.99)$$

where c is the speed of light in free space.

2.3 Superconducting qubit

The ideal LC resonator and transmission line resonator are both linear circuit components with equally-spaced energy levels, making it difficult to selectively address a particular eigen-

state of the system using classical electronics. To enable quantum control of the system, a nonlinear element must be introduced. Fortunately, there exists a nonlinear, nondissipative superconducting element, the Josephson junction (JJ) [34].

2.3.1 Josephson junction

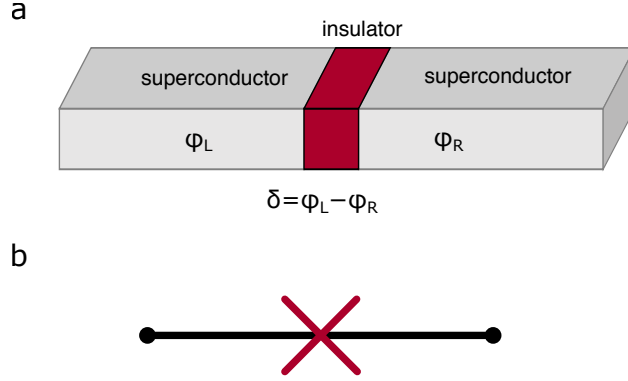


Figure 2.10: (a) Schematic of a Josephson junction, comprising an insulating barrier sandwiched by two superconducting electrodes. (b) Circuit diagram for a Josephson junction.

One form of a JJ is essentially a thin insulating layer sandwiched by two superconducting layers (Fig. 2.10(a)). The presence of the insulating layer allows the phase of the macroscopic superconducting order parameter to differ in the two superconducting layers. Denoting the phase difference as δ , the current through the junction I_J and the voltage across the junction V_J obey the Josephson relations [34]:

$$I_J = I_0 \sin(\delta), \quad (2.100)$$

$$V_J = \frac{\Phi_0}{2\pi} \frac{d\delta}{dt}, \quad (2.101)$$

where I_0 is the critical current of the junction and $\Phi_0 = h/2e = 2.067 \times 10^{-15}$ Wb is the magnetic flux quantum. The circuit diagram of a JJ is shown in Fig. 2.10(b).

It is generally more convenient to use the flux variable $\Phi = \int_{-\infty}^t V_J(t') dt'$ to describe superconducting circuits involving junctions. Comparing with Eq. 2.101, we see that $\delta =$

$2\pi\Phi/\Phi_0$. The JJ can also be treated as a nonlinear inductor with inductance L_J given by

$$L_J(\Phi) = \frac{d\Phi}{dI_J} = \frac{\Phi_0}{2\pi I_0 \cos(2\pi \frac{\Phi}{\Phi_0})}. \quad (2.102)$$

The energy stored in the junction is given by integrating $V_J I_J$ over time,

$$E = \int_{-\infty}^t V_J I_J dt' = -E_J \cos(2\pi \frac{\Phi}{\Phi_0}), \quad (2.103)$$

where $E_J = I_0 \Phi_0 / 2\pi$ is called the Josephson energy.

2.3.2 Transmon qubit

The capacitor, inductor and JJ are the “periodic table” elements of superconducting circuits. Different artificial atoms (superconducting qubits) can be formed by rearranging the combination of these elements, among which now the version known as the transmon has become the most outstanding because of its high coherence and accurate control [35, 36, 37].

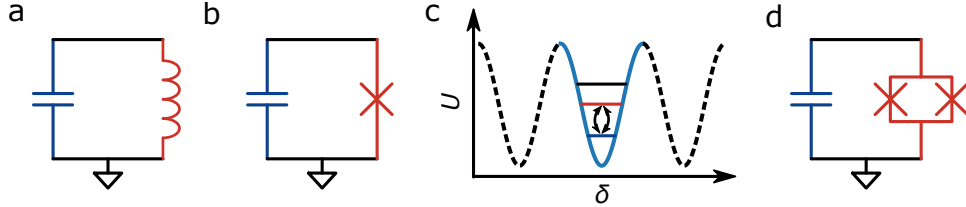


Figure 2.11: (a) A stand-alone LC resonator. (b) A transmon is made by replacing the linear inductor in (a) with a JJ. (c) The cosine-shape potential and the energy level diagram of a transmon. (d) In practice, the single JJ is typically replaced by a SQUID for frequency tuning.

A transmon is essentially an LC resonator (Fig. 2.11(a)), except that the linear inductor is replaced by a JJ to make it nonlinear (Fig. 2.11(b)). The Hamiltonian of the transmon is given by [35]

$$H = \frac{Q^2}{2C} - E_J \cos(2\pi \frac{\Phi}{\Phi_0}) \quad (2.104)$$

where C is the shunting capacitance, and Q is the charge stored in the capacitor. It turns

out that Φ and Q are canonically conjugate variables, with $[\Phi, Q] = i\hbar$. The potential and energy level diagram of this Hamiltonian are shown in Fig. 2.11(c). The cosine-shaped potential well leads to unequally spaced energy levels, the lowest two of which can be used as an effective two-level system, i.e. a qubit.

To understand the transmon Hamiltonian better, we can rewrite Eq. 2.104 as

$$H = 4E_C n^2 - E_J \cos \delta, \quad (2.105)$$

where $n = Q/2e$ is the number of Cooper pairs, $E_C = e^2/2C$ is the charging energy, with n and δ satisfying the commutation relation $[\delta, n] = 1$. We can expand the cosine term assuming δ is small:

$$\cos \delta \approx 1 - \frac{\delta^2}{2!} + \frac{\delta^4}{4!} + \dots \quad (2.106)$$

To lowest order, we obtain the harmonic oscillator Hamiltonian (ignoring the constant term):

$$H \approx 4E_C n^2 + E_J \frac{\delta^2}{2} = \sqrt{8E_J E_C} (a^\dagger a + \frac{1}{2}), \quad (2.107)$$

where

$$\delta = \left(\frac{2E_C}{E_J} \right)^{1/4} (a + a^\dagger), \quad (2.108)$$

$$n = -i \left(\frac{E_J}{8E_C} \right)^{1/4} \frac{1}{\sqrt{2}} (a - a^\dagger). \quad (2.109)$$

The quartic term correction to each energy level is given by [35]

$$\Delta E_m = \langle m | -E_J \frac{\delta^4}{24} | m \rangle \quad (2.110)$$

$$= -\frac{E_C}{12} \langle m | (a + a^\dagger)^4 | m \rangle \quad (2.111)$$

$$= -\frac{E_C}{12} (6m^2 + 6m + 3). \quad (2.112)$$

Adding this correction term to Eq. 2.107, we have

$$E_m = m\sqrt{8E_J E_C} - \frac{E_C}{12}(6m^2 + 6m + 3). \quad (2.113)$$

The qubit transition energy is simply

$$E_{10} = E_1 - E_0 = \sqrt{8E_J E_C} - E_C, \quad (2.114)$$

and the nonlinearity (anharmonicity) of the qubit is defined as the difference of the $|1\rangle \leftrightarrow |2\rangle$ transition frequency and the $|0\rangle \leftrightarrow |1\rangle$ transition frequency:

$$\eta = \omega_{21} - \omega_{10} = (E_{21} - E_{10})/\hbar = -E_C/\hbar. \quad (2.115)$$

This frequency sets a limit on how fast the qubit can be controlled using on-resonant microwave pulses. Indeed, short control pulses have a broad frequency bandwidth that may exceed η , inducing undesired $|1\rangle \leftrightarrow |2\rangle$ transition. Therefore, having larger η , and thus larger E_C , is preferred from this aspect. However, larger E_C means smaller capacitance, making the qubit more sensitive to charge fluctuations. Analytical calculations show that the sensitivity of the energy levels to the charge is proportional to $\exp(\sqrt{8E_J/E_C})$ [35]. Therefore the transmon parameters must be carefully chosen to balance the nonlinearity and the qubit coherence.

In practice, the single JJ is typically replaced by a superconducting quantum interference device (SQUID) consisting of a pair of JJs in parallel (Fig. 2.11(d)). The SQUID loop acts similar to a single JJ except that its critical current depends on the external flux threading through the loop, which allows the transition frequency of the transmon to be tuned experimentally [35].

2.3.3 Qubit control and readout

The quantum state of a qubit can be generally expressed as

$$|\psi\rangle = \cos(\theta/2)|g\rangle + \sin(\theta/2)e^{i\phi}|e\rangle. \quad (2.116)$$

It is often useful to represent a qubit state with a vector on a unit sphere in Cartesian space which is called the Bloch sphere, see Fig. 2.12(a). The θ and ϕ in Eq. 2.116 corresponds to the polar and azimuthal angle of the unit vector on the Bloch sphere. All single qubit gate operations can be decomposed as X, Y and Z rotations on the Bloch sphere.

The transmon qubit is controlled through an XY control line and a Z control line, as shown in Fig. 2.12(b). The XY control line is capacitively coupled to the qubit, which can deliver on-resonant microwave pulses to drive the qubit state transition. This operation is equivalent to a rotation operation around the X axis or Y axis, or any other axis on the equator of the Bloch sphere, depending on the phase of the microwave pulse. The Z control line is inductively coupled to the SQUID loop of the qubit. Applying a quasi-DC pulse to the Z control line can change the equivalent E_J of the qubit, hence varying the qubit frequency. This operation is equivalent to a rotation around the Z axis of the Bloch sphere.

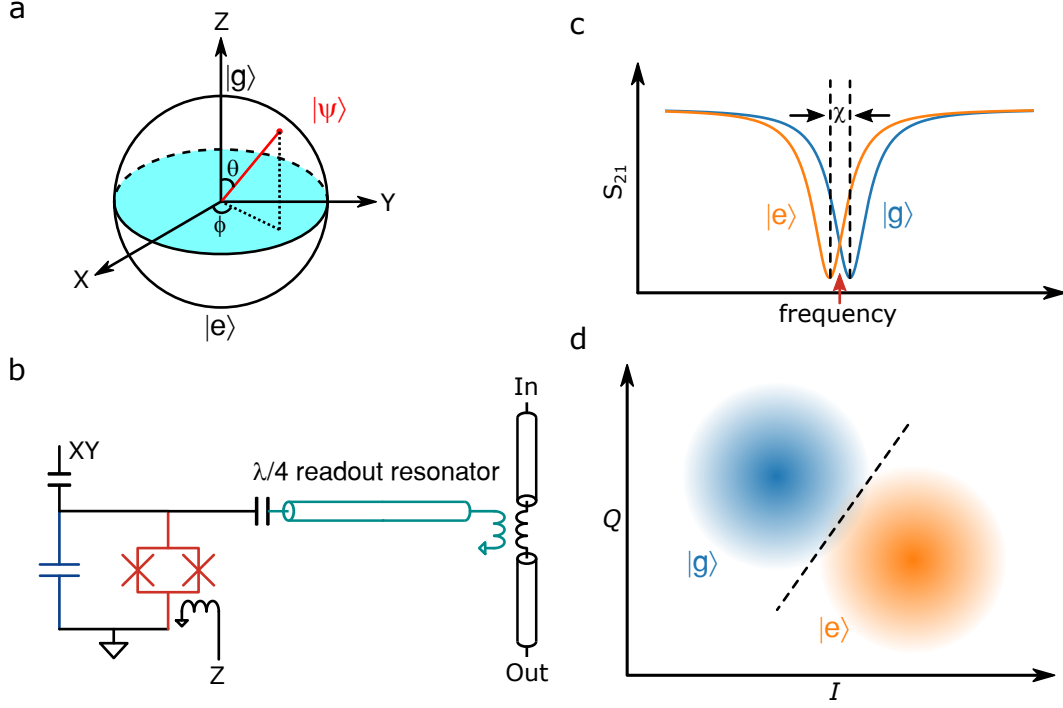


Figure 2.12: (a) Bloch sphere. A qubit state can be represented by a unit vector on the Bloch sphere. (b) Qubit control and readout schematic. (c) The transmission of the feedline in (b) depends on the qubit state due to dispersive shift. (d) when measuring at a certain frequency (indicated by the red arrow in panel (c)), different qubit states will be projected into different transmission (or reflection) coefficients. Expressing the transmission (or reflection) coefficient in forms of a complex number $I + iQ$, one can find out that the measured signals for a qubit being in the ground state and excited state correspond to two distinct regimes in the I - Q plane, allowing for the single-shot discrimination of the qubit state.

The transmon is measured using a technique called dispersive readout, which exploits the nonlinearity of a superconducting cavity coupled to the transmon qubit [38, 39]. When a transmon is capacitively coupled to a resonator, the system Hamiltonian is given by [40]

$$H/\hbar = \omega_r a^\dagger a - \frac{\omega_q}{2} \sigma_z + g(\sigma^\dagger a + \sigma a^\dagger), \quad (2.117)$$

where ω_r and ω_q are the resonant frequencies of the resonator and qubit, a and σ are the annihilation operators of the resonator and qubit excitations respectively, σ_z is the Pauli operator, and g is the coupling strength.

Denoting the detuning as $\Delta = \omega_q - \omega_r$, when $\omega_r \gg |\Delta| \gg |g|$, we are in the so-called

“dispersive limit”. In this regime the interaction can be simplified with a change of basis which eliminates the interaction to first order in g/Δ . We rotate the Hamiltonian by the unitary operator

$$U = \exp(\lambda T) \quad (2.118)$$

where $T = \sigma^\dagger a - \sigma a^\dagger$ and $\lambda = g/\Delta$, then expand it in λ [41]:

$$U^\dagger H U = \exp(-\lambda T) H \exp(\lambda T) \quad (2.119)$$

$$= H - \lambda [T, H] + \frac{\lambda^2}{2!} [T, [T, H]] + \dots \quad (2.120)$$

$$\approx \hbar(\omega_r - \frac{g^2}{\Delta} \sigma_z) a^\dagger a - \hbar \frac{\omega_q}{2} \sigma_z. \quad (2.121)$$

We see that when the qubit is in $|e\rangle$ state, the resonator frequency is shifted by

$$\chi = -g^2/\Delta \quad (2.122)$$

compared to that of qubit in $|g\rangle$ state. This dispersive shift, therefore the qubit state, can be detected using a scattering measurement with a feedline coupled to the readout resonator, see Fig. 2.12(b) and (c). When sending microwave signals through the feedline at a certain frequency (indicated by the red arrow in Fig. 2.12(c)), different qubit states will be projected into different transmission (or reflection) coefficients. Expressing the transmission (or reflection) coefficient in forms of a complex number $I + iQ$, one can find out that the measured signals for a qubit being in the ground state and excited state correspond to two distinct regimes in the I - Q plane, allowing for the single-shot discrimination of the qubit state, see Fig. 2.12(d).

In practice, the transmon is not a perfect two-level system. The dispersive shift taking the second excited state $|f\rangle$ into account is given by [35]

$$\chi = -\frac{g^2}{\Delta} \frac{1}{1 + \eta/\Delta}, \quad (2.123)$$

here η is the nonlinearity defined in Eq. 2.115.

A practical transmon with control and readout circuit is shown in Fig. 2.13. This design is adapted from Ref. [36]. Because this design features excellent performance in both control, coherence and easy connectivity thanks to its signature cross-shape capacitor, a special name called “Xmon” is given to this version of transmon.

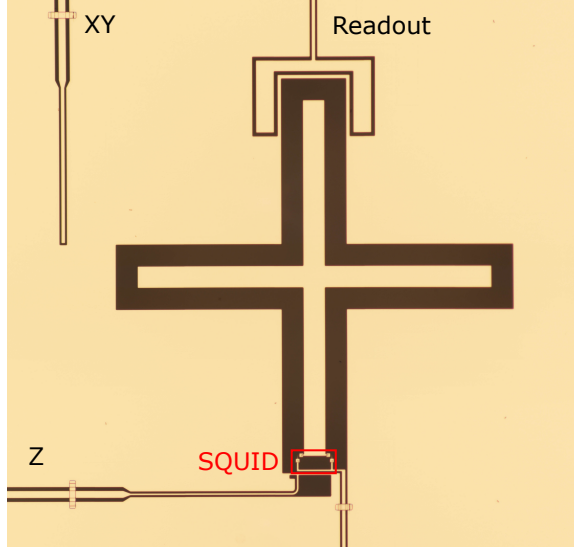


Figure 2.13: A practical transmon, with control and readout circuit. The qubit is capacitively coupled to a $\lambda/4$ readout resonator (top), an XY drive line (left), and inductively coupled to a Z control line (bottom).

2.4 Coupling

In the previous sections I have introduced the building blocks of superconducting circuits. A practical device usually comprises of several building blocks coupled with each other. Coupling is necessary for external control, gate operation and readout of the device. We can categorize couplings by physical mechanism, i.e., capacitive coupling or inductive coupling. We can also categorize couplings by tunability, i.e., fixed coupling or tunable coupling.

2.4.1 Capacitive and inductive coupling

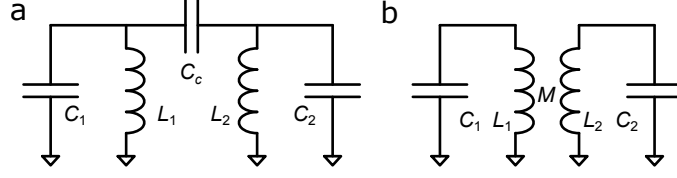


Figure 2.14: (a) Capacitive coupling. (b) Inductive coupling.

Two parallel LC resonators can be coupled together by simply connecting them with a small coupling capacitance C_c , see Fig. 2.14(a). Similarly, two series LC resonators can be coupled together by introducing a weak mutual inductance M between them, see Fig. 2.14(b).

Following the circuit quantization procedure in Ref. [42], one can obtain the Jaynes-Cummings coupling Hamiltonian for these systems:

$$H_{JC}/\hbar = \sum_{i=1,2} \omega_i a_i^\dagger a_i + g(a_1^\dagger a_2 + a_1 a_2^\dagger), \quad (2.124)$$

where a_1, a_2 are the annihilation operators for the two resonators, g is the coupling strength given by

$$g = \frac{1}{2} \frac{C_c}{\sqrt{C_1 C_2}} \sqrt{\omega_1 \omega_2} \quad (2.125)$$

for capacitive coupling, and

$$g = \frac{1}{2} \frac{M}{\sqrt{L_1 L_2}} \sqrt{\omega_1 \omega_2} \quad (2.126)$$

for inductive coupling. Here ω_1 and ω_2 are the resonant frequencies of the two resonators.

Because the transmon qubit is a weakly nonlinear LC resonator, these formulae can be used to estimate its coupling strength by replacing the inductance with the equivalent junction inductance. This linear approximation works well as long as the coupling is not too strong, i.e. $g \ll \sqrt{\omega_1 \omega_2}$.

2.4.2 Tunable coupling

Fixed coupling between qubits is an “always-on” coupling that is determined by design. The coupling is turned “on” by bringing two qubits into resonance, and it is turned “off” by detuning them, with a small residual coupling. However, as the number of qubits increases, the frequency spectrum becomes increasingly crowded, making this approach prohibitively difficult: Increased frequency crowding makes residual couplings harder to suppress; Moreover, when adjusting qubit frequencies to perform entangling gates, state leakage can occur due to the Landau-Zener effect [43], degrading the gate fidelity.

Tunable coupling can mitigate frequency crowding in a scalable quantum processor architecture. Tunable coupling is also desirable in a hybrid quantum system where a high coherence qubit is coupled to a lossy quantum element [12]. The coupling is turned on during the hybrid system interaction, and turned off otherwise to minimize the impact on the qubit coherence. In quantum simulation, tunable coupling provides a unique opportunity to investigate nonequilibrium dynamic processes [44, 45, 46, 47]. Furthermore, high fidelity quantum state transfer with microwave photons requires the coupling to be dynamically tuned [27, 28]. With all these important applications, various tunable couplers have been proposed and demonstrated [48, 49, 50, 51, 52, 53, 54, 55, 56], among which the “gmon” tunable coupler [54] distinguishes itself with simple design, large tuning range and high coherence. More details about gmon will be presented in chapter 3.

2.4.3 Input-output theory

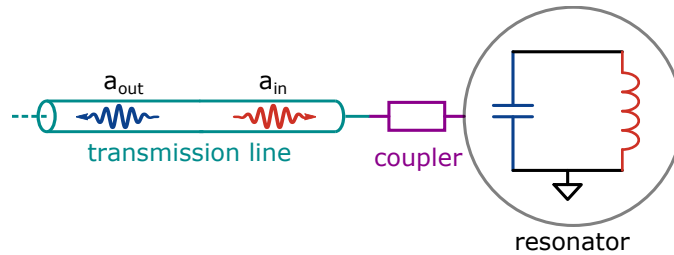


Figure 2.15: A resonator coupled to a long transmission line.

Consider a resonator coupled to a long transmission line in Fig. 2.15. Compared to the interaction between the resonator and the stationary photons, the interaction between the resonator and the itinerant photons in the transmission line has more features. In the Jaynes-Cummings model in Eq. 2.124, there is a single mode in each resonator, and the coupling is quantized by a single coupling strength g , see the schematic in Fig. 2.16(a). On the other hand, the transmission line supports multiple modes equally spaced in frequency by the free spectral range ω_{FSR} , and the interaction with each mode is characterized by the corresponding coupling strength g_i , see Fig. 2.16(b). These coupling values are not independent, they satisfy $g_i \propto \sqrt{i}$. The on-resonant coupling strength g_n where $\omega_n \approx \omega_r$ is of particular interest. When $g_n \ll \omega_{\text{FSR}}$, the resonator only interacts with a few modes whose frequencies are close to ω_r , and the Jaynes-Cummings Hamiltonian can still be used to describe the interaction:

$$H/\hbar = \omega_r a_r^\dagger a_r + \sum_m \omega_m a_m^\dagger a_m + \sum_m g_m (a_r^\dagger a_m + a_r a_m^\dagger), \quad (2.127)$$

where a_r is the annihilation operator for the resonator, and a_m the annihilation operator for the m th bosonic mode whose frequency is close to ω_r enough that need to be taken into account.

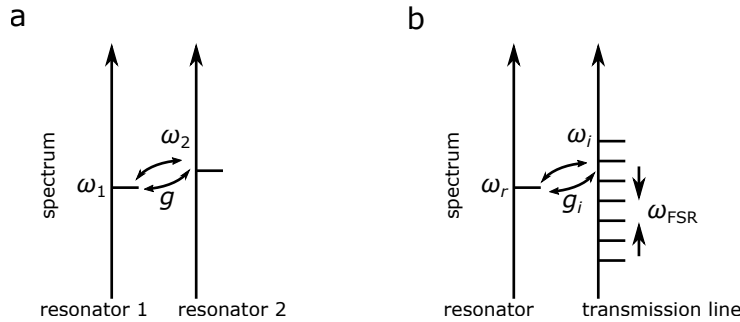


Figure 2.16: Interaction spectrum for (a) two coupled resonators; (b) a resonator coupled to a transmission line. The transmission line supports multiple modes whose frequencies are equally spaced by the free spectral range ω_{FSR} .

When the on-resonant coupling strength g_n becomes comparable with ω_{FSR} , the number

of modes needed to be taken into account becomes prohibitively large. For such case, a more practical approach is to use input-output theory [57, 27, 28], which treats the mode spectrum in the transmission line as continuous, and thus is well-suited for simulating the dynamics with large g_n/ω_{FSR} . Under this limit, a photon in the resonator exponentially decays into the transmission line. Denote the decay rate as κ , according to Fermi's golden rule,

$$\kappa = \frac{2\pi}{\hbar} (\hbar g_n)^2 \frac{1}{\hbar \omega_{\text{FSR}}}. \quad (2.128)$$

According to the input-output theory, the evolution of the resonator operator a_r in the Heisenberg picture follows [57]

$$\frac{da_r(t)}{dt} = -i\Delta\omega(t)a_r(t) - \frac{\kappa(t)}{2}a_r(t) + \sqrt{\kappa(t)}a_{\text{in}}(t), \quad (2.129)$$

with the reflection in the interface given by

$$a_{\text{out}}(t) = \sqrt{\kappa(t)}a_r(t) - a_{\text{in}}(t), \quad (2.130)$$

where a_{in} and a_{out} are the input and output field operators respectively, $\Delta\omega$ is the detuning between the resonator and the itinerant photons. If the output field is reflected back from the far end of the transmission line with efficiency η with a round-trip travel time τ , then we have

$$a_{\text{in}}(t) = \sqrt{\eta}a_{\text{out}}(t - \tau). \quad (2.131)$$

CHAPTER 3

CIRCUIT DESIGN

Circuit design plays a key role in the whole experiment flow. A good design is a prerequisite for a successful experiment. The circuit design rationale is discussed in detail in this chapter.

Our goal is to achieve high fidelity quantum state transfer and entanglement generation between remotely connected qubits. Although a lot of effort has been devoted to this goal, emitting and detecting itinerant photons efficiently is still a long-standing challenge. Naturally emitted itinerant photons have a sharp rising and exponentially decaying envelope, for which a receiver with fixed coupling can have at most 54% absorption fidelity even if it is identical and perfectly matched to the emitter [25, 26]. It is proposed that by using a tunable coupler to shape the emitted itinerant photon envelope and tuning the receiver coupler in a time-reversed manner, the fidelity of state transfer can reach 100% [27, 28], see the schematic in Fig. 3.1. Experimentally, the emission of a time-symmetric envelope photon state has been demonstrated in Ref. [58]. On the other hand, catching time-reversed microwave coherent state photons with 99.4% absorption efficiency using a tunable coupler and an external microwave source has been demonstrated in Ref. [59]. More recently, a few experiments have demonstrated the deterministic state transfer and entanglement generation between two separate chips with fidelities between 70% and 80% [21, 22, 23]. In these experiments, quantum states are transferred through a superconducting coaxial cable using microwave-controlled tunable coupling [60]. This microwave-controlled tunable coupling is

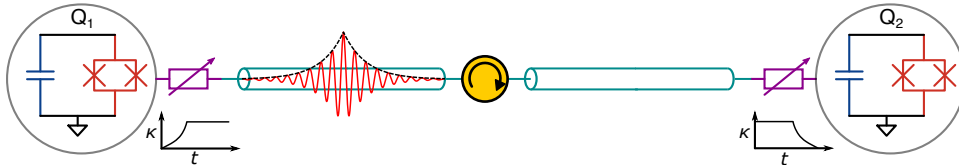


Figure 3.1: Quantum state transfer using time-reversal symmetry. Two qubits are coupled through an unidirectional channel via a pair of tunable couplers. An itinerant photon with time-symmetric envelope is emitted by properly tuning the emitting coupler. If the receiving coupler is tuned in the time-reversed manner, the itinerant photon can be caught with efficiency approaching 100%.

a second-order coupling, and is limited to less than about 10 MHz by the anharmonicity of transmon [60]. As a result, the state transfer speeds were significantly slower than the photon travel time in the channel, making reflections and their interference nearly unmanageable. To eliminate retro-reflections in the channel, a circulator has to be used to interrupt the channel in these experiments. But doing so also introduces significant loss, limiting the transfer fidelity to about 80%. If the tunable coupling can be sufficiently strong such that the state transfer process is faster than the photon round-trip travel in the channel, then the circulator can in principle be avoided, significantly reducing the channel loss.

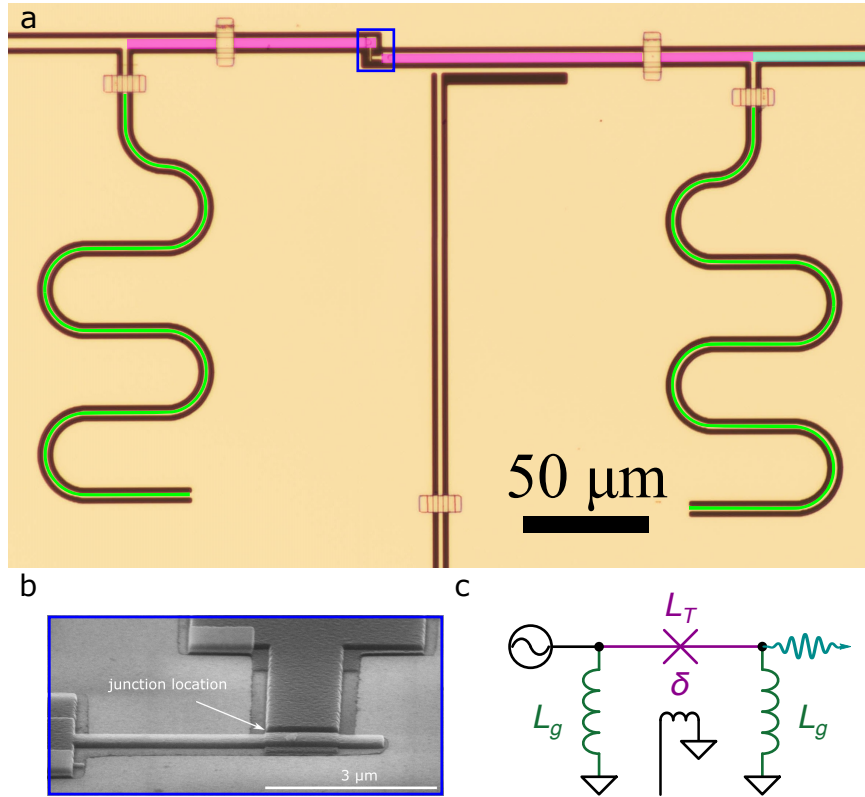


Figure 3.2: Gmon tunable coupler (design adapted from Ref. [54]). (a) Optical micrograph of a gmon tunable coupler. (b) Scanning electron microscope image of the coupler junction. (c) Schematic of the tunable coupler. The coupler junction is essentially a tunable inductance L_T . By controlling the external flux threaded through the loop formed by L_T and L_g , we can change the junction phase δ , hence L_T , thereby controlling the emission of the microwave signal.

In superconducting circuits, different kinds of tunable couplers have been explored, both between two qubits and between a qubit and a resonator [48, 49, 50, 51, 52, 55, 56, 53, 54].

The “gmon” tunable coupler [54], as shown in Fig. 3.2, distinguishes itself among these tunable couplers with its simple design, large tuning range, and high coherence. The coupler can be tuned from off to maximum coupling in just a few nanoseconds. These features make the gmon a promising candidate tunable coupler for highly efficient quantum state transfer.

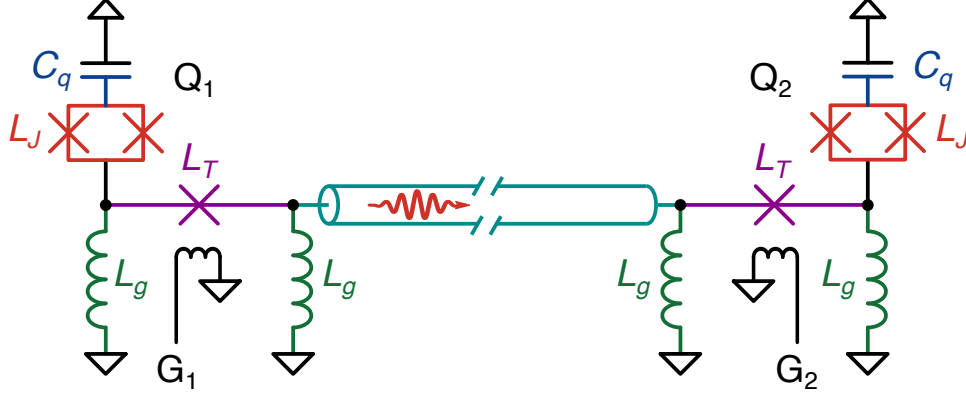


Figure 3.3: Circuit architecture for realizing high fidelity quantum state transfer and entanglement generation. The maximum coupling must be strong enough that the itinerant photon can be released and captured faster than the photon round-trip travel time in the channel, avoiding interference from the retro-reflections.

By adopting the gmon tunable coupler into our design, we obtain a circuit architecture for quantum state transfer as shown in Fig. 3.3. In Ref. [54], the coupling strength $g/2\pi$ can be tuned from off to 55 MHz between the two qubits. If we can achieve similar tuning range of the coupling between the qubit and the channel, we then can emit an itinerant photon into the channel in a time of around $\pi/2g = 4.5$ ns. If the channel is long enough that the photon round-trip travel time in the channel is longer than the emission time, then we can avoid interference from retro-reflections even without using a circulator, which introduces significant channel loss. In Ref. [61], a 68 cm-long CPW line was fabricated on a single sapphire chip with a free spectral range of $\omega_{\text{FSR}}/2\pi = 92$ MHz, corresponding to a round-trip travel time of $2\pi/\omega_{\text{FSR}} = 10.8$ ns, twice the photon emission time estimated above. It is therefore possible to use a similar length on-chip CPW delay line instead of a superconducting coaxial cable to connect the two qubits, further reducing the channel loss caused by the normal-metal connectors between the coaxial cable and the device.

Here we consider the detailed implementation of each circuit component in Fig. 3.3.

3.1 Xmon qubit

We adapt the Xmon qubit design from Ref. [62], with some modifications to accommodate the tunable coupler.

The capacitance of the qubit is provided by a cross-shaped high quality coplanar waveguide capacitor, the signature of the Xmon qubit [36]. This capacitance can be closely approximated by the coplanar waveguide formula:

$$C_q = \frac{8\epsilon_0 L(1 + \epsilon_r)K(k_0)}{K(\sqrt{1 - k_0^2})}, \quad (3.1)$$

where $\epsilon_0 = 8.85 \times 10^{-12}$ F/m is the vacuum permittivity, ϵ_r is the relative permittivity of the substrate, $k_0 = a/b$, and K is the complete elliptic integral (see section 2.2).

$C_q = 90$ fF is a reasonable value for a transmon that gives an anharmonicity of (see Eq. 2.115)

$$\eta/2\pi = -\frac{e^2}{2C_q}/\hbar = -215\text{MHz}. \quad (3.2)$$

According to Ref. [36], $a = 12 \mu\text{m}$, $b = 36 \mu\text{m}$ gives better coherence because widening the capacitor reduces the surface participation. With this configuration, Eq. 3.2 suggests that $L = 163 \mu\text{m}$ gives the desired capacitance, but numerical simulation with Sonnet¹, taking the control and readout coupling circuits into account, suggests that $L = 184 \mu\text{m}$ gives $C_q = 90$ fF.

The qubit capacitance can be analytically estimated due to its simple shape, but for other circuit components, e.g. the qubit XY control line and Z bias line, which have irregular shapes, numerical simulations must be carried out to balance between controllability and coherence of the qubit. We use Sonnet extensively to verify and optimize our designs.

1. <http://www.sonnetsoftware.com>

Before we start to design the XY drive line, we first estimate the reasonable range of the coupling capacitance C_d between the qubit and the XY control line. Assuming the on-resonant driving voltage amplitude is V_d , under linear approximation, the coupling Hamiltonian is given by

$$H_d = \frac{C_d}{C_q} V_d \hat{Q} = -i \sqrt{\frac{\hbar \omega}{2C_q}} C_d V_d (\sigma - \sigma^\dagger) = -i \hbar \Omega_d (\sigma - \sigma^\dagger), \quad (3.3)$$

where $\Omega_d = \sqrt{\frac{\omega}{2\hbar C_q}} C_d V_d$ is the qubit Rabi oscillation frequency. The typical wiring in the dilution refrigerator has -65 dB attenuation at around 6 GHz for the XY drive line, and the typical output power of the control electronics is -15 dBm, so the microwave drive power to the sample is $P_d = -80$ dBm. We can estimate that $V_d = 2\sqrt{2P_d Z_L}$ where $Z_L = 50 \Omega$ is the characteristic impedance of the XY line (note the open-ended node voltage is enhanced by a factor of 2 by reflection). The qubit typically operates at $\omega/2\pi = 6$ GHz with $C_q = 90$ fF, so we have

$$\Omega_d/2\pi = C_d \times 2 \sqrt{10^{-8-3} \times 50 \times \frac{6 \times 10^9}{6.63 \times 10^{-34} \times 90 \times 10^{-15}}} \text{ Hz/F} \quad (3.4)$$

$$\approx 0.45 \times C_d \text{ MHz/aF}. \quad (3.5)$$

For a coupling capacitance of $C_d = 30$ aF, the Rabi frequency is $\Omega_d/2\pi \approx 13.5$ MHz, the π pulse length is then $\pi/2\Omega_d = 18.5$ ns, a reasonable value. The quality factor due to the XY line load is given by

$$Q_{XY} = \left(\frac{C_q}{C_d}\right)^2 \frac{1}{\omega C_q Z_L} \approx 5 \times 10^7, \quad (3.6)$$

so the dissipation through the XY line is negligible. We conclude that $C_d = 30$ aF is a reasonable coupling capacitance.

We use Sonnet to simulate the circuit and find that by placing the XY drive line $80 \mu\text{m}$ away from an arm of the qubit cross capacitor, we obtain $C_d = 28$ aF, see the pattern below:

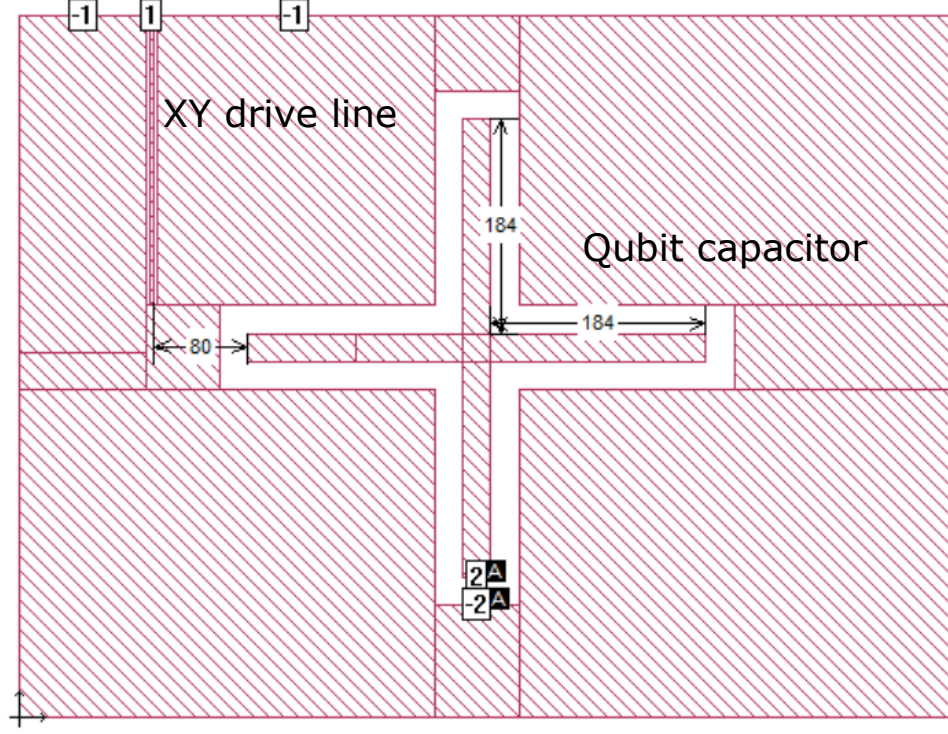


Figure 3.4: Sonnet simulation of the XY drive line. By placing a vertical XY drive line $80 \mu\text{m}$ away from an arm of the qubit cross capacitor, we obtain a $C_d = 28 \text{ aF}$.

The Z bias design is slightly more complicated. We want to achieve a reasonable mutual inductance M between the Z bias line and the qubit SQUID loop, while minimizing the stray coupling M_{stray} with the qubit resonant mode, see Fig. 3.5. The specific design here is adapted from the Xmon design in Ref. [62] with modification to accommodate the tunable coupler. Sonnet simulations indicate that $M = 2.22 \text{ pH}$ and $M_{\text{stray}} = 0.14 \text{ pH}$. The typical DC line wiring has $1.5 \text{ k}\Omega$ in the dilution refrigerator (see chapter 5), and the control electronics has a DC voltage output range of -2.5 V to 2.5 V (see section 5.2.5), so the mutual coupling here allows for a tuning range of about four flux quanta threaded through the SQUID loop:

$$\frac{MI}{\Phi_0} = \frac{2.2 \times 10^{-12} \times \frac{5}{1.5 \times 10^3}}{2.067 \times 10^{-15}} \approx 4, \quad (3.7)$$

which is enough for tuning the qubit frequency.

3.2 Gmon tunable coupler

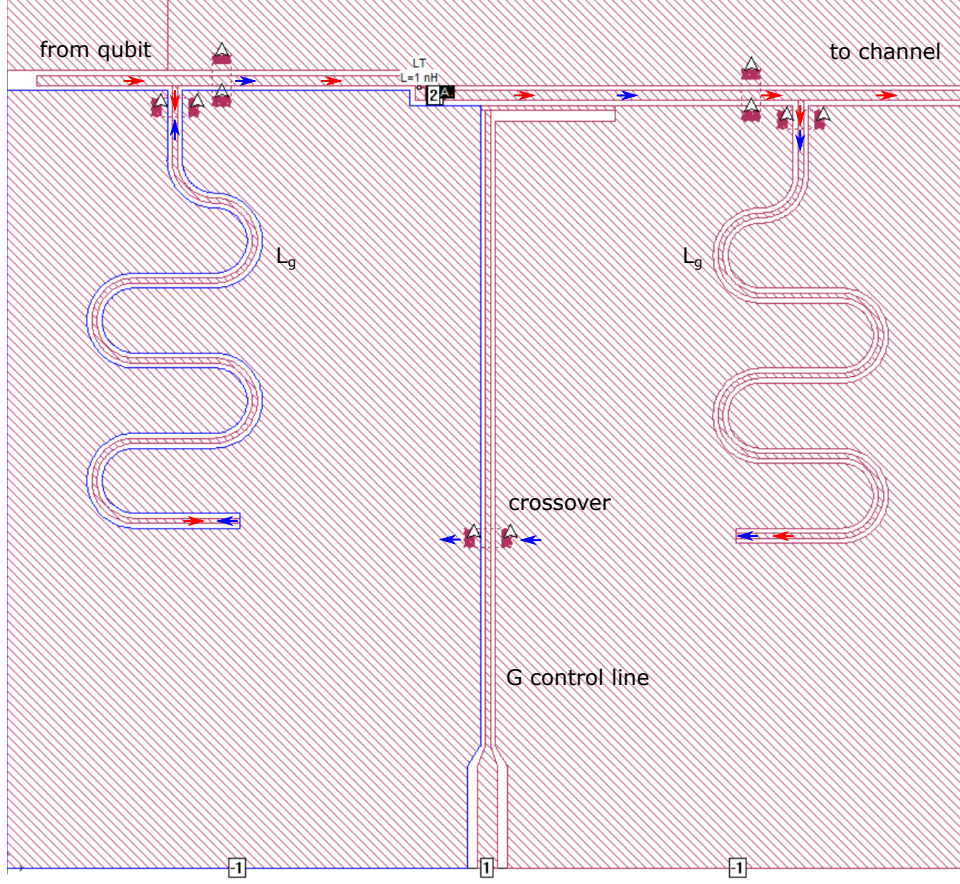


Figure 3.7: Sonnet simulation of the tunable coupler. The blue arrows indicate the circulating current flow that changes the superconducting phase δ across the tunable coupler junction. The red arrows indicate the current from the qubit that flows through the coupler, part of which is emitted to the channel. Several crossovers are placed in critical places to connect the ground planes together to suppress undesired slotline modes/stray coupling.

The tunable coupler design is adapted from Ref. [54] with modifications to the junction and the control line design to achieve larger dynamic tuning range of the coupling, see Fig. 3.7. Each L_g is made of a 400 μm -long CPW line with $W = S = 2 \mu\text{m}$. The G control line is designed to have $M_g = 1.7 \text{ pH}$ mutual inductance to the circulating current mode, allowing for efficient tuning of the superconducting phase δ across the coupler junction. The stray coupling of the qubit mode to the control line is verified to be less than 1 pH even if the coupler junction is shorted. Using the circuit transformation shown in Fig. 3.6, we a loaded

quality factor of $Q_g \gtrsim 10^7$, corresponding to an energy lifetime of about $300 \mu\text{s}$. The dissipation through the coupler control line is negligible even in the worst case.

3.3 Coplanar waveguide delay line

With the qubit and tunable coupler layout given, we then create a CPW delay line that is as long as possible to connect them together, while fitting everything into a custom aluminum sample holder designed for a $6 \times 15 \text{ mm}^2$ chip. Using PLayout (see Appendix B), we can create a 78 cm long meandered CPW line to connect the two qubits, covering most of the area of the chip. This CPW line has an estimated free spectral range of $\omega_{\text{FSR}}/2\pi = 79 \text{ MHz}$ and a round-trip travel time of $2\pi/\omega_{\text{FSR}} = 12.6 \text{ ns}$. 390 crossovers are evenly distributed along the line, every 2 mm, to suppress slot-line and other unwanted resonances. The design rationale is discussed below.

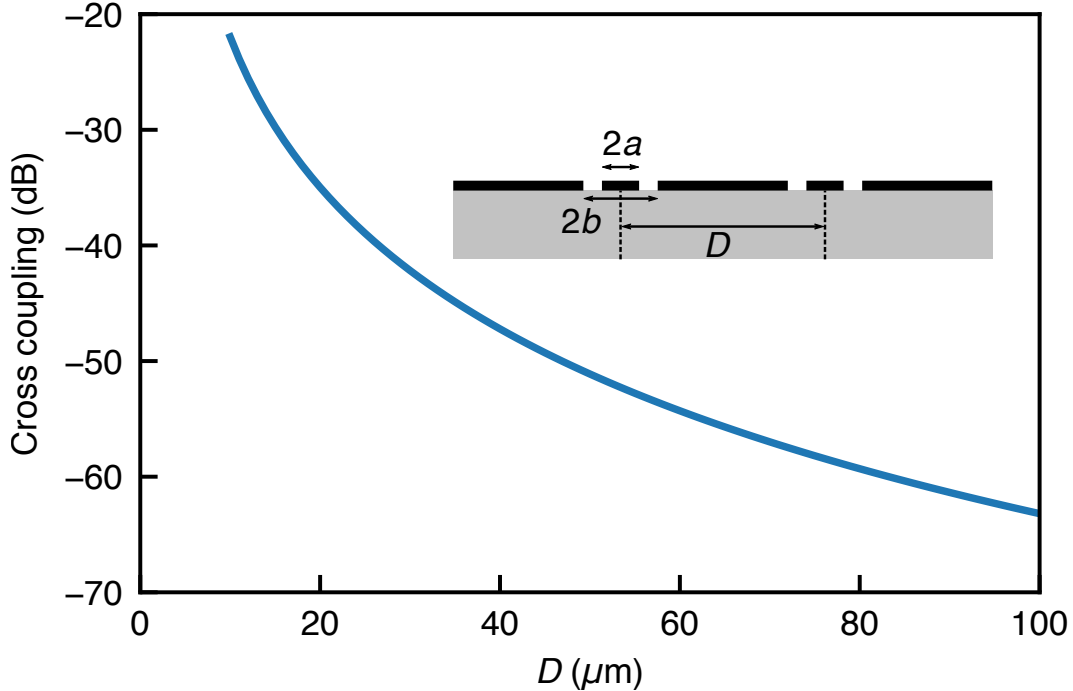


Figure 3.8: The cross coupling between neighbouring CPW segments versus their distance D . Inset: delay line cross section schematic, where the trace width is $2a = 4 \mu\text{m}$, and the ground planes separated by $2b = 8 \mu\text{m}$. At $D = 60 \mu\text{m}$, the cross coupling is as small as -54 dB .

The dimensions of the CPW line are chosen to be $a = 2 \mu\text{m}$, $b = 4 \mu\text{m}$ (see Fig. 3.9 inset). The neighbouring segments of the meandered line are separated by $D = 60 \mu\text{m}$, about one order of magnitude larger than the dimension of the CPW line, sufficient to reduce any cross coupling between adjacent CPW segments.

Following Ref. [63], the cross coupling between two parallel CPW lines is defined as

$$C = \frac{Z_e - Z_o}{Z_e + Z_o}, \quad (3.9)$$

where Z_e and Z_o are the even and odd mode impedances of the two CPW lines. If the coupling between them is small, it can be estimated with the following analytical expression:

$$C \approx 1 - \frac{K(k_1)K(k_2')}{K(k_1')K(k_2)}, \quad (3.10)$$

where K is the elliptic integral of the first kind, and

$$k_1 = \frac{2\sqrt{ab}}{a+b}, \quad (3.11)$$

$$k_2 = \frac{k_1}{[1 - (b-a)^2/D^2]^{1/2}}, \quad (3.12)$$

$$k_i' = \sqrt{1 - k_i^2}. \quad (3.13)$$

The estimated cross coupling between adjacent CPW lines versus their separation distance D is shown in Fig. 3.9. At $D = 60 \mu\text{m}$, the cross coupling is as small as -54 dB , which is negligible, so we set the CPW line distance to this value.

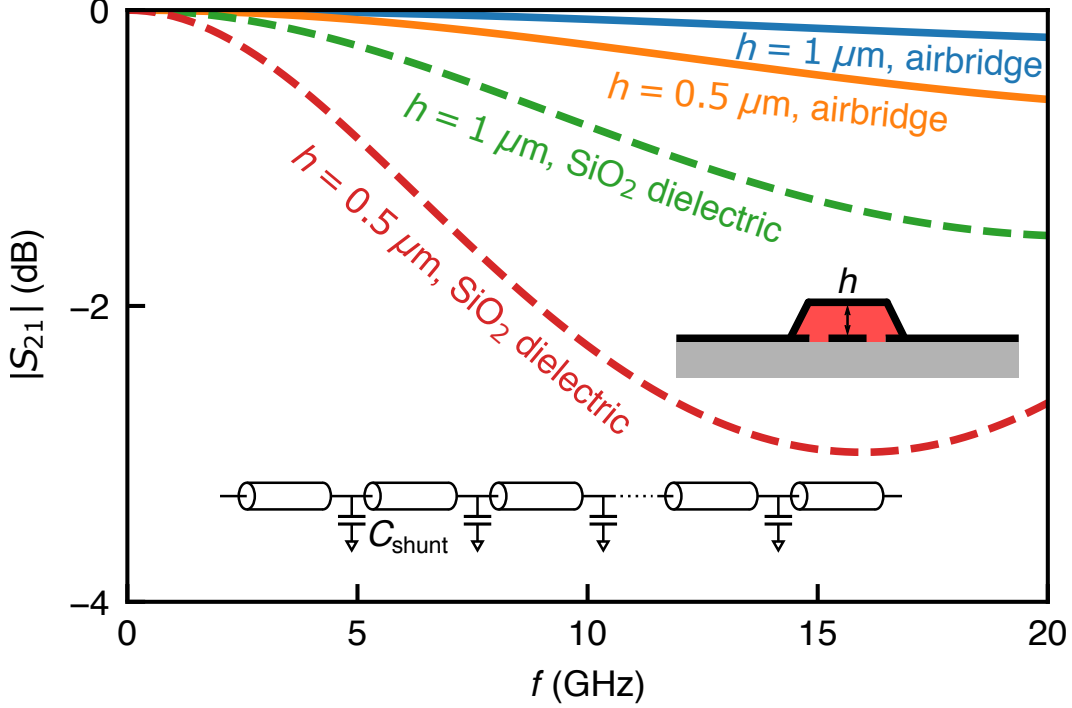


Figure 3.9: CPW delay line transmission ripples caused by the shunting capacitance C_{shunt} of each crossover. In the simulation, 390 crossovers are evenly distributed every 2 mm along the line. We find that the delay line transmission is hardly affected by the shunting capacitance of airbridge crossovers with $h = 1 \mu\text{m}$. Inset: crossover cross section schematic (middle); crossover shunting capacitance interrupting the delay line (bottom).

Slotline modes can be significant in the 78 cm long meandered CPW line due to the segmentation of the ground plane by the CPW trace. Crossovers can be used to suppress the slotline modes by connecting the ground planes together. Amorphous oxides such as SiO_2 are commonly used as the insulating layer for crossovers in conventional integrated circuits. However these oxides have loss tangents of order 10^{-3} at cryogenic temperature [64], which could reduce the quality of the circuit to 10^4 [65]. They are therefore not suitable for loss-sensitive resonant circuits except for the control wiring. To reduce the loss caused by the dielectric, airbridge crossovers have been developed [66, 65], where the scaffold layer, either made of photoresist or SiO_2 dielectric, is removed after the fabrication.

In addition to loss, the crossovers also introduce a small shunting capacitance C_{shunt} to ground, interrupting the continuity of the CPW line. While the shunting capacitance of a single crossover might be negligible, the shunting capacitance of 390 crossovers could

drastically affect the transmission of the delay line. Here we use the $ABCD$ matrix method (see Appendix C) to calculate the transmission parameter S_{21} of the delay line with a small shunting capacitance of

$$C_{\text{shunt}} \approx \frac{\epsilon_0 \epsilon_r \cdot 2aL}{h} \quad (3.14)$$

interrupting the delay line every 2 mm, where ϵ_0 is the vacuum permittivity, ϵ_r is the crossover dielectric constant, $L = 6 \mu\text{m}$ is the crossover width, and h is the crossover height.

The $ABCD$ matrix of a CPW line of length $\ell_a = 2 \text{ mm}$ is [29]

$$M_{TL} = \begin{bmatrix} \cos \beta \ell_a & iZ_0 \sin \beta \ell_a \\ i \sin \beta \ell_a / Z_0 & \cos \beta \ell_a \end{bmatrix} \quad (3.15)$$

where $\beta = 2\pi f \sqrt{L_\ell C_\ell}$ is the propagation constant. The $ABCD$ matrix of a shunting capacitance C_{shunt} is [29]

$$M_{\text{shunt}} = \begin{bmatrix} 1 & 0 \\ i2\pi f C_{\text{shunt}} & 1 \end{bmatrix} \quad (3.16)$$

The $ABCD$ matrix of a 78 cm CPW delay line interrupted by the shunting capacitance of 390 crossovers is simply the product of the $ABCD$ matrix of each component:

$$M_{\text{line}} = (M_{TL} M_{\text{shunt}})^{390} M_{TL} = \begin{bmatrix} A & B \\ C & D \end{bmatrix}, \quad (3.17)$$

from which we can calculate the delay line transmission:

$$S_{21} = \frac{2}{A + B/Z_0 + CZ_0 + D}. \quad (3.18)$$

The calculated S_{21} is shown in Fig. 3.9, with different crossover configurations. We see that the airbridge crossovers of $1 \mu\text{m}$ height has negligible impact on the transmission. However, if the crossover height is reduced to $< 0.5 \mu\text{m}$, or the SiO_2 dielectric is not removed,

the impact of the shunting capacitance on the transmission becomes more significant.

CHAPTER 4

FABRICATION

In the previous chapter, we have created a circuit layout aiming at high fidelity quantum state transfer and entanglement generation. In this chapter, we discuss the subsequent step, the device fabrication. The fabrication process can also provide feedback to the design, which is typical when developing a new fabrication process. For example, several iterations of design-fabrication has been spent to obtain a stable recipe for the airbridge fabrication process. All the fabrication in this thesis was done in the Pritzker Nanofabrication Facility (PNF), a brand new ISO Class 5 cleanroom located in the William Eckhardt Research Center.

4.1 Base layer

The base layer of our device is a 100 nm aluminum thin film deposited on sapphire wafer. We choose aluminum as the superconducting material for the following reasons: (1) high quality thin films of aluminum can be easily made using electron-beam evaporation due to its low melting point; (2) aluminum has a superconducting energy gap of about 100 GHz that is much larger than the qubit transition frequency; (3) and most importantly, aluminum can be easily and controllably oxidized to form a high quality Josephson junction. Both superconducting resonators and qubits fabricated from aluminum on sapphire have shown high quality factors and long coherence times [67, 36]. Other materials such as niobium [68], titanium nitride [69] and niobium titanium nitride [70] have also been used in superconducting circuits, but the junction oxidation step is challenging. Silicon can also be used as a low loss substrate for superconducting circuits. Compared to sapphire, silicon can be easily micromachined, opening up the possibilities of routing the circuits in the third dimension [71].

4.1.1 Deposition

Prior to deposition, we clean the bare sapphire wafer by sonicating it in acetone and isopropanol alcohol (IPA) for five minutes each, and then rinse the wafer with deionized water. After the cleaning, the wafer is first put in a spinner to spin water off the wafer, then heated on a 200° C hot plate for 10 minutes. After the dehydration, the wafer is loaded into the load-lock chamber of an Evo-Vac, a high-vacuum electron beam evaporation system made by Angstrom Engineering, Inc¹. When the chamber reaches high vacuum (10^{-7} Torr typically), high energy electrons (10 keV typically) are emitted to bombard the high purity aluminum target, which melts and evaporates into a gaseous phase and coats the wafer uniformly. The deposition rate is controlled at 0.2 nm/s, with the wafer rotated at a 5 rpm speed.

4.1.2 Lithography

After the deposition of the 100 nm aluminum film, we coat the wafer with AZ MiR 703 photoresist of 0.9 μm thickness, then pattern it using optical lithography. Traditionally, optical lithography requires the creation of a photomask or reticle made of a chrome-coated quartz plate. An exposure tool then projects the image of the photomask onto the wafer using an UV source, exposing the photoresist coated on the wafer. Alternatively, we use a maskless aligner, the MLA150 from Heidelberg instruments², which eliminates the need for a photomask, as the system exposes the pattern directly onto the photoresist-coated wafer with 1 μm resolution. Should design changes be required, they can be quickly implemented by changing the circuit layout without the need for a new reticle. This saves money as well as time and provides extreme adaptability. Exposing an area of a 4 inch wafer with structures as small as 1 μm can be finished in less than 20 minutes independent of the fill factor or the number of structures within this area. Alignment in multi-layer applications is achieved by using the integrated cameras with an accuracy of better than 500 nm.

1. <https://angstromengineering.com/>

2. <https://www.himt.de/index.php/MLA150.html>

AZ MiR 703 photoresist is typically developed in AZ 300 MIF developer. However, this developer can etch the base aluminum layer in a few minutes. This opens up the possibility for combining the development and etching process together in a single step, although this wet-etching method typically results in rough edges and is difficult to control. Instead, we prefer to use inductively coupled plasma (ICP) etching, as will be described below. To avoid the aluminum being etched by the developer, we typically use an alternative developer, AZ Developer 1:1, which does not attack aluminum, although sometimes its performance is not stable. In some case where AZ Developer 1:1 is not usable, we can coat a protection layer between the photoresist and the wafer, which will be described in section 4.2.

4.1.3 Etching

We etch the base layer aluminum in a Plasma-Therm Apex SLR Inductively Coupled Plasma (ICP) etcher³ with the parameters listed in Table 4.1.

ICP run power	400 W
bias run power	33 W
Cl ₂ flow	30 sccm
BCl ₃ flow	30 sccm
Ar flow	10 sccm
process pressure	5 mTorr
etch time	24 s

Table 4.1: ICP etch parameters.

3. http://www.plasma-therm.com/Apex_SLR.html

4.2 Airbridge

The airbridge fabrication recipe here is adapted from Ref. [65], although with a different photoresist stack and vapor HF etch tool.

4.2.1 Lithography and deposition

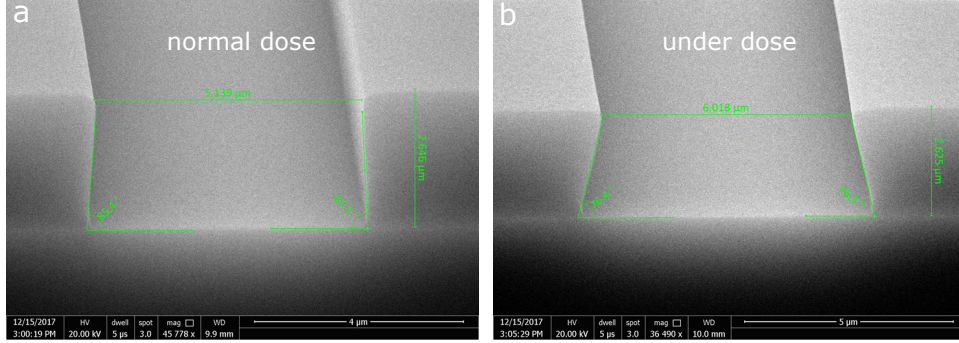


Figure 4.1: Negative photoresist nLOF2020 dose test. (a) nLOF2020 has an almost vertical profile with normal dose. (b) As a negative photoresist, nLOF2020 can achieve a 76° retrograde profile when under-dosed, which is preferable for a lift-off process.

As we calculated in section 3.3, to reduce the impact of the airbridge shunting capacitance on the delay line transmission, the airbridge height is chosen to be $1 \mu\text{m}$. This requires the deposition of a $1 \mu\text{m}$ SiO_2 scaffold layer using lift-off. For such a thick layer lift-off, a much thicker photoresist stack with a large undercut profile is required. This is typically achieved using a bi-layer resist with different dose sensitivity for each layer, where the less sensitive top layer resist defines the pattern and the bottom layer resist defines the undercut [65]. Alternatively, a large undercut can be obtained with a negative photoresist when under-dosed, see the dose test of nLOF2020 in Fig. 4.1 for example. We find that the thickness and the undercut of nLOF2020 is enough for the lift-off deposition of a $1 \mu\text{m}$ thick SiO_2 layer and the subsequent 500 nm thick top Al layer.

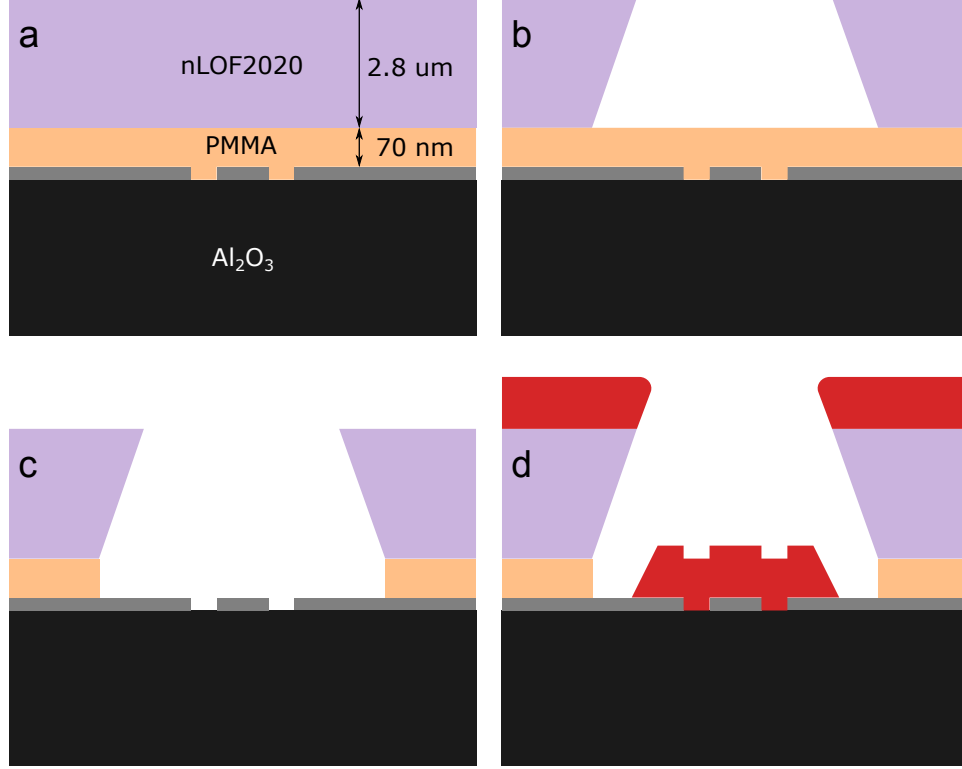


Figure 4.2: Schematic for SiO₂ layer lithography and deposition. (a) nLOF2020/PMMA bi-layer resist stack (not to scale), where the nLOF2020 is 2.8 μm thick, the PMMA is about 70 nm thick. (b) Under-dosed optical lithography with retrograde profile suitable for lift-off. (c) Removal of the PMMA e-beam resist by O₂ downstream ashing. (d) Deposition of 1 μm SiO₂ using electron beam evaporation.

nLOF2020 can be developed in AZ 300 MIF, but as mentioned in the previous section, this developer can attack the base layer Al. Following Ref. [65], we coat a thin PMMA (950K Polymethylmethacrylate 2% in Anisole) layer beneath the nLOF2020 layer to protect the base Al layer during the development, see Fig. 4.2(a). The PMMA layer is removed by O₂ downstream ashing after the development using the YES-CV200RFS Downstream Asher⁴ (Fig. 4.2(c)). We then deposit a 1 μm SiO₂ layer using electron beam evaporation (Fig. 4.2(d)). The 500 nm thick top aluminum layer is deposited using the same lithography step, except that the deposition is preceded by *in situ* ion mill to remove the native oxide of the base Al layer, forming galvanic contact between the top and bottom Al layers.

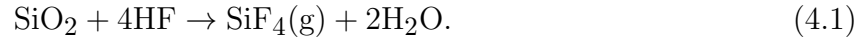
Note: we have observed obvious loading effects in the O₂ downstream ashing process,

4. <https://www.yieldengineering.com/Products/Plasma-Strip-Descum-Systems/CV200RF-Series>

i.e., the PMMA etch rate depends on the size of the wafer. The time needed to completely remove the PMMA layer for a full 4 inch wafer is about 60% longer than that for a quarter of a 4 inch wafer.

4.2.2 Release the SiO_2 scaffold

The SiO_2 scaffold is released using vapor hydrogen fluoride (HF):



This process is widely used for Micro-Electro-Mechanical Systems (MEMS) applications and is fully compatible with the qubit fabrication process, i.e., the vapor HF does not attack other materials like aluminum, aluminum oxide, silicon or sapphire in the qubit fabrication. Because the airbridge is mechanically fragile after releasing the scaffold, this process is done in the last step, after the Josephson junctions are fabricated and the wafer is diced up.

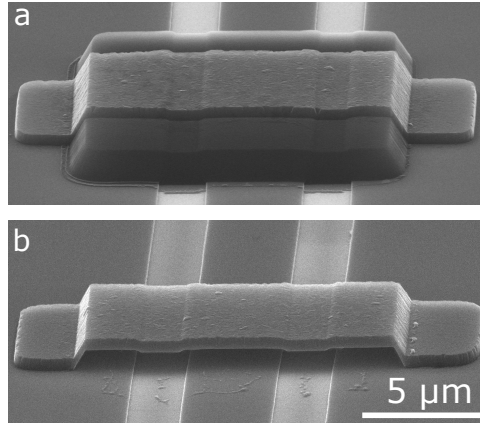


Figure 4.3: (a) Crossover with the SiO_2 scaffold. (b) Free-standing crossover after releasing the SiO_2 scaffold using vapor HF etch.

We use the Memsstar Orbis Alpha system⁵ to do the vapor HF etch. A batch of dies is loaded into the chamber first, then the chamber is pumped down to ~ 0.1 Torr. A mixture of HF vapor, nitrogen, and H_2O vapor is then bled into the chamber, with the pressure

5. <https://memsstar.com/mems-tools/wafer-processing-system-orbis-alpha-rd/>

gradually ramped up to 15 Torr in about 20 seconds, held at 15 Torr for 30 seconds, then rapidly ramped down in about 5 seconds. The SiO_2 scaffold is removed in the end, as shown in Fig. 4.3. The detailed etch parameters are tabulated in Table 4.2.

HF flow	40 sccm
N_2 flow	20 sccm
H_2O flow	5 mg/min
Pressure	15 Torr
Pressure ramp up time	~ 20 s
Etch time	30 s
Pressure ramp down time	~ 5 s

Table 4.2: Vapor HF etch parameters.

Note 1: There is often residue left on site after the SiO_2 is etched. Care must be taken when cleaning the die, as the airbridge is not strong enough to sustain sonication. We find that most of the residue can be removed by simply rinsing with acetone and IPA. The residue is likely inorganic, as it cannot be removed by O_2 descum.

Note 2: The etch time and pressure here are chosen so that the SiO_2 is slightly over-etched. According to Ref. [65], heavy over-etch can affect the device performance.

4.3 Josephson junction

The Josephson junctions in this thesis have a minimum feature size of about 200 nm, which is too small for the optical lithography tools we have in the PNF. Instead, we use a Raith EBPG5000 Plus E-Beam Writer to fabricate the junctions, which is an electron beam lithography system with a minimum feature size smaller than 8 nm when operating at 100 kV beam voltage. Prior to the electron beam lithography, Ti/Au alignment marks are patterned on the substrate using optical lithography and deposited with electron beam evaporation for

aligning the junction layer with the base aluminum layer.

4.3.1 Dolan bridge

We use the Dolan bridge technique [72] to fabricate the junctions, as illustrated by the schematic in Fig. 4.4. This fabrication process is almost directly adapted from Ref. [62]. A bi-layer e-beam resist stack with a 300 nm PMMA (950K Polymethylmethacrylate 4% in Anisole) layer on top of a 500 nm methacrylic acid (MAA) copolymer layer is used for creating patterns with a well-defined undercut area, see Fig. 4.4(a). MAA is more sensitive to the e-beam dose than PMMA. A $350 \mu\text{C}/\text{cm}^2$ exposure dose at 100 kV beam voltage is enough for the MAA layer to be fully exposed while the PMMA layer is hardly affected; a $1500 \mu\text{C}/\text{cm}^2$ dose is enough to expose both resist. This property allows us to create patterns with defined undercut area by controlling the exposure dosage across the pattern. Fig. 4.4(b) shows the lithography pattern for a Josephson junction, with different e-beam dosage for each region, defining the junction pattern, the undercut area and the electrode connection area. After exposure, the resist is developed in 3:1 IPA/MIBK mixture for 40 seconds with gentle agitation.

After e-beam lithography, the Josephson junction is fabricated in a Plassys electron beam evaporator⁶ using double angle deposition. Prior to the metal deposition, we typically use an *in situ* Ar-ion mill to remove the native oxide of the base layer electrodes to create galvanic contact between the junction layer and the base layer electrodes. As will be mentioned below, this method has some issues, which can be addressed with an additional bandage layer. We first deposit a 65 nm thick Al layer at 60° tilt angle, resulting in a shifted junction pattern (magenta region in Fig. 4.4(b)). This metal is then controllably oxidized in the Plassys chamber for 50 minutes under 30 mbar pressure (15% O₂ in Ar), forming a thin AlO_x barrier layer, which is followed by a second deposition of a 100 nm thick Al layer at normal angle (red region in Fig. 4.4(b)). A small junction is formed in the overlapping region

6. <https://plassys.com/>

of the two depositions. The junction critical current can be tuned by adjusting the junction's width and height. The importance of the Dolan bridge is clear here: without the bridge, the small junction is shorted.

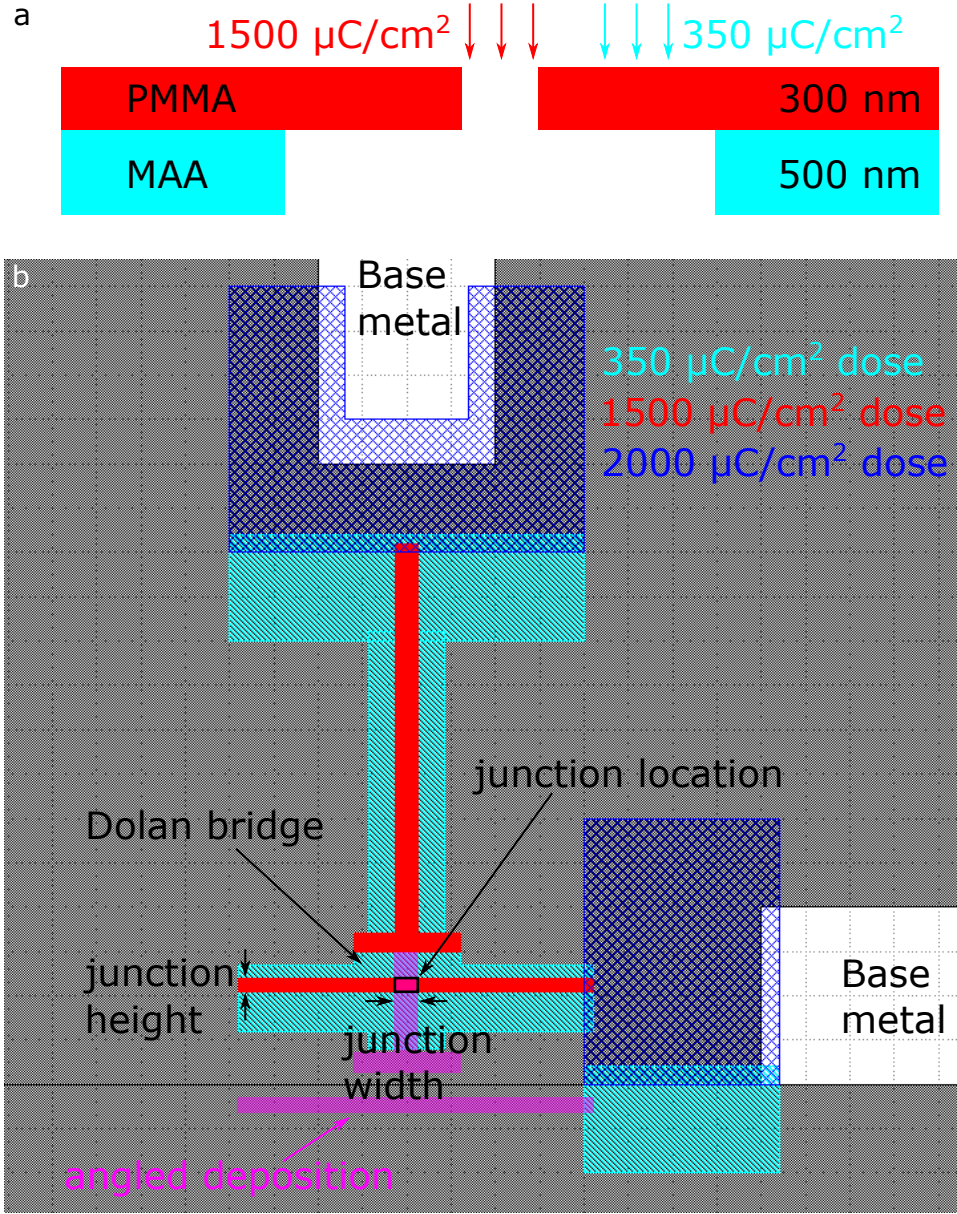


Figure 4.4: Schematic for junction fabrication. (a) PMMA/MAA bi-layer e-beam resist stack. By controlling the e-beam dosage, one can create a pattern with defined undercut area. (b) The junction lithography pattern. The cyan region is exposed with a $350 \mu\text{C}/\text{cm}^2$ dose, defining the undercut area; The red region is exposed with a $1500 \mu\text{C}/\text{cm}^2$ dose, defining the junction pattern; The blue region is exposed with a $2000 \mu\text{C}/\text{cm}^2$ dose, defining the connection area with the base metal electrode. See the main text for junction double angle deposition.

A Josephson junction fabricated with the Dolan bridge technique is shown in Fig. 4.5.

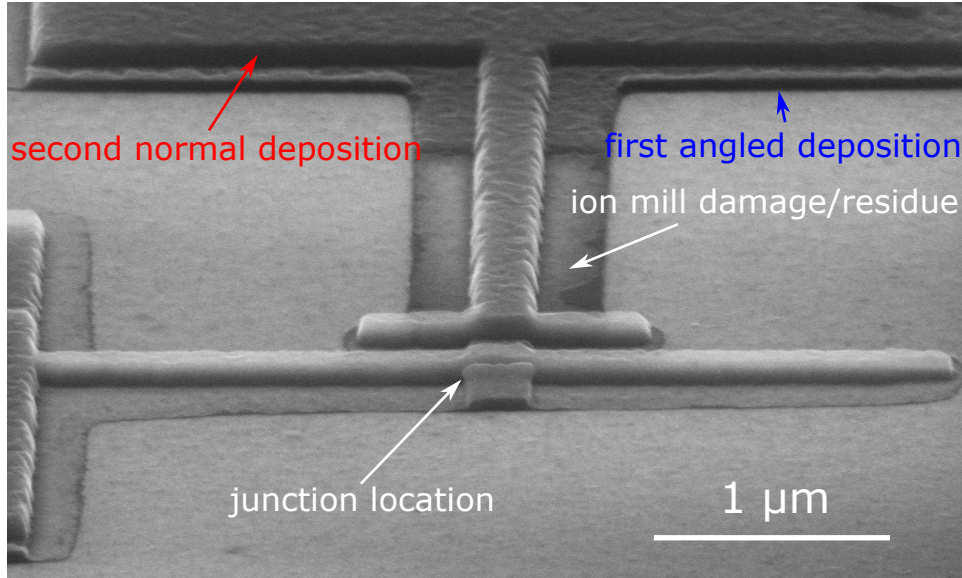


Figure 4.5: 70° tilt angle SEM image of a Josephson junction fabricated with the Dolan bridge technique. A small junction is formed in the overlapping area of the first angled deposition and the second normal deposition. Near the junction electrodes, substrate damage from the ion mill can be seen.

4.3.2 Bandage

In Fig. 4.5, besides the desired features, we can see some darkened regions near the junction electrodes, where the substrate surface is damaged during the Ar-ion mill process [73]. When connecting the junction to a capacitor to form a qubit, the capacitance of the junction electrodes is just a small fraction of the total qubit capacitance, but due to its small feature size, the nearby electric field is more concentrated in the dielectric volume close to the junction and can contribute substantially to the total dissipation. Following Ref. [73], we remove the ion mill step in the junction fabrication, and instead use a bandage layer to create galvanic contact between the junction layer and the base layer electrodes, see Fig. 4.6. The deposition of the bandage layer is preceded by an *in situ* Ar-ion mill to remove the native oxide of the junction and the base metal layer, but distinct from typical junction fabrication process, the substrate is not exposed in this step, hence not damaged by the ion mill. The

detailed ion mill parameters are listed in Table 4.3.

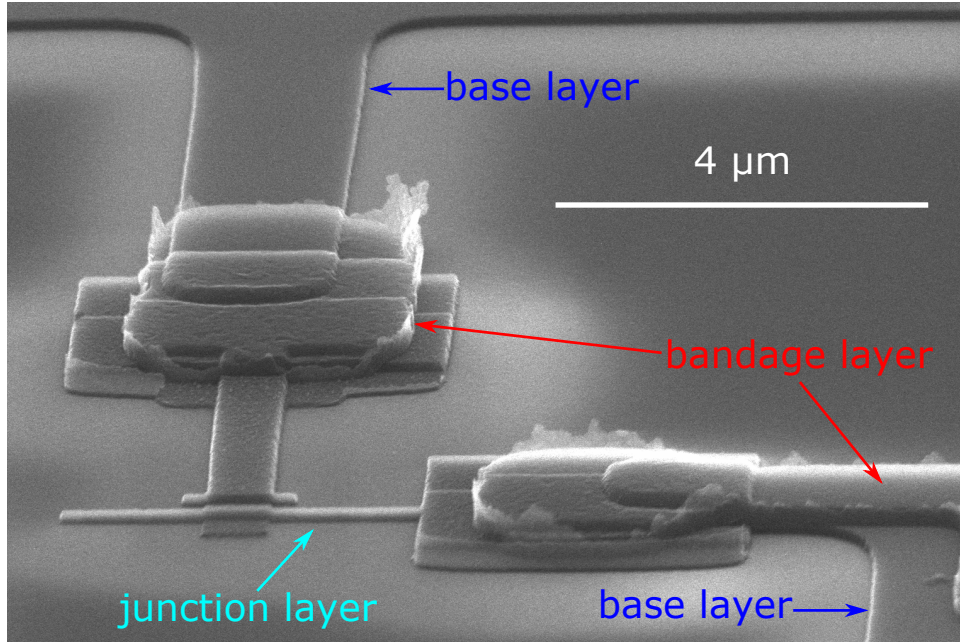


Figure 4.6: Bandage layer connecting the junction layer and the base aluminum layer. The substrate damage or ion mill residue is not seen here.

Ar flow rate	6 sccm
Pressure	4.5×10^{-4} mbar
Beam voltage	400 V
Accelerating voltage	80 V
Beam current	15 mA
Etch time	4 minutes

Table 4.3: Ar-ion mill parameters.

Note 1: The actual junction area is substantially expanded by the ion mill in the non-bandage junction fabrication process. If the bandage method is adopted, the junction area has to be adjusted to compensate for this effect.

Note 2: The Kaufman source we use for Ar-ion mill is not quite reliable, which can cause failure in the non-bandage junction fabrication process. In contrast, the bandage layer is

more tolerant of fluctuations in the ion mill process due to the large feature size. This is another benefit of the bandage method in addition to the prevention of substrate damage.

Note 3: The 4 minutes ion mill time is slightly over in the bandage process to make sure the native oxide is completely removed. For no-bandage junction fabrication, 3 minutes and 30 seconds is enough to remove the native oxide on the base electrodes.

4.3.3 Room temperature test

The Josephson junction is the most delicate component in the device due to its small size and the thin oxidation layer. Most of the failures in the experiments are caused by a shorted or open junction, or a junction with too high/low critical current. Because it takes days to cool down the dilution refrigerator before we know if the device is working or not at cryogenic temperature, it is therefore very important to do some room temperature tests of the junctions on each die, to diagnose if the junctions are working properly, and pick the most promising die to wirebond and cool down. For this purpose, we typically put a few test junction structures on the periphery of each die, with four test pads available to measure the DC resistance of the junctions using a probe station. Care must be taken to avoid blowing out of the junctions from electrostatic discharge during the resistance measurement.

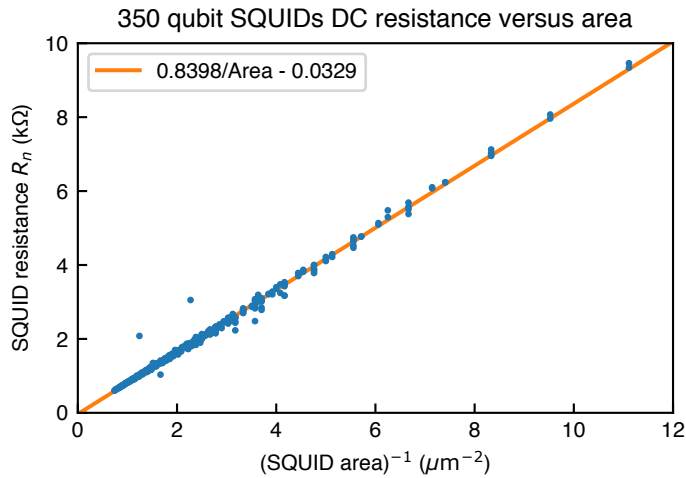


Figure 4.7: Qubit SQUID DC resistance measurement.

We performed extensive measurements on test junctions and find that the junction room

temperature resistance R_n is inversely proportional to the total junction design area over a broad dimension range. In Fig. 4.7, we show the R_n of 350 qubit SQUID junctions from a single deposition, with SQUID areas (twice the single junction area) varied from $0.09 \mu\text{m}^2$ to $1.35 \mu\text{m}^2$. We find that R_n fits well with the linear curve

$$R_n(k\Omega) = \frac{0.8398}{\text{Area } (\mu\text{m}^2)} - 0.0329. \quad (4.2)$$

In Fig. 4.8, we show the R_n of 350 tunable coupler junctions from a single deposition whose feature size are much larger than the qubit junctions, with junction areas varied from $0.88 \mu\text{m}^2$ to $3.136 \mu\text{m}^2$. We find that R_n fits well with the linear curve

$$R_n(k\Omega) = \frac{0.7730}{\text{Area } (\mu\text{m}^2)} + 0.0418. \quad (4.3)$$

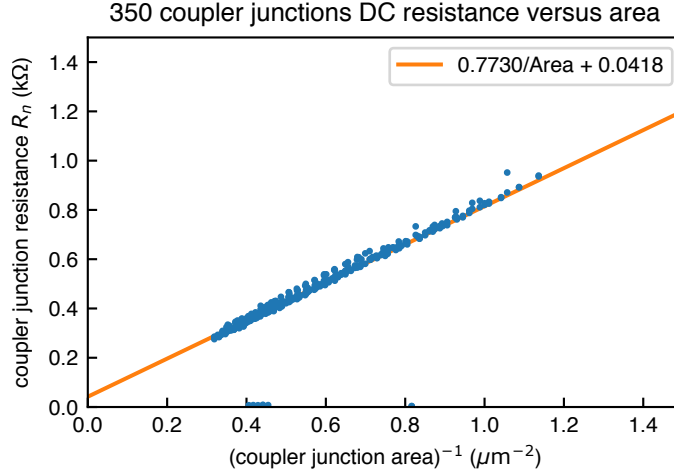


Figure 4.8: Coupler junction DC resistance measurement.

We note that the resistance versus area relationship is very sensitive to the junction fabrication conditions, especially the junction oxidation pressure and time, the application of ion mill etc. Nevertheless, we find that the empirical relationship obtained here is quite repeatable with the same fabrication recipe.

According to the Ambegaokar-Baratoff relations for Josephson junction [74], the critical

current I_0 of a junction is related to its normal resistance at critical temperature \tilde{R}_n as:

$$I_0 = \frac{\pi\Delta}{2e\tilde{R}_n} \quad (4.4)$$

where Δ is the superconducting gap. Experimentally, we find that the coupler junction obeys this rule very well by directly replacing the critical temperature \tilde{R}_n with the room temperature R_n in Eq. 4.4. This thus gives us a guideline to target for a coupler junction with desired coupling range.

Unfortunately, the qubit junctions are too small in size that the proximity effect becomes significant, and as a result they do not follow the same rule as the coupler junctions. Still, we have found an empirical formula that the maximum qubit frequency f_{\max} is roughly determined by the SQUID room temperature resistance R_n as

$$f_{\max} = \frac{12.3}{\sqrt{R_n}} \text{GHz}/\sqrt{\text{k}\Omega}, \quad (4.5)$$

for a qubit with 90 fF capacitance. This empirical rule, together with the fitting result in Fig. 4.7 provides a guideline to target for junctions with desired qubit frequency range.

EXPERIMENTAL SETUP

Figure 5.1 shows the schematic of the experiment setup in this thesis, illustrating the overall control and readout wiring inside the dilution refrigerator and the corresponding electronics at room temperature. In this chapter, we discuss the details about the experiment setup, especially the custom electronics.

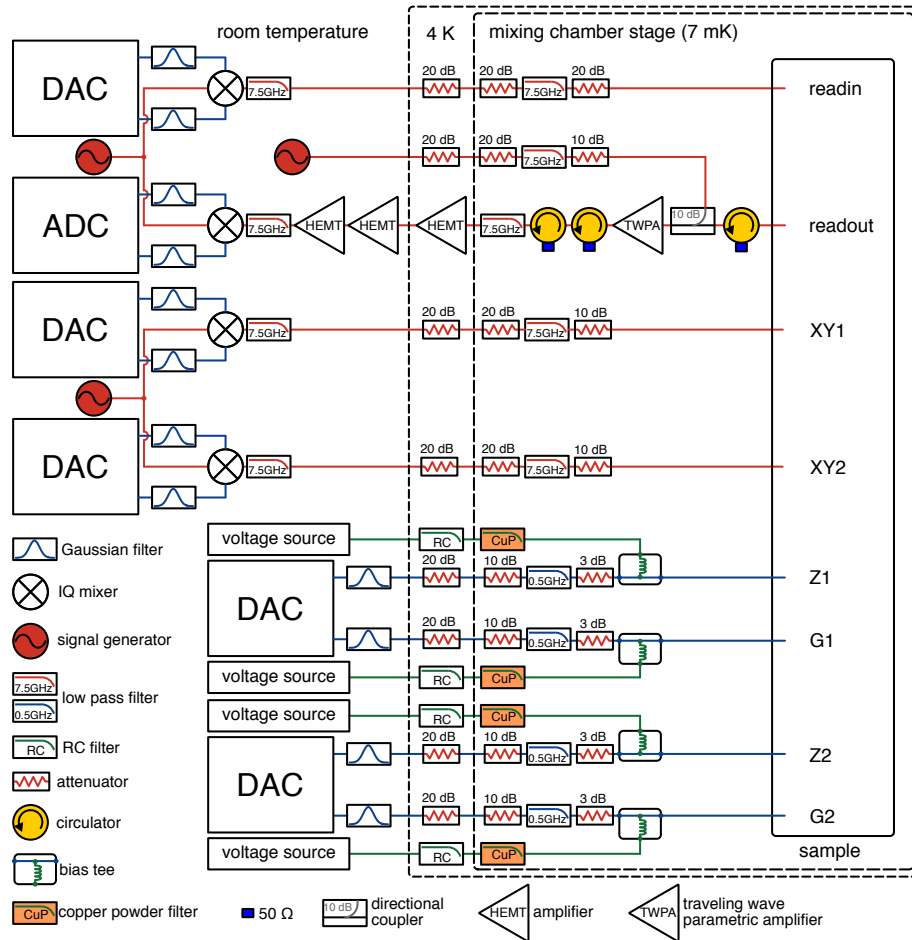


Figure 5.1: Schematic for electronics and wiring setup. Red lines correspond to RF/microwave signals for qubit XY control and measurement, blue lines correspond to intermediate frequency (IF) signals for fast qubit Z or coupler control, and green lines correspond to quasi-DC signals for steady qubit Z or coupler bias offset. The IF and DC signals for each bias channel are combined using a custom-made cryogenic bias tee mounted at the mixing chamber stage.

5.1 Dilution refrigerator

Microwave quantum states are vulnerable due to their susceptibility to thermal excitation, electronic noise and magnetic noise from the environment. The frequency range of the superconducting quantum circuits is typically several GHz, which corresponds to a few hundred milliKelvin thermal noise level. To protect the quantum state from thermal excitation, a cryogenic environment with a temperature much lower than a hundred milliKelvin is required. In this thesis, we used a BlueFors BF-LD400 dilution refrigerator¹ (DR) as our cryogenic platform which can reduce the temperature of its mixing chamber stage, the coldest part in the DR, to below 7 mK. To allow access to the device from outside the DR, 40 microwave coaxial cables have been installed in the DR. Attenuators, low-pass filters, copper powder filters and many other components are included in the wiring to reduce electrical noise. The device package is enclosed in a double-layer magnetic shield made of high permeability μ -metal to reduce DC and low frequency magnetic noise. A low-noise cryogenic High Electron Mobility Transistor (HEMT) amplifier with nominal 39 dB gain and 4 Kelvin noise temperature is installed at the 4 K stage of the DR to amplify the readout microwave signal.

5.2 Electronics

We used custom electronics extensively in this thesis. Some of them came from the University of California-Santa Barbara (UCSB), some were developed at the University of Chicago. While all the custom electronics have commercial counterparts, the major motivation for customization is cost, integration and fun. Generally speaking, the cost for custom electronics is about one order of magnitude smaller than their commercial counterparts. More than that, we can integrate different parts on a single board to make the electronics system more compact and scalable for more complicated quantum experiments. The specifications of our

1. <https://www.bluefors.com/index.php/ld-series>

custom electronics are discussed below.

5.2.1 GHz DAC board

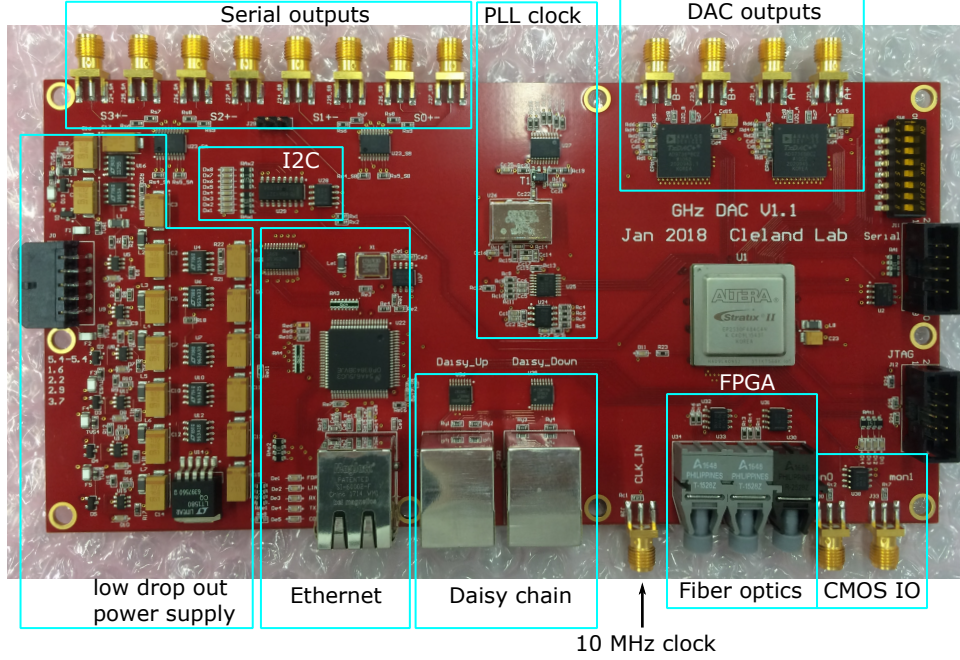


Figure 5.2: Custom made DAC board.

We use custom GHz Digital to Analog Converter (DAC) boards for qubit control and measurement. The DAC board can generate nanosecond-scale bias pulses for fast qubit Z control, or modulate the envelope of a microwave frequency signal with an IQ mixer (see section 5.2.3), which can be used to implement the qubit X and Y rotation or drive the readout resonator feedline for scattering measurements (see section 2.3.3).

The GHz DAC board we used in this thesis was originally designed by Prof. John Martinis at UCSB [75]. Recently we have reproduced Martinis’s design with slight modifications, see Fig. 5.2. The specification of the DAC board used to be publicly available². For the integrity of this thesis, and for documentation purposes, the specification is replicated here (with slight modifications):

². <https://web.physics.ucsb.edu/~martinisgroup/electronics.shtml>

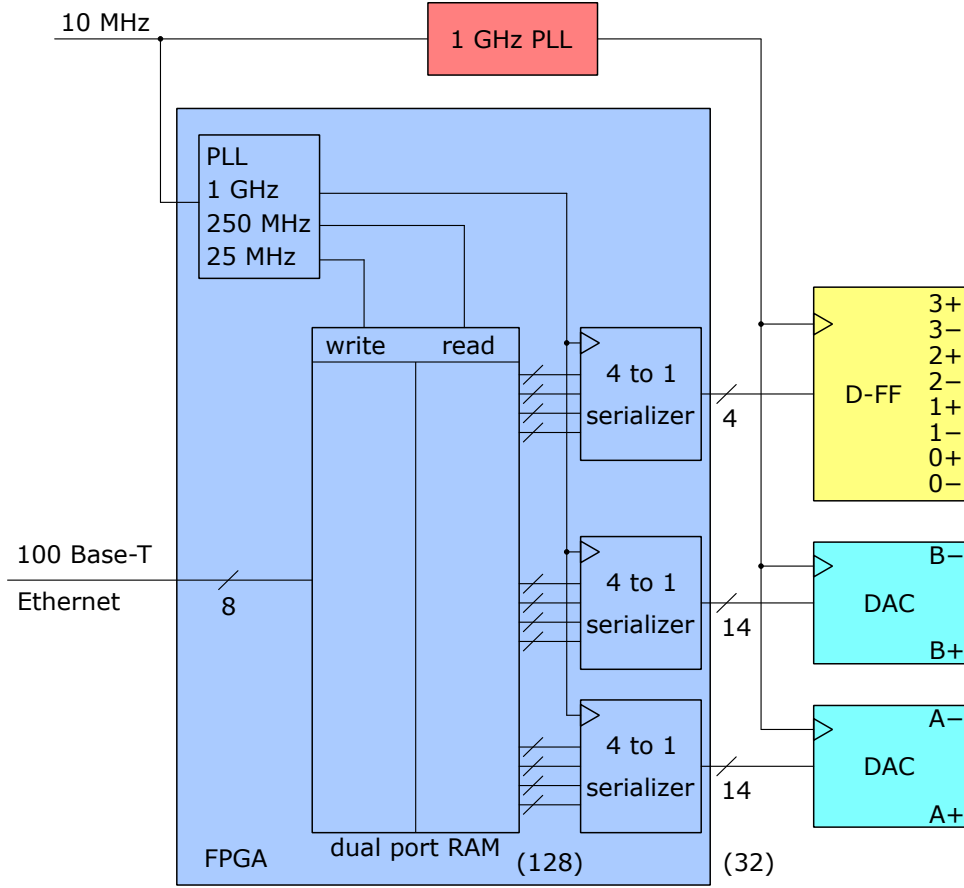


Figure 5.3: Block diagram of the DAC board.

The DAC board uses two AD9736 D/A converter chips³ from Analog Devices, Inc. to generate output waveforms, and an Altera Stratix II field-programmable gate array (FPGA)⁴ to store, manage, and generate the digital data. The FPGA is controlled by the computer through a 100 base-T Ethernet interface. A 10 MHz clock input and a 250 MHz low-voltage differential signaling (LVDS) daisy-chain interface allows multiple DAC boards to be synchronized together. Additional serial, CMOS, Versalink fiber optic, and I2C interfaces are provided for greater connectivity. The board is powered through low-dropout voltage regulators with input protection and fuses.

Figure 5.3 shows a block diagram for the board, outlining the Ethernet interface, the

3. <http://www.analog.com/en/products/ad9736.html>

4. part number: EP2S30F484C4N

phase-locked-loop (PLL) clock distribution, the main FPGA structures, two DACs and four D flip-flop digital serial outputs. The 10 MHz input reference drives a 1 GHz PLL clock connected to the outputs and three clocks internal to the FPGA. Dual-port static random-access-memory (RAM) in the FPGA stores the waveform data, which can be downloaded to the FPGA via an Ethernet interface. The data is read from the RAM at 250 MHz with a 128-bit width bus, which is then serialized to 32 bits with 4-to-1 serializers at 1 GHz and sent to the outputs.

DAC: The AD9736 D/A converter gives a spurious free dynamic range (SFDR) of 77 dBc at 100 MHz and 55 dBc at 500 MHz when the output is (optimally) connected with a differential drive. The loss of 2 to 4 bits of effective resolution is typical of high-speed DACs, and the choice of a 14-bit DAC ensures sufficient waveform accuracy even when using the DAC at high frequencies. The output current of the device is nominally 20 mA. With a 50 Ohm double termination, the single-ended output voltage ranges from 0 to 0.5 volts. Note that the clock feedthroughs at multiples of 1 GHz are quite strong, especially the 2 GHz clock feedthrough which is approximately 6 dBc at full scale. Custom Gaussian filters are constructed to suppress these clock feedthroughs, see section 5.2.2.

FPGA: The digital data that is used to generate the output waveforms is stored and controlled by an Altera Stratix II FPGA. The internal FPGA logic is clocked at 250 MHz, and high-speed parallel-to-serial converters produce the 1 GHz output data stream (2x14 bits wide) that is transmitted to the DAC chips. The waveform is limited to 16 μ s by the on-chip memory capacity of the FPGA.

Clock: The input frequency to the board is 10 MHz, clocked by a Rubidium frequency standard from Stanford Research Systems. In order to achieve small amplitude errors, high-speed DACs need a very low magnitude of clock jitter, typically less than 1 ps. A high-performance voltage-controlled oscillator (VCO) and PLL is used to generate the main 1 GHz clock signal that is then distributed via ECL logic to the DAC converters and D flip-flops. A low phase noise reference is mandatory in order to obtain good DAC performance.

The digital logic in the FPGA uses internal clocks with jitter performance around 100 ps. All high-speed signals from the FPGA are reclocked by the low phase-noise 1 GHz clock on the board to reduce jitter on all output signals to the ps level. Jitter in the DACs and serial outputs are in the few ps range.

Ethernet Interface: The FPGA is controlled and data is downloaded through a 100 base-T Ethernet interface. For simplicity in coding the FPGA, the standard TCP/IP protocol has not been implemented. Instead the lower-level IEEE 802.3 standard has been used, which defines a data packet based on a 6 byte destination IP address, a 6 byte source IP address, a 2 byte length, and then 46 to 1500 bytes of data. Each board can be programmed to have a unique IP address, with the lowest 6 bits defined by the lowest 6 bits of the dipswitch. For interfacing to a computer, this low-level interface requires a dedicated Ethernet port to connect to one or multiple boards. Open-source interface and control software (see section 5.3) is available that may be used to directly program waveforms into the DAC board. LEDs indicate proper link conditions and receive and transmit activity on the Ethernet wires.

Digital Serial Outputs: Four channels of GHz digital serial outputs are also available, with timing and programming capabilities as for the DAC digital data. These outputs are 3.3 V PECL, generated by D flip-flops clocked from the low phase-noise GHz clock. Typical timing jitter is a few ps. These outputs are typically used as a low-noise trigger for the DAC waveforms.

High-speed LVDS daisy chain: Data and synchronization signals may be sent from board to board via two Ethernet-style connectors that each have 2 digital LVDS inputs and outputs. This interface can operate at the 250 MHz clock rate of the internal FPGA logic, and is used primarily to synchronize the start of the output waveforms through daisy-chain connections between all boards (see section 5.2.6). In order to present a well-defined clock phase to all of the boards, the 10 MHz clock input must be driven with clock cables with equal length from a master source. To eliminate data errors in this LVDS interface, valid setup and hold times must be maintained at the input buffer of the FPGA by specifying the cable length (and thus

delay) in the daisy chain. The length of the interface cables may be calibrated for maximally stable operation by using a separate FPGA test program. The optimum length of the cable was measured to be 32 inches. The closest standard length cable is 36 inches, which gives error free operation from 8.5 to 10.8 MHz. This latter cable length is recommended.

CMOS interface: Two 3.3V CMOS input/output lines are available that connect directly to the FPGA. These lines have series level-translators that act as protection circuitry to the FPGA. Presently, `mon[0]` is programmed as a start waveform synchronization pulse, and `mon[1]` is the 250 MHz clock. If desired, these lines can be reprogrammed in the FPGA code to provide other test and synchronization signals.

I2C: An I2C serial interface is provided that operates at approximately 100 kbaud. It may be accessed via a 3-pin connector that is internal to the board. This interface is typically used to control (relatively) low-speed DACs, A/Ds, or logic external to the board. This is especially useful for adjustment of microwave components that are connected to the board, allowing for channel-by-channel control of the entire waveform chain. An I2C logic receiver with 8 LED outputs is placed on the board, and can be used for functionality tests of the interface or as a light indicator. A simple I2C interface is provided by the FPGA coding.

Versalink Fiber Optic Interface: The Versalink fiber optic interface has two outputs and one input, and can operate at a maximum data rate of 10 Mbaud. A fiber optic interface is useful when connecting to low-noise electronics (see section 5.2.5) since digital noise and clock feedthrough can be entirely eliminated.

Power: On-board voltage regulators are used on all power supplies to decrease the risk of damage by improper connection of power leads. Additionally, this methodology greatly decreases any board-to-board noise coupling through these leads. To minimize the power dissipated by the board, low-dropout voltage regulators are used on all supplies. The input voltages need to be approximately 0.4 volts greater than the internal levels. Insufficient input voltage causes the LEDs located near the regulators to be turned off. As the DAC requires its 3.3 V supply to be powered up last, its regulator circuit has a power-up delay tied to the

1.8 Volt supply. Normally this delay causes the 3.3 LED to briefly flash off during power up. All power inputs are fused, and have a reverse Schottky diode and transient voltage element to protect against negative and large positive voltages. In this case, large current will be drawn by the protection element, causing the fuse to blow. The regulator integrated circuits were also chosen because of various protection features.

5.2.2 Gaussian filter and differential amplifier

As mentioned in the previous section, the DAC output has significant clock feedthrough at multiples of 1 GHz. A low-pass filter with suitable bandwidth is desired to suppress this clock signal. While there are many kinds of low-pass filters available from the market, care must be taken when making the choice. For example, the popular Butterworth and Chebyshev low-pass filters have good frequency response (Fig. 5.4(a)), but in the time domain, they have obvious ripples in a step response (Fig. 5.4(b)). To achieve optimal quantum control, a low-pass filter with Gaussian step response is desired. With the Gaussian shape, the signal rises and falls smoothly and then rapidly settles to its final value.

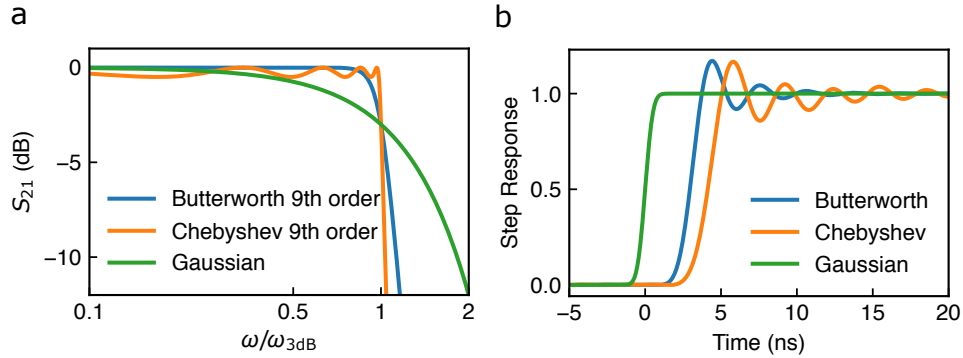


Figure 5.4: Comparison of frequency and step responses for the Butterworth, Chebyshev and Gaussian low-pass filters with the same -3 dB cut-off frequency of $\omega_{3dB}/2\pi = 332$ MHz. The Chebyshev filter has 0.5 dB maximum ripples in the pass-band. (a) Frequency response comparison. The Butterworth and Chebyshev low-pass filters have a much sharper transition from pass-band to stop-band, which is preferable for frequency domain applications. (b) Step response comparison. The Butterworth and Chebyshev low-pass filters have obvious ripples in the step response, while the Gaussian filter has a smooth response and the signal settles to its final value in just a few nanoseconds, preferable for time domain applications.

For this work, we custom-made some lumped-element Gaussian filters with a -3 dB bandwidth of 250 MHz, which can suppress the clock feedthrough to below -80 dBm/Hz, see Fig. 5.5.

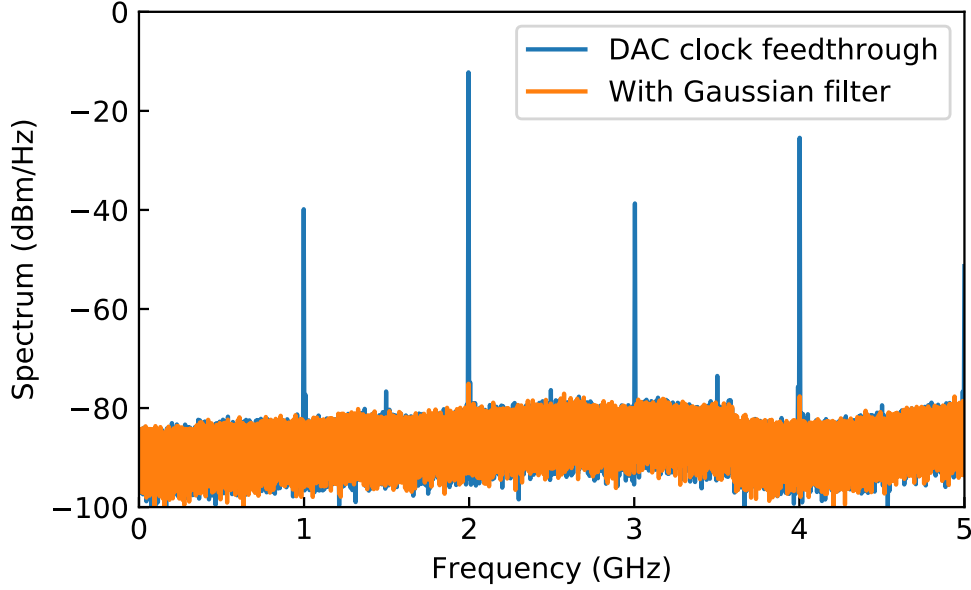


Figure 5.5: Suppressing the DAC clock feedthrough below -80 dBm/Hz with a custom Gaussian filter.

Following Ref. [76], here we show how the custom Gaussian filter is constructed using lumped elements. Let's start from the standard lumped element model for a damped transmission line shown in Fig. 2.4, where R_ℓ , C_ℓ , G_ℓ and R_ℓ represent the inductance per length, capacitance per length, conductance per length and resistance per length of the transmission line. When satisfying the Heaviside condition:

$$\frac{R_\ell}{L_\ell} = \frac{G_\ell}{C_\ell}, \quad (5.1)$$

the damped transmission line becomes distortionless, i.e., the attenuation coefficient α is independent of frequency:

$$\alpha = \sqrt{R_\ell G_\ell}. \quad (5.2)$$

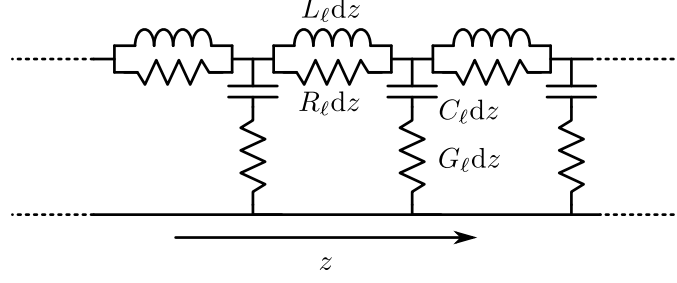


Figure 5.6: Lumped-element model of a lossy transmission line with Gaussian response.

By a simple rearrangement of the elements in Fig. 2.4, we can obtain a lossy transmission line, shown in Fig. 5.6, whose transfer characteristic is similar to an ideal Gaussian filter. Applying the formalisms in Section 2.2 to this transmission line, we can obtain the propagation coefficient

$$\gamma = \alpha + j\beta = j\omega \sqrt{\frac{L_\ell R_\ell C_\ell G_\ell}{(j\omega L_\ell + R_\ell)(j\omega C_\ell + G_\ell)}}. \quad (5.3)$$

Assuming the Heaviside condition Eq. 5.2 still holds here, we have

$$\gamma = j\omega \frac{\sqrt{L_\ell C_\ell}}{j\omega \frac{L_\ell}{R_\ell} + 1}. \quad (5.4)$$

Here we introduce the break-point angular frequency,

$$\omega_b = \frac{R_\ell}{L_\ell}, \quad (5.5)$$

where below this frequency, the real part in the denominator of Eq. 5.4 dominates, and we can approximate it as

$$\gamma = j\omega \frac{\sqrt{L_\ell C_\ell}}{j\omega/\omega_b + 1} \approx \omega_b \sqrt{L_\ell C_\ell} \left[\left(\frac{\omega}{\omega_b} \right)^2 - \left(\frac{\omega}{\omega_b} \right)^4 \right] + j\omega_b \sqrt{L_\ell C_\ell} \left[\frac{\omega}{\omega_b} - \left(\frac{\omega}{\omega_b} \right)^3 \right]. \quad (5.6)$$

This approximation is valid as long as $\omega \ll \omega_b$.

The attenuation coefficient of the line is the real part of Eq. 5.6:

$$\alpha = \frac{\omega_b \sqrt{L_\ell C_\ell} (\omega/\omega_b)^2}{1 + (\omega/\omega_b)^2} \approx \omega_b \sqrt{L_\ell C_\ell} \left[\left(\frac{\omega}{\omega_b} \right)^2 - \left(\frac{\omega}{\omega_b} \right)^4 \right]. \quad (5.7)$$

We can see that the attenuation of the line is proportional to frequency squared when $\omega \ll \omega_b$, the desired feature of a Gaussian filter. At large frequency, the attenuation coefficient saturates at $\omega_b \sqrt{L_\ell C_\ell}$.

The phase coefficient β is the imaginary part of Eq. 5.6, we can see that it is approximately linear with frequency, $\beta \approx \omega \sqrt{L_\ell C_\ell}$ when $\omega \ll \omega_b$, therefore the phase velocity v_p is approximately constant and equals to $1/\sqrt{L_\ell C_\ell}$, and the group velocity, which is given by

$$v_g = \frac{d\omega}{d\beta} \approx \frac{1}{\sqrt{L_\ell C_\ell}}, \quad (5.8)$$

is also frequency-independent.

Although the math here is quite straightforward, engineering such a transmission line is by no means easy. A lumped-element approximation to this transmission line can be made with a finite section of the circuit in Fig. 5.6, with the infinitesimal dz replaced by a finite length Δz . This approximation is valid at frequencies much lower than the cutoff angular frequency of each section:

$$\omega_c = \frac{2}{\sqrt{L_\ell C_\ell} \Delta z}. \quad (5.9)$$

For a given -3 dB frequency $\omega_{3\text{dB}}$, the length of the transmission line D should be chosen to satisfy

$$8.686 \sqrt{L_\ell C_\ell} \frac{\omega_{3\text{dB}}^2}{\omega_b} D = 3. \quad (5.10)$$

If we approximate this line with a N -section lumped element circuit, then $\Delta z = D/N$. Combining Eq. 5.9 and 5.10, we have

$$N = 0.173 \frac{\omega_b \omega_c}{\omega_{3\text{dB}}^2}. \quad (5.11)$$

To make a good approximation, ω_b and ω_c should both be significantly larger than $\omega_{3\text{dB}}$. If we choose ω_b and ω_c to be at least five times larger than $\omega_{3\text{dB}}$, then $N > 4$. In practice, we find that $N = 7$ is already good enough, see Fig. 5.7. The lumped-element parameters in each end section are tuned with a parameter q to minimize reflection at high frequencies. When $q = 1$, the sections on both ends are identical to the other sections.

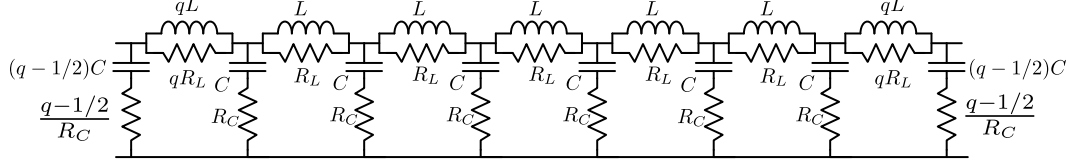


Figure 5.7: 7-section lumped element Gaussian filter. In each end, the component parameters are tuned with a parameter q to minimize reflection at high frequency.

To match the $Z_0 = 50 \, \Omega$ impedance, the lumped elements should satisfy

$$Z_0^2 = L/C = R_L R_C. \quad (5.12)$$

Inserting this into Eq. 5.9, we have

$$\omega_c = \frac{2Z_0}{L}. \quad (5.13)$$

For a 7-section lumped element filter with $\omega_{3\text{dB}}/2\pi = 250 \, \text{MHz}$, we have

$$\omega_b \omega_c = \frac{R_L}{L} \frac{2Z_0}{L} = \frac{7}{0.173} (2\pi \times 250 \, \text{MHz})^2. \quad (5.14)$$

The impedance matching condition in Eq. 5.12 and the $\omega_{3\text{dB}}$ condition in Eq. 5.14 are not sufficient to determine the lumped elements. By introducing another free parameter

$p = R_L/Z_0$, we can determine the lumped elements as follows:

$$R_L = pZ_0, \quad (5.15)$$

$$R_C = Z_0/p, \quad (5.16)$$

$$L = \frac{Z_0}{\sqrt{\frac{7}{0.173 \cdot 2p}} \times 2\pi \times 250 \text{ MHz}}, \quad (5.17)$$

$$C = L/Z_0^2. \quad (5.18)$$

Using the $ABCD$ matrix method (see Appendix C) to numerically calculate the transmission parameter S_{21} of this lumped-element filter for various p and q , we find that when $p = 4$, the line transmission approximates the ideal Gaussian filter very well, see Fig. 5.8. In practice, we choose $R_L = 210 \Omega$, $R_C = 12 \Omega$, $L = 15 \text{ nH}$ and $C = 6.2 \text{ pH}$.

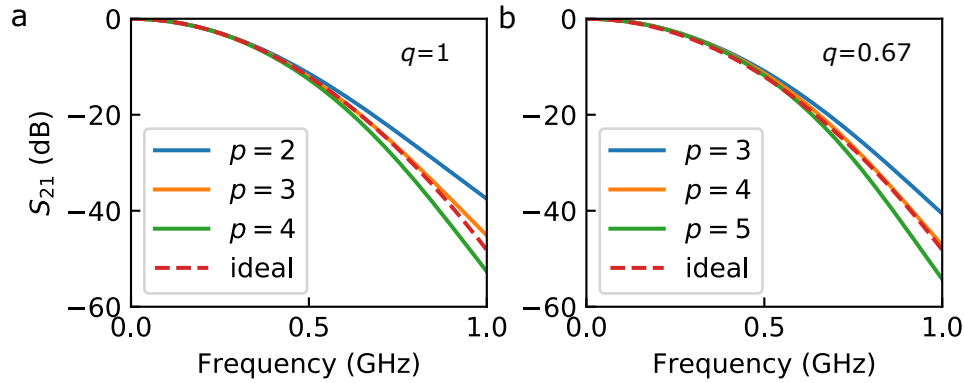


Figure 5.8: Optimizing the 7-section Gaussian filter parameter. (a) Using the default value of $q = 1$, we find the lumped element filter approximates the ideal Gaussian filter well when $p \approx 3$. (b) $ABCD$ matrix simulation suggests that the reflection at high frequency is minimized at $q = 0.67$. Using this value, we find that when $p = 4$ the lumped element filter approximates the ideal Gaussian filter well.

So far we have discussed the filtering of the high-frequency noise in the DAC output. Now let's focus on the low-frequency part.

The DAC board provides differential outputs for each channel, while the qubit control wiring is single ended. We could simply use one end of the differential outputs to control the qubits, but the DC offset and the common mode noise in the differential signal could not

then be cancelled out. To zero out the DC offset and the common mode noise, we use the ADA4927 differential amplifier⁵ from Analog Devices, Inc.

The ADA4927 is fabricated using a silicon-germanium complementary bipolar process, enabling very low levels of distortion with an input voltage noise of only $1.3 \text{ nV}/\sqrt{\text{Hz}}$. It has a typical DC offset of 0.3 mV and a -3 dB bandwidth of 2.3 GHz. The low noise, low DC offset and excellent dynamic performance of the ADA4927 make it well suited for our purpose.

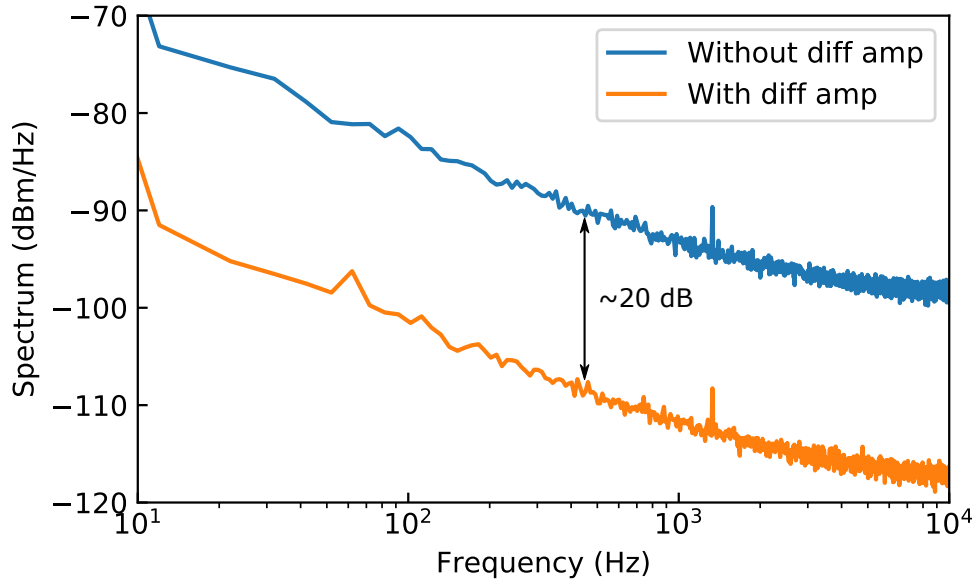


Figure 5.9: The differential amplifier can suppress the DAC low frequency noise by about 20 dB.

In Fig. 5.9, we show the comparison of the DAC output low-frequency noise with and without the ADA4927 differential amplifier, measured by a microwave spectrum analyzer. We see that the differential amplifier reduces the low frequency noise by about 20 dB, which is important for maintaining the qubit phase coherence.

Since both the Gaussian filter and the differential amplifier are used to filter the DAC output, we have integrated four Gaussian filters and two differential amplifiers on a single printed circuit board, see Fig. 5.10, which can be directly connected to the dual differential

5. <http://www.analog.com/en/products/ada4927-1.html>

outputs of the DAC board, providing a smooth and clean output signal.

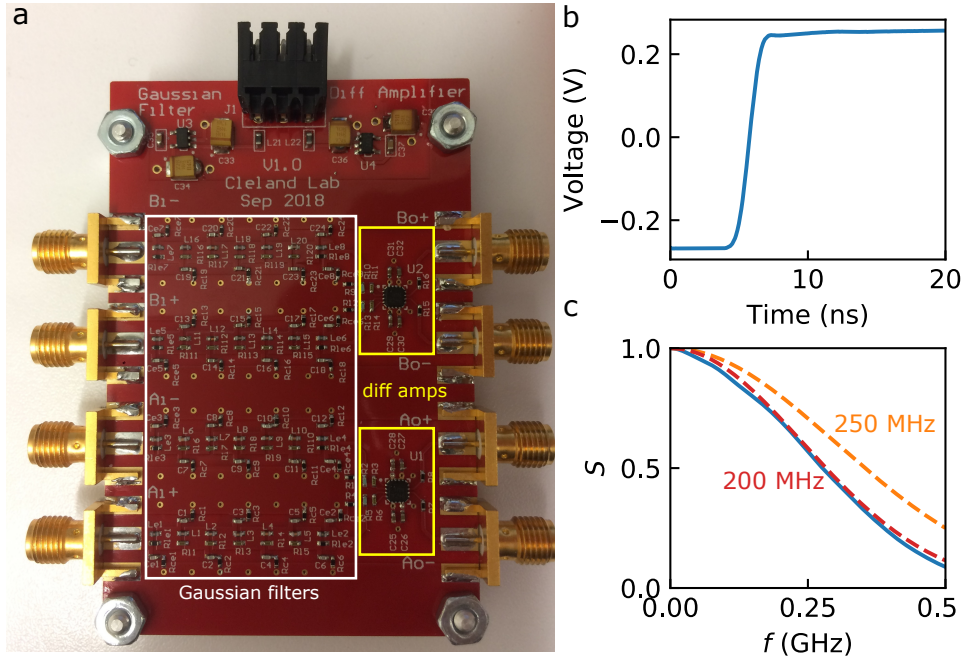


Figure 5.10: (a) Four Gaussian filters and two differential amplifiers integrated on a single board, which can be directly connected to the dual differential output of the DAC board. (b) DAC output step response captured by a high speed sampling oscilloscope, with the output filtered by the device in (a). (c) DAC output spectral response S estimated from (b). S is normalized at $f = 0$. The spectrum is closer to a $\omega_{3dB}/2\pi = 200$ MHz Gaussian filter instead of the nominal 250 MHz one, after adding the differential amplifier.

Although the DAC board operates at a 1 Gsps speed, by properly correcting the digital signal streamed to the FPGA in advance, we can achieve a step resolution much smaller than 1 ns. Once we obtain the DAC output spectrum $S(f)$ (see Fig. 5.10(c)), the correction can be carried out using the following procedure:

Assume we want to generate a rectangle pulse $R(t)$. Instead of working in the time domain, we switch to the frequency domain function $\tilde{R}(f)$. We correct for imperfections in the DAC output by dividing $\tilde{R}(f)$ with $S(f)$. This de-convolution correction greatly amplifies signal components close to the 500 MHz Nyquist frequency, causing various artifacts. We add a digital Gaussian filter $G(f)$ with 3 dB frequency of 150 MHz to prevent this amplification of high frequency components, as well as ringing due to a sharp cutoff at the Nyquist frequency. The corrected frequency function $\tilde{R}'(f) = G(f)\tilde{R}(f)/S(f)$ is converted back to the time

domain function $R'(t)$, and then digitized and streamed to the FPGA on the DAC board [8].

In Fig. 5.11, we show a series of rectangle pulses with 10 ps step resolution, obtained with the calibration procedure described above. The fact that we can achieve 10 ps step resolution might sound counterintuitive, with a 1 Gsps speed DAC. Actually, it is true that for an arbitrary signal, the best step resolution we can get is 1 ns. However, if we know the output behavior of the DAC, and we know the past and the future of the signal, we then can strategically adjust the voltage at each point in advance to achieve a fine step resolution. This requires a fine voltage adjust resolution and the sacrificing about half the DAC output range. As we will see in chapter 6, the ability to tune the output pulse with such a fine step resolution is critical for tuning up the quantum state transfer process.

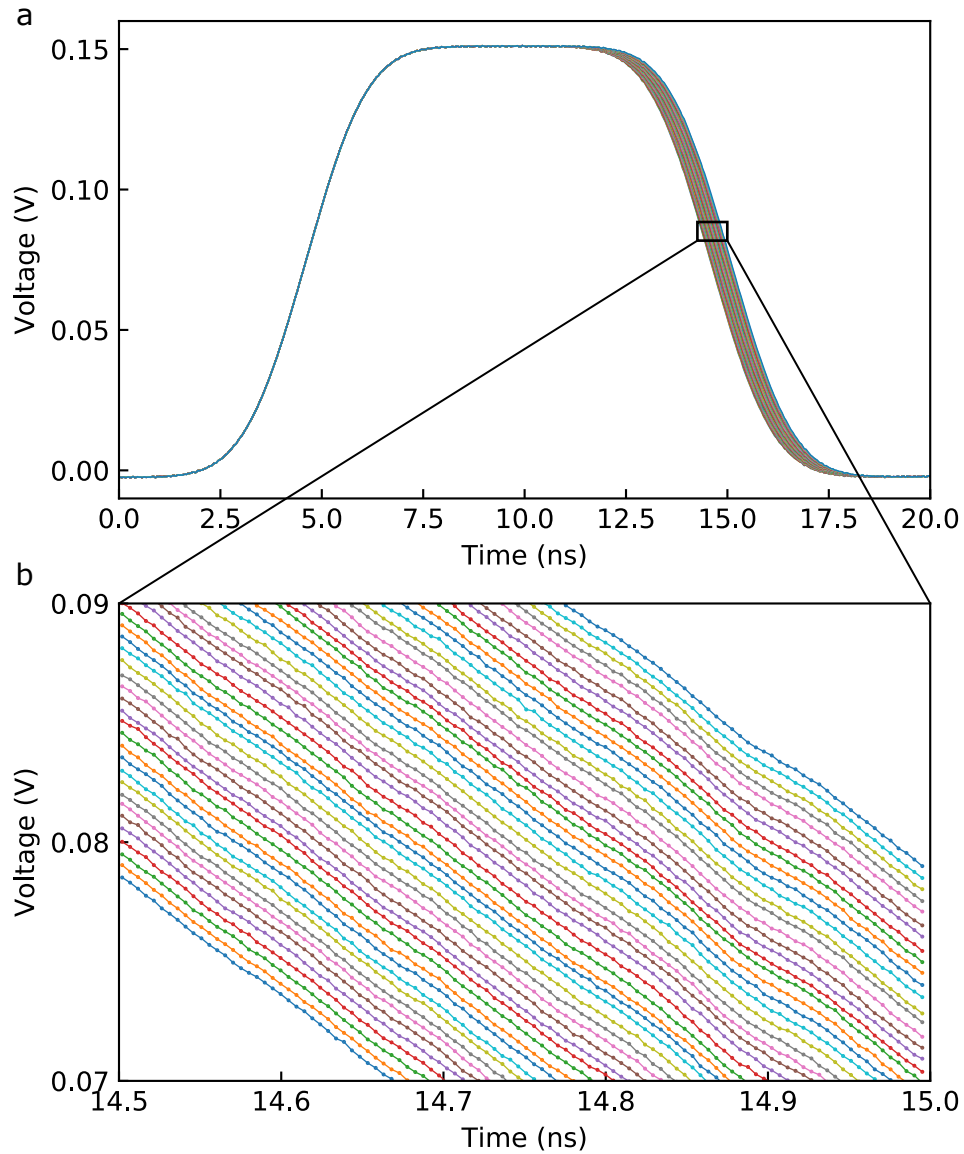


Figure 5.11: Rectangle pulses with 10 ps step resolution. (a) Time trace of a series of rectangle pulses captured by a high speed sampling oscilloscope, with the width varying from 10 ns to 10.5 ns at a step of 10 ps. (b) Zoom in of the falling edges in (a). We can clearly see the gradual increase in the pulse width, with ~ 1 ps signal jittering.

5.2.3 IQ mixer

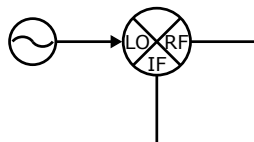


Figure 5.12: Schematic of a mixer.

A mixer is a three-port device that uses a nonlinear or time-varying element to achieve frequency conversion [29]. The three ports are the Local Oscillator (LO) port, the Radio Frequency (RF) port, and the Intermediate Frequency (IF) port, as shown in Fig. 5.12. The LO port is typically driven with a sinusoidal continuous wave (CW) signal represented as

$$v_{\text{LO}} = \cos 2\pi f_{\text{LO}} t. \quad (5.19)$$

When using the mixer for frequency up-conversion, a lower frequency signal is applied to the IF port. This signal typically contains the information or data to be transmitted. For simplicity, here we represent it as

$$v_{\text{IF}} = \cos 2\pi f_{\text{IF}} t. \quad (5.20)$$

The RF port output of the mixer is (ideally) the product of the LO and IF signals:

$$v_{\text{RF}} = \cos 2\pi f_{\text{LO}} t \cos 2\pi f_{\text{IF}} t = \frac{1}{2} \cos 2\pi(f_{\text{LO}} - f_{\text{IF}})t + \frac{1}{2} \cos 2\pi(f_{\text{LO}} + f_{\text{IF}})t. \quad (5.21)$$

Conversely, the mixer can be used to perform frequency down-conversion. In this process, the RF port becomes the input port. For simplicity, we consider a sinusoidal input signal

$$v_{\text{RF}} = \cos 2\pi f_{\text{RF}} t \quad (5.22)$$

along with the LO drive signal of Eq. 5.19. The IF output is (ideally) the product of the LO and the RF signal:

$$v_{\text{IF}} = \cos 2\pi f_{\text{LO}} t \cos 2\pi f_{\text{RF}} t = \frac{1}{2} \cos 2\pi(f_{\text{LO}} - f_{\text{RF}})t + \frac{1}{2} \cos 2\pi(f_{\text{LO}} + f_{\text{RF}})t. \quad (5.23)$$

We can see from Eq. 5.21 and Eq. 5.23 that for a single frequency input, we obtain both the lower sideband and the upper sideband outputs instead of a single frequency output.

In practice, f_{LO} is chosen to be close to f_{RF} , and f_{IF} is much smaller than f_{LO} and f_{RF} , therefore $f_{\text{LO}} - f_{\text{RF}} \ll f_{\text{LO}} + f_{\text{RF}}$. Then the second term in Eq. 5.23 can be easily removed with a low-pass filter. But the two terms in Eq. 5.21 are very close in frequency, making it difficult to distinguish one from the other. One way to remove the image sideband is by using destructive interference from another mixer.

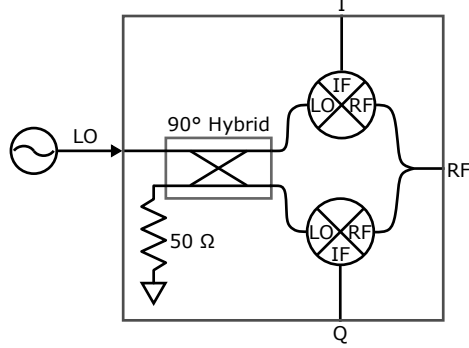


Figure 5.13: Schematic of an IQ mixer.

An in-phase/quadrature (IQ) mixer consists of two mixers where the RF ports are connected with an in-phase power divider and the LO ports are connected with a quadrature hybrid, see Fig. 5.13. This combination allows the in-phase and quadrature components of the output signal to be modulated independently with each IF port:

$$v_{\text{RF}}(t) = I(t) \cos 2\pi f_{\text{LO}}t - Q(t) \sin 2\pi f_{\text{LO}}t. \quad (5.24)$$

The inherent architecture of IQ mixer eliminates the image sideband in down-conversion and allows the selection of desired sideband in up-conversion. For example, if we modulate the I channel as $\cos 2\pi f_{\text{IF}}t$, and modulate the Q channel as $\sin 2\pi f_{\text{IF}}t$, we obtain the upper sideband:

$$v_{\text{RF}}(t) = \cos 2\pi f_{\text{IF}}t \cos 2\pi f_{\text{LO}}t - \sin 2\pi f_{\text{IF}}t \sin 2\pi f_{\text{LO}}t \quad (5.25)$$

$$= \cos 2\pi(f_{\text{LO}} + f_{\text{IF}})t. \quad (5.26)$$

Alternatively, if the Q channel signal phase is shifted by 180° , then the down sideband is selected. This offers a robust frequency mixing solution for applications that require high image rejection or sideband suppression, for example driving the superconducting qubits. In practice, although the image sideband is suppressed with the IQ mixer, a low-pass filter is still necessary to suppress the higher harmonics ($n \times f_{\text{LO}}$) due to the nonlinearity of the mixer.

Realistic IQ mixers have imperfections that can be calibrated and corrected for *in situ* to improve their performance. For example, one common imperfection is DC offset, where each of the IF input signals in Eq. 5.24 is shifted by an unknown DC voltage:

$$v_{\text{RF}} = [I(t) + I_0] \cos 2\pi f_{\text{LO}} t - [Q(t) + Q_0] \sin 2\pi f_{\text{LO}} t. \quad (5.27)$$

This results in the leakage of microwave signals at the carrier frequency f_{LO} even when the IF ports are set to zero, which is called *carrier bleedthrough*. To calibrate this imperfection, one can vary the DC bias of the IF ports while monitoring the RF output power with a microwave spectrum analyzer. A minimum microwave leakage can be obtained when $I = -I_0$, $Q = -Q_0$. The correction can be done by simply adding the DC offset $-I_0$ or $-Q_0$ to the desired signal. A proper zero calibration can reduce the carrier bleedthrough from about -20 dBm to below -80 dBm typically. Note the DC offset is dependent on the carrier frequency. Usually we calibrate the DC offset for an array of carrier frequencies and estimate the DC offset for intermediate frequencies using linear interpolation.

Another common imperfection is IQ imbalance:

$$v_{\text{RF}} = I(t) \cos 2\pi f_{\text{LO}} t - \alpha Q(t) \sin 2\pi f_{\text{LO}} t, \quad (5.28)$$

where α is an unknown complex imbalance factor. For an ideal IQ mixer, $\alpha = 1$. If the I and Q channels are not perfectly balanced in amplitude, then the amplitude of α is not equal to 1. If the phase difference between the I and Q channels is not exactly 90° , then α

has a nontrivial phase. The signature of IQ imbalance is the generation of unwanted image sidebands, for example, if we modulate the mixer as Eq. 5.25, the output becomes

$$v_{\text{RF}}(t) = \cos 2\pi f_{\text{IF}}t \cos 2\pi f_{\text{LO}}t - \alpha \sin 2\pi f_{\text{IF}}t \sin 2\pi f_{\text{LO}}t \quad (5.29)$$

$$= \frac{1+\alpha}{2} \cos 2\pi(f_{\text{LO}} + f_{\text{IF}})t + \frac{1-\alpha}{2} \cos 2\pi(f_{\text{LO}} - f_{\text{IF}})t. \quad (5.30)$$

We see that in addition to the desired upper sideband signal, there is an unwanted lower sideband signal. The image sideband can be as large as -20 dBc in practice. This imperfection can be corrected by adding a compensation factor $\text{Im}[\alpha]$ to the I channel and $1 - \text{Re}[\alpha]$ to the Q channel to minimize the image sideband. A successful calibration can reduce the image sideband to below -90 dBc typically. Note the imbalance factor α depends on both f_{LO} and f_{IF} . Usually we calibrate the IQ imbalance for an array of f_{LO} and f_{IF} respectively, and then do linear interpolation to obtain the compensation factor for other carrier and sideband frequencies.

Marki Microwave IQ mixers⁶ are commonly used in the superconducting circuits community due to their high quality. Meanwhile, semiconductor manufacturers have introduced compact surface-mount IQ mixers with similar features at a much cheaper price, for example the HMC8193⁷ from Analog Devices, Inc., and the CMD252C4⁸ from Custom MMIC. If these surface-mount IQ mixers can be used for qubit experiments, it not only reduces the cost, but also allows for integrating the IQ mixer with the DAC board and other components together on a single printed circuit board to form a compact electronics system.

6. <https://www.markimicrowave.com/mixers/mixers-products.aspx>

7. <http://www.analog.com/en/products/hmc8193.html>

8. <https://www.custommmic.com/cmd252c4/>

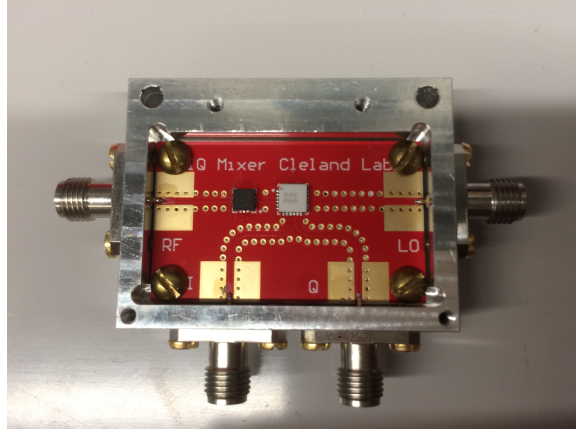


Figure 5.14: Custom IQ mixer based on HMC8193.

We have developed our custom IQ mixers based on the HMC8193 chip in addition to using the Marki Microwave mixers, see Fig. 5.14. After careful calibration with the custom GHz DAC board, we obtain very clean microwave pulses suitable for driving superconducting qubits, see Fig. 5.15. We carried out randomized benchmarking [37] on an Xmon qubit using this custom IQ mixer and achieved a qubit X gate fidelity as high as 99.9%, comparable to the state-of-the-art result [37].

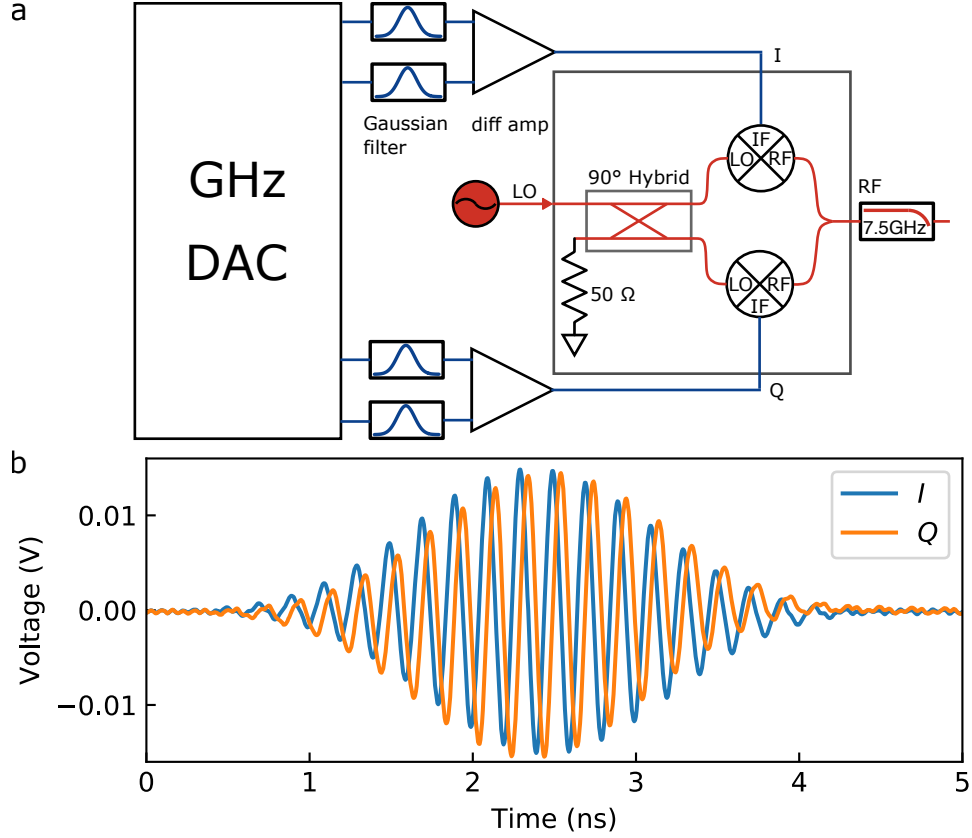


Figure 5.15: The impulse response of the custom IQ mixer. (a) The setup schematic. We use the custom GHz DAC board to generate a 1 ns rectangle pulse, which is filtered by the Gaussian filter and the differential amplifier introduced in the previous section before it drives the I or the Q port of the IQ mixer. Red lines correspond to RF/microwave signals, blue lines correspond to intermediate frequency (IF) signals. (b) The RF output captured by a high speed sampling oscilloscope. The short pulse from the DAC modulates the RF output of the mixer, resulting in a high frequency microwave pulse with a smooth, Gaussian envelope.

5.2.4 GHz ADC board

The GHz analog-to-digital (ADC) converter board is the dual of the DAC board, which is used for qubit dispersive readout. It was designed by Prof. John Martinis at UCSB and Steve Waltman at High Speed Circuits Consultant⁹. The circuit architecture of the ADC board is very similar to that of the DAC board, with the same FPGA, ethernet interface, clock distribution system and power module etc, except the dual DAC chips are replaced by

9. <http://www.hscc.biz>

the dual ADC chips ADC081000¹⁰ from Texas Instruments.

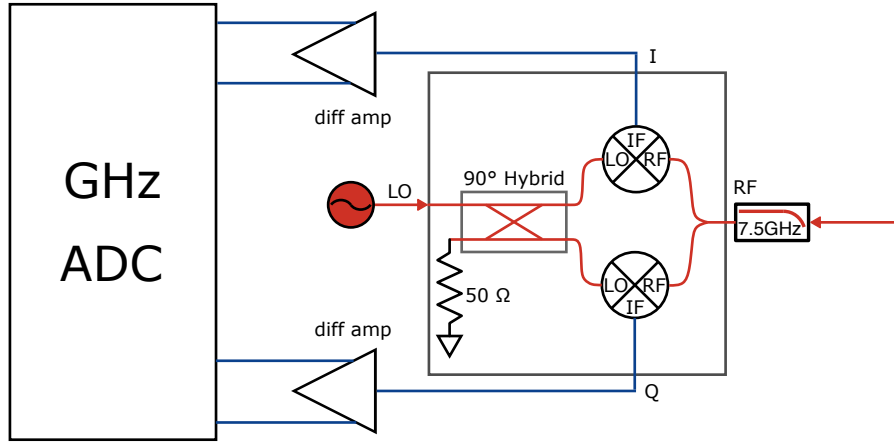


Figure 5.16: ADC board and IQ mixer configuration. Red lines correspond to RF/microwave signals, blue lines correspond to IF signals.

The ADC board operates at 1 Gbps with 8 bits resolution. The qubit dispersive readout pulse typically runs at a few GHz, therefore an IQ mixer is needed to down-convert the signal before it can be digitized by the ADC, see the configuration in Fig. 5.16. The ADA4927 differential amplifier introduced in section 5.2.2 is used to adapt the single-ended IF signal from the IQ mixer to the differential input of the ADC. After digitization, the FPGA can perform fast on-chip demodulation of the time trace, resulting in a single complex value $I + iQ$ in the phase space. With a proper readout configuration, the position of $I + iQ$ in the readout phase space for the qubit in its ground state is well separated from that of the qubit in its excited state, allowing for single-shot qubit state discrimination.

5.2.5 Fastbias card

A fastbias card is a 3U quad-channel low frequency DAC board designed by Erik Lucero and Prof. John Martinis at UCSB, which can provide low noise, quasi-DC bias for the qubit or coupler junctions. Each channel has two 16-bit DACs (MAXIM 542), one is used to ramp the voltage quickly in the range between -2.5 and $+2.5$ V, and the other provides even finer

10. <http://www.ti.com/product/ADC081000>

resolution between 0 and +2.5 V. An Altera Cyclone II FPGA is used to receive waveform data and control the output of the DACs. All of the waveform data is sent from the GHz DAC board Versalink fiber optic interface so that the ground of this card is well isolated from other electronics. This card is designed to have less than $5 \text{ nV}/\sqrt{\text{Hz}}$ input noise. For low noise performance, The MAXIM 542 DAC digital inputs and clock are held constant during qubit operation.

5.2.6 *Synchronization*

Multiple GHz DAC/ADC boards are synchronized through the 250 MHz daisy chain interface, as shown in Fig. 5.17. The DAC/ADC boards start asynchronously after being configured by the computer through the ethernet interface, then each DAC configures the corresponding fastbias card through its optical fiber interface (optional) and waits for the bias voltage to settle ($20 \mu\text{s}$ typically). These are all done at a 25 MHz clock speed. Then all boards enter the high speed mode (250 MHz/1 GHz), the slave boards wait for the daisy chain signal for synchronization while the master board initiates the daisy chain signal. Once a slave board receives the daisy chain signal, it relays this signal to the next board and waits for a user-defined delay called the “start delay” at a step of 4 ns before it streams its digital data from the FPGA SRAM to the DAC chip or digitizes/demodulates the data from the ADC chip. The calibration of the “start delay” allows for the synchronization of multiple boards within 4 ns. Finally, the boards wait for a long-enough reset settling time (typically $200 \mu\text{s}$) to passively reset the quantum system to ground state, and then repeat the whole sequence for thousands of times to obtain the qubit state probabilities.

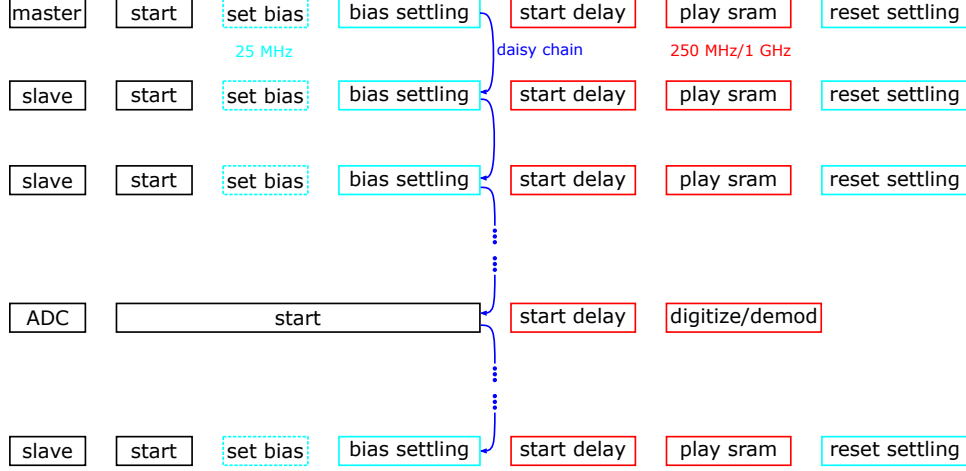


Figure 5.17: Multiple GHz DAC/ADC boards synchronization protocol.

5.3 LabRAD

LabRAD (where RAD stands for Rapid Application Development) is an open source platform for quickly and easily creating distributed instrument control and data acquisition systems. It is developed by Markus Ansmann and Matthew Neeley at UCSB¹¹. We use LabRAD to control the custom electronics and perform quantum experiments.

A LabRAD setup consist of three types of components: The *LabRAD Manager*, *Server Modules* and *Client Modules*. Detailed introduction and documentation can be found in Sourceforge¹², in github¹³ and in Ref. [77]. Here I will briefly describe the specific LabRAD setup used in this thesis.

The *LabRAD Manager* is the backbone of the LabRAD system. It handles the communication between different modules of the setup. It provides basic functionality like traffic routing, connection authentication and monitoring, protocol enforcement, error checking, feature discovery, as well as on-the-fly unit conversion. The *LabRAD Manager* is written in Delphi, see the screenshot in Fig. 5.18.

11. <https://sourceforge.net/projects/labrad/>

12. <https://sourceforge.net/p/labrad/wiki/Home/>

13. <https://github.com/labrad/labrad/wiki>

The screenshot shows the LabRAD v1.1.3 manager window. It contains a table with 5 columns: ID, Name, Protocol, Sent, and Received. The table lists 22 components, including the Manager, Registry, node Luwin, Data Vault, Anritsu Server, Keysight Signal Generator Server, Luwin Direct Ethernet, GHz FPGAs, DAC Calibration, and multiple Python Clients. The status bar at the bottom indicates 'Serving'.

ID	Name	Protocol	Sent	Received
1	Manager	v2.0	180094	180094
2	Registry	v2.0	39227	39227
3	node Luwin	v2.0	47	33
4	Data Vault	v2.0	1072366	1208478
6	Anritsu Server	v2.0	10083	8921
7	Keysight Signal Generator Server	v2.0	10080	8921
8	Luwin Direct Ethernet	v2.0	17040831	17040829
9	GHz FPGAs	v2.0	39190859	39189700
10	DAC Calibration	v2.0	23641467	23640461
11	Python Client (Luwin)	v2.0	5748	5748
12	Registry Editor	v2.0	6261	6152
13	Python Client (Luwin)	v2.0	49	49
14	Python Client (Luwin)	v2.0	3100	3100
15	Python Client (Luwin)	v2.0	13	13
16	Python Client (Luwin)	v2.0	6063	6063
17	Python Client (Luwin)	v2.0	1433	1433
18	Python Client (Luwin)	v2.0	1847	1847
19	Python Client (Luwin)	v2.0	11491	11491
20	Python Client (Luwin)	v2.0	6404	6404
5	Grapher	v2.0	255582	170560
21	Python Client (Luwin)	v2.0	2749939	2749940
22	Python Client (Luwin)	v2.0	56702	56702

Figure 5.18: Screenshot of the LabRAD manager.

Server Modules connect to the *LabRAD Manager* to provide general functionality to the LabRAD setup. The following servers are required for running the qubit experiment:

- Registry server. This server provides access to the LabRAD registry, which stores all the configuration information for running an experiment.
- Data vault server. This server provides access to the data vault which stores all the experiment data and the corresponding configuration information.
- Direct ethernet server. This server provides access to the local computer ethernet interface.
- GHz FPGA server. This server provides access to the custom GHz DAC/ADC boards via direct ethernet server.
- DAC calibration server. This server loads the calibration data for the DAC boards via the data vault server, and corrects the control pulse waveform before streaming the waveform data to the DAC boards in each experiment.

- Signal generator servers (Keysight, Anritsu, signalCore). These servers provide access to the corresponding signal generators, allowing users to change the frequency, power and output status etc.

Client Modules are situated at the highest operating level in a LabRAD setup. They complete specific tasks, like taking a certain dataset. The Registry Editor client allows the user to view and modify the LabRAD registry values via the Registry server, see Fig. 5.19. The Grapher client allows the user to view the experiment data in the data vault, see Fig. 5.20.

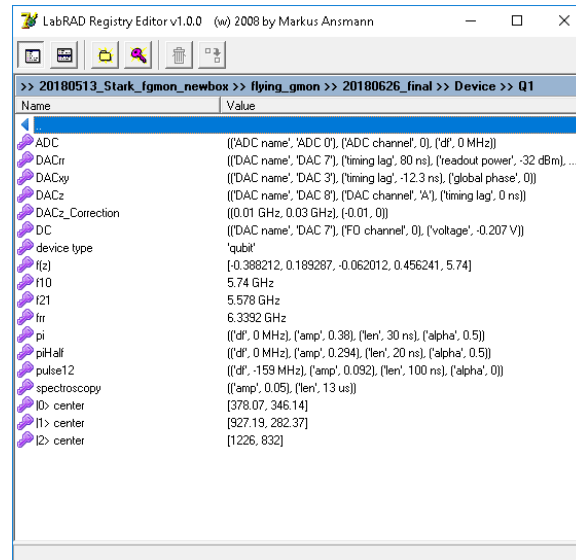


Figure 5.19: Screenshot of the Registry Editor.

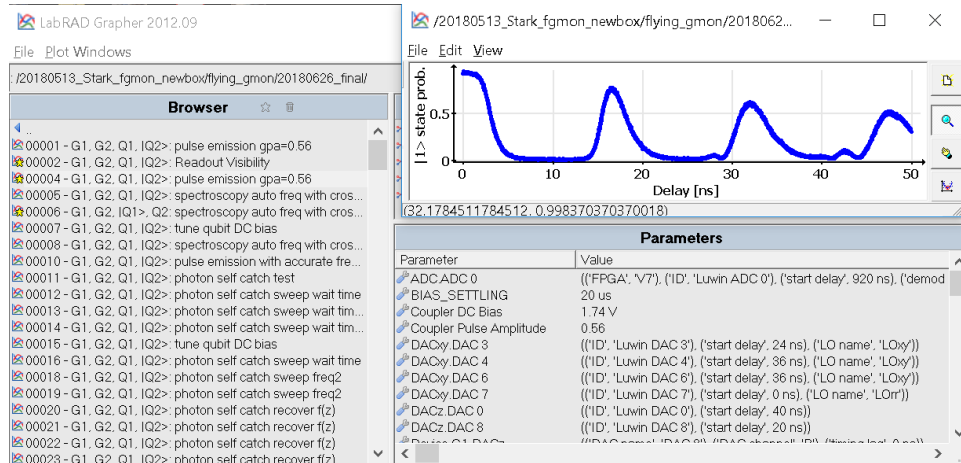


Figure 5.20: Screenshot of the Grapher.

A dedicated Python package called `dataking` is provided for automating qubit experiments with scripting. Routine experiments such as spectroscopy, T_1 measurement, Ramsey fringe interference etc are standardized in the `dataking.routine.py` script. Below is the T_1 experiment code as an example:

```
def t1(registry_session, delay=st.r[0:16:0.05,us], zpa = None,
qubit='Q1', reps=300, save=True, collect=False, noisy=True, name=''):
    """qubit T1 measurement.

    :param registry_session: registry wrapper that contains the
    hardware configuration, control and readout parameters of
    the qubits.

    :param delay: delay between pi pulse and measurement. If
    not scan over zpa, delay can be set as long as more than
    100 us; If scan over zpa, length is limited to 16 us.

    :param zpa: Z Pulse Amplitude. if zpa is None, set to 0.0
    and not scan over zpa.

    :param qubit: which qubit to measure.

    :param reps: number of repetitions.

    :param save: save the data to data vault or not.

    :param collect: return the data or not.

    :param noisy: print the data during the scan or not.
```

```

:param name: dataset name.
:return: return None if collect = False; return data
if collect = True.
"""

reps = int(np.ceil(float(reps)/TIMING_PACKET_LEN))*TIMING_PACKET_LEN
with labrad.connect() as cxn:
    # convert registry_wrapper to attribute dictionary:
    reg_dict = registry_session.copy()
    expConfig = EXPConfig(cxn, reg_dict)
    runner = Runner(cxn, expConfig)
    q = expConfig.devices[qubit]
    # force the ADC demod channel to 0 for single qubit meas.
    q.ADC['ADC channel'] = 0
    if zpa is None:
        zpa = 0.0
        sweep_z = False
    else:
        sweep_z = True
    axes = [(zpa, 'Z Pulse Amplitude'), (delay, 'Delay')]
    if save is True:
        deps = [('|1> state prob.', '', ''),
                ('IQ Amplitude', '', ''),
                ('IQ phase', '', 'rad'),
                ('I', '', ''),
                ('Q', '', '')]
        dset = prepDataset(reg_dict, 'T1 '+name, axes, deps,
                           measure=qubit, kw={'reps': reps})
    else:
        dset = None

def func(_zpa, _delay):
    # runner.qubits is a dict.
    for _q in runner.devices.values():

```

```

        _q.measure = False
q.measure = True # only measure this qubit.
q.xy = q.piPulse(0*ns)
if sweep_z is True:
    q.z = env.flattop(q.pi['len'],_delay,_zpa)
else:
    q.z = env.NOTHING
# Set the DACrr pulse.
# The 0*ns is with respect to runner.readout_start.
q.rr = q.readoutPulse(0*ns)
# set when readout starts.
# Note the pi pulse covers from -piLen/2 to piLen/2.
runner.readout_start = _delay+q.pi['len']/2.0
if hasattr(q, 'readout_zpa'):
    q.z += env.rect(runner.readout_start,
                    q.DACrr['readout length'], q.readout_zpa)
IQdata = runner(reps,True)
Is = IQdata[0,:,0,0]
Qs = IQdata[0,:,0,1]
I = np.mean(Is)
Q = np.mean(Qs)
prob = _iq2prob(Is, Qs, q['|0> center'], q['|1> center'])
IQ = 1j*Q + I
data = np.array([prob,np.abs(IQ),np.angle(IQ),I,Q])
return data

data = sweep.grid(func, axes, dataset = dset, noisy=noisy, collect
                  =collect)

# turn off the LO output and set bias voltage to 0 V.
runner.cleanup()
return data

```

Scripts for specific experiments can be composed by the user following the template in

routine.py.

CHAPTER 6

EXPERIMENTAL RESULTS

In this chapter, we discuss the main experimental results of this thesis. We present two distinct methods that violate the Clauser-Horne-Shimony-Holt (CHSH) form of the Bell inequality (see Ref. [78] and Appendix A), using a pair of superconducting qubits coupled through a 78 cm-long transmission line, with the photon emission and capture rates controlled by a pair of electrically-tunable couplers [54]. In one experiment, we use a single standing mode of the transmission line to relay quantum states between the qubits, achieving a transfer fidelity of 0.952 ± 0.009 . This enables the deterministic generation of a Bell state with a fidelity of 0.957 ± 0.005 . Measurements on this remotely-entangled Bell state achieve a CHSH correlation $S = 2.237 \pm 0.036$, exceeding the classical correlation limit of $|S| \leq 2$ by 6.6 standard deviations. In the second experiment, we control the time-dependent emission and capture rates of itinerant photons through the transmission line, a method independent of transmission distance. These shaped photons enable quantum state transfer with a fidelity of 0.940 ± 0.008 , and deterministic generation of a Bell state with a fidelity of 0.936 ± 0.006 . Measurements on this Bell state demonstrate a CHSH correlation of $S = 2.223 \pm 0.023$, exceeding the classical limit by 9.7 standard deviations. The Bell state fidelities for both methods are close to the threshold fidelity of 0.96 for surface code quantum communication [79]. This simple yet efficient circuit architecture thus provides a powerful tool to explore complex quantum communication protocols and network designs, and can serve as a testbed for distributed implementations of the surface code.

6.1 Room temperature characterization

In Fig. 6.1, we show a photograph of a packaged device ready for measurement. The device comprises two xmon qubits[35, 36], Q_1 and Q_2 , connected via two tunable couplers [54], G_1 and G_2 , to a coplanar waveguide (CPW) transmission line of length $\ell = 0.78$ m. The device

is fabricated on a single sapphire substrate, with the serpentine transmission line covering most of the area of a $6 \times 15 \text{ mm}^2$ chip. The room temperature DC test result is shown in Table 6.1, with junction resistances having reasonable values.

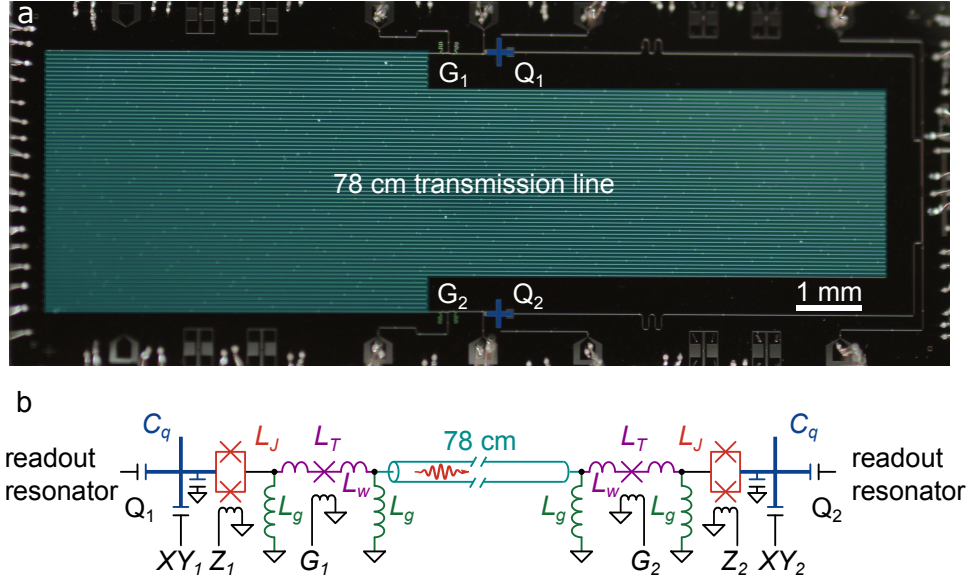


Figure 6.1: (a) Photograph of device, showing two qubits Q_1 and Q_2 (blue) connected via tunable couplers G_1 and G_2 (green) to a 78 cm-long coplanar transmission line (cyan). (b) Circuit schematic.

Test structure	junction size	predicted R_n	measured R_n	inferred f_{\max}	inferred L_T
SQUID 1	$0.6 \mu\text{m} \times 0.2 \mu\text{m}$	3.466 k Ω	2.924 k Ω	7.19 GHz	N/A
SQUID 2	$0.6 \mu\text{m} \times 0.2 \mu\text{m}$	3.466 k Ω	2.956 k Ω	7.37 GHz	N/A
Coupler 1	$3 \mu\text{m} \times 0.5 \mu\text{m}$	0.557 k Ω	0.535 k Ω	N/A	0.62 nH
Coupler 2	$3 \mu\text{m} \times 0.5 \mu\text{m}$	0.557 k Ω	0.534 k Ω	N/A	0.62 nH

Table 6.1: Room temperature tests on the device shown in Fig. 6.1. There are two test SQUIDs and two test coupler junctions on the periphery of the device, here labeled as 1 and 2. The predicted R_n is calculated from Eq. 4.2 and Eq. 4.3. The inferred qubit maximum frequencies are higher than the desired value of ~ 6 GHz, but the coupler junction inductances have good values.

6.2 Cryogenic temperature characterization

One important feature of the gmon tunable coupler is that the coupling can be turned off by biasing the coupler junction phase δ to $\pi/2$ [54]. This allows us to bring up each qubit independently without affected by the long transmission line.

With the help of a travelling-wave parametric amplifier (TWPA) [80], we are able to achieve very high fidelity single-shot measurement of each qubit, see Fig. 6.2. We characterize the qubit readout fidelity by turning the coupler for each qubit as close to zero as possible, to isolate the qubit from the rest of the circuit. With the qubit in its equilibrium state (supposedly in its ground state $|g\rangle$), we then perform a standard single-shot readout measurement, and record the values of the microwave quadratures I and Q corresponding to the readout result. We accumulate a large number of these events, shown in blue in Fig. 6.2. We then repeat this process, but precede the measurement with an on-resonant microwave pulse calibrated to put the qubit in its excited state $|e\rangle$. The results of these measurements are shown in red in Fig. 6.2. These calibrations allow us to assign any single-shot measurement, based on its de-convolved I and Q values, to the $|g\rangle$ or $|e\rangle$ state based on which side of the dashed line in Fig. 6.2 the measurement falls. For Q_1 , the $|g\rangle$ state readout fidelity is $F_g = 0.984$, and the $|e\rangle$ state readout fidelity is $F_e = 0.950$. For Q_2 , the $|g\rangle$ state readout fidelity is $F_g = 0.984$, and the $|e\rangle$ state readout fidelity is $F_e = 0.942$.

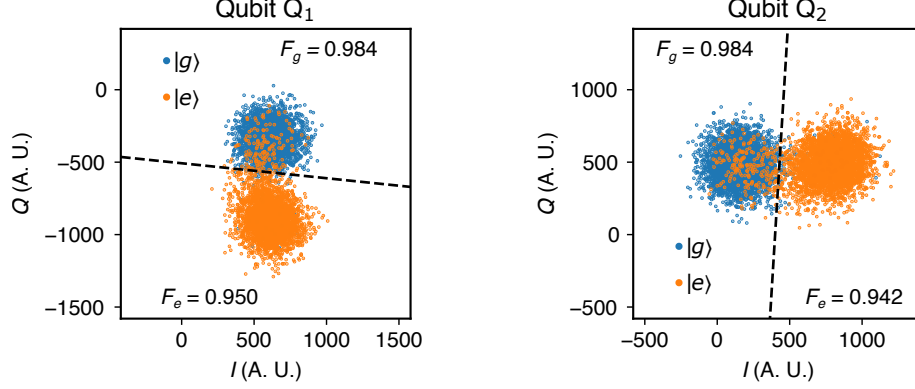


Figure 6.2: Qubit single-shot readout. A large number of measurements were made with each qubit in either its ground $|g\rangle$ or its excited $|e\rangle$ state, and data accumulated as the blue or orange points respectively. This calibration allows us to assign any given measurement to the ground or excited state, as separated by the dashed lines in the IQ plane. For Q_1 , the $|g\rangle$ state readout fidelity is $F_g = 0.984$, and the $|e\rangle$ state readout fidelity is $F_e = 0.950$. For Q_2 , the $|g\rangle$ state readout fidelity is $F_g = 0.984$, and the $|e\rangle$ state readout fidelity is $F_e = 0.942$.

Ignoring the qubits and the couplers, the transmission line is shorted to ground on both sides, supporting a sequence of standing modes with frequencies equally-spaced by $\omega_{\text{FSR}}/2\pi = 1/2T_\ell = 79$ MHz, where $T_\ell = 6.3$ ns is the photon travel time along the line. After bringing up the qubits, we can characterize the long transmission line using a qubit. By slightly turning on the G_1 coupling between the qubit Q_1 and the transmission line while keeping the G_2 coupling off, we can clearly see the multimode features of the transmission line in both the frequency domain and the time domain, see Fig. 6.3. In Fig. 6.3(a), we observe a series of avoided level crossings in the qubit spectroscopy when sweeping Q_1 's frequency across that of a standing mode. In the time domain measurement in Fig. 6.3(b), we clearly observe vacuum Rabi oscillations between Q_1 and each standing mode when their frequencies are matched.

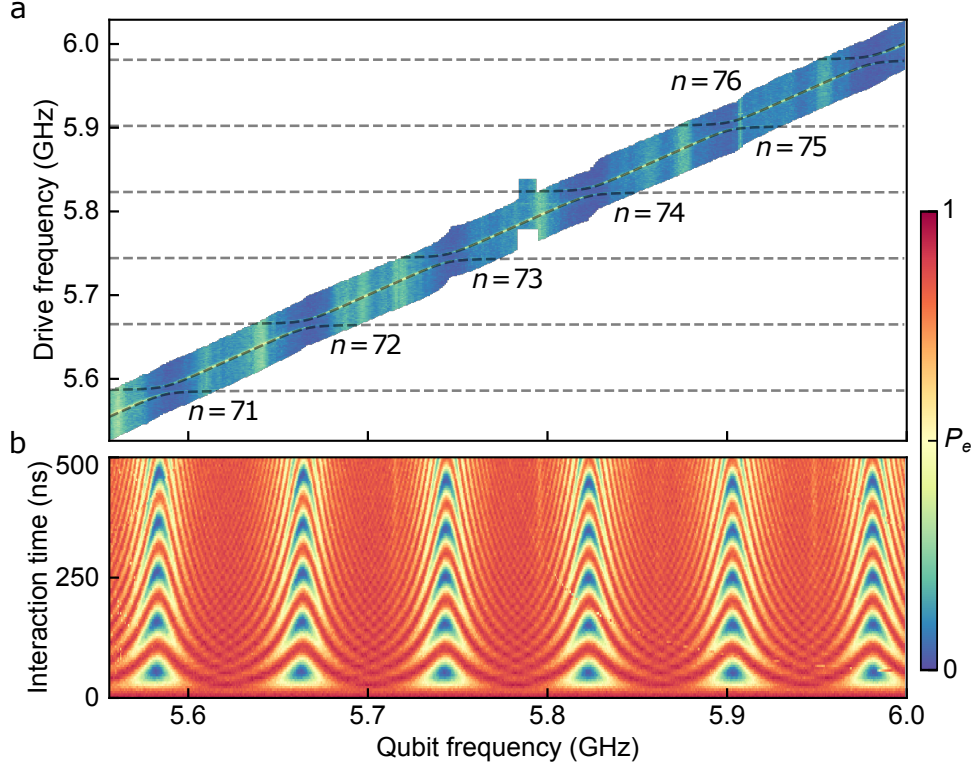


Figure 6.3: Multimode feature of the long transmission line. (a) Spectroscopy of qubit Q_1 interacting with six transmission line standing modes. Black dashed lines: Numerical simulations. (b) Vacuum Rabi swaps between Q_1 and the six standing modes. The coupling is set to $g_1/2\pi = 5$ MHz $\ll \omega_{\text{FSR}}/2\pi$.

The 78 cm-long coplanar waveguide transmission line has a $4\text{ }\mu\text{m}$ -wide center trace and a $2\text{ }\mu\text{m}$ gap to the ground plane on each side, with specific capacitance $\mathcal{C} = 173$ pF/m and specific inductance $\mathcal{L} = 402$ nH/m (see Eq. 2.94). Neglecting the coupler, the line is shorted by L_g at its far end, where this inductance is provided by a short segment of transmission line. We absorb this length in the overall transmission line, so that the input impedance is given by

$$Z_{\text{in}} = Z_0 \tanh(\alpha + i\beta)\ell = Z_0 \frac{\tanh \alpha \ell + i \tan \beta \ell}{1 + i \tan(\beta \ell) \tanh(\alpha \ell)}, \quad (6.1)$$

where $\alpha + i\beta$ is the complex propagation parameter, and $Z_0 = \sqrt{\mathcal{L}/\mathcal{C}}$ is the characteristic impedance of the transmission line [29].

Near the n th mode resonance,

$$\beta\ell = n\pi + \frac{\pi\Delta\omega}{\omega_{\lambda/2}}, \quad (6.2)$$

where $\omega_{\lambda/2}$ is the half-wave radial frequency. Near this frequency we have the input impedance

$$Z_{\text{in}} \approx Z_0 \left(\alpha\ell + i \frac{\pi\Delta\omega}{\omega_{\lambda/2}} \right), \quad (6.3)$$

where we assume $\alpha\ell \ll 1$, a safe assumption for a superconducting transmission line on a very low-loss substrate such as sapphire.

This impedance is equivalent to a series RLC resonant circuit with equivalent lumped-element parameters

$$\omega_n = n\omega_{\lambda/2}, \quad (6.4)$$

$$R_n = Z_0\alpha\ell, \quad (6.5)$$

$$L_n = \frac{\pi Z_0}{2\omega_{\lambda/2}} = \frac{1}{2}\mathcal{L}\ell, \quad (6.6)$$

$$C_n = \frac{1}{n^2\omega_{\lambda/2}^2 L_n}, \quad (6.7)$$

$$Q_n = \frac{\omega_n L_n}{R_n} = \frac{\beta}{2\alpha}. \quad (6.8)$$

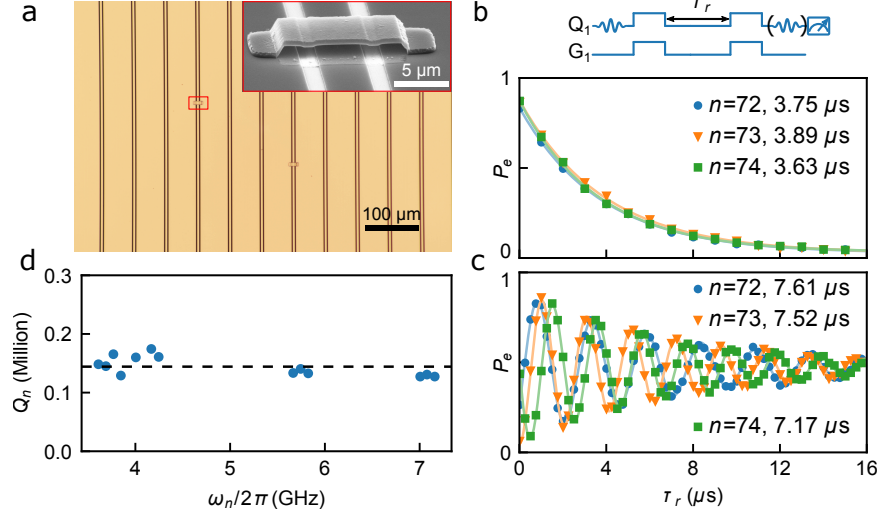


Figure 6.4: Transmission line characterization. (a) Optical micrograph of a small portion of the transmission line, which has a $4\ \mu\text{m}$ wide center trace and a $2\ \mu\text{m}$ gap to the ground plane on either side. The transmission line meanders are separated by $60\ \mu\text{m}$, and the line has 390 air-bridge crossovers evenly distributed along the line every $2\ \text{mm}$, suppressing unwanted slot-line modes and other microwave resonances. Inset: Scanning electron micrograph picture of an air-bridge crossover. (b), (c) The lifetime T_{1n} and Ramsey dephasing time T_{2n} of three of the six resonant modes shown in Fig. 1d. We find $T_{2n} \approx 2T_{1n}$, indicating negligible dephasing noise in the transmission line. Solid lines: Fits to each mode's data. Top: Control pulse sequence. (d) Quality factor $Q_n = \omega_n T_{1n}$ measured for different modes from 3.6 GHz to 7.2 GHz. We find that the quality factor is more or less constant over this frequency range, with an average $\langle Q \rangle \sim 1.44 \times 10^5$ as indicated by the horizontal dashed line.

In Fig. 6.4, we display the transmission line and its characterization. Figure 6.4(a) shows an optical micrograph of a small portion of the transmission line and a scanning electron micrograph picture of one of the 390 air-bridge crossovers evenly distributed along the line. In Fig. 6.4(b) and (c), we use Q_1 , weakly coupled to the line, to measure the lifetime T_{1n} and the Ramsey dephasing time T_{2n} of three resonator modes, with $T_{2n} \approx 2T_{1n}$ indicating that dephasing noise is negligible in the channel. In Fig. 6.4(d), we show the quality factor $Q_n = \omega_n T_{1n}$ for different modes ranging from 3.6 GHz to 7.2 GHz. We find that Q_n is more or less constant over this span of frequencies, with an average $\langle Q \rangle \sim 1.44 \times 10^5$. Comparing to Eq. (6.8), this suggests that the attenuation parameter α has a linear frequency dependence similar to β , indicating that dielectric loss dominates in this frequency range (see Eq. 2.99 and Ref. [29]). We note that similar quality factors can be achieved with superconducting coaxial

cables [81], so in principle the transmission line here can be replaced by a superconducting cable for inter-chip quantum communication. Note that for planar transmission lines that include crossovers where the SiO₂ dielectric is left as a support structure, measurements find quality factors roughly one order of magnitude smaller than here [65]. Removing the SiO₂ crossover scaffold, as was done here, is therefore an important step for reducing transmission line loss.

Each qubit Q_i is coupled to the transmission line via a tunable coupler G_i , based on a design in Ref. [54]. This configuration is accurately modeled [82] as a tunable inductance, with fixed inductances L_g on each side of this tunable inductance. The effective mutual inductance between each qubit and the transmission line through the coupler is given by

$$M = \frac{L_g^2}{2L_g + L_w + L_T / \cos \delta}. \quad (6.9)$$

Here δ is the phase across the Josephson junction that determines the equivalent inductance $L_T / \cos \delta$, and $L_w \approx 0.1$ nH represents the stray wiring inductance, which cannot be ignored when L_T becomes very small (the stray wiring term does not appear in Ref. [54]).

The system can be modeled with the following rotating-frame qubit-multimode Hamiltonian:

$$H/\hbar = \sum_{i=1,2} \Delta\omega_i \sigma_i^\dagger \sigma_i + \sum_{n=1}^N \left(n - \frac{N+1}{2} \right) \omega_{\text{FSR}} a_n^\dagger a_n + \sum_{i=1,2} \sum_{n=1}^N g_{i,n} \left(\sigma_i a_n^\dagger + \sigma_i^\dagger a_n \right), \quad (6.10)$$

where σ_i and a_n are the annihilation operators for qubit Q_i and photons in the n th standing wave mode, respectively, $\Delta\omega_i$ is the qubit frequency detuning in the rotating frame, and N is the number of standing modes included in the model.

In the harmonic limit and assuming weak coupling, the coupling between qubit Q_i and the n th mode is

$$g_{i,n} = -\frac{M}{2} \sqrt{\frac{\omega_i \omega_n}{(L_g + L_J)(L_g + L_n)}}. \quad (6.11)$$

We see that $g_{i,n} \propto \sqrt{\omega_n} \propto \sqrt{n}$, a well-known result for multimode coupling. The coupling depends on the control signals sent to the coupler G_i , and must be calibrated by fitting to measurements similar to those shown in Fig. 6.3(a), involving typically 4 to 6 adjacent modes. It is experimentally more practical to approximate the coupling in these calibrations by a single value g_i , since for mode numbers $n \sim 70$, the variation in $g_{i,n}$ with n in the calibration is only about 2%. Experiments reported here using these calibrations involve up to roughly 10 modes, for which the total variation in coupling is less than 5%. These variations are small enough that this approximation is justified. The calibration of the coupling g_i as a function of the coupler phase is shown in Fig. 6.5 for each qubit Q_i .

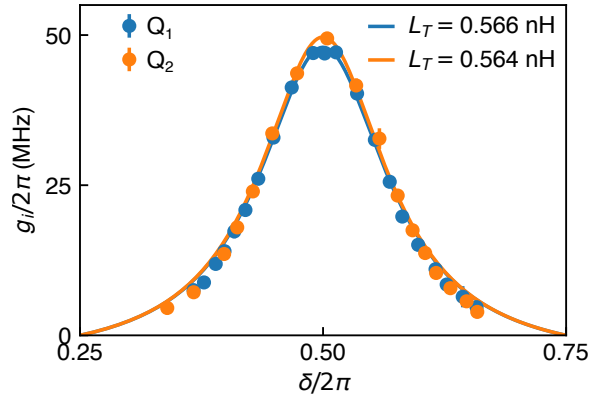


Figure 6.5: Coupling strength versus coupler junction phase δ . We measure the qubit spectrum at different coupler bias values, similar to Fig. 3a, and fit the spectrum to obtain the coupling strength g_i . The maximum coupling is about 47 MHz for Q_1 and 49 MHz for Q_2 . Error bars are one standard deviation.

The analytical result Eq. (6.11) agrees well with the experimental data, using $L_T = 0.566$ nH for G_1 and $L_T = 0.564$ nH for G_2 . The comparison between this calculation and the measured coupling for both qubits is shown in Fig. 6.5. Maximum coupling occurs at junction phase $\delta = \pi$, where we find $g_{i,\text{max}}/2\pi \approx 47$ MHz for qubit frequencies near 5.8 GHz. The coupling can be turned off by setting $\delta = \pi/2$, making $L_T/\cos \delta$ very large. We turn the couplers off when characterizing the qubits.

Ideally, the tunable couplers used here only change the qubit-transmission line coupling strength. However, changes in the coupler junction inductance L_T affect the qubit reso-

nance frequency, as can be seen from the circuit diagram in Fig. 6.1. This is accounted for by including the coupler mutual inductance M , Eq. (6.9), in the calculation of the qubit frequency, through its effect on the qubit inductance L_q , which is given by

$$L_q = L_J + L_g - M. \quad (6.12)$$

In the experiment, $\omega_n \sim \omega_i \approx \frac{1}{\sqrt{(L_g + L_J)C_q}}$, so we can use Eq. (6.11) to relate the mutual inductance to the coupling,

$$M = -2g_i \sqrt{C_q(L_g + L_n)(L_g + L_J)}. \quad (6.13)$$

The qubit inductance is then given by

$$L_q = (L_g + L_J) \left(1 + 2g_i \sqrt{C_q(L_g + L_n)} \right), \quad (6.14)$$

so that the qubit frequency including the coupler is given by

$$\omega'_i = \frac{1}{\sqrt{L_q C_q}} \quad (6.15)$$

$$= \frac{1}{\sqrt{(L_g + L_J)C_q}} \frac{1}{\sqrt{1 + 2g_i \sqrt{C_q(L_g + L_n)}}} \quad (6.16)$$

$$\approx \omega_i \left(1 - g_i \sqrt{C_q(L_g + L_n)} \right). \quad (6.17)$$

We therefore find that the qubit frequency is shifted by the coupler by an amount

$$\Delta\omega_i = -g_i \omega_i \sqrt{C_q(L_g + L_n)} = -g_i \sqrt{\frac{L_g + L_n}{L_g + L_J}}. \quad (6.18)$$

Similarly, we can show that the transmission line's n th mode resonant frequency is shifted

by

$$\Delta\omega_n = -g_i\omega_n\sqrt{C_n(L_g + L_J)} = -g_i\sqrt{\frac{L_g + L_J}{L_g + L_n}}. \quad (6.19)$$

Because $L_n \gg L_J$, $\Delta\omega_i$ is much larger than $\Delta\omega_n$. According to Fig. 6.5, with maximum coupling $g_{i,\text{max}}/2\pi \approx 47$ MHz, the qubit frequency can be shifted by as much as -200 MHz by tuning the coupling from off to its maximum value. This frequency shift can be compensated by adjusting the qubit junction inductance L_J accordingly.

In Table 6.2 we summarize the characteristics for each qubit Q_1 and Q_2 . Parameters preceded by * are design values; others are experimentally determined.

Parameters	Q_1	Q_2
*Qubit capacitance, C_q	90 fF	90 fF
Qubit junction inductance, L_J	8.34 nH	8.57 nH
*Coupler inductance to ground, L_g	0.2 nH	0.2 nH
*Coupler stray wiring inductance, L_w	0.1 nH	0.1 nH
Coupler junction inductance, L_T	0.566 nH	0.564 nH
Qubit operating frequency, $\omega_i/2\pi$	5.809 GHz	5.731 GHz
Qubit anharmonicity, α	-160 MHz	-162 MHz
Qubit lifetime, T_1	16 μ s	11 μ s
Qubit Ramsey dephasing time, T_2	0.89 μ s	0.85 μ s
Readout resonator frequency, $\omega_r/2\pi$	6.4527 GHz	6.3390 GHz
*Readout coupling, $g_r/2\pi$	38 MHz	38 MHz
Readout dispersive shift, κ_r	0.6 MHz	0.8 MHz
$ g\rangle$ state readout fidelity, F_g	0.984	0.984
$ e\rangle$ state readout fidelity, F_e	0.950	0.942

* These are design parameters.

Table 6.2: Device parameters.

6.3 Relay method

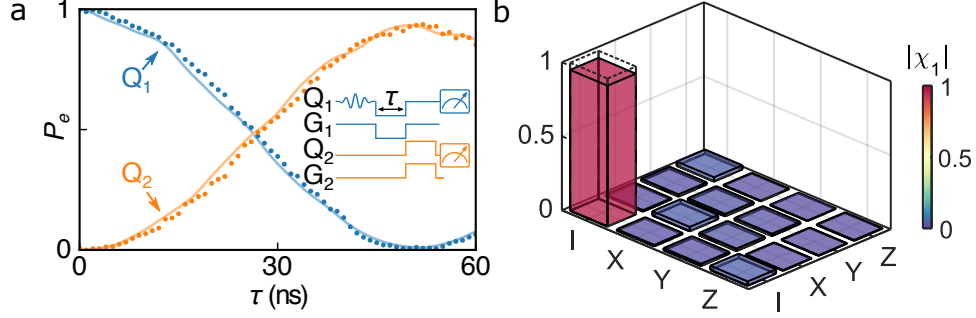


Figure 6.6: Quantum state transfer with relay method. (a) Quantum state transfer from Q_1 to Q_2 using the $n = 73$, $\omega_n/2\pi = 5.744$ GHz standing mode as a relay, showing the $|e\rangle$ state probability P_e for each qubit versus swap time τ . Solid lines: Numerical simulations. Inset: Control pulse sequence. (b) Process matrix (absolute values shown as colored bars) of the state transfer process with a fidelity $\mathcal{F}_1^p = 0.952 \pm 0.009$. Dashed-outline frames: Ideal process matrix.

By weakly coupling both qubits to a single mode, we can relay qubit states through that mode (Fig. 6.6(a)) [83, 31]. We prepare Q_1 in its excited state $|e\rangle$, then turn on the G_1 coupler for a time τ , while simultaneously adjusting Q_1 's frequency to match the selected mode, swapping the excitation to the mode. We then turn on the G_2 coupler and adjust Q_2 's frequency to swap the excitation to Q_2 . At $\tau_{\text{swap}} = 52$ ns, one photon is completely transferred from Q_1 to Q_2 , with a transfer probability of 0.936 ± 0.008 . We perform quantum process tomography [84] to characterize this transfer process, yielding the process matrix χ_1 shown in Fig. 6.6(b), with a process fidelity $\mathcal{F}_1^p = \text{Tr}(\chi_1 \cdot \chi_{\text{ideal}}) = 0.952 \pm 0.009$. Here χ_{ideal} is the ideal process matrix for the identity operation \mathcal{I} .

Because the coupling is relatively weak in this process, we simulate the relay process using the multimode Hamiltonian Eq. 6.10 with five modes included, where the third mode relays the quantum state. The rotating frame frequency is chosen to be the third mode resonant frequency so that the modes are symmetrically distributed. The coupling is assumed to be turned on and off abruptly, as the coupler rise and fall times are significantly shorter than the swap time. Decoherence is taken into account using the Lindblad master equation. According to Ref. [85], the effective dephasing time is enhanced by $\sqrt{2}$ when transferring

the quantum state from one qubit to the other, because the dephasing noise at each qubit is uncorrelated. Taking this into account, we obtain a process fidelity $\mathcal{F}_1^p = 0.955$, in good agreement with experiment. According to the simulations, more than half of the infidelity is attributed to dephasing noise. Simulations that take $T_2 = 10 \mu s$ for both qubits give a state transfer process fidelity of $\mathcal{F}_1^p = 0.977$, a Bell state fidelity $\mathcal{F}_1^s = 0.983$ and a concurrence $\mathcal{C}_1 = 0.980$. The remaining 2 percent infidelity is attributed to energy dissipation and interference from adjacent modes.

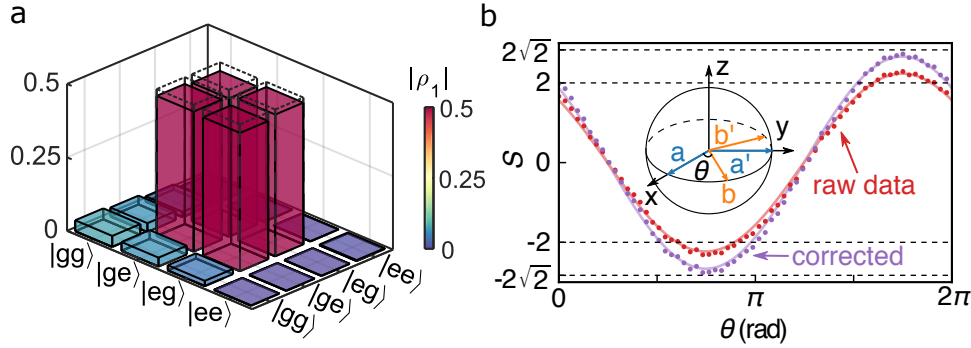


Figure 6.7: Quantum state transfer with relay method. (a) Bell state density matrix (absolute values shown as colored bars), with a state fidelity $\mathcal{F}_1^s = 0.950 \pm 0.005$. Dashed-outline frames: Ideal density matrix. (b) Bell test, showing CHSH correlation S versus measurement angle θ . Red dots: No measurement correction; purple dots: With measurement correction. Solid lines: Numerical simulations using ρ_1 from Fig. 6.6(b). The classical and quantum limits are marked with horizontal dashed lines. Inset: Measurement axes a, a', b, b' on Bloch sphere.

We also use the relay mode to generate a Bell singlet state $|\psi_{\text{Bell}}^-\rangle = (|ge\rangle - |eg\rangle)/\sqrt{2}$ between the two qubits, by terminating the Q_1 swap process at the half-swap time $\tau_{\text{half}} = 26 \text{ ns}$. We perform quantum state tomography [86], with the reconstructed density matrix ρ_1 displayed in Fig. 6.7(a), from which we calculate a state fidelity $\mathcal{F}_1^s = \langle \psi_{\text{Bell}}^- | \rho_1 | \psi_{\text{Bell}}^- \rangle = 0.950 \pm 0.005$ and a concurrence $\mathcal{C}_1 = 0.927 \pm 0.013$. This experimental result agrees well with the numerically-simulated state fidelity $\mathcal{F}_1^s = 0.947$ and concurrence $\mathcal{C}_1 = 0.914$.

We next perform the CHSH Bell inequality test [31] on this remotely entangled Bell state (see Appendix A). We measure Q_1 along the direction $a = x$ or $a' = y$, and simultaneously measure Q_2 along b or $b' \perp b$, varying the angle θ between a and b (Fig. 6.7(b) inset). We then

calculate the CHSH correlation S , as shown in Fig. 6.7(b). We find that S is maximized at $\theta = 5.5$ rad, very close to the ideal value of $7\pi/4 \cong 5.498$, where $S = 2.237 \pm 0.036$ with no measurement correction, exceeding the maximum classical value of 2 by 6.6 standard deviations. If we correct for readout error [31], we find $S = 2.665 \pm 0.044$, approaching the quantum limit of $2\sqrt{2} \cong 2.828$. The entanglement is deterministic and the measurement is single-shot (see section 6.2), so the detection loophole [87] is closed in this experiment.

6.4 Quantum ping-pong

In Fig. 6.3, each standing mode is well resolved because the coupling strength $g_1/2\pi = 5$ MHz is much smaller than $\omega_{\text{FSR}}/2\pi = 79$ MHz. In Fig. 6.8 we show a different set of spectroscopy and time domain data, measured at maximum coupling $|g_1|/2\pi = 47$ MHz, with Q_2 's coupler turned off.

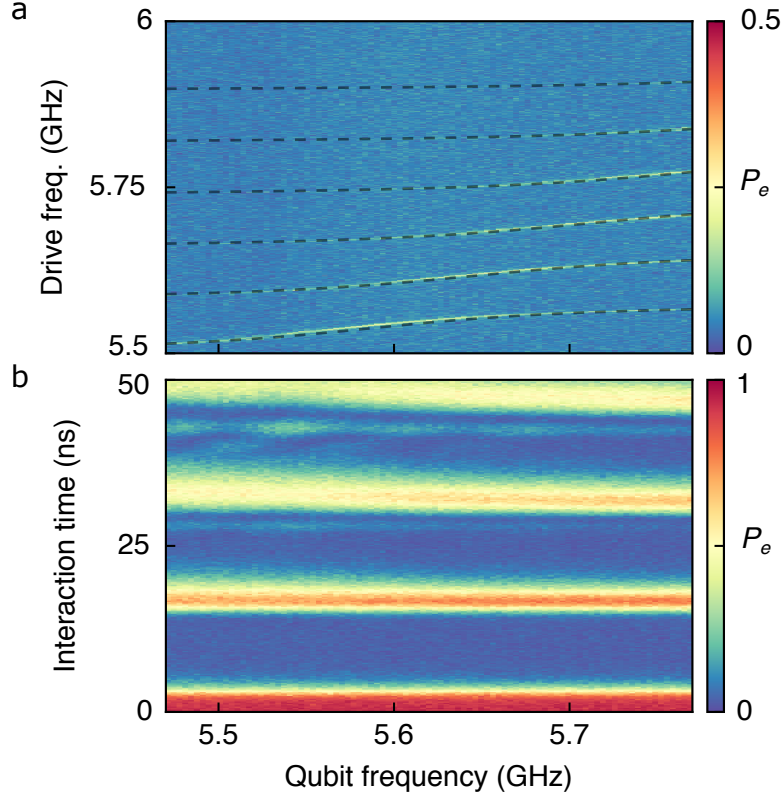


Figure 6.8: Single qubit “ping-pong” with itinerant photons. (a) Qubit Q_1 spectrum when strongly coupled to the transmission line, showing multiple modes interacting with the qubit. Dashed lines: Numerical simulations. (b) Quantum time-domain reflectometry of Q_1 with the transmission line. The coupling is sufficiently strong that the interaction is essentially independent of the qubit frequency.

In Fig. 6.8(a), the avoided-level crossing with each mode (see Fig. 6.3(a)) disappears; instead multiple modes are coupled with the qubit. In Fig. 6.8(b) we perform quantum time-domain reflectometry, where Q_1 is excited to $|e\rangle$, then we immediately turn G_1 ’s coupling to its maximum value while fixing the qubit frequency by adjusting the qubit Z bias, both for a duration τ_g , following which we monitor the qubit response. The qubit excitation is released into the transmission line in a few nanoseconds, leaving the qubit in its ground state $|g\rangle$ until the photon reflects off the far end of the transmission line and returns to the qubit, re-exciting the qubit to its $|e\rangle$ state. This “ping-pong” process does not depend on qubit frequency, other than some small features.

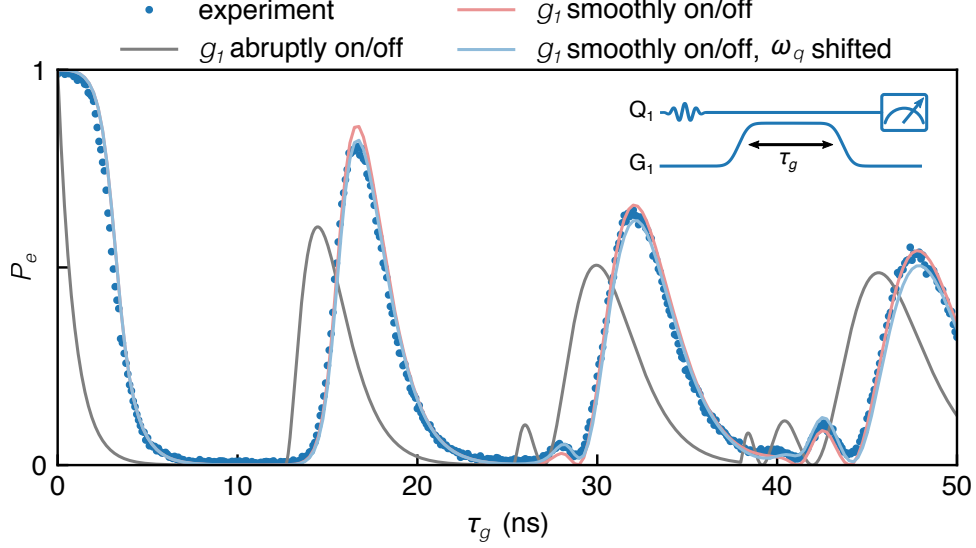


Figure 6.9: Variant of the reflectometry “ping-pong” dynamics, with Q_1 ’s frequency initially set to 5.809 GHz with the qubit in $|e\rangle$, following which its Z bias remains unchanged. Q_1 emits an itinerant photon in about 8 ns, which is reflected from the far end of the transmission line and caught by Q_1 a time $2T_\ell = 12.6$ ns later, the process here repeated three times. Solid lines: Numerical simulations (see text for details). Inset: Control pulse sequence, with the rise and fall times indicated; qubit frequency is changed by the coupling control signals.

In Fig. 6.9, we perform a variant of the reflectometry “ping-pong” experiment, where after exciting Q_1 to $|e\rangle$, we leave Q_1 ’s Z bias fixed, allowing Q_1 ’s frequency to vary due to changes in the coupling. We see that the emission takes about 8 ns, with the round trip then completed in $2T_\ell = 12.6$ ns. Three full transits are shown, with the peak amplitude falling and small ripples appearing, mainly due to scattering from each photon-qubit interaction.

For the experiment here, the maximum coupling $g_{1,\max}$ becomes comparable to the free spectral range ω_{FSR} . To maintain the multimode model accuracy, the number of modes N needed for the simulation (and thus the Hilbert space dimension) is so large that it becomes overly computer-intensive to complete the simulations. An alternative is to use input-output theory [57, 27, 28], which treats the mode spectrum in the transmission line as continuous, and thus is well-suited for simulating the dynamics with large $g_{i,\max}/\omega_{\text{FSR}}$.

According to the input-output theory (see section 2.4.3), the evolution of the qubit op-

erator σ_1 follows

$$\frac{d\sigma_1(t)}{dt} = -i\Delta\omega_1(t)\sigma_1(t) - \frac{\kappa_1(t)}{2}\sigma_1(t) + \sqrt{\kappa_1(t)}a_{\text{in},1}(t), \quad (6.20)$$

$$\sqrt{\kappa_1(t)}\sigma_1(t) = a_{\text{in},1}(t) + a_{\text{out},1}(t), \quad (6.21)$$

$$a_{\text{in},1}(t) = a_{\text{out},1}(t - 2T_\ell), \quad (6.22)$$

where κ_1 is the qubit Q_1 energy decay rate to the transmission line, which can be calculated according to Fermi's golden rule:

$$\kappa_1 = \frac{2\pi}{\hbar}(\hbar g_1)^2 \frac{1}{\hbar\omega_{\text{FSR}}}. \quad (6.23)$$

The input and output field operators are $a_{\text{in},1}$ and $a_{\text{out},1}$, respectively. Note we have replaced the resonator annihilation operator in Eq. 2.129 by the qubit annihilation operator; this replacement is valid because we only consider situations with at most one excitation in the system.

These are delay differential equations and should be solved in a stepwise fashion. Starting from $a_{\text{in},1} = a_{\text{out},1} = 0$ at $t = 0$, Eqs. (6.20,6.21,6.22) can be transformed to the following stepwise functions:

$$\left. \begin{aligned} a_{\text{in},1}(t) &= 0, \\ a_{\text{out},1}(t) &= \sqrt{\kappa_1(t)}\sigma_1(t), \\ \frac{d\sigma_1(t)}{dt} &= -i\Delta\omega_1(t)\sigma_1(t) - \frac{\kappa_1(t)}{2}\sigma_1, \end{aligned} \right\} 0 < t \leq 2T_\ell, \quad (6.24)$$

$$\left. \begin{aligned} a_{\text{in},1}(t) &= \sqrt{\kappa_1(t - 2T_\ell)}\sigma_1(t - 2T_\ell), \\ a_{\text{out},1}(t) &= \sqrt{\kappa_1(t)}\sigma_1(t) - \sqrt{\kappa_1(t - 2T_\ell)}\sigma_1(t - 2T_\ell), \\ \frac{d\sigma_1(t)}{dt} &= -i\Delta\omega_1(t)\sigma_1(t) - \frac{\kappa_1(t)}{2}\sigma_1 + \sqrt{\kappa_1(t)}\sqrt{\kappa_1(t - 2T_\ell)}\sigma_1(t - 2T_\ell), \end{aligned} \right\} 2T_\ell < t \leq 4T_\ell. \quad (6.25)$$

This can be generalized to arbitrary segments.

We observe that as the coupling becomes strong, the non-zero rise and fall time of the control signal has to be taken into account. In the simulations, we assume the phase due to the external flux threaded through the coupler loop δ_{ext} is proportional to the control pulse amplitude. The coupler junction phase δ is related to δ_{ext} by [82]

$$\delta_{\text{ext}} = \delta + \frac{2L_g + L_w}{L_T} \sin \delta. \quad (6.26)$$

The coupler is first biased with a DC current to give

$$\delta_{\text{ext}} = \delta_{\text{off}} = \pi/2 + \frac{2L_g + L_w}{L_T}, \quad (6.27)$$

where $\delta = \pi/2$ and $g_1 = 0$. We then use the high-speed control signal output of the DAC to rapidly tune the coupling g_1 , combined with a separate DC current source via a bias tee mounted on the mixing chamber stage. The filter in the DAC output has a Gaussian spectrum, so that when we generate a rectangular output signal to set the coupling to its maximum value (where $\delta_{\text{ext}} = \delta = \pi$), the actual output is a convolution of the filter Gaussian and the rectangular control signal. The external flux then changes as

$$\delta_{\text{ext}}(t) = (\pi - \delta_{\text{off}}) \left(G(w_{\text{FWHM}}, t) \otimes \text{Rect}(\tau_g, t) \right) (t) + \delta_{\text{off}}, \quad (6.28)$$

where $G(w_{\text{FWHM}}, t)$ is a Gaussian function with a full-width at half-maximum (FWHM) of w_{FWHM} , and $\text{Rect}(\tau, t)$ is a rectangle function with unit amplitude from 0 to τ_g . We then solve Eq. (6.26) to obtain $\delta(t)$, and use this result in Eq. (6.11) to obtain $g_1(t)$. The energy decay rate κ_1 can then be calculated with Eq. (6.23).

In Fig. 6.9, we compare the experimental data with different assumptions for the simulations. The light black line treats the coupling as switched abruptly between its on and off values, i.e. we assume $w_{\text{FWHM}} = 0$. We see that the qubit occupation decays exponentially in the simulation, and the recapture probability is limited to $\sim 54\%$, consistent with the

predictions of Refs. [25, 26]. The light red line corresponds to setting $w_{\text{FWHM}} = 2$ ns, which is determined by the bandwidth of the control signal output filter, and agrees well with the experimental data, except the photon recapture probability is higher. This is because the qubit frequency is shifted when tuning the coupling to the maximum, see Eq. (6.18), not accounted for in this simulation. The light blue line takes the frequency shift into account and is in good agreement with the experiment.

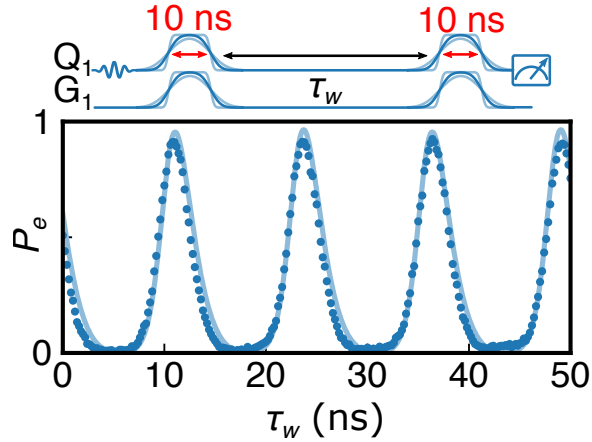


Figure 6.10: Optimizing photon catch by adjusting control pulse envelope. Maximum catch probability is improved from ~ 0.8 in Fig. 6.9 to 0.922 ± 0.004 by adjusting the control pulse slope. Solid line: Numerical simulations. Top: Control pulse sequence, showing the pulse shaping. The rising edge of the first control pulse determines the emission process, and the falling edge of the second control pulse determines the capture process. The qubit bias pulses cancel the coupler-generated frequency shift.

Next, to tune up the photon emission and capture process, we set the emission and capture times to 10 ns, and vary the wait time τ_w between them, see Fig. 6.10. We dynamically tune Q_1 's coupling, while compensating the qubit frequency shift with the qubit Z control bias. Ideally, the itinerant photon can be captured with unit probability if the emission and capture control pulses are properly tuned [27, 28]. However, the bandwidth of our control electronics is insufficient to allow the desired sub-nanosecond tuning of the itinerant photon envelope, so we instead approximately tune the coupling by convolving a Gaussian and a rectangle pulse; the width of the Gaussian shapes the edges of the convolved pulse. In

Fig. 6.10, the coupler control signal changes as:

$$\delta_{\text{ext}}(t) = (\pi - \delta_{\text{off}}) \left\{ G(w_{\text{FWHM}}, t) \otimes [\text{Rect}(\tau_g, t) + \text{Rect}(\tau_g, t - \tau_w - \tau_g)] \right\}(t) + \delta_{\text{off}}. \quad (6.29)$$

In addition to the Gaussian filter effect, we program the control signal output to adjust w_{FWHM} to 3 ns to optimize the photon catch probability, and compensate the qubit frequency shift with the qubit Z bias pulse. This frequency compensation is assumed to be perfect in the simulation, i.e., $\Delta\omega_1 = 0$. We find that this sub-optimal shaping still achieves a self-capture probability of 0.922 ± 0.004 . The robustness of this protocol to control pulse imperfections is as expected [88].

6.5 Itinerant photon method

The relay method requires $g_i \ll \omega_{\text{FSR}}$ so that the swap process only involves a single mode. However, ω_{FSR} scales inversely with transmission distance ℓ , making g_i impractically small as ℓ increases. An alternative approach, independent of transmission distance, is to use itinerant photons for state transfer [27, 28]. This is experimentally challenging, and has only recently been demonstrated with superconducting qubits [21, 22, 23]. In these experiments, quantum states were transferred through a ~ 1 m-long superconducting coaxial cable interrupted by a circulator. The state transfer speeds were significantly slower than the photon travel time in the channel, making reflections and their interference nearly unmanageable without the circulator. The circulator however also introduces loss, limiting transfer fidelities to about 80%. With the one to two orders of magnitude stronger coupling achieved here, we perform remote state transfer and entanglement generation using shaped itinerant photons without a circulator, allowing sufficient fidelity to violate the Bell inequality.

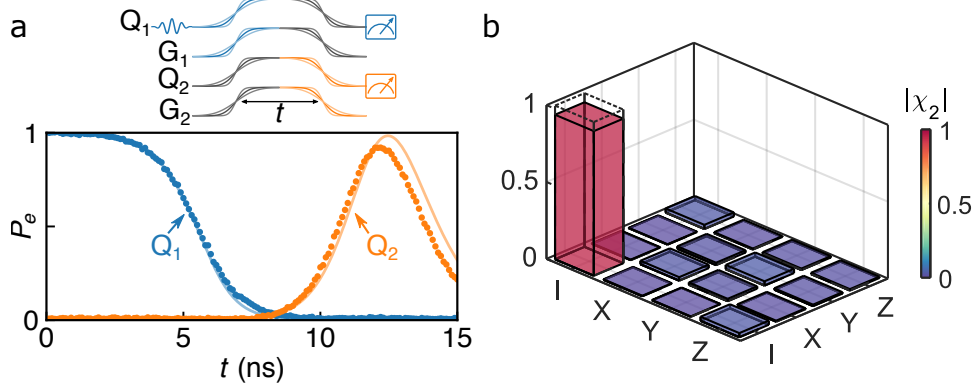


Figure 6.11: Quantum state transfer with itinerant photons. (a) Using optimized control pulses for the couplers while keeping the qubit frequency fixed, we achieve a high-fidelity state transfer, with a maximum transfer probability of 0.919 ± 0.004 in 12.2 ns. Solid lines: Numerical simulations. Top: Control pulse sequence. The rising edge of Q_1 's control pulse determines the emission process, and the falling edge of Q_2 's control pulse determines the capture process. (b) Quantum process tomography, with a process fidelity $\mathcal{F}_2^p = 0.940 \pm 0.008$. Dashed-outline frames: Ideal process matrix.

We perform the single qubit tune-up shown in Fig. 6.10 for each qubit separately, then combine these processes to perform qubit-to-qubit state transfer using itinerant photons, see Fig. 6.11(a). We first excite Q_1 to $|e\rangle$, with Q_2 in $|g\rangle$, then turn on the tuned G_1 and G_2 time-dependent couplings simultaneously for a duration t . The itinerant photon is released from Q_1 into the channel in about 10 ns, and begins to interact with Q_2 after $T_\ell = 6.3$ ns. The photon is captured by Q_2 , with a maximum probability of 0.919 ± 0.004 at $t = 12.2$ ns. We carry out quantum process tomography for this sequence, and reconstruct the process matrix χ_2 as shown in Fig. 6.11(b), with a fidelity $\mathcal{F}_2^p = \text{Tr}(\chi_2 \cdot \chi_{\text{ideal}}) = 0.940 \pm 0.008$.

Here we model the state transfer process in Fig. 6.11(a) using the input-output theory [57]:

$$\frac{d\sigma_1}{dt} = -i\Delta\omega_1\sigma_1 - \frac{\kappa_1(t)}{2}\sigma_1 + \sqrt{\kappa_1(t)}a_{\text{in},1}(t), \quad (6.30)$$

$$\frac{d\sigma_2}{dt} = -i\Delta\omega_2\sigma_2 - \frac{\kappa_2(t)}{2}\sigma_2 + \sqrt{\kappa_2(t)}a_{\text{in},2}(t), \quad (6.31)$$

$$\sqrt{\kappa_1(t)}\sigma_1(t) = a_{\text{in},1}(t) + a_{\text{out},1}(t), \quad (6.32)$$

$$\sqrt{\kappa_2(t)}\sigma_2(t) = a_{\text{in},2}(t) + a_{\text{out},2}(t), \quad (6.33)$$

$$a_{\text{in},1}(t) = a_{\text{out},2}(t - T_\ell), \quad (6.34)$$

$$a_{\text{in},2}(t) = a_{\text{out},1}(t - T_\ell). \quad (6.35)$$

The time evolution of the decay rates $\kappa_i(t)$ are calculated as mentioned above for single qubit “ping-pong” with itinerant photons. The qubit frequency shifts are assumed to be perfectly compensated in the simulation, so we take $\Delta\omega_i = 0$. The simulated emission agrees very well with the Q_1 data, and the simulated capture agrees with the Q_2 data at the beginning, but reaches a higher maximum capture probability than the experiment. According to ref. [88], the state transfer protocol is robust against control pulse imperfections, but is sensitive to qubit frequency mismatch. The discrepancy between the simulation and the experiment is likely due to the frequency mismatch between the two qubits. Note the state transfer process fidelity is not affected by changes in the transmission line length ℓ in this simulation, unless the channel decoherence is taken into account.

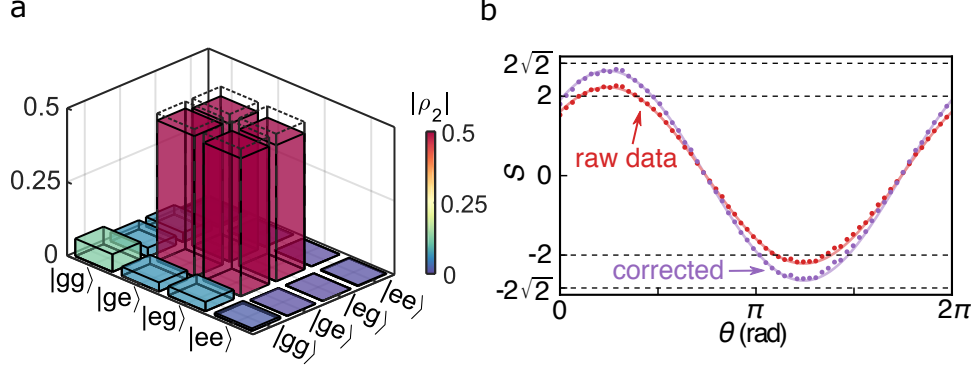


Figure 6.12: Remote entanglement generation with itinerant photons. (a) Density matrix of the Bell state generated by sending half an itinerant photon from Q_1 to Q_2 , with a state fidelity $\mathcal{F}_2^s = 0.936 \pm 0.006$ and a concurrence $\mathcal{C}_2 = 0.914 \pm 0.014$. Dashed-outline frames: Ideal density matrix. (b) Bell test, showing the CHSH correlation S versus measurement angle θ . Red dots: No measurement correction; purple dots: With measurement correction. Solid lines: Numerical simulations using ρ_2 from panel c. The correlation is maximized at $\theta = 0.84$ rad, where $S = 2.223 \pm 0.023$ without measurement correction. Classical and quantum limits are marked with horizontal dashed lines.

With the high fidelity state transfer achieved, we use half an itinerant photon to generate entanglement between the two qubits: We first prepare Q_1 in $|e\rangle$, then control Q_1 's coupling to release half its excitation to the channel, which is captured by Q_2 using the same time-domain coupling as in the state transfer experiment. This generates a Bell triplet state $|\psi_{\text{Bell}}^+\rangle = (|ge\rangle + |eg\rangle)/\sqrt{2}$ between the two qubits as shown in Fig. 6.12(a), with a reconstructed Bell state fidelity $\mathcal{F}_2^s = \langle \psi_{\text{Bell}}^+ | \rho_2 | \psi_{\text{Bell}}^+ \rangle = 0.936 \pm 0.006$ and a concurrence $\mathcal{C}_2 = 0.914 \pm 0.014$.

As with the relay mode method, we carry out a CHSH Bell inequality test with no detection loophole [87], see Fig. 6.12(b). We find that S is maximized at $\theta = 0.84$ rad, close to the ideal value of $\pi/4 \cong 0.785$, where $S = 2.223 \pm 0.023$ without applying a measurement correction, exceeding the classical limit of 2 by 9.7 standard deviations. If we correct for readout error, we find $S = 2.629 \pm 0.028$, close to the quantum limit of $2\sqrt{2}$.

In the experiments in Refs. [21, 22, 23], a circulator was interposed in the transmission line connecting the two communication nodes, eliminating reflections and at the same time providing a means to probe the emitted photon waveform, allowing tune-up of the emission

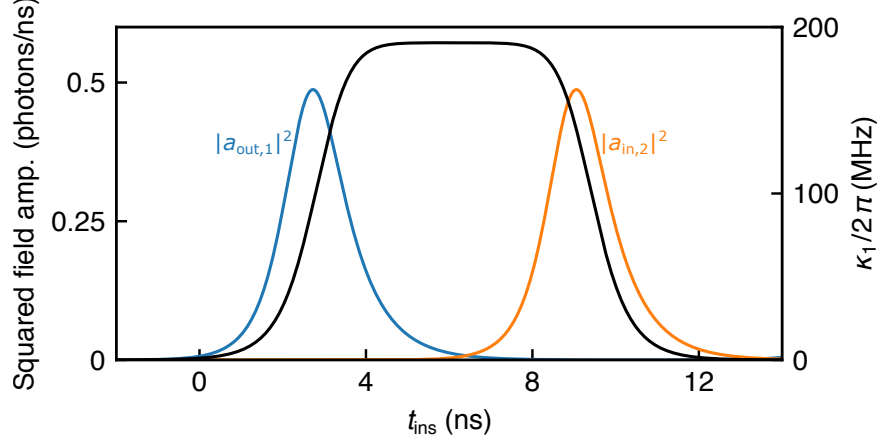


Figure 6.13: Traveling photon envelope estimated from simulations. The horizontal axis is the instantaneous time t_{ins} of the dynamic evolution, calculated for a control pulse width set to $t = 12.2$ ns for optimized state transfer. The blue curve shows the emitted photon envelope $|a_{\text{out},1}|^2$; the orange curve shows the captured photon envelope $|a_{\text{in},2}|^2$. The black curve (right axis) shows the decay rate $\kappa_1/2\pi$ for qubit Q_1 ; qubit Q_2 is very similar.

profile to achieve the desired symmetric envelope. In our itinerant photon experiment, we have no direct means to probe the emitted photon envelope. However, the emitted and captured photon envelope can be estimated from input-output theory. In Fig. 6.13 we show $|a_{\text{out},1}|^2$ and $|a_{\text{in},2}|^2$ calculated from the simulation results shown in Fig. 4a in the main text, these results being close to the experimental data. We see that the emitted photon envelope is relatively symmetric, even with the simple coupler control pulse used in the experiment. This symmetry is the key reason that we are able to achieve such high-fidelity state transfers using the itinerant photon method.

CHAPTER 7

CONCLUSION

In conclusion, we present a simple architecture that allows efficient quantum state transfer and remote entanglement between two superconducting qubits, connected by a 78 cm-long transmission line. The fidelities are sufficient to violate the Bell inequality using two different methods. This architecture can be expanded to multiple communication channels, allowing the exploration of more complex quantum communication protocols, and could serve as a backbone for fault-tolerant distributed quantum computing.

7.1 Summary

In Table 7.1 we summarize the main results of this thesis and compare with state-of-the-art experiments.

Source	coupling rate $\kappa/2\pi$ ($g/2\pi$)	Transfer efficiency	Process fidelity \mathcal{F}^p	State fidelity \mathcal{F}^s	Concurrence \mathcal{C}	CHSH correlation S
This work (relay mode)	(5 MHz)	0.936	0.952	0.950	0.927	2.237
This work (itinerant photon)	~ 175 MHz	0.919	0.940	0.936	0.914	2.223
Kurpiers <i>et al.</i> [21]	~ 10 MHz	0.676	0.8002	0.789	0.747	N/A
Axline <i>et al.</i> [22]	~ 1 MHz	0.74	0.76	0.61	0.51	N/A
Campagne-Ibarcq <i>et al.</i> [23]	~ 1 MHz	0.7	N/A	0.73	N/A	N/A
Leung <i>et al.</i> [89]	(~ 2 MHz)	N/A	0.61	0.793	N/A	N/A

Table 7.1: Comparison of similar deterministic remote state transfer and entanglement generation experiments on superconducting circuits. Here $\kappa/2\pi$ is the photon decay rate into the channel (itinerant photon method), $g/2\pi$ is the on-resonant coupling between the qubit and the relay mode, \mathcal{F}^p is the state transfer process fidelity, \mathcal{F}^s the Bell state fidelity, \mathcal{C} the Bell state concurrence, and S the CHSH correlation.

7.2 Outlook

The comparison in Table 7.1 is somewhat unfair because the other experiments are inter-chip while the experiment in this thesis is single-chip. However, the technology we develop here is by no means limited to single-chip. As shown in Ref. [81], the quality factor for superconducting coaxial cables can be as high as 0.9×10^5 , similar level as that of the on-chip transmission line in this thesis (1.44×10^5), so in principle the transmission line here can be replaced by a superconducting cable for inter-chip quantum communication, although care must be taken in the chip-cable interface. To achieve a similar level of transfer fidelity, normal-metal SMA connectors and circulators must be avoided. The coaxial cable can be connected to the chip by direct soldering or wirebonding to reduce loss.

Limited by the feature size of a coaxial cable, it is difficult to scale up the number of channels using this approach. A more scalable way might be using micro-fabricated superconducting flexible cable based on polyimide dielectric [90]. By patterning the cable spirally on a standard silicon wafer, one can fabricate superconducting cable of meter scale length [91]. Cryogenic measurement at 20 mK shows that a quality factor as high as 0.428×10^5 can be achieved with a Niobium microstrip resonator on HD-4100 polyimide dielectric [90]. It is therefore possible to use high quality, multi-channel superconducting flexible cables to link high performance superconducting quantum processors together, forming a more powerful distributed quantum computing cluster [19, 20].

APPENDIX A

BELL’S INEQUALITY

The fundamentally probabilistic nature of quantum mechanics was not accepted by some physicists, including Albert Einstein. The fact that quantum mechanics does not provide a way to predict outcomes of all possible measurements with certainty led to the suspicion that quantum mechanics was incomplete [92]. A deterministic classical theory called “hidden variable theory” was proposed as an alternative to quantum mechanics, which assumes the existence of extra “hidden variables” capturing the missing information.

In 1964, John S. Bell investigated the theoretical implications of a possible local hidden variable theory and showed that quantum mechanics could not be derived from such a theory to arbitrary accuracy [93]. In 1969, J. F. Clauser, M. A. Horne, A. Shimony, and R. A. Holt formulated an example of the incompatibility between a local hidden variable theory and quantum mechanics into an experiment that could test whether quantum mechanics was indeed incomplete [78]. In the proposed experiment a source is used to produce pairs of particles in a perfectly anti-correlated state, for example two particles A and B with their spin in the Bell singlet state $\frac{1}{\sqrt{2}}(|01\rangle - |10\rangle)$, where $|0\rangle$ and $|1\rangle$ represent spin up and down states respectively. These particles are then physically separated by a large enough distance that classical information cannot be transferred between them throughout the remainder of the experiment. At those remote locations the particles are then measured along random axes. Rewriting the Bell singlet state in the basis of the measurement axes, say $|a\rangle$ and $|b\rangle$, where

$$|0\rangle = \alpha|a\rangle + \beta|b\rangle, \tag{A.1}$$

$$|1\rangle = \delta|a\rangle + \gamma|b\rangle, \tag{A.2}$$

we have

$$\frac{1}{\sqrt{2}}(|01\rangle - |10\rangle) = (\alpha\gamma - \beta\delta)\frac{1}{\sqrt{2}}(|ab\rangle - |ba\rangle), \tag{A.3}$$

we see that the state is still perfectly anti-correlated, so that every time both particles are measured along the same axis, independent of which axis it is, they will yield an opposite outcome with certainty. Quantum mechanics states that a measurement of particle A instantaneously collapses the wavefunction of particle B despite the fact that they are causally disconnected by their distance. Einstein called this non-local effect of entanglement “spooky action at a distance”. A local hidden variable theory would instead state that the particles agree on all possible measurement outcomes before their separation. This information was encoded in the state of the particles in some extra unmeasured degrees of freedom, the hidden variables.

Now we consider a slightly more complicated experiment. If we measure both particles along two axes, say a and a' for particle A , b and b' for particle B , and encode the outcomes in binary (say 0 for spin up and 1 for spin down), the local hidden variable theory implies that the particles have to choose at the time of separation to belong to one of the 16 possible populations shown in Table A.1. Next, we define a correlation measurement E_{xy} which equals 1 if the outcome of a measurement on particle A along axis x and particle B along axis y yields the same result, and $E_{xy} = 0$ for opposite results. The expectation value of E_{xy} is then given by

$$\langle E_{xy} \rangle = P_{00}(x, y) - P_{01}(x, y) - P_{10}(x, y) + P_{11}(x, y), \quad (\text{A.4})$$

and the CHSH correlation S is defined as

$$S = \langle E_{ab} \rangle + \langle E_{a'b} \rangle - \langle E_{ab'} \rangle + \langle E_{a'b'} \rangle. \quad (\text{A.5})$$

Population	a	a'	b	b'	E_{ab}	$E_{a'b}$	$E_{ab'}$	$E_{a'b'}$	S
n_0	0	0	0	0	1	1	1	1	2
n_1	0	0	0	1	1	1	-1	-1	2
n_2	0	0	1	0	-1	-1	1	1	-2
n_3	0	0	1	1	-1	-1	-1	-1	-2
n_4	0	1	0	0	1	-1	1	-1	-2
n_5	0	1	0	1	1	-1	-1	1	2
n_6	0	1	1	0	-1	1	1	-1	-2
n_7	0	1	1	1	-1	1	-1	1	2
n_8	1	0	0	0	-1	1	-1	1	2
n_9	1	0	0	1	-1	1	1	-1	-2
n_{10}	1	0	1	0	1	-1	-1	1	2
n_{11}	1	0	1	1	1	-1	1	-1	-2
n_{12}	1	1	0	0	-1	-1	-1	-1	-2
n_{13}	1	1	0	1	-1	-1	1	1	-2
n_{14}	1	1	1	0	1	1	-1	-1	2
n_{15}	1	1	1	1	1	1	1	1	2

Table A.1: Possible outcome populations for a deterministic theory.

According to Table A.1, the value of S for each of the 16 possible pair-populations is either 2 or -2 . Therefore, a measurement of the expectation value of S over an ensemble of many particles will result in a weighted average of -2 and 2, which has the following restriction:

$$|S| \leq 2. \quad (\text{A.6})$$

This is called the Bell's inequality. Note the derivation does not assume anything about the choice of measurement axes a , a' , b and b' , nor the population distribution of the outcomes.

It turns out that quantum mechanics allows for stronger correlations. For example, if we choose a and a' to be the X axis and Y axis respectively, and b and b' are chosen to be at 45° with respect to a and a' in the XY plane, then it can be shown that

$$S = \langle E_{ab} \rangle + \langle E_{a'b} \rangle - \langle E_{ab'} \rangle + \langle E_{a'b'} \rangle = 2\sqrt{2}, \quad (\text{A.7})$$

clearly violating Bell's inequality. The experimental violation of Bell's inequality is an important benchmark for quantum entanglement, providing a straightforward test of whether a local and deterministic theory can explain measured correlations. Violations of the Bell or Leggett-Garg [94] inequalities have been demonstrated using optical photons, trapped ions and electronic spins etc since the 1970s [95, 96, 97, 98], and locally-coupled superconducting qubits about ten years ago [31, 99]. In this thesis, we have achieved this benchmarking result again with remotely-connected superconducting qubits for the first time, see chapter 6.

APPENDIX B

PLAYOUT

PLayout is a custom Python package for generating circuit patterns. All the device patterns in this thesis were generated by PLayout. There are many electronic design automation (EDA) or computer aided design (CAD) softwares available, either commercial or open source, so why do we bother creating the wheel again? There are a few reasons for doing this:

1. Our circuit designs are distinct from those of the well established printed circuit boards (PCB) or machining drawings. The automation tools developed for these applications are generally not suitable here.
2. The circuit patterns we want to create have a lot of arcs and repetitive structures with slight variations. It is cumbersome and error-prone to create all these by hand. Generating this kind of pattern with scripting is preferable.
3. Some commercial EDA tools dedicated to semiconductor manufacturing might be suitable, but the license fee is usually unacceptably high.
4. Some layout software supports scripting, but in their native language, e.g. C, LISP, Ruby etc, which forces the user to learn an unfamiliar or unpopular programming language. The open source software KLayout¹ supports Python scripting, but only with the Python interpreter provided by KLayout for license reasons, limiting its flexibility.
5. There are a few Python packages available for handling layout, for example gdspy², dxfwrite³, dxfgrabber⁴. These significantly reduce the effort needed to build a custom package for generating circuit patterns.

1. <https://www.klayout.de>

2. <https://github.com/heitzmann/gdspy>

3. <https://github.com/mozman/dxfwrite>

4. <https://github.com/mozman/dxfgrabber>

Given these reasons, I have spent some effort creating a custom Python package called “PLayout”, where the first letter “P” refers to Python.

Polygon is the fundamental geometry in our circuit pattern. Arcs are rendered to poly-lines with resolution much smaller than that of the fabrication tools. In PLayout, there are two fundamental classes, based on which we create all circuit patterns. One is `Polygon`, and the other is `Structure`, which is essentially a collection of polygons, representing certain circuit elements like qubit, coupler etc.

To begin, here we show how to create a `Polygon` object with PLayout in different ways:

```
from playout import Polygon
# construct polygon directly from points.
p11 = Polygon([(0,0),(1,0),(1,1),(0,1)], layer='polygon1')
```

Or we can create the `Polygon` object first, then add points subsequently to it with the overloaded `+=` operator:

```
# construct polygon by adding points using the += operator.
p12 = Polygon(layer='polygon2')
p12 += (2,2) # add a single point.
p12 += [(3,2),(3,3),(2,3)] # add a list of points.
```

Sometimes we want to add a point to the polygon with relative coordinates, this can be done with the overloaded `>` operator:

```
# add points with relative coordinate using the > operator.
# p1 > (dx,dy) adds a point that is (dx,dy) with respect to
# the last point.
p13 = Polygon(layer='polygon3')
p13 > (4,0) # if the polygon is empty, the reference is (0,0),
# so the first point coordinate is (4,0)+(0,0)=(4,0).
p13 > (1,0) # the coordinate is (1,0)+(4,0) = (5,0)
p13 > (0,1) # the coordinate is (0,1)+(5,0) = (5,1)
p13 > (-1,0) # coordinate is (5,1)+(-1,0) = (4,1)
```

We can `copy`, `displace`, `rotate`, or `mirror` the `Polygon` object:

```
p13_disp = p13.copy() # make a copy of the object.
p13_disp.displace(0,2) # displace it by (0,2).
p13_rot = p13.copy()
p13_rot.rotate(45,ref_point=(4,0)) # rotate by 45 degrees about the point
                                   (4,0).
p13_x = p13.copy().mirror(axis='x') # mirror with respect to x axis.
p13_y = p13.copy().mirror(axis='y') # mirror with respect to y axis.
```

The polygons can be added together, forming a `Structure` object:

```
# adding polygons creates a structure object.
p1_together = p1+p2+p3+p13_disp+p13_rot+p13_x+p13_y
```

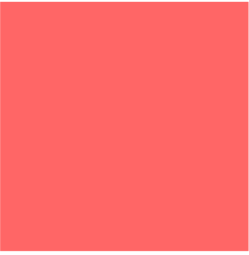
To output the pattern, simply call the `save_dxf()` function:

```
p1_together.save_dxf('test_polygon.dxf')
```

PLayout also supports scalable vector graphics (SVG) format output:

```
p1_together.save_svg('test_polygon.svg')
```

The `Polygon` and `Structure` class have implemented the `_repr_svg_()` function, so that one can see the generated pattern directly in a Jupyter notebook environment:

```
In [1]: from playout import *
In [2]: Polygon([(0,0), (1,0), (1,1), (0,1)])
Out[2]: 
```

```
In [ ]:
```

Figure B.1: The generated pattern can be embedded in a Jupyter notebook environment.

The coordinates of the points are stored as a numpy array in the attribute `Polygon.points`, and each `Polygon` object has a `layer` and `color` attribute.

A `Structure` object is essentially a collection of polygons stored as a list in the attribute `Structure.polygons`. `Polygon` and `Structure` can add together with `+` or `+=` operator, where the `+` operator returns a new `Structure` while the `+=` operator modifies the operand. We can `copy`, `displace`, `rotate` and `mirror` a `Structure` in the same way as for `Polygon`.

The polygons in a `Structure` object might locate in different layers. Some methods are provided to handle polygons in a specific layer, for example `Structure.get_layer([layer])` returns a new `Structure` containing a copy of all the polygons in that layer, and `Structure.delete_layer([layer])` deletes all polygons in that layer from the current `Structure`.

Boolean operations are nontrivial and important in layout design. Both `Polygon` and `Structure` supports the `intersection`, `union`, and `difference` operations. The boolean operations are implemented with a high performance open source library `clipper`⁵ written in C. In PLayout, boolean operations are layer specific, for example if we apply `A.union(B)`, then the polygons in layer 1 of A will only merge with the polygons of B in layer 1, and the polygons in layer 2 of A will only merge with the polygons of B in layer 2 and so on. A boolean operation on two layers can be done by first extracting the polygons in the target layer using `Structure.get_layer([layer])`, then change the `layer` attribute of each polygon before applying the boolean operation:

```
# union layer1 of Structure A and layer2 of Structure B as layer3.
B_layer2 = B.get_layer('layer2')
for pl in B_layer2.polygons:
    pl.layer = 'layer1'
result = A.get_layer('layer1').union(B_layer2)
for pl in result.polygons:
    pl.layer = 'layer3'
```

5. <http://www.angusj.com/delphi/clipper.php>

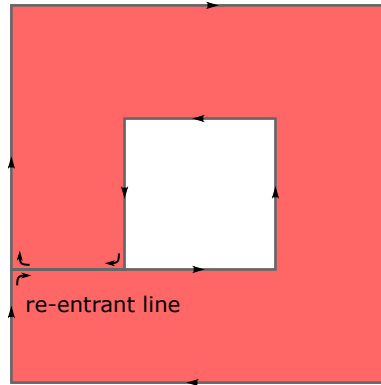


Figure B.2: Re-entrant hole from boolean operation. The curve direction of the inner boundary is different from that of the outer boundary to avoid creating a self-crossing polygon.

One important feature of `clipper` is that the inner holes from a boolean operation are created as re-entrant holes (also known as keyhole), see Fig. B.2 for example, which is compliant with the GDSII stream file format, a format that most fabrication tools prefer. There are some other Python packages that can implement boolean operations, for example Shapely⁶, but it treats the inner holes as interior boundaries, which is incompatible with the file format of the fabrication tools.

Besides boolean operations, `clipper` also provides a method to offset polygons, which can be very useful in some cases, see the example below, with the result shown in Fig. B.3.

```
p1 = Polygon([(0,0),(1,0),(1,1)])
p11 = p1.copy().offset(0.2,'miter',tolerance=2).displace(2,0)
p12 = p1.copy().offset(0.2,'miter',tolerance=3).displace(4,0)
p13 = p1.copy().offset(0.2,'round',tolerance=100).displace(6,0)
pls = p1 + p11 + p12 + p13
pls += p1.copy().displace(2,0)+p1.copy().displace(4,0)+p1.copy().displace(
    6,0) # for on site comparison.
```

6. <http://toblerity.org/shapely/manual.html>

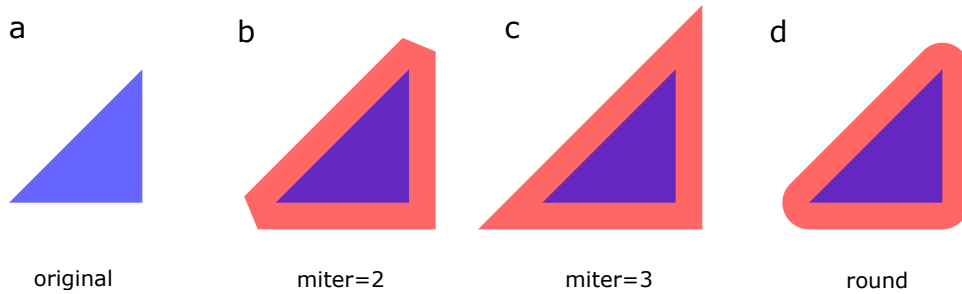


Figure B.3: Offset a polygon.

Now we can start to construct real circuit components on top of **Polygon** and **Structure**. The most frequently used circuit component is the coplanar waveguide (CPW) transmission line. Regarding this, PLayout has a built-in class **CPW** that facilitates the creation and manipulation of CPW lines. Here is a simple example of creating a straight segment of CPW line:

```
from playout import CPW
cpw1 = CPW((0,0),W=8,S=4) # first argument is the start point, then
# follows the center trace width W, the separation to ground S.
# now create a straight line.
cpw1.add_line(100,0) # The end point of the line is (30,0)
# relative to the start point.
```

Here is how it looks:

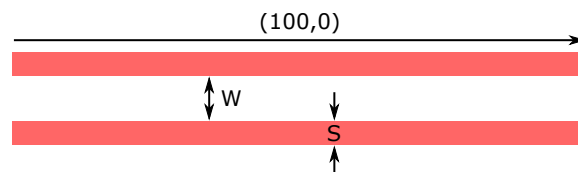


Figure B.4: CPW line creation. We use positive photoresist for lithography and etch to create pattern on the wafer, so the area where metal will be removed is enclosed (color in red).

Note in the fabrication, we use positive photoresist for lithography, and use Inductively Coupled Plasma (ICP) etch to create the pattern on the wafer (see chapter 4), so the area where the metal will be removed is enclosed in the pattern.

To create an arc segment of CPW line, we simply call the `add_arc()` function:

```
cpw1.add_arc((0,15),180) # first argument is the center of the arc
# relative to the current CPW line end, the second argument is the
# arc angle. Positive angle rotates counter-clockwise, negative
# angle rotates clockwise.
```



Figure B.5: Add an arc to the CPW line.

We can continue to add more lines and arcs to make a serpentine shape CPW line step by step:

```
cpw1.add_line(-100,0) # go back.
cpw1.add_arc((0,15),-180) # turn around.
cpw1.add_line(100,0) # go ahead.
cpw1.add_arc((0,15),180) # turn around.
# repeat the above.
cpw1.add_line(-100,0)
cpw1.add_arc((0,15),-180)
cpw1.add_line(100,0)
cpw1.add_arc((0,15),180)
```



Figure B.6: Serpentine shape CPW line creation.

Sometimes we need to connect two CPW lines with different dimensions. The `CPW` class provides a function `adapt2()` to adapt the current CPW line to a different dimension CPW line, see the example below:

```
cpw1 = CPW((0,0),W=8,S=4)
cpw1.add_line(30,0)
cpw1.adapt2(W=4,S=2,gap=10) # adapt to a W=4,S=2 line.
cpw1.add_line(30,0)
```

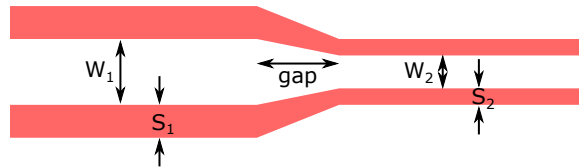


Figure B.7: Adapt a CPW line to another CPW line with different size.

By default the CPW line is shorted to ground at each end. We can make each end open by calling the `add_end()` function:

```
cpw1.add_end() # add an open to the end point.
```

```
cpw1.switch_end() # switch the first point and last point.  
cpw1.add_end() # add an open to the start point.
```

We can also create a CPW line with crossovers evenly distributed along the line, which may be important in some applications, see the example in Fig. B.8. Creating such a circuit pattern is challenging without scripting. This function is not supported in the built-in CPW class as it is more complicated and specific.

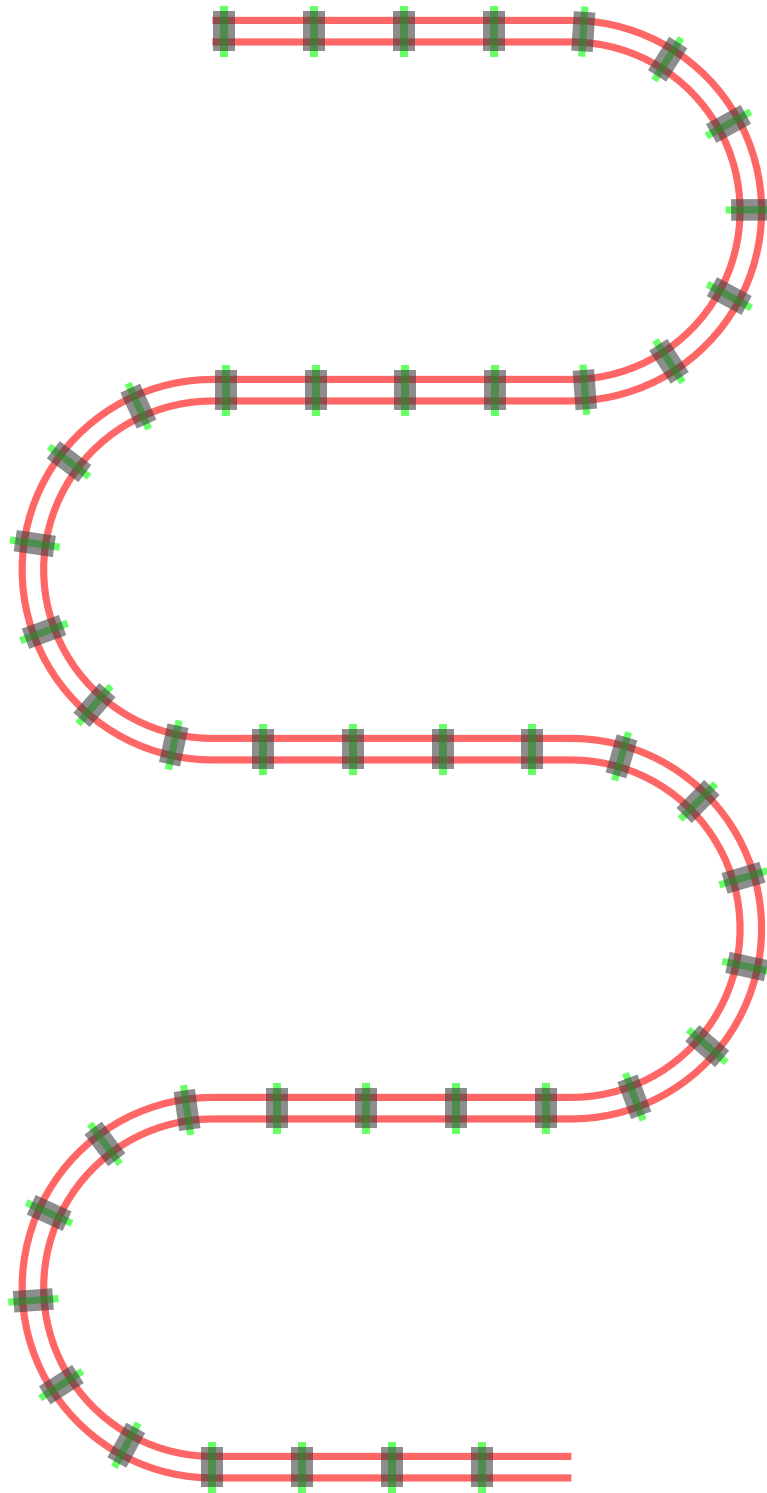


Figure B.8: Serpentine CPW line with evenly distributed crossovers. This kind of pattern is preferable to create using scripting.

APPENDIX C

ABCD MATRIX

The $ABCD$ matrix is a 2×2 matrix describing the transmission of a two-port network. This matrix is defined in such a way that the $ABCD$ matrix of the cascade connection of two or more two-port networks is simply the multiplication of the $ABCD$ matrices of each component [29].

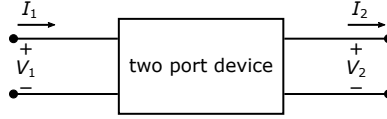


Figure C.1: Schematic of a two-port device.

For a two-port device shown in Fig. C.1, the $ABCD$ matrix is defined in terms of the voltages and currents in both ports:

$$\begin{bmatrix} V_1 \\ I_1 \end{bmatrix} = \begin{bmatrix} A & B \\ C & D \end{bmatrix} \begin{bmatrix} V_2 \\ I_2 \end{bmatrix} \quad (\text{C.1})$$

When two two-port networks are cascaded, as shown in Fig. C.2, we have

$$\begin{bmatrix} V_1 \\ I_1 \end{bmatrix} = \begin{bmatrix} A_1 & B_1 \\ C_1 & D_1 \end{bmatrix} \begin{bmatrix} V_2 \\ I_2 \end{bmatrix}, \quad \begin{bmatrix} V_2 \\ I_2 \end{bmatrix} = \begin{bmatrix} A_2 & B_2 \\ C_2 & D_2 \end{bmatrix} \begin{bmatrix} V_3 \\ I_3 \end{bmatrix}. \quad (\text{C.2})$$

Combining these two equations together we have

$$\begin{bmatrix} V_1 \\ I_1 \end{bmatrix} = \begin{bmatrix} A_1 & B_1 \\ C_1 & D_1 \end{bmatrix} \begin{bmatrix} A_2 & B_2 \\ C_2 & D_2 \end{bmatrix} \begin{bmatrix} V_3 \\ I_3 \end{bmatrix}. \quad (\text{C.3})$$

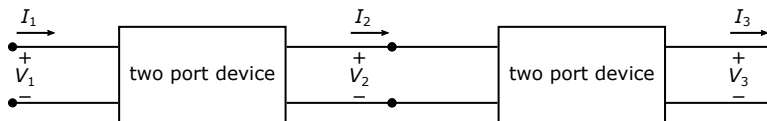


Figure C.2: A cascade connection of two-port devices.

This property makes $ABCD$ matrix suitable for analyzing cascaded network systems.

The conversion from $ABCD$ matrix to scattering matrix is [29]:

$$S_{11} = \frac{A + B/Z_0 - CZ_0 - D}{A + B/Z_0 + CZ_0 + D}, \quad (\text{C.4})$$

$$S_{12} = \frac{2(AD - BC)}{A + B/Z_0 + CZ_0 + D}, \quad (\text{C.5})$$

$$S_{21} = \frac{2}{A + B/Z_0 + CZ_0 + D}, \quad (\text{C.6})$$

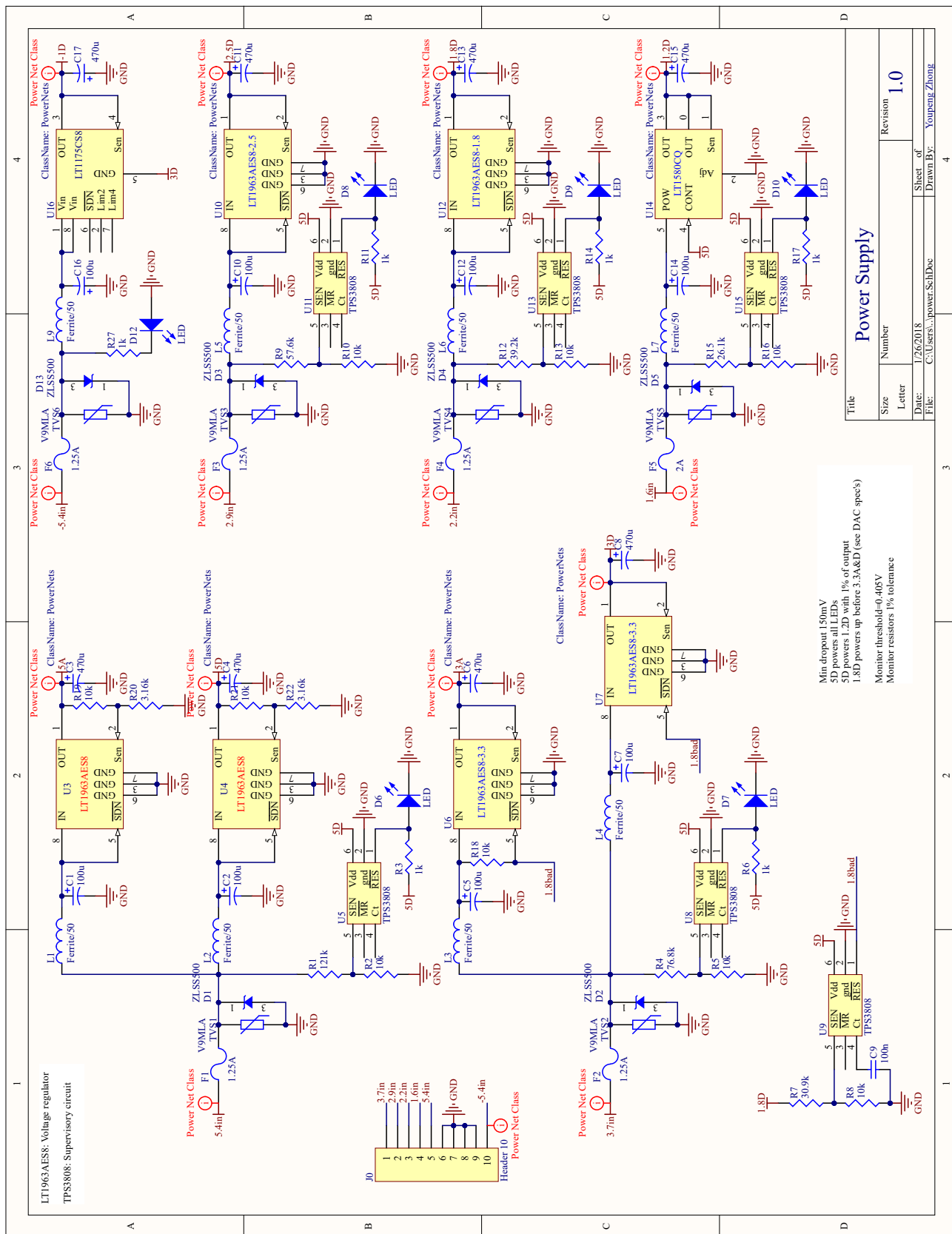
$$S_{22} = \frac{-A + B/Z_0 - CZ_0 + D}{A + B/Z_0 + CZ_0 + D}. \quad (\text{C.7})$$

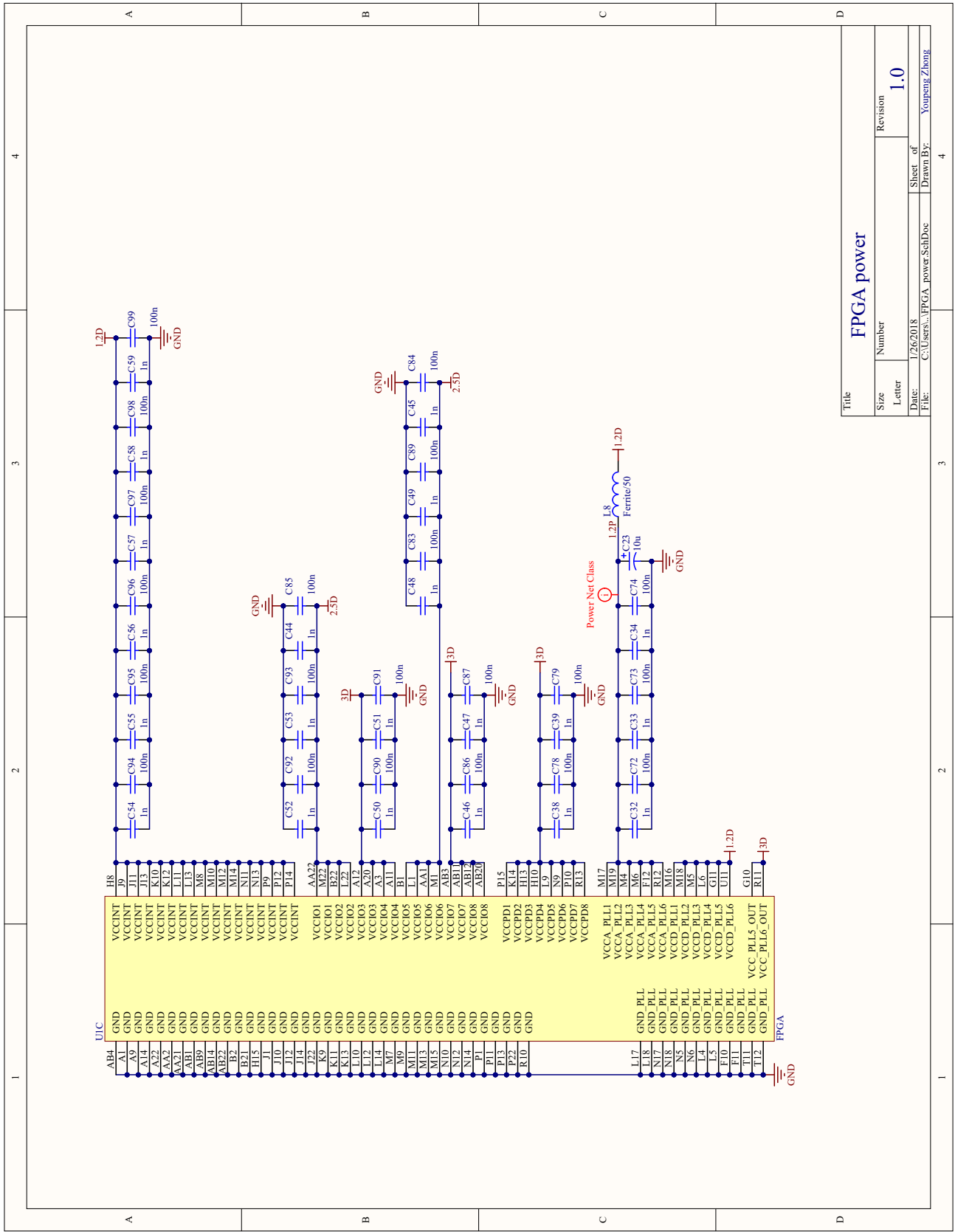
APPENDIX D

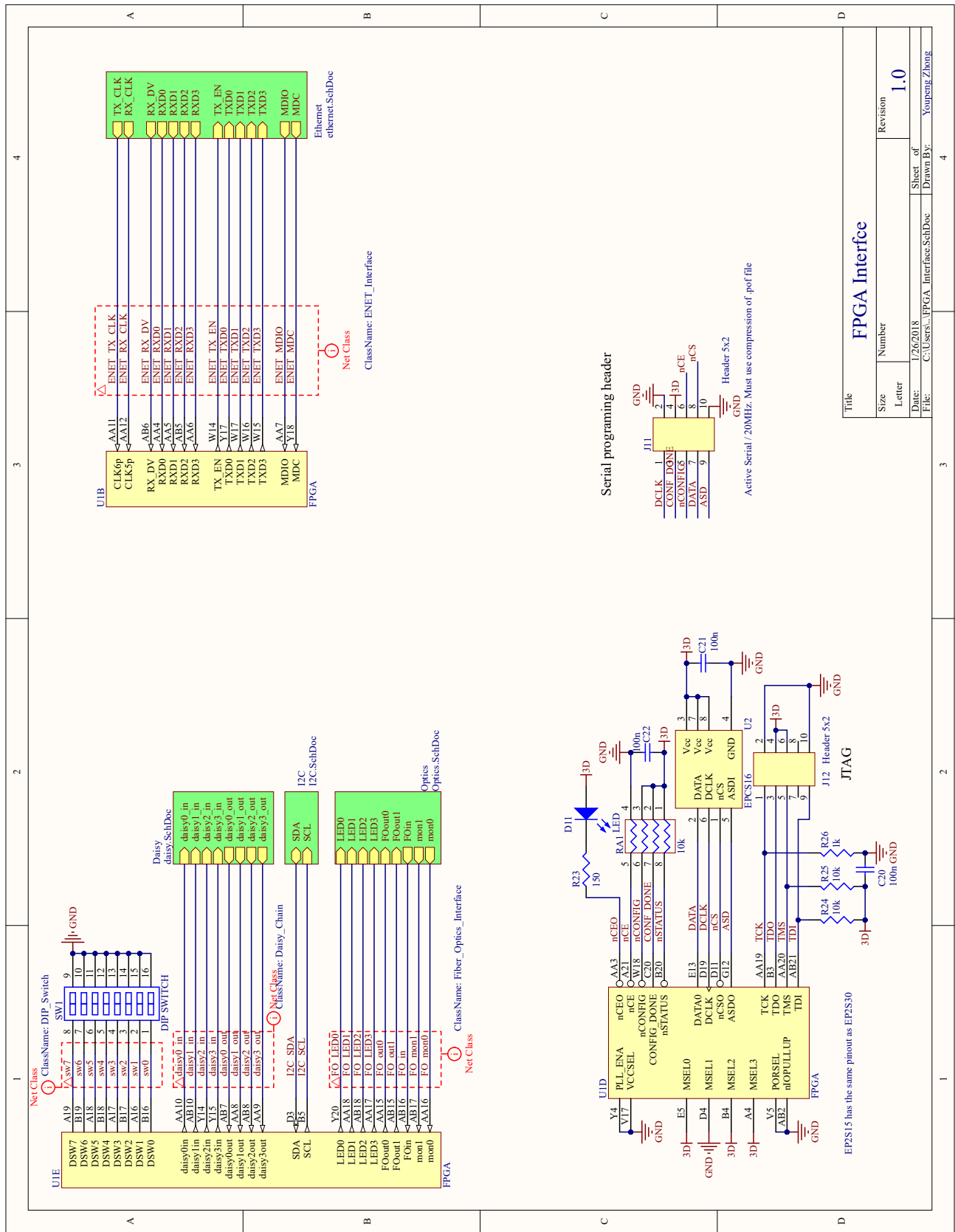
ELECTRONICS DOCUMENTS

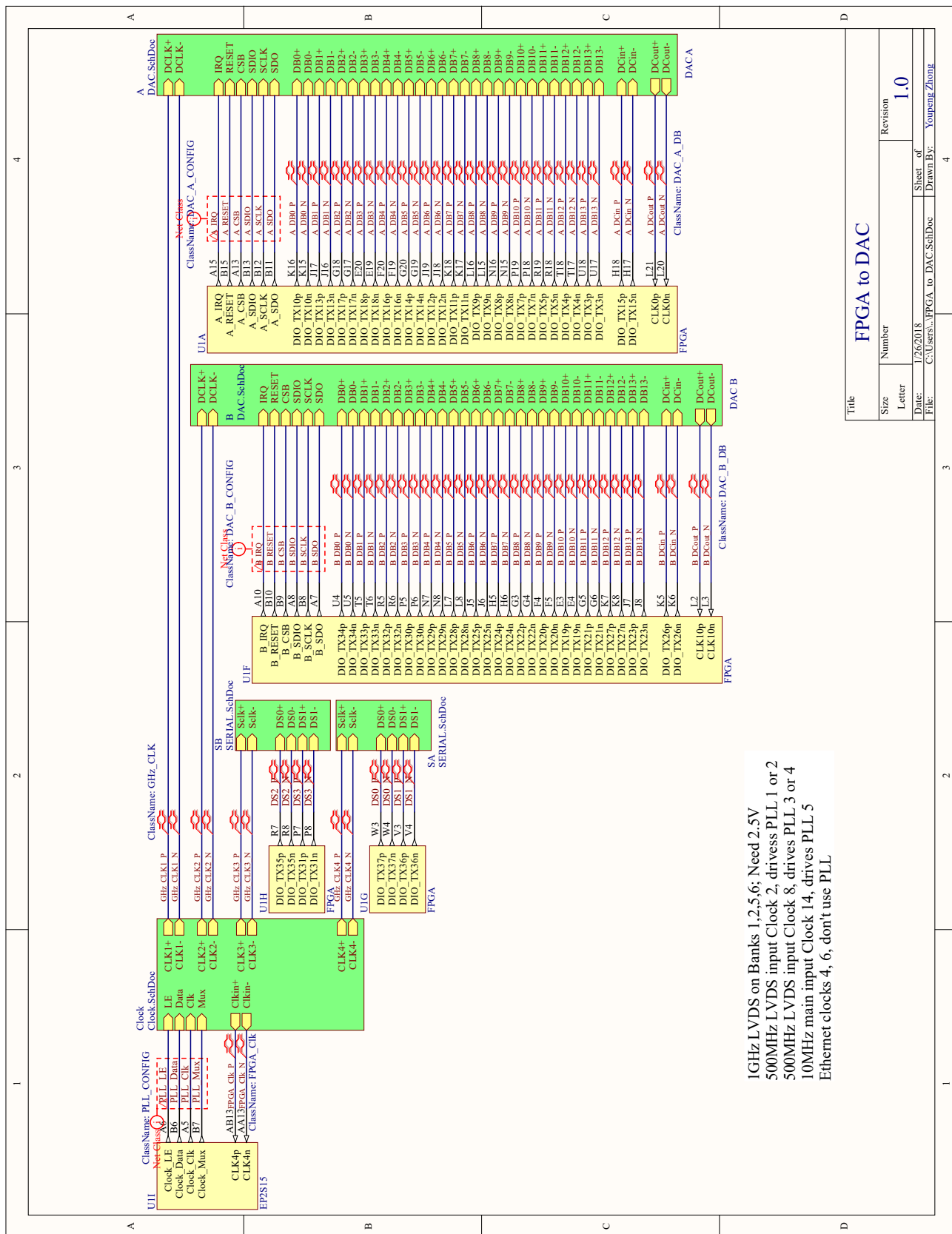
D.1 GHz DAC board

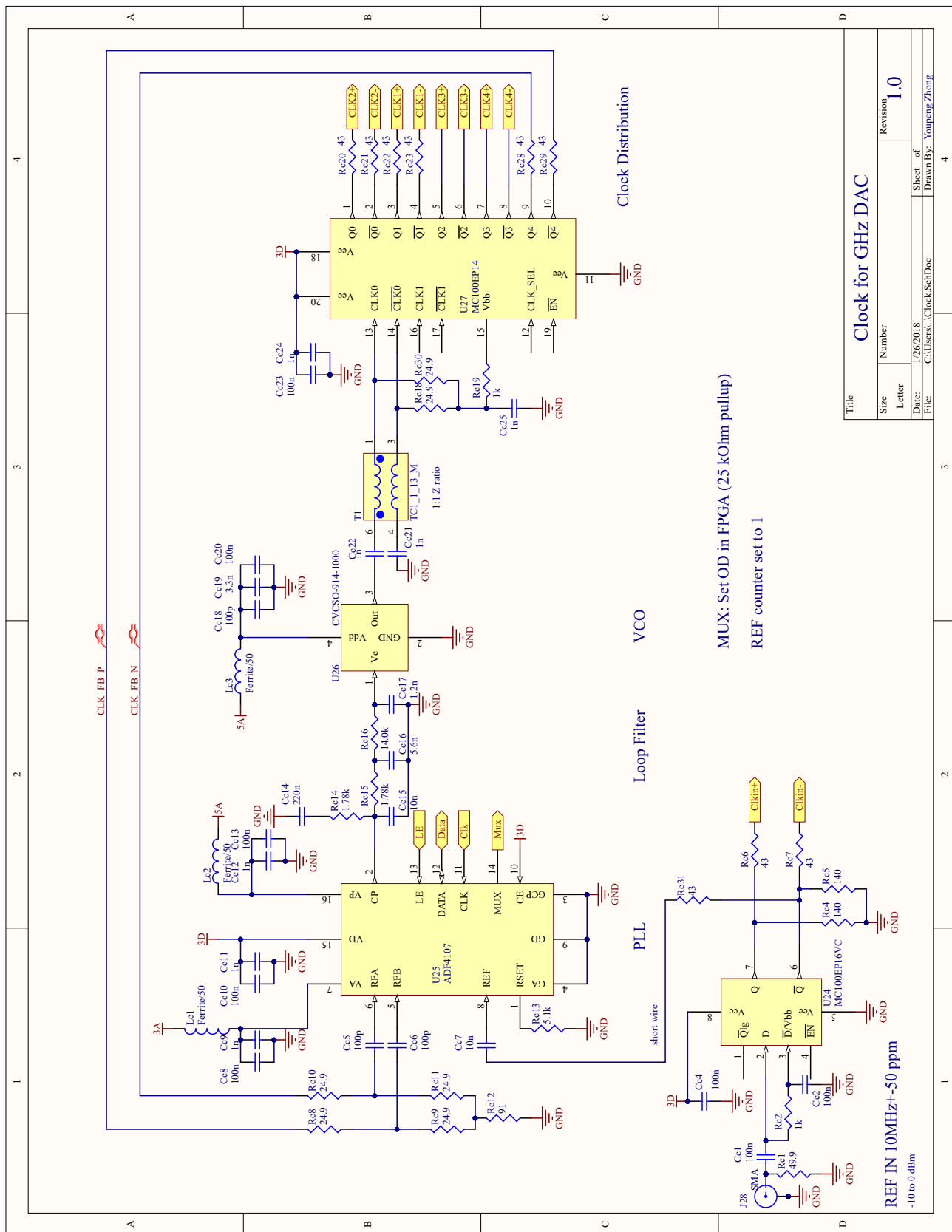
Here is the GHz DAC V1.1 schematic, adopted from John Martinis's design.

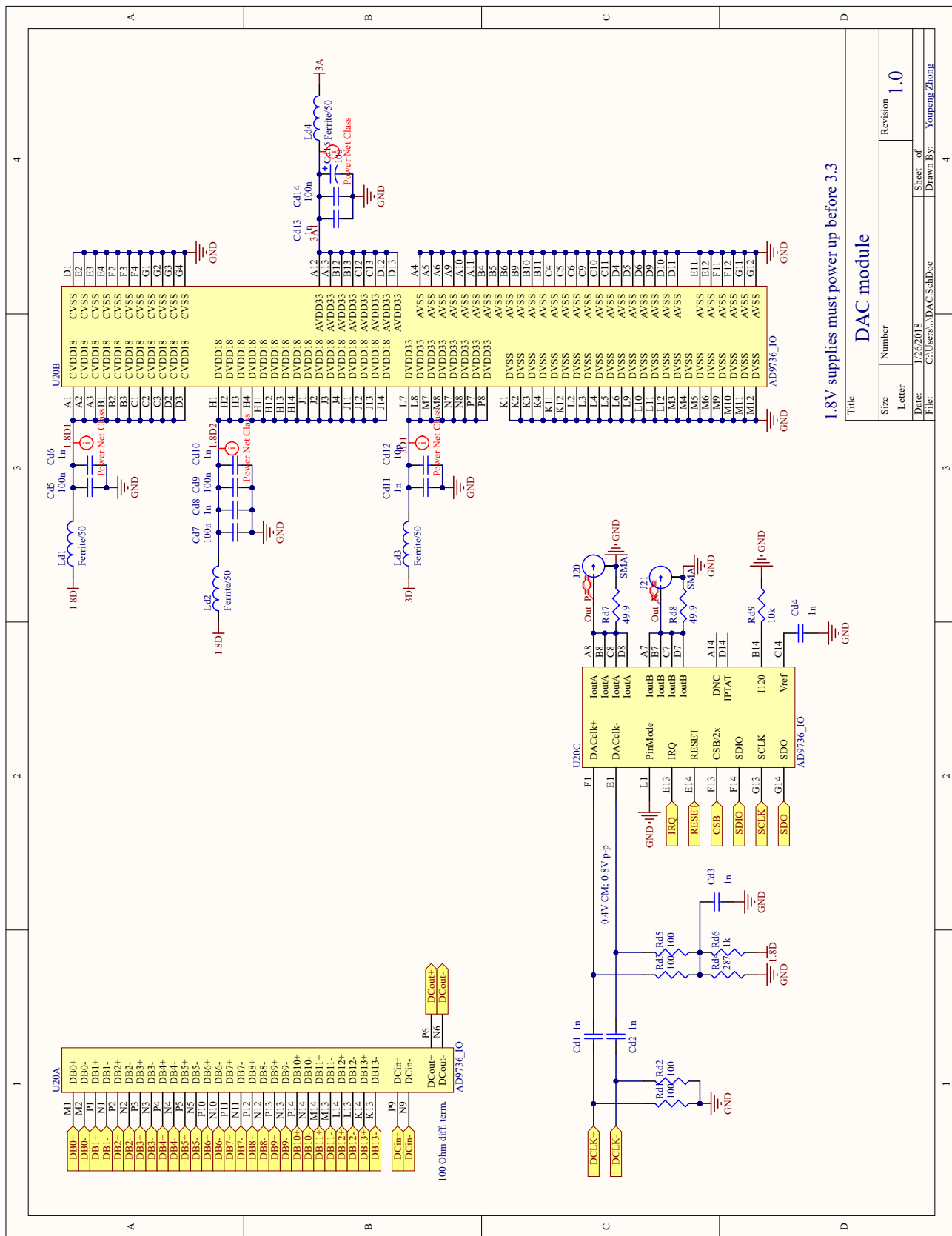


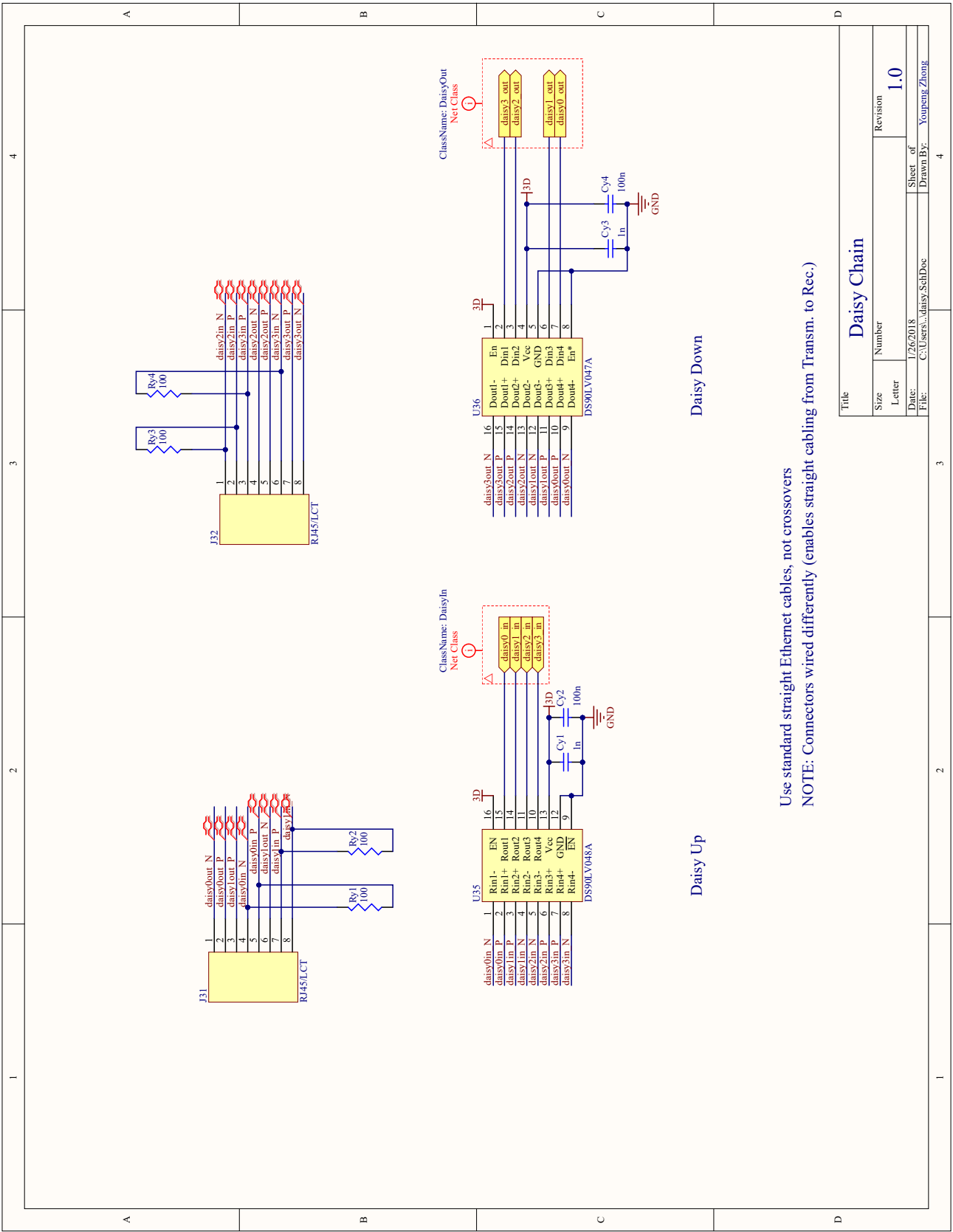






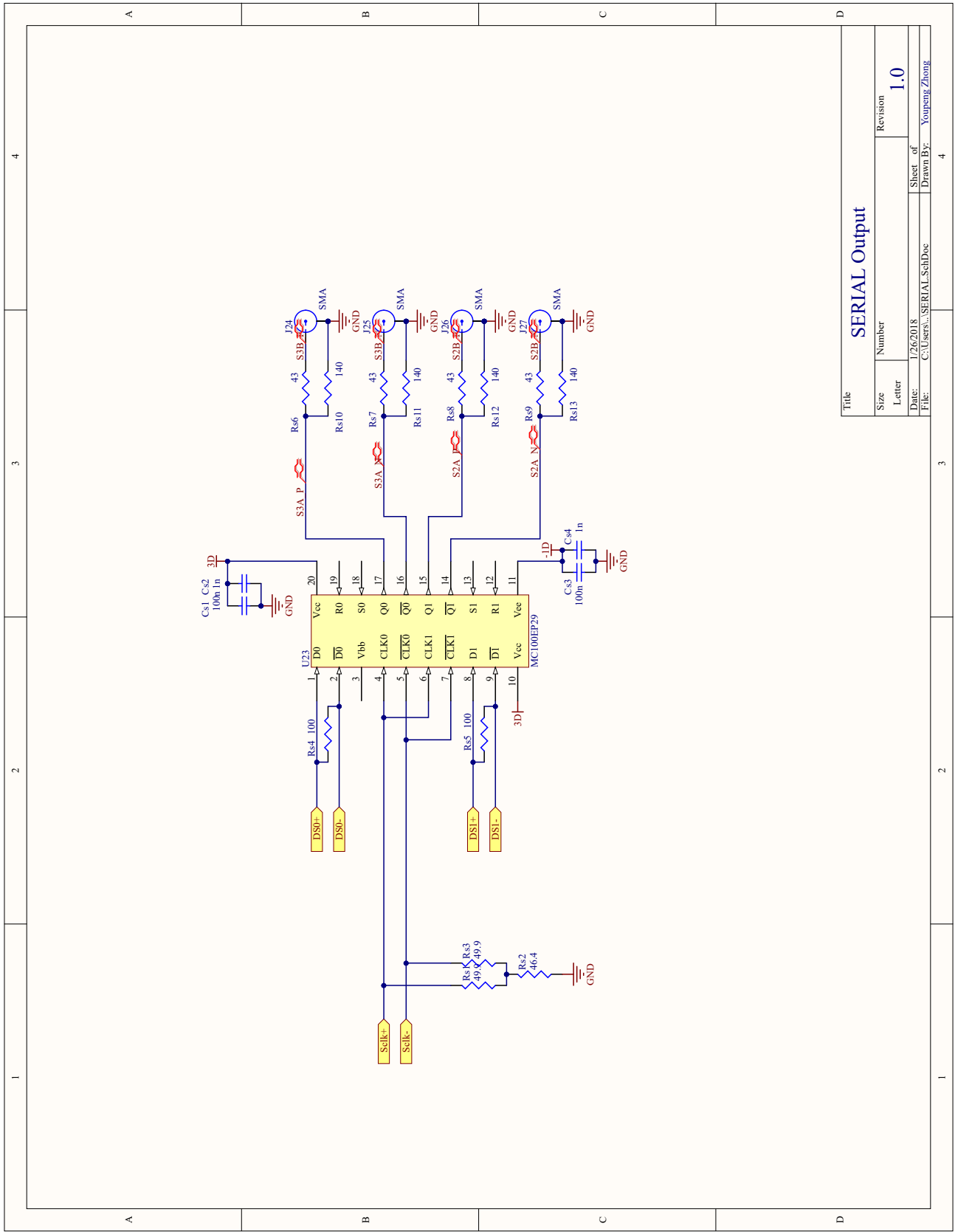






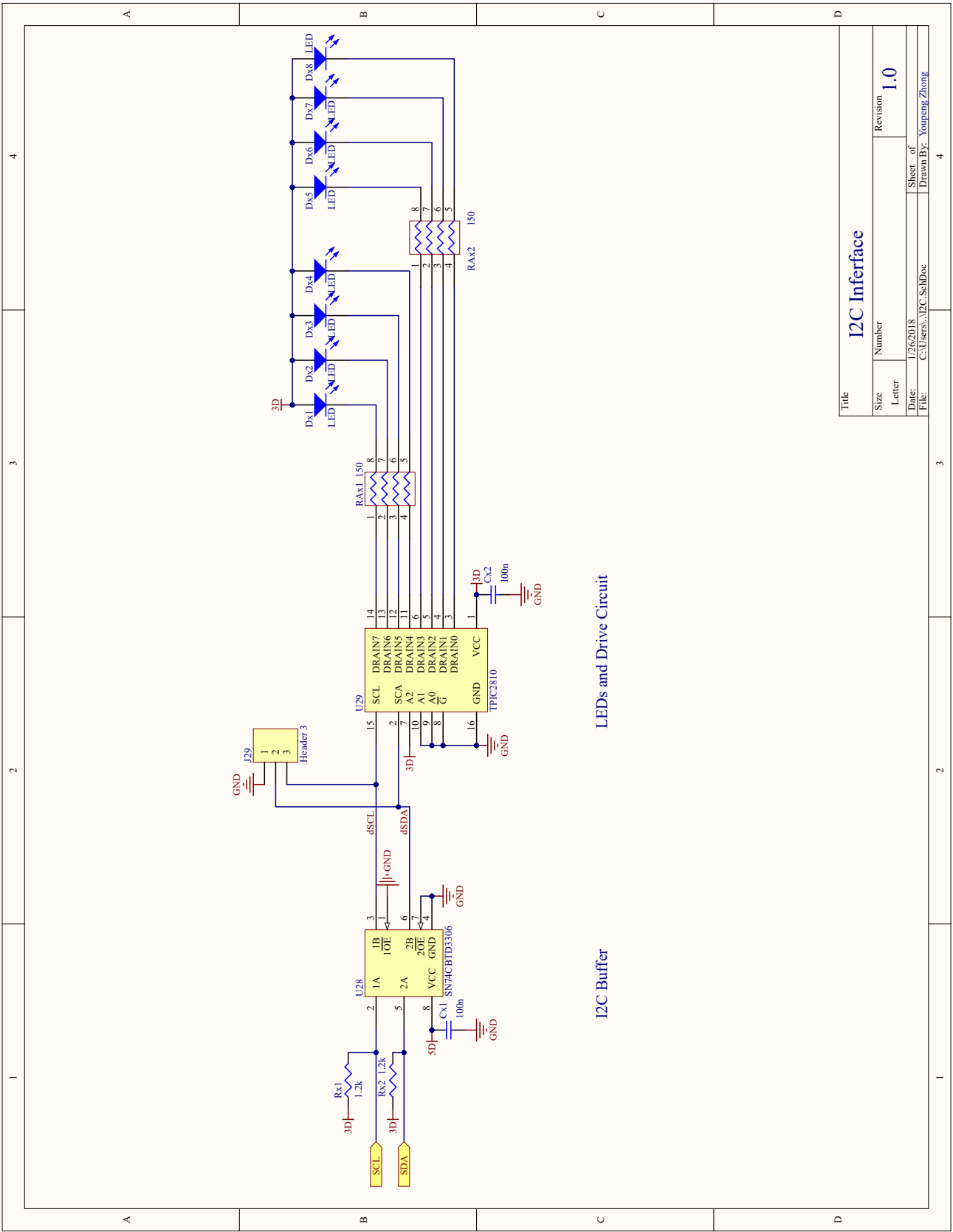
Use standard straight Ethernet cables, not crossovers
NOTE: Connectors wired differently (enables straight cabling from Transm. to Rec.)

Title		Revision	
Size	Number	1.0	
Date	Letter	1/26/2018	
File	Drawn By:	Youpeng Zhong	



SERIAL Output

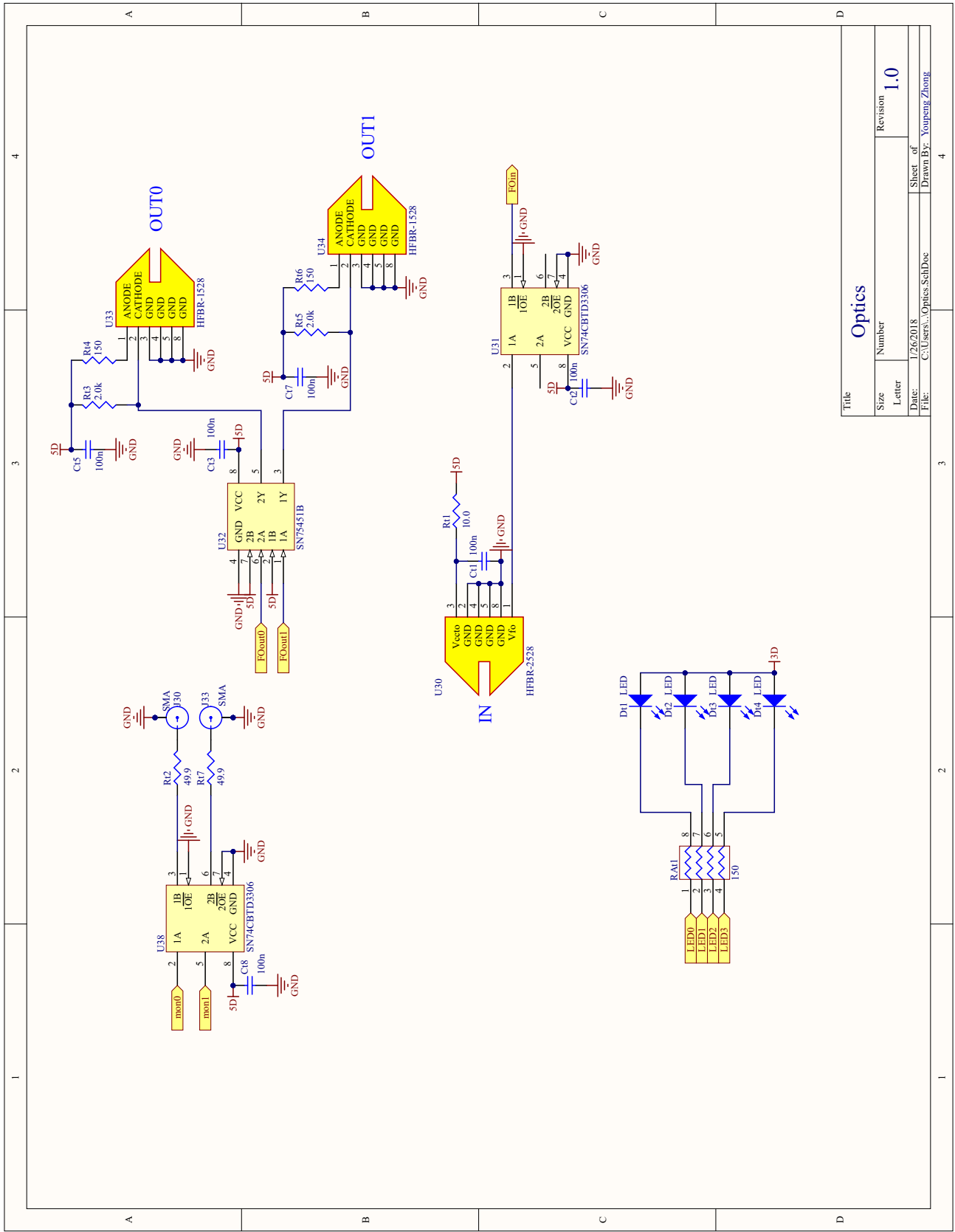
Title	Size	Number	Revision
	Letter		1.0
Date:	1/26/2018	Sheet of	
File:	C:\Users\...SERIAL.SchDoc	Drawn By:	Youpeng Zhong



I2C Buffer

LEDs and Drive Circuit

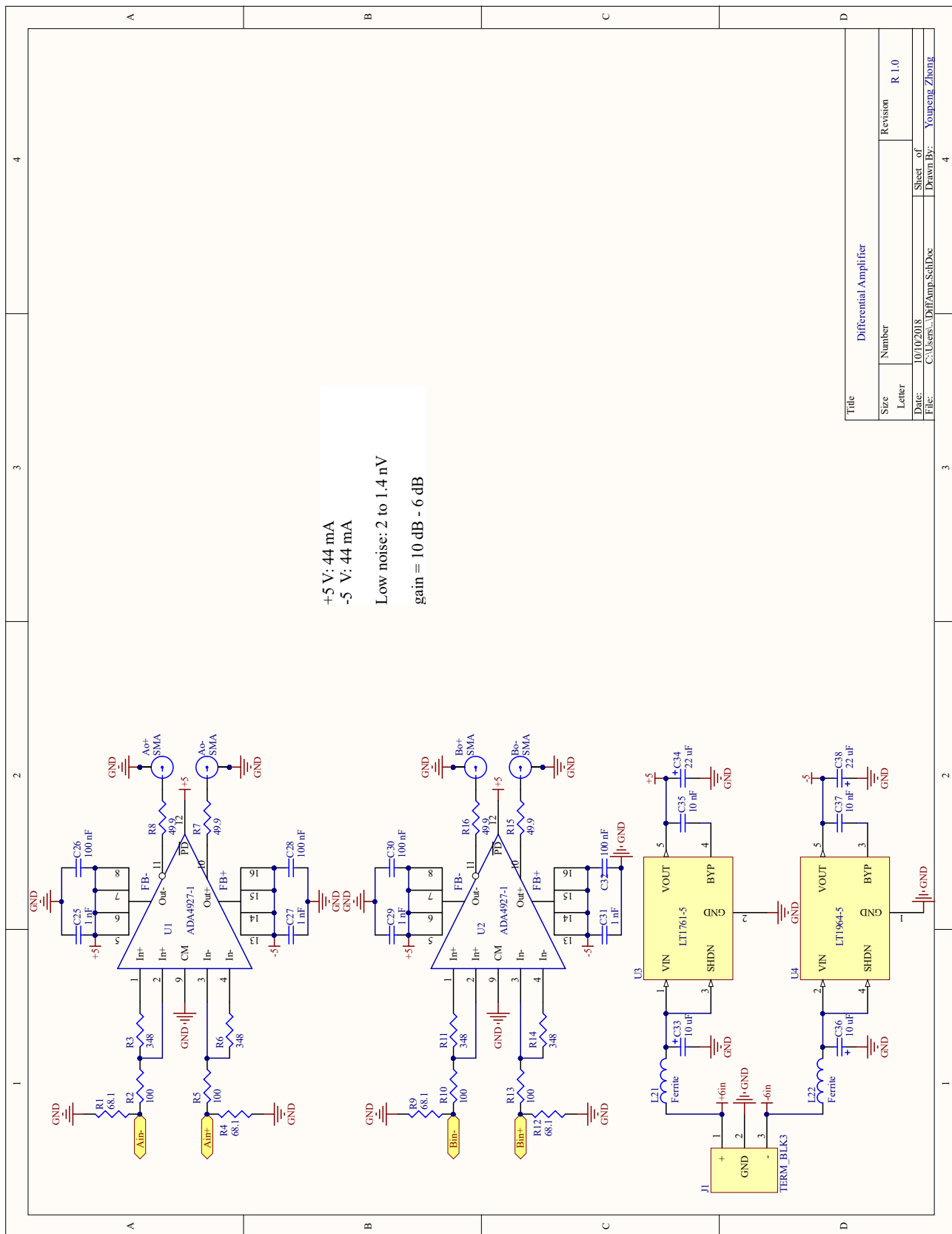
Title			I2C Interface				
Size	Number	Revision					
Letter		1.0					
Date:	1/26/2018	Sheet of					
File:	C:\Users\JLC_SchDoc	Drawn By: Youpeng Zhong					

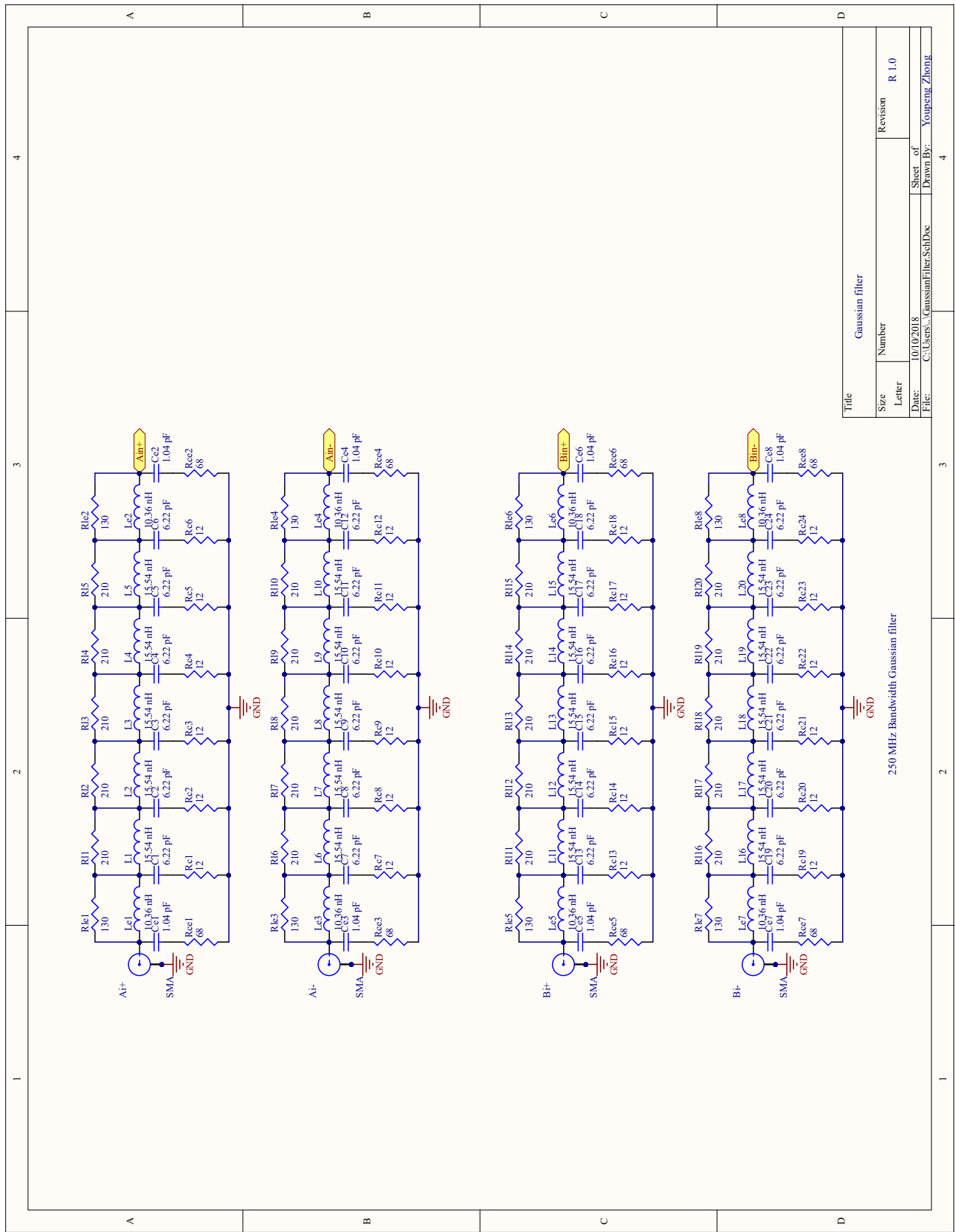


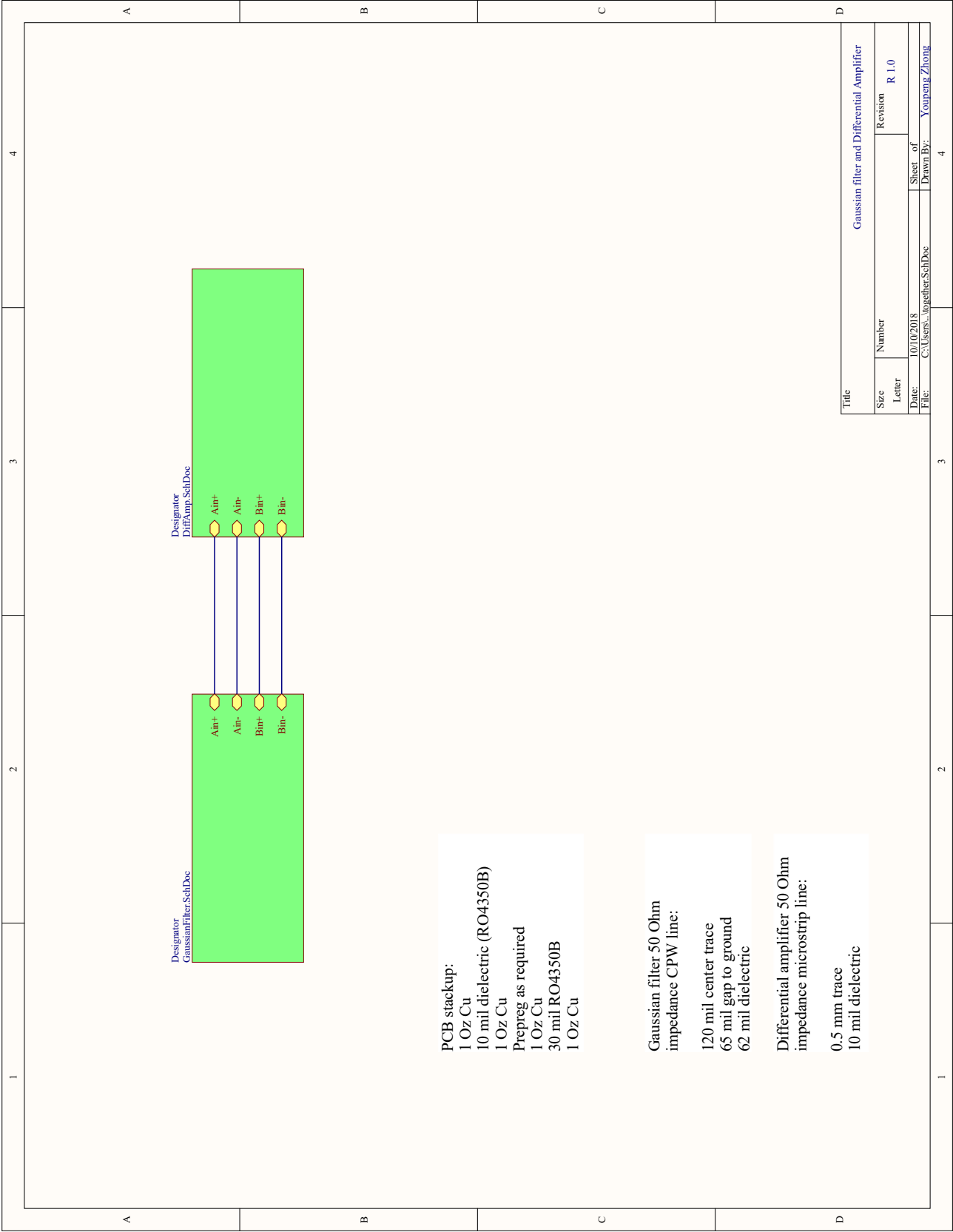
Title		Revision	
Size	Number	1.0	
Letter			
Date:	1/26/2018	Sheet of	
File:	C:\Users\Yongpeng.Zhong	Drawn By: Yongpeng.Zhong	

D.2 Gaussian filter and differential amplifier

Here is the Gaussian filter and differential amplifier schematic, adopted from John Martinis's design.

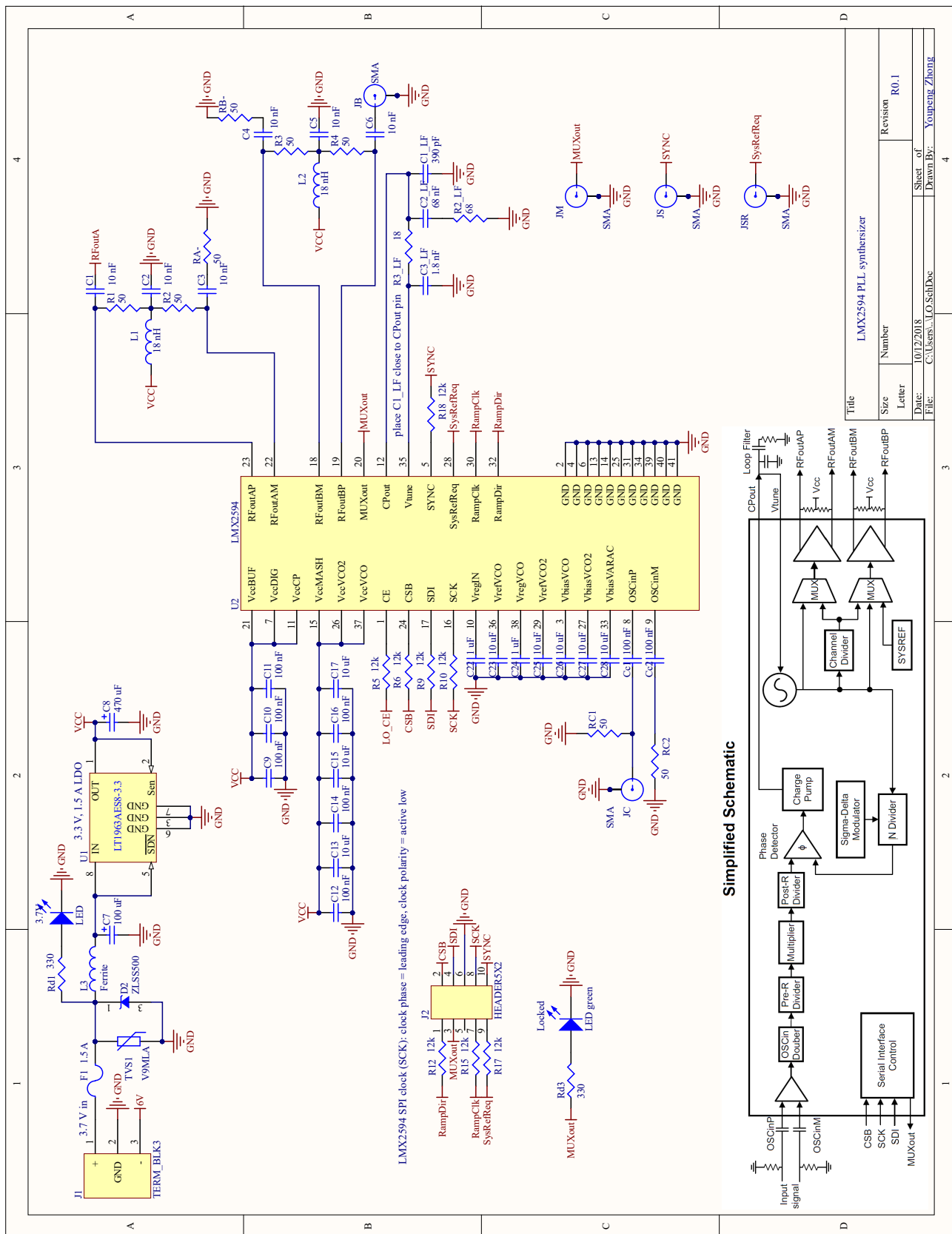


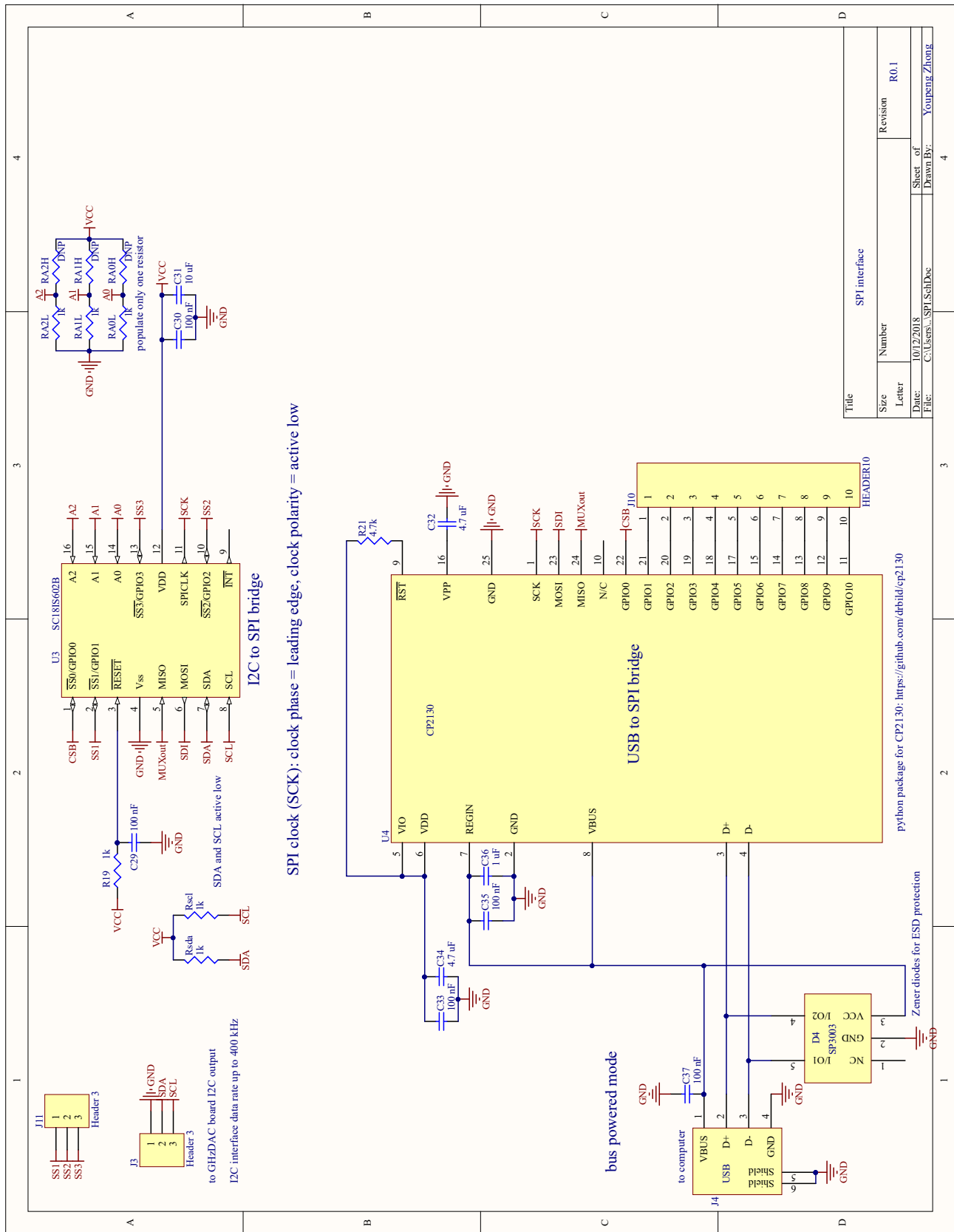


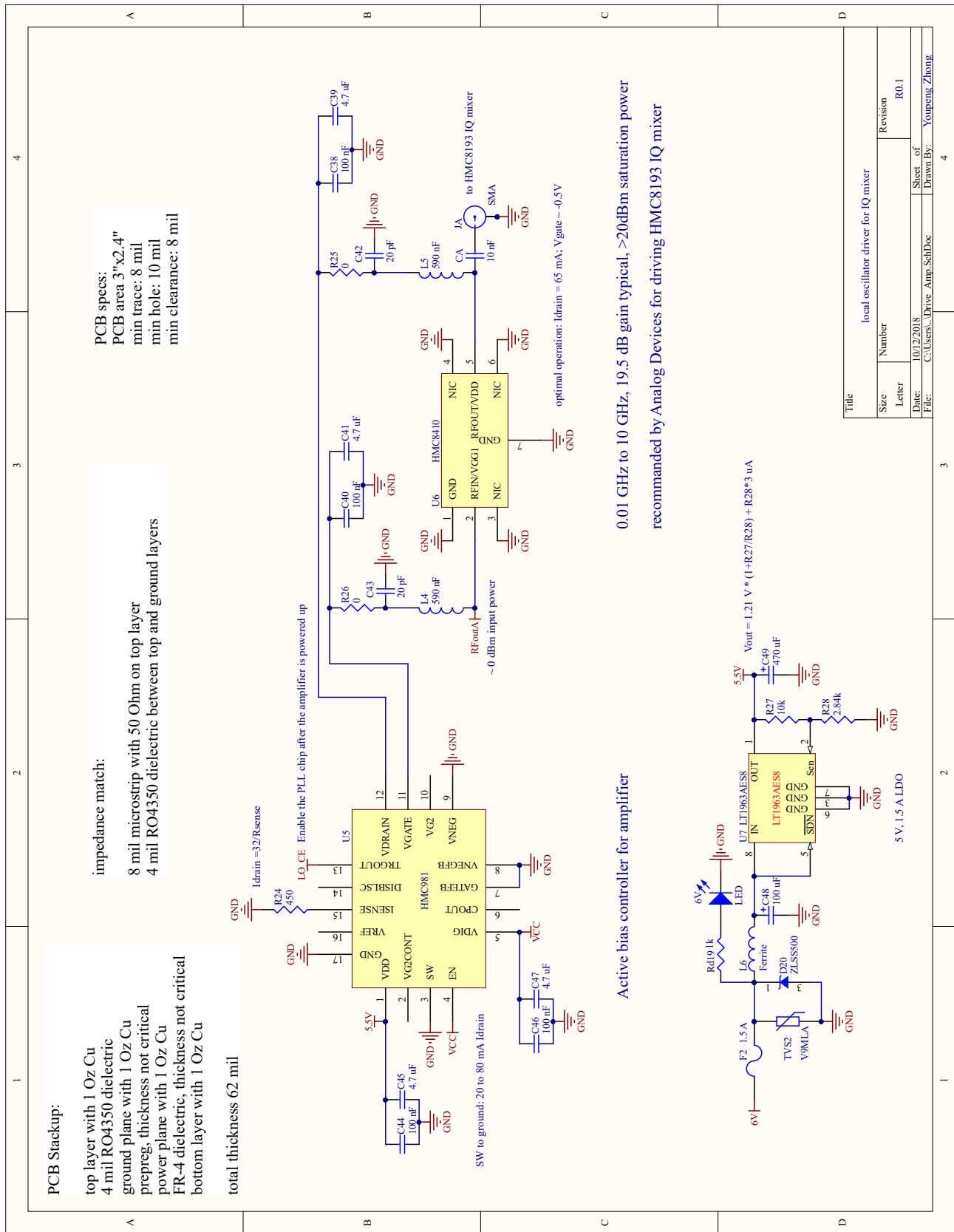


D.3 Signal generator

Here is the schematic for a custom signal generator based on Texas Instruments's LMX2594 PLL synthesizer. The performance needs further investigation.







local oscillator driver for IQ mixer

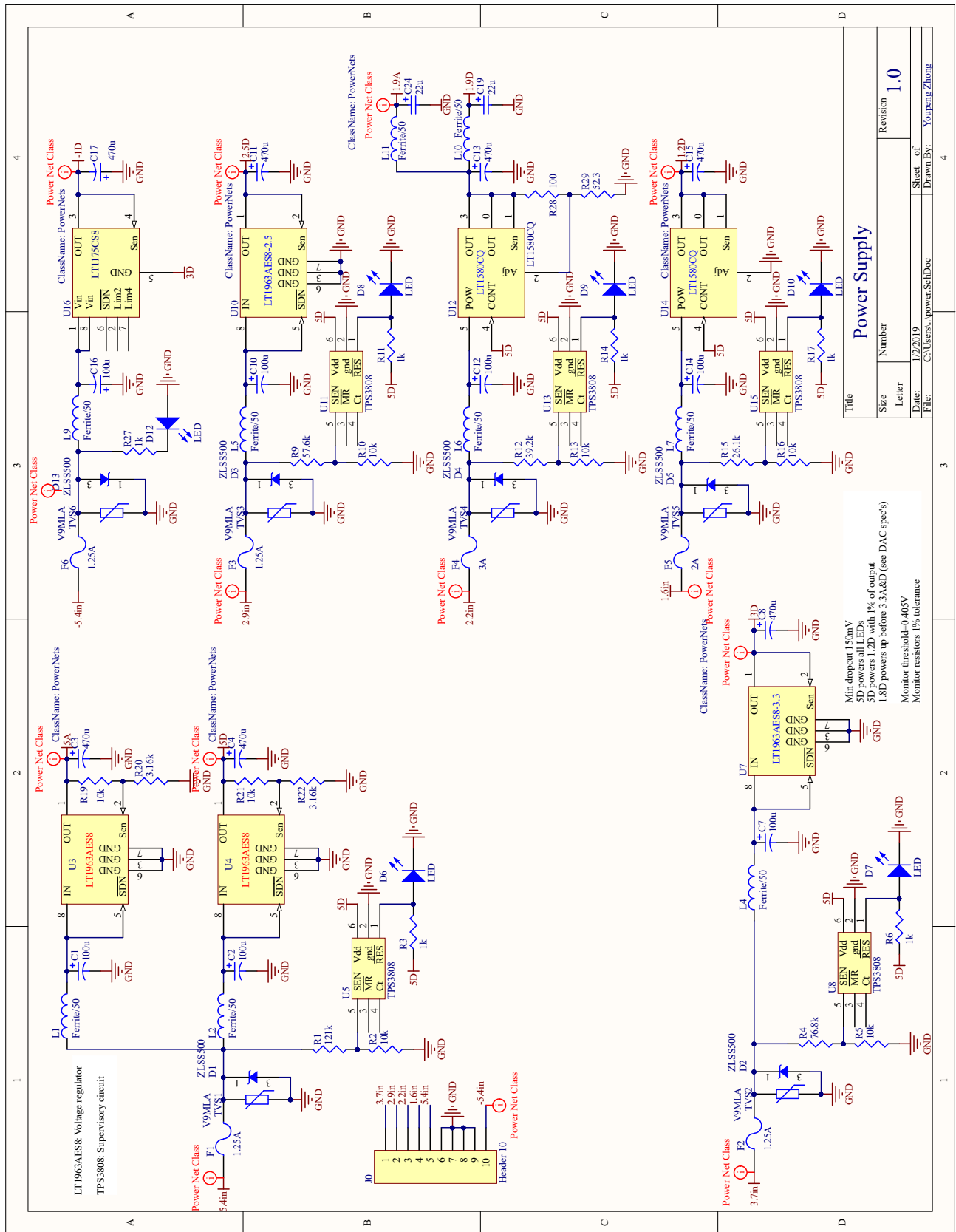
Size Number Revision
 Letter R0.1
 Date: 10/12/2018
 File: C:\Users\A\Drive Amp SchDoc
 Drawn By: Youpeng Zhong

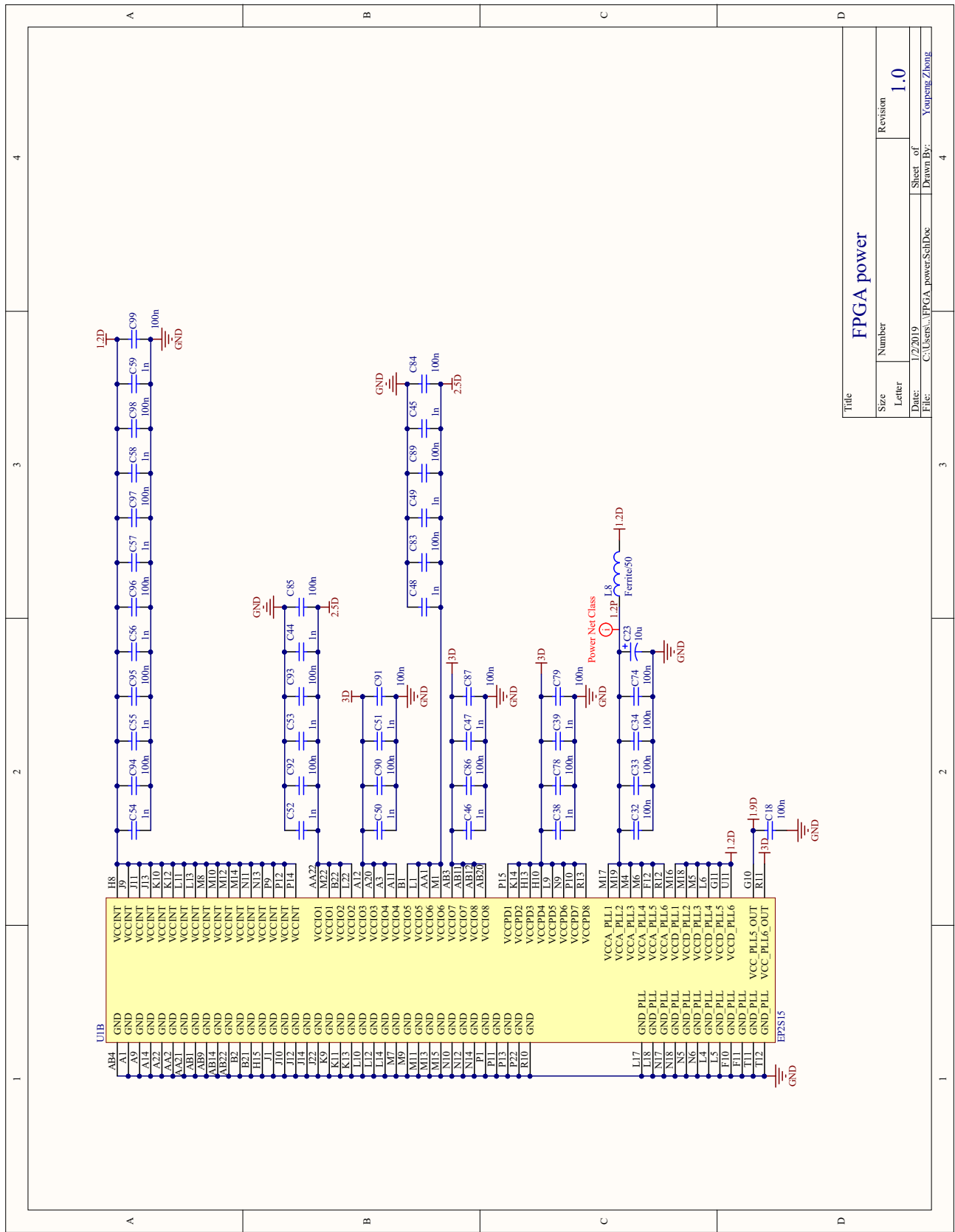
D.4 IQ mixer

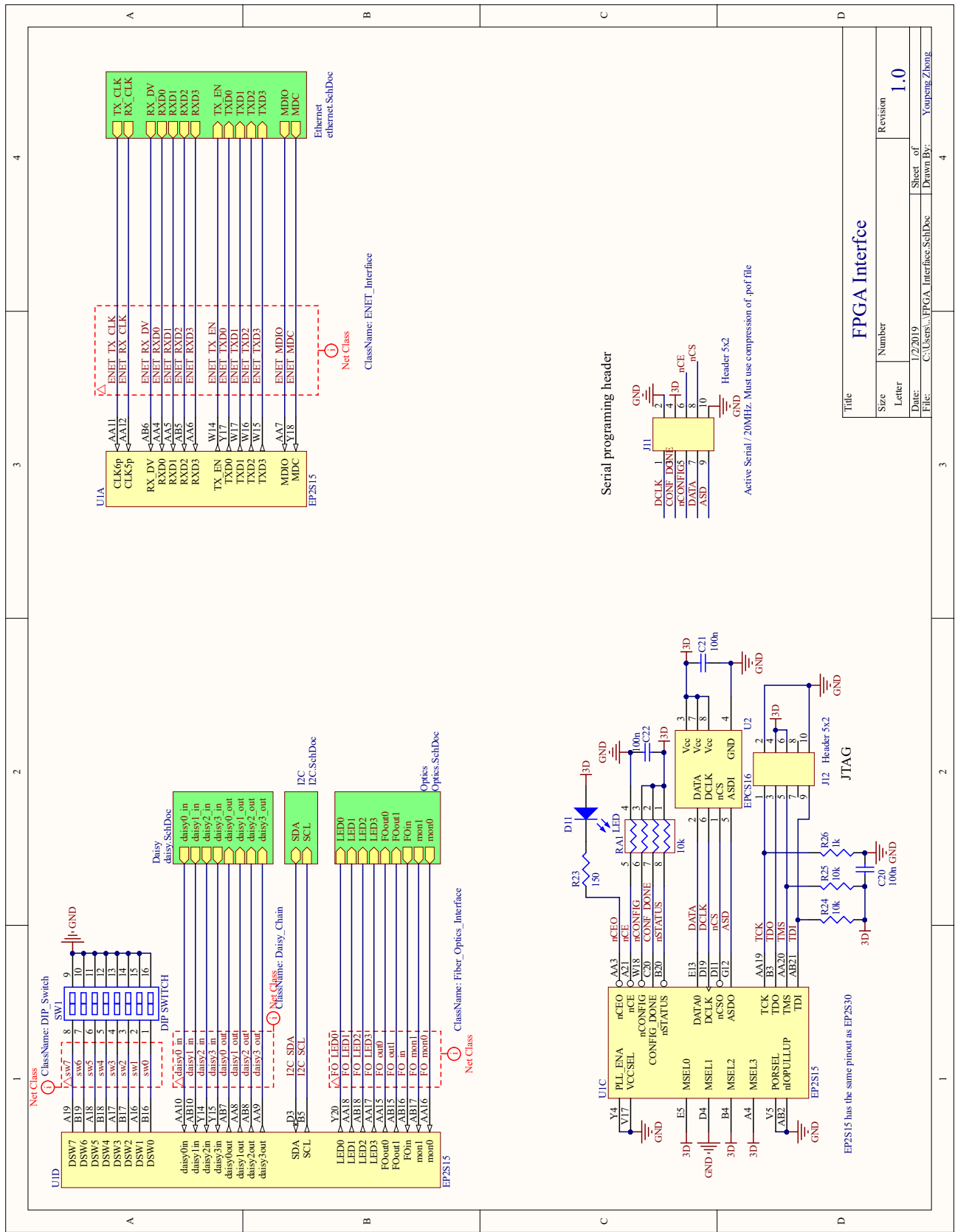
Here is the schematic for a custom IQ mixer based on Analog Devices's HMC8193. This design is also pin-to-pin compatible with HMC525ALC4 and Custom MMIC's CMD252C4 IQ mixer, which might have better conversion gain.

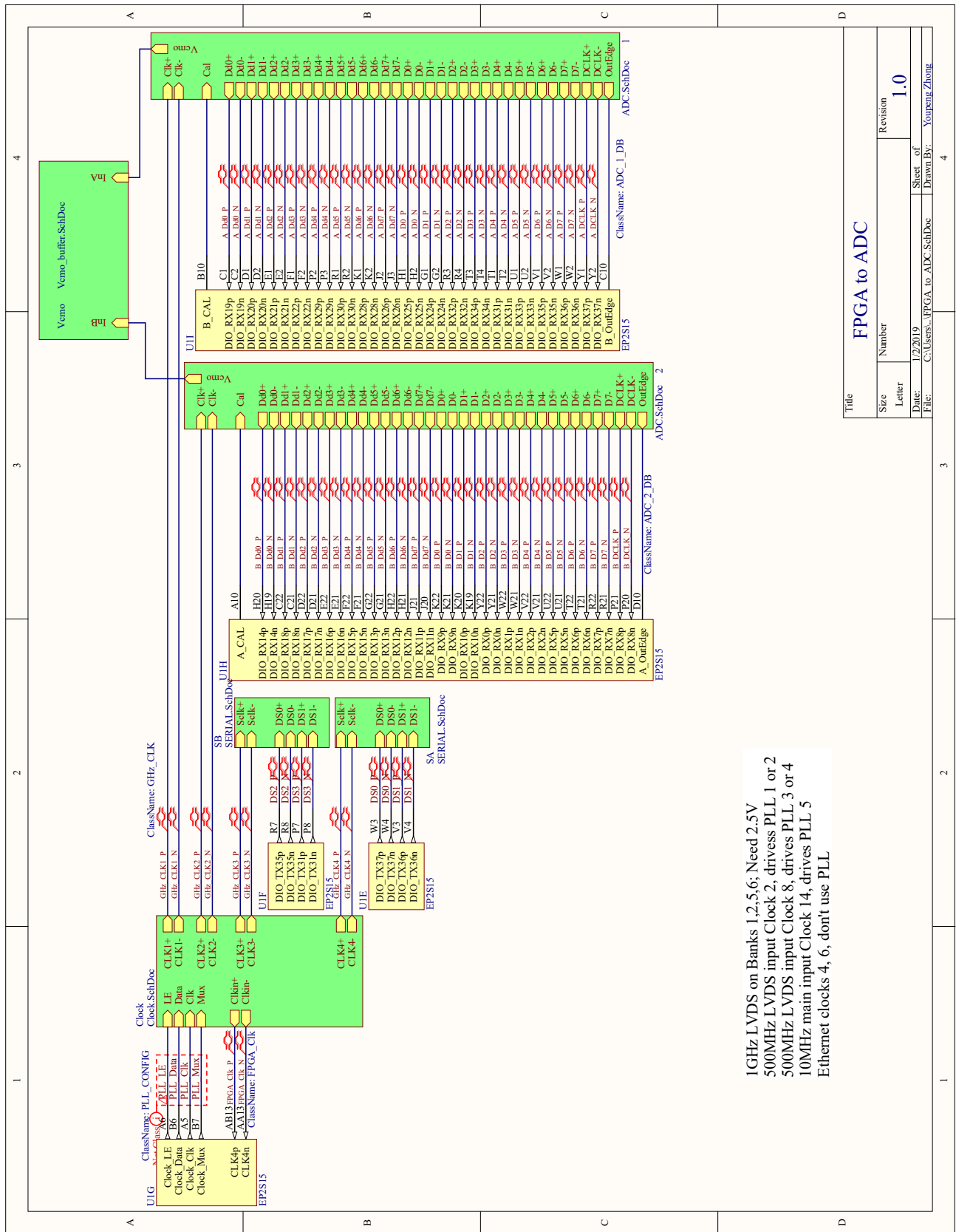
D.5 GHz ADC board

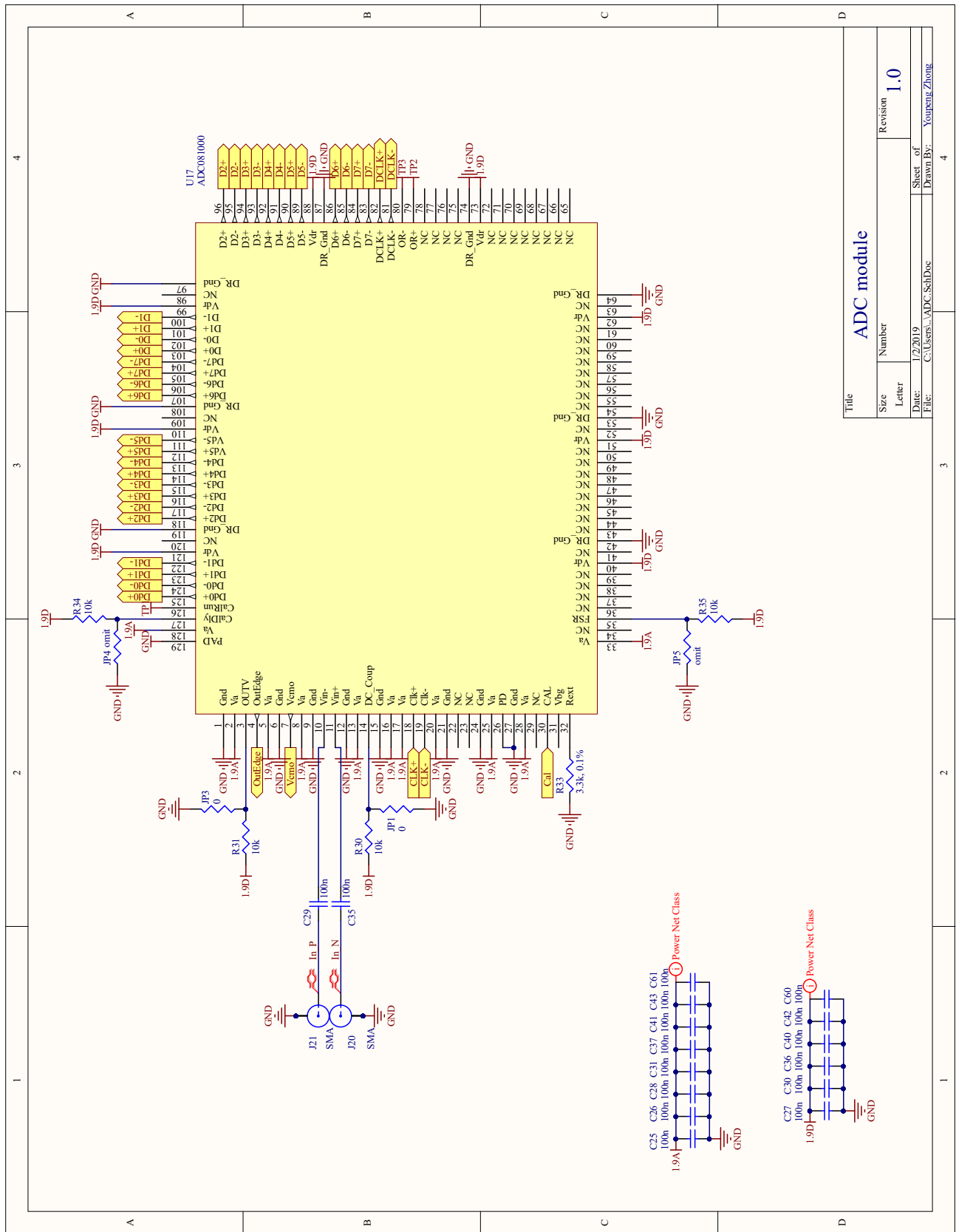
Here is the GHz ADC V1.0 schematic, adopted from John Martinis and Steve Waltman's design.

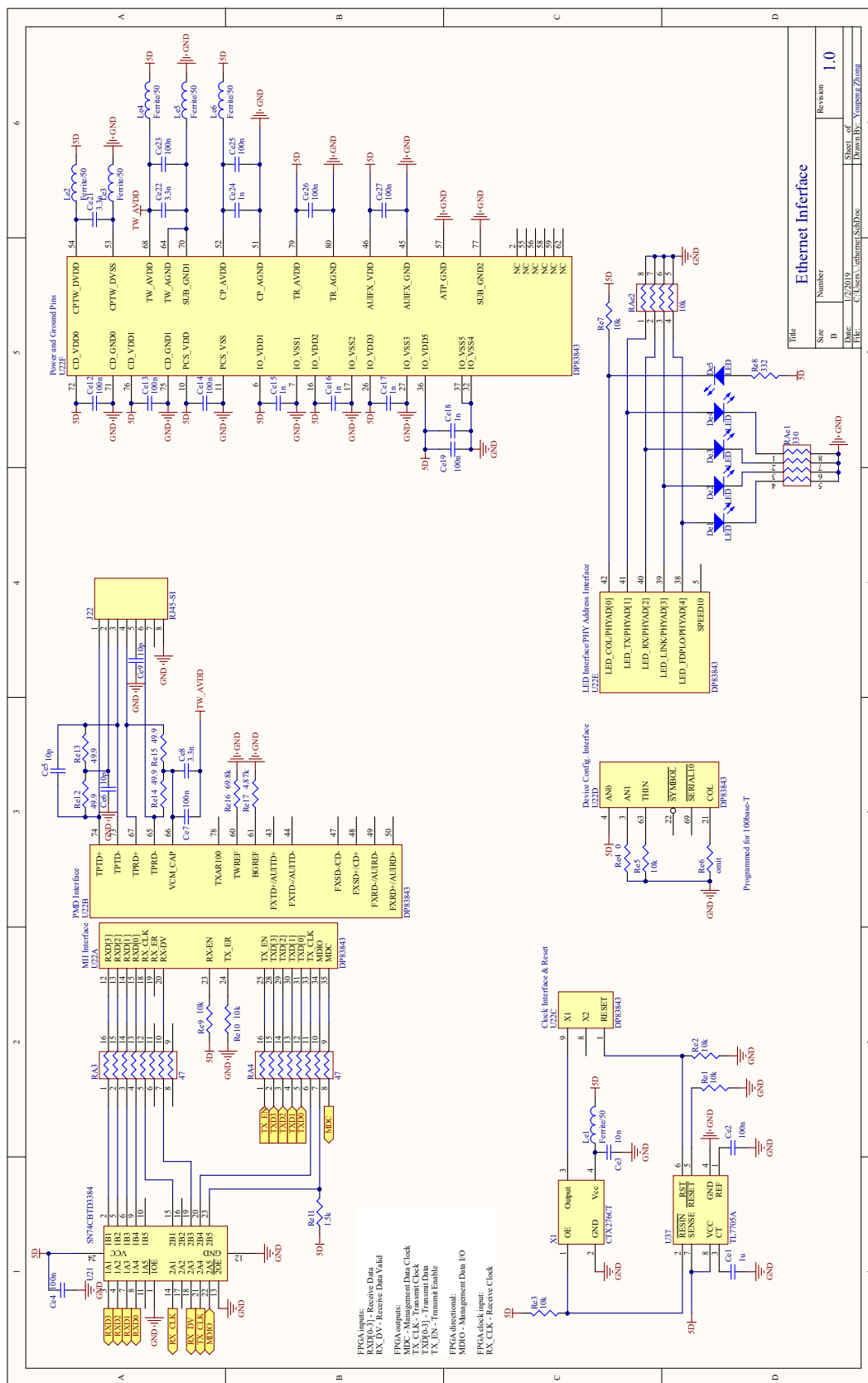


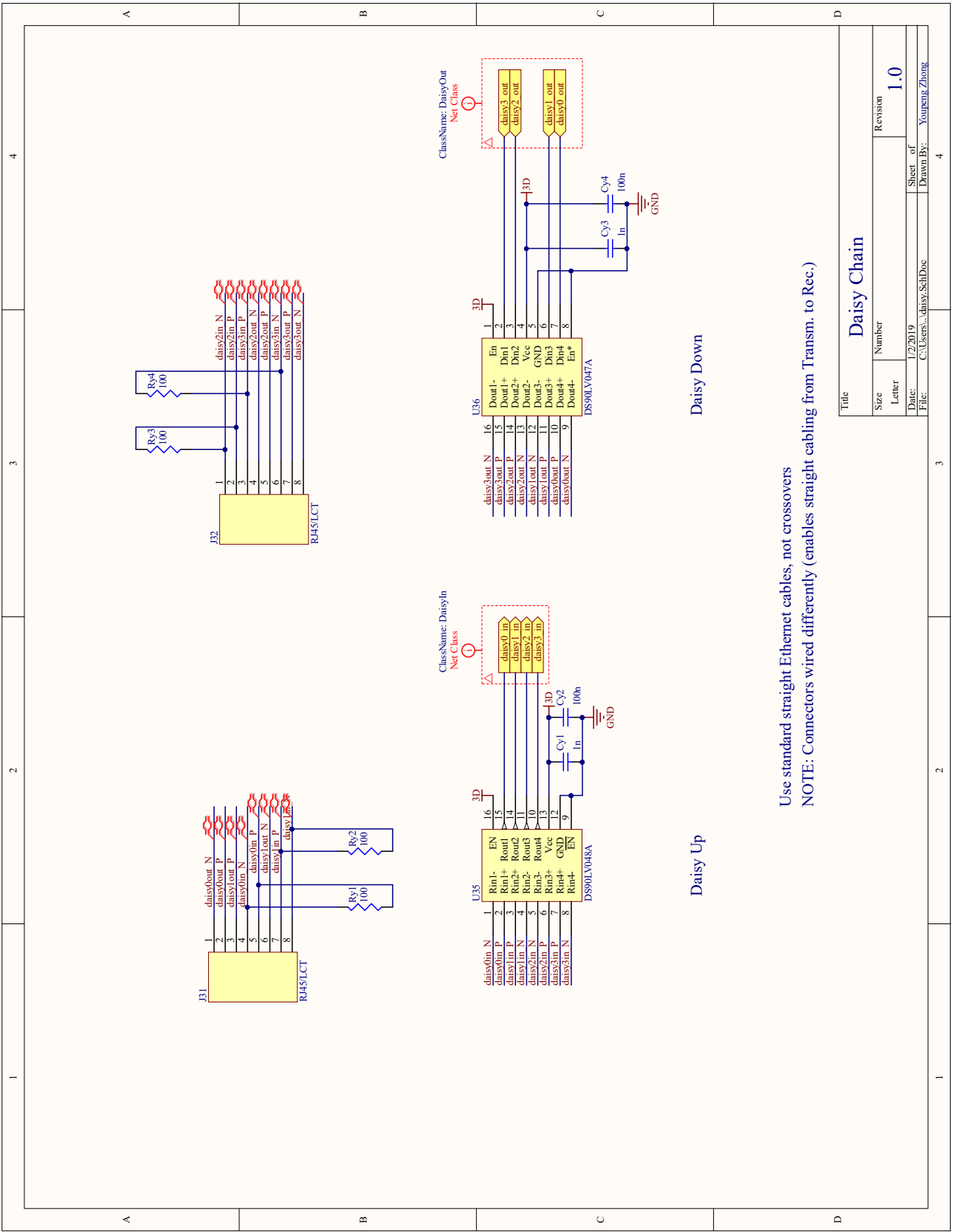






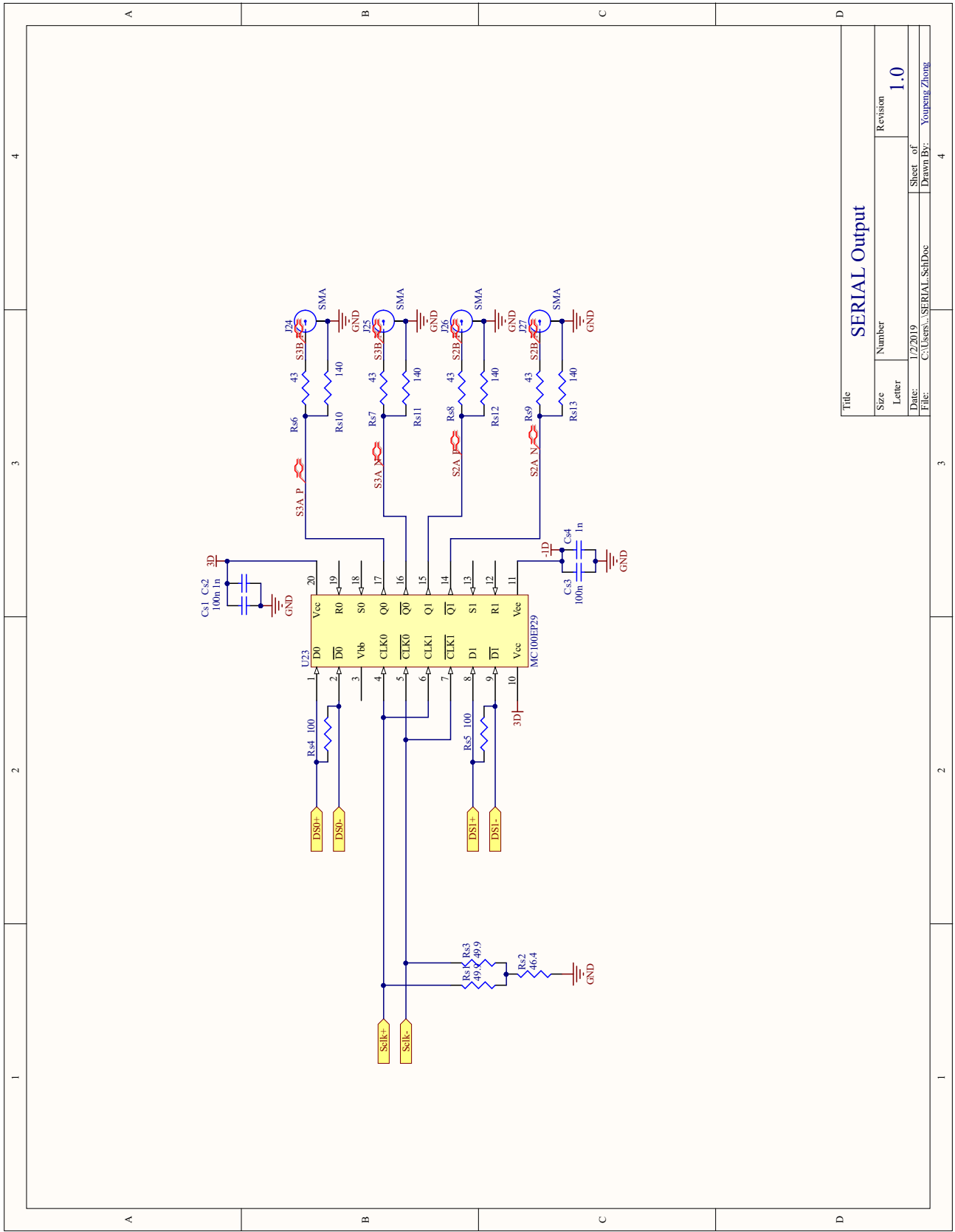


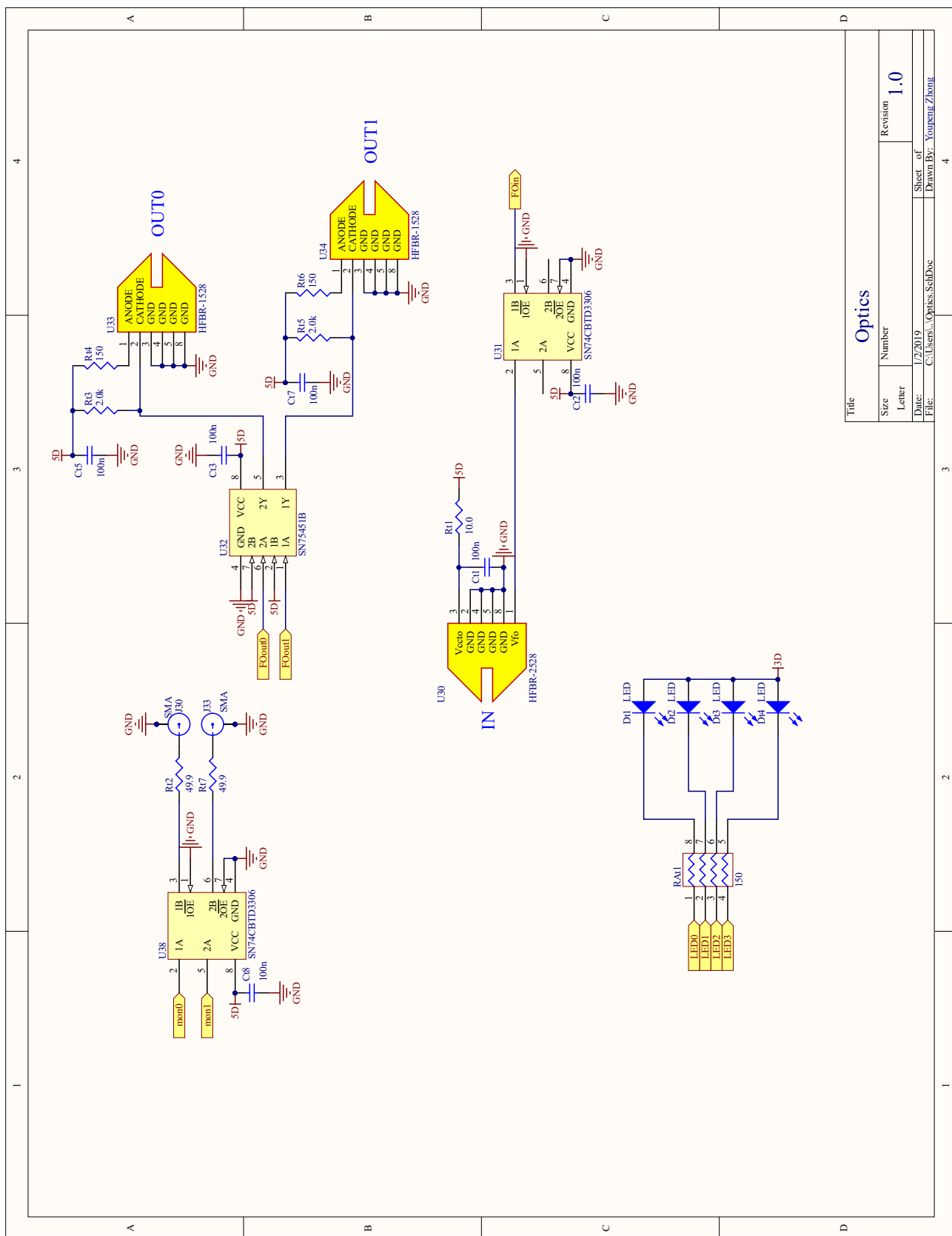




Use standard straight Ethernet cables, not crossovers
NOTE: Connectors wired differently (enables straight cabling from Transm. to Rec.)

Title		Daisy Chain	
Size	Number	Revision	1.0
Letter			
Date:	1/2/2019	Sheet of	4
File:	C:\Users\zhong\Documents	Drawn By:	Younpeng Zhong





Stackup Information:

Layer	Info	Thickness
TOP		0.5+Plating
L2	Core TU-768 0.1	3.940 (mil)
L3	PP TU-768P 2116+2116H	1 Oz
L4	Core TU-768 0.13	9.548 (mil)
L5	PP TU-768P 2116+2116H	1 Oz
L6	Core TU-768 0.13	5.120 (mil)
L7	PP TU-768P 2116+2116H	1 Oz
BOT	Core TU-768 0.18	9.633 (mil)
		1 Oz
		7.090 (mil)
		0.5+Plating

finished board thickness	62.992 (6.299/-6.299) mil	1.6 (+0.16/-0.16) mm
designed board thickness	58.976 mil	1.498 mm
material type	TU-768	TU-768

Dimension: 4 inches x 8 inches, 63 mils (1.6 mm) thick
Material: FR4-High Tg 180C
Copper weight: 1 Oz for all layers
Surface finish: ENIG
Smallest holes: 0.008 inch
Min. Tracing/Spacing: 0.004 inch
Impedance control: 10%
Inspection Standard: IPC 2

5 mils skew within differential pair
50 mils skew between differential pairs in the same bus

GHZ_DAC							
part number		board thickness:		1.6mm		Tolerance of board thickness:	
layer		Impedance control	Tracing (mil)	Spacing mil	clearance of copper plane	finished copper weight OZ	Required OHM
designed in the file	L1	characteristic impedance	6			1	50+/-10% L2
	L3	characteristic impedance	5			1	50+/-10% L2/L4
	L3	differential impedance	4.5	11.5		1	100+/-10% L2/L4
	L5	differential impedance	4.5	11.5		1	100+/-10% L4/L6
	L5	characteristic impedance	5			1	50+/-10% L4/L6

Layer Stackup			
Title	Size	Number	Revision
	Letter		
Date: 1/2/2019	File: C:\Users\Layer Stackup\SchDoc	Sheet of	1.0
Drawn By: Youpeng Zhang			

BIBLIOGRAPHY

- [1] Peter W Shor. Algorithms for quantum computation: Discrete logarithms and factoring. In *Foundations of Computer Science, 1994 Proceedings., 35th Annual Symposium on*, pages 124–134. Ieee, 1994.
- [2] Richard P Feynman. Simulating physics with computers. *International journal of theoretical physics*, 21(6-7):467–488, 1982.
- [3] Juan I Cirac and Peter Zoller. Quantum computations with cold trapped ions. *Physical review letters*, 74(20):4091, 1995.
- [4] MV Gurudev Dutt, L Childress, L Jiang, E Togan, J Maze, F Jelezko, AS Zibrov, PR Hemmer, and MD Lukin. Quantum register based on individual electronic and nuclear spin qubits in diamond. *Science*, 316(5829):1312–1316, 2007.
- [5] William F Koehl, Bob B Buckley, F Joseph Heremans, Greg Calusine, and David D Awschalom. Room temperature coherent control of defect spin qubits in silicon carbide. *Nature*, 479(7371):84, 2011.
- [6] M. H. Devoret and R. J. Schoelkopf. Superconducting circuits for quantum information: An outlook. *Science*, 339(6124):1169–1174, 2013.
- [7] J. Kelly, R. Barends, A. G. Fowler, A. Megrant, E. Jeffrey, T. C. White, D. Sank, J. Y. Mutus, B. Campbell, Yu Chen, Z. Chen, B. Chiaro, A. Dunsworth, I.-C. Hoi, C. Neill, P. J. J. O’Malley, C. Quintana, P. Roushan, A. Vainsencher, J. Wenner, A. N. Cleland, and John M. Martinis. State preservation by repetitive error detection in a superconducting quantum circuit. *Nature*, 519(7541):66–69, 2015.
- [8] Max Hofheinz, H. Wang, M. Ansmann, Radoslaw C. Bialczak, Erik Lucero, M. Neeley, A. D. O’Connell, D. Sank, J. Wenner, John M. Martinis, and A. N. Cleland. Synthesizing

- arbitrary quantum states in a superconducting resonator. *Nature*, 459(7246):546–549, 2009.
- [9] Brian Vlastakis, Gerhard Kirchmair, Zaki Leghtas, Simon E Nigg, Luigi Frunzio, Steven M Girvin, Mazyar Mirrahimi, Michel H Devoret, and Robert J Schoelkopf. Deterministically encoding quantum information using 100-photon Schrödinger cat states. *Science*, 342(6158):607–610, 2013.
- [10] A. D. O’Connell, M. Hofheinz, M. Ansmann, Radoslaw C. Bialczak, M. Lenander, Erik Lucero, M. Neeley, D. Sank, H. Wang, M. Weides, J. Wenner, John M. Martinis, and A. N. Cleland. Quantum ground state and single-phonon control of a mechanical resonator. *Nature*, 464(7289):697–703, mar 2010.
- [11] Yiwen Chu, Prashanta Kharel, William H. Renninger, Luke D. Burkhardt, Luigi Frunzio, Peter T. Rakich, and Robert J. Schoelkopf. Quantum acoustics with superconducting qubits. *Science*, 358(6360):199–202, 2017.
- [12] Kevin J. Satzinger, Youpeng Zhong, Hung-Shen Chang, Gregory A. Peairs, Audrey Bienfait, Ming-Han Chou, A. Y. Cleland, Cristopher R. Conner, Étienne Dumur, Joel Grebel, Ivan Gutierrez, B. H. November, Rhys G. Povey, S. J. Whiteley, David D. Awschalom, David I. Schuster, and Andrew N. Cleland. Quantum control of surface acoustic-wave phonons. *Nature*, 563:661–665, 2018.
- [13] Yiwen Chu, Prashanta Kharel, Taekwan Yoon, Luigi Frunzio, Peter T Rakich, and Robert J Schoelkopf. Creation and control of multi-phonon fock states in a bulk acoustic-wave resonator. *Nature*, 563:666–670, 2018.
- [14] Samuel K Moore. IBM edges closer to quantum supremacy with 50-qubit processor. *IEEE Spectrum*, 2017.
- [15] Julian Kelly. Engineering superconducting qubit arrays for quantum supremacy. *Bulletin of the American Physical Society*, 2018.

- [16] Aram W Harrow and Ashley Montanaro. Quantum computational supremacy. *Nature*, 549(7671):203, 2017.
- [17] John Preskill. Quantum computing in the nisq era and beyond. *arXiv preprint arXiv:1801.00862*, 2018.
- [18] Elizabeth Gibney. D-wave upgrade: How scientists are using the world’s most controversial quantum computer. *Nature*, 541(7638):447, 2017.
- [19] H Jeff Kimble. The quantum internet. *Nature*, 453(7198):1023, 2008.
- [20] Stephanie Wehner, David Elkouss, and Ronald Hanson. Quantum internet: A vision for the road ahead. *Science*, 362(6412):eaam9288, 2018.
- [21] P. Kurpiers, P. Magnard, T. Walter, B. Royer, M. Pechal, J. Heinsoo, Y. Salathe, A. Akin, S. Storz, J.-C. Besse, S. Gasparinetti, A. Blais, and A. Wallraff. Deterministic quantum state transfer and remote entanglement using microwave photons. *Nature*, 558:264–267, 2018.
- [22] C. J. Axline, L. D. Burkhardt, W. Pfaff, M. Zhang, K. Chou, P. Campagne-Ibarcq, P. Reinhold, L. Frunzio, S. M. Girvin, L. Jiang, M. H. Devoret, and R. J. Schoelkopf. On-demand quantum state transfer and entanglement between remote microwave cavity memories. *Nature Physics*, 14:705–710, 2018.
- [23] P. Campagne-Ibarcq, E. Zalys-Geller, A. Narla, S. Shankar, P. Reinhold, L. Burkhardt, C. Axline, W. Pfaff, L. Frunzio, R. J. Schoelkopf, and M. H. Devoret. Deterministic remote entanglement of superconducting circuits through microwave two-photon transitions. *Physical Review Letters*, 120:200501, 2018.
- [24] Morgan M Weston, Sergei Slussarenko, Helen M Chrzanowski, Sabine Wollmann, Lynnden K Shalm, Varun B Verma, Michael S Allman, Sae Woo Nam, and Geoff J Pryde.

- Heralded quantum steering over a high-loss channel. *Science advances*, 4(1):e1701230, 2018.
- [25] M. Stobińska, G. Alber, and G. Leuchs. Perfect excitation of a matter qubit by a single photon in free space. *Europhysics Letters*, 86(1):14007, 2009.
- [26] Yimin Wang, Jiri Minar, Lana Sheridan, and Valerio Scarani. Efficient excitation of a two-level atom by a single photon in a propagating mode. *Physical Review A*, 83:063842, Jun 2011.
- [27] J. I. Cirac, P. Zoller, H. J. Kimble, , and H. Mabuchi. Quantum state transfer and entanglement distribution among distant nodes in a quantum network. *Physical Review Letters*, 78:3221, 1997.
- [28] A. N. Korotkov. Flying microwave qubits with nearly perfect transfer efficiency. *Physical Review B*, 84:014510, 2011.
- [29] D. M. Pozar. *Microwave engineering*. Wiley, fourth edition, 2011.
- [30] Max Hofheinz, EM Weig, M Ansmann, Radoslaw C Bialczak, Erik Lucero, M Neeley, AD Oconnell, H Wang, John M Martinis, and AN Cleland. Generation of Fock states in a superconducting quantum circuit. *Nature*, 454(7202):310, 2008.
- [31] M. Ansmann, H. Wang, R. C. Bialczak, M. Hofheinz, E. Lucero, M. Neeley, A. D. O’Connell, D. Sank, M. Weides, J. Wenner, A. N. Cleland, and J. M. Martinis. Violation of Bell’s inequality in Josephson phase qubits. *Nature*, 461:504–506, 2009.
- [32] Ramesh Garg, Inder Bahl, and Maurizio Bozzi. *Microstrip lines and slotlines*. Artech house, 2013.
- [33] Abigail Shearrow, Gerwin Koolstra, Samuel J Whiteley, Nathan Earnest, Peter S Barry, F Joseph Heremans, David D Awschalom, Erik Shirokoff, and David I Schuster. Atomic

- layer deposition of titanium nitride for quantum circuits. *Applied Physics Letters*, 113(21):212601, 2018.
- [34] B. D. Josephson. Possible new effects in superconductive tunnelling. *Physics Letters*, 1(7):251–253, 1962.
- [35] Jens Koch, Terri M. Yu, Jay Gambetta, A. A. Houck, D. I. Schuster, J. Majer, Alexandre Blais, M. H. Devoret, S. M. Girvin, and R. J. Schoelkopf. Charge-insensitive qubit design derived from the Cooper pair box. *Physical Review A*, 76(4), 2007.
- [36] R. Barends, J. Kelly, A. Megrant, D. Sank, E. Jeffrey, Y. Chen, Y. Yin, B. Chiaro, J. Mutus, C. Neill, P. O’Malley, P. Roushan, J. Wenner, T. C. White, A. N. Cleland, and John M. Martinis. Coherent josephson qubit suitable for scalable quantum integrated circuits. *Phys. Rev. Lett.*, 111:080502, Aug 2013.
- [37] R. Barends, J. Kelly, A. Megrant, A. Veitia, D. Sank, E. Jeffrey, T. C. White, J. Mutus, A. G. Fowler, B. Campbell, Y. Chen, Z. Chen, B. Chiaro, A. Dunsworth, C. Neill, P. O’Malley, P. Roushan, A. Vainsencher, J. Wenner, A. N. Korotkov, A. N. Cleland, and John M. Martinis. Superconducting quantum circuits at the surface code threshold for fault tolerance. *Nature*, 508(7497):500–503, 2014.
- [38] A Wallraff, DI Schuster, A Blais, L Frunzio, J Majer, MH Devoret, SM Girvin, and RJ Schoelkopf. Approaching unit visibility for control of a superconducting qubit with dispersive readout. *Physical review letters*, 95(6):060501, 2005.
- [39] Francois Mallet, Florian R Ong, Agustin Palacios-Laloy, Francois Nguyen, Patrice Bertet, Denis Vion, and Daniel Esteve. Single-shot qubit readout in circuit quantum electrodynamics. *Nature Physics*, 5(11):791, 2009.
- [40] Alexandre Blais, Ren-Shou Huang, Andreas Wallraff, Steven M Girvin, and R Jun Schoelkopf. Cavity quantum electrodynamics for superconducting electrical circuits: An architecture for quantum computation. *Physical Review A*, 69(6):062320, 2004.

- [41] Daniel T. Sank. *Fast, Accurate State Measurement in Superconducting Qubits*. PhD thesis, University of California Santa Barbara, 2014.
- [42] Uri Vool and Michel Devoret. Introduction to quantum electromagnetic circuits. *International Journal of Circuit Theory and Applications*, 45(7):897–934, 2017.
- [43] C. M. Quintana, K. D. Petersson, L. W. McFaul, S. J. Srinivasan, A. A. Houck, and J. R. Petta. Cavity-mediated entanglement generation via Landau-Zener interferometry. *Phys. Rev. Lett.*, 110:173603, Apr 2013.
- [44] Andrew A Houck, Hakan E Türeci, and Jens Koch. On-chip quantum simulation with superconducting circuits. *Nature Physics*, 8(4):292, 2012.
- [45] A Mezzacapo, L Lamata, S Filipp, and E Solano. Many-body interactions with tunable-coupling transmon qubits. *Physical review letters*, 113(5):050501, 2014.
- [46] Anatoli Polkovnikov, Krishnendu Sengupta, Alessandro Silva, and Mukund Vengalattore. Colloquium: Nonequilibrium dynamics of closed interacting quantum systems. *Reviews of Modern Physics*, 83(3):863, 2011.
- [47] Pedram Roushan, C Neill, Yu Chen, M Kolodrubetz, C Quintana, N Leung, M Fang, R Barends, B Campbell, Z Chen, et al. Observation of topological transitions in interacting quantum circuits. *Nature*, 515(7526):241, 2014.
- [48] Travis Hime, PA Reichardt, BLT Plourde, TL Robertson, C-E Wu, AV Ustinov, and John Clarke. Solid-state qubits with current-controlled coupling. *science*, 314(5804):1427–1429, 2006.
- [49] AO Niskanen, K Harrabi, F Yoshihara, Y Nakamura, S Lloyd, and JS Tsai. Quantum coherent tunable coupling of superconducting qubits. *Science*, 316(5825):723–726, 2007.
- [50] M. S. Allman, F. Altomare, J. D. Whittaker, K. Cicak, D. Li, A. Sirois, J. Strong, J. D. Teufel, and R. W. Simmonds. rf-squid-mediated coherent tunable coupling be-

- tween a superconducting phase qubit and a lumped-element resonator. *Phys. Rev. Lett.*, 104:177004, Apr 2010.
- [51] A. J. Hoffman, S. J. Srinivasan, J. M. Gambetta, and A. A. Houck. Coherent control of a superconducting qubit with dynamically tunable qubit-cavity coupling. *Phys. Rev. B*, 84:184515, Nov 2011.
- [52] RC Bialczak, M Ansmann, M Hofheinz, M Lenander, E Lucero, M Neeley, AD O’Connell, D Sank, H Wang, M Weides, et al. Fast tunable coupler for superconducting qubits. *Physical review letters*, 106(6):060501, 2011.
- [53] Yi Yin, Yu Chen, Daniel Sank, P. J. J. O’Malley, T. C. White, R. Barends, J. Kelly, Erik Lucero, Matteo Mariantoni, A. Megrant, C. Neill, A. Vainsencher, J. Wenner, Alexander N. Korotkov, A. N. Cleland, and John M. Martinis. Catch and release of microwave photon states. *Phys. Rev. Lett.*, 110:107001, Mar 2013.
- [54] Yu Chen, C. Neill, P. Roushan, N. Leung, M. Fang, R. Barends, J. Kelly, B. Campbell, Z. Chen, B. Chiaro, A. Dunsworth, E. Jeffrey, A. Megrant, J. Y. Mutus, P. J. J. O’Malley, C. M. Quintana, D. Sank, A. Vainsencher, J. Wenner, T. C. White, Michael R. Geller, A. N. Cleland, and John M. Martinis. Qubit architecture with high coherence and fast tunable coupling. *Phys. Rev. Lett.*, 113:220502, Nov 2014.
- [55] J. D. Whittaker, F. C. S. da Silva, M. S. Allman, F. Lecocq, K. Cicak, A. J. Sirois, J. D. Teufel, J. Aumentado, and R. W. Simmonds. Tunable-cavity QED with phase qubits. *Phys. Rev. B*, 90:024513, Jul 2014.
- [56] Mathieu Pierre, Ida-Maria Svensson, Sankar Raman Sathyamoorthy, Göran Johansson, and Per Delsing. Storage and on-demand release of microwaves using superconducting resonators with tunable coupling. *Applied Physics Letters*, 104(23):232604, 2014.

- [57] CW Gardiner and MJ Collett. Input and output in damped quantum systems: Quantum stochastic differential equations and the master equation. *Physical Review A*, 31(6):3761, 1985.
- [58] Srikanth J. Srinivasan, Neereja M. Sundaresan, Darius Sadri, Yanbing Liu, Jay M. Gambetta, Terri Yu, S. M. Girvin, and Andrew A. Houck. Time-reversal symmetrization of spontaneous emission for quantum state transfer. *Phys. Rev. A*, 89:033857, Mar 2014.
- [59] J. Wenner, Yi Yin, Yu Chen, R. Barends, B. Chiaro, E. Jeffrey, J. Kelly, A. Megrant, J. Y. Mutus, C. Neill, P. J. J. O’Malley, P. Roushan, D. Sank, A. Vainsencher, T. C. White, Alexander N. Korotkov, A. N. Cleland, and John M. Martinis. Catching time-reversed microwave coherent state photons with 99.4% absorption efficiency. *Phys. Rev. Lett.*, 112:210501, May 2014.
- [60] Marek Pechal, Lukas Huthmacher, Christopher Eichler, S Zeytinoglu, AA Abdumalikov Jr, Simon Berger, Andreas Wallraff, and Stefan Filipp. Microwave-controlled generation of shaped single photons in circuit quantum electrodynamics. *Physical Review X*, 4(4):041010, 2014.
- [61] Neereja M. Sundaresan, Yanbing Liu, Darius Sadri, László J. Szócs, Devin L. Underwood, Moein Malekakhlagh, Hakan E. Türeci, and Andrew A. Houck. Beyond strong coupling in a multimode cavity. *Phys. Rev. X*, 5:021035, Jun 2015.
- [62] Julian S. Kelly. *Fault-tolerant superconducting qubits*. PhD thesis, University of California Santa Barbara, 2015.
- [63] Giovanni Ghione and Carlo U Naldi. Coplanar waveguides for MMIC applications: Effect of upper shielding, conductor backing, finite-extent ground planes, and line-to-line coupling. *IEEE transactions on Microwave Theory and Techniques*, 35(3):260–267, 1987.

- [64] A. D. O’Connell, M. Ansmann, R. C. Bialczak, M. Hofheinz, N. Katz, Erik Lucero, C. McKenney, M. Neeley, H. Wang, E. M. Weig, A. N. Cleland, and John M. Martinis. Microwave dielectric loss at single photon energies and millikelvin temperatures. *Applied Physics Letters*, 92(11):112903, 2008.
- [65] A. Dunsworth, R. Barends, Y. Chen, Z. Chen, B. Chiaro, A. Fowler, B. Foxen, E. Jeffrey, J. Kelly, P. V. Klimov, E. Lucero, J. Y. Mutus, M. Neeley, C. Neill, C. Quintana, P. Roushan, D. Sank, A. Vainsencher, J. Wenner, T. C. White, H. Neven, J. M. Martinis, and A. Megrant. A method for building low loss multi-layer wiring for superconducting microwave devices. *Applied Physics Letters*, 112:063502, 2018.
- [66] Zijun Chen, A. Megrant, J. Kelly, R. Barends, J. Bochmann, Yu Chen, B. Chiaro, A. Dunsworth, E. Jeffrey, J. Y. Mutus, P. J. J. O’Malley, C. Neill, P. Roushan, D. Sank, A. Vainsencher, J. Wenner, T. C. White, A. N. Cleland, and John M. Martinis. Fabrication and characterization of aluminum airbridges for superconducting microwave circuits. *Applied Physics Letters*, 104(5):052602, 2014.
- [67] A. Megrant, C. Neill, R. Barends, B. Chiaro, Yu Chen, L. Feigl, J. Kelly, Erik Lucero, Matteo Mariantoni, P. J. J. O’Malley, D. Sank, A. Vainsencher, J. Wenner, T. C. White, Y. Yin, J. Zhao, C. J. Palmstrøm, John M. Martinis, and A. N. Cleland. Planar superconducting resonators with internal quality factors above one million. *Applied Physics Letters*, 100(11):113510, 2012.
- [68] Philip Krantz, Andreas Bengtsson, Michaël Simoen, Simon Gustavsson, Vitaly Shumeiko, WD Oliver, CM Wilson, Per Delsing, and Jonas Bylander. Single-shot readout of a superconducting qubit using a Josephson parametric oscillator. *Nature communications*, 7:11417, 2016.
- [69] Josephine B Chang, Michael R Vissers, Antonio D Córcoles, Martin Sandberg, Jiansong Gao, David W Abraham, Jerry M Chow, Jay M Gambetta, Mary Beth Rothwell,

- George A Keefe, et al. Improved superconducting qubit coherence using titanium nitride. *Applied Physics Letters*, 103(1):012602, 2013.
- [70] A Bruno, G De Lange, S Asaad, KL Van der Enden, NK Langford, and L DiCarlo. Reducing intrinsic loss in superconducting resonators by surface treatment and deep etching of silicon substrates. *Applied Physics Letters*, 106(18):182601, 2015.
- [71] B. Foxen, J. Y. Mutus, E. Lucero, R. Graff, A. Megrant, Yu Chen, C. Quintana, B. Burkett, J. Kelly, E. Jeffrey, Yan Yang, Anthony Yu, K. Arya, R. Barends, Zijun Chen, B. Chiaro, A. Dunsworth, A. Fowler, C. Gidney, M. Giustina, T. Huang, P. Klimov, M. Neeley, C. Neill, P. Roushan, D. Sank, A. Vainsencher, J. Wenner, T. C. White, and John M. Martinis. Qubit compatible superconducting interconnects. *Quantum Science and Technology*, 3(1):014005, 2017.
- [72] G. J. Dolan. Offset masks for lift-off photoprocessing. *Applied Physics Letters*, 31(5):337–339, 1977.
- [73] A. Dunsworth, A. Megrant, C. Quintana, Zijun Chen, R. Barends, B. Burkett, B. Foxen, Yu Chen, B. Chiaro, A. Fowler, R. Graff, E. Jeffrey, J. Kelly, E. Lucero, J. Y. Mutus, M. Neeley, C. Neill, P. Roushan, D. Sank, A. Vainsencher, J. Wenner, T. C. White, and John M. Martinis. Characterization and reduction of capacitive loss induced by sub-micron Josephson junction fabrication in superconducting qubits. *Applied Physics Letters*, 111(2):022601, 2017.
- [74] Vinay Ambegaokar and Alexis Baratoff. Tunneling between superconductors. *Phys. Rev. Lett.*, 10:486–489, Jun 1963.
- [75] Thomas Kaufmann, Timothy J Keller, John M Franck, Ryan P Barnes, Steffen J Glaser, John M Martinis, and Songi Han. DAC-board based X-band EPR spectrometer with arbitrary waveform control. *Journal of Magnetic Resonance*, 235:95–108, 2013.

- [76] Antonije R Djordjevic, Alenka G Zajic, Aleksandra S Stekovic, Marija M Nikolic, Zoran A Maricevic, and Marcel FC Schemmann. On a class of low-reflection transmission-line quasi-gaussian low-pass filters and their lumped-element approximations. *IEEE Transactions on Microwave Theory and Techniques*, 51(7):1871–1877, 2003.
- [77] Markus Ansmann. *Benchmarking the Superconducting Josephson Phase Qubit: The Violation of Bell’s Inequality*. PhD thesis, University of California Santa Barbara, 2009.
- [78] John F Clauser, Michael A Horne, Abner Shimony, and Richard A Holt. Proposed experiment to test local hidden-variable theories. *Physical review letters*, 23(15):880, 1969.
- [79] Austin G. Fowler, David S. Wang, Charles D. Hill, Thaddeus D. Ladd, Rodney Van Meter, and Lloyd C. L. Hollenberg. Surface code quantum communication. *Physical Review Letters*, 104:180503, May 2010.
- [80] C. Macklin, K. O’Brien, D. Hover, M. E. Schwartz, V. Bolkhovskiy, X. Zhang, W. D. Oliver, and I. Siddiqi. A near-quantum-limited Josephson traveling-wave parametric amplifier. *Science*, 350(6258):307–310, 2015.
- [81] Philipp Kurpiers, Theodore Walter, Paul Magnard, Yves Salathe, and Andreas Wallraff. Characterizing the attenuation of coaxial and rectangular microwave-frequency waveguides at cryogenic temperatures. *EPJ Quantum Technology*, 4(1):8, 2017.
- [82] Michael R. Geller, Emmanuel Donate, Yu Chen, Michael T. Fang, Nelson Leung, Charles Neill, Pedram Roushan, and John M. Martinis. Tunable coupler for superconducting Xmon qubits: Perturbative nonlinear model. *Phys. Rev. A*, 92:012320, Jul 2015.
- [83] Mika A Sillanpää, Jae I Park, and Raymond W Simmonds. Coherent quantum state storage and transfer between two phase qubits via a resonant cavity. *Nature*, 449(7161):438, 2007.

- [84] Matthew Neeley, Markus Ansmann, Radoslaw C Bialczak, Max Hofheinz, Nadav Katz, Erik Lucero, A O’connell, Haohua Wang, Andrew N Cleland, and John M Martinis. Process tomography of quantum memory in a Josephson-phase qubit coupled to a two-level state. *Nature Physics*, 4(7):523, 2008.
- [85] D. V. Averin, K. Xu, Y. P. Zhong, C. Song, H. Wang, and Siyuan Han. Suppression of dephasing by qubit motion in superconducting circuits. *Physical Review Letters*, 116:010501, Jan 2016.
- [86] Matthias Steffen, M. Ansmann, R. McDermott, N. Katz, Radoslaw C. Bialczak, Erik Lucero, Matthew Neeley, E. M. Weig, A. N. Cleland, and John M. Martinis. State tomography of capacitively shunted phase qubits with high fidelity. *Physical Review Letters*, 97(5), aug 2006.
- [87] Anupam Garg and N David Mermin. Detector inefficiencies in the Einstein-Podolsky-Rosen experiment. *Physical Review D*, 35(12):3831, 1987.
- [88] Eyob A. Sete, Eric Mlinar, and Alexander N. Korotkov. Robust quantum state transfer using tunable couplers. *Phys. Rev. B*, 91:144509, Apr 2015.
- [89] N Leung, Y Lu, S Chakram, RK Naik, N Earnest, R Ma, K Jacobs, AN Cleland, and DI Schuster. Deterministic bidirectional communication and remote entanglement generation between superconducting quantum processors. *arXiv preprint arXiv:1804.02028*, 2018.
- [90] David B Tuckerman, Michael C Hamilton, David J Reilly, Rujun Bai, George A Hernandez, John M Hornibrook, John A Sellers, and Charles D Ellis. Flexible superconducting Nb transmission lines on thin film polyimide for quantum computing applications. *Superconductor Science and Technology*, 29(8):084007, 2016.
- [91] Hieng Tiong Su, Yi Wang, Frederick Huang, and Michael J Lancaster. Superconducting delay lines. *Journal of Superconductivity and Novel Magnetism*, 21(1):7–16, 2008.

- [92] Albert Einstein, Boris Podolsky, and Nathan Rosen. Can quantum-mechanical description of physical reality be considered complete? *Physical review*, 47(10):777, 1935.
- [93] John S Bell. On the Einstein Podolsky Rosen paradox. *Physics Physique Fizika*, 1(3):195, 1964.
- [94] Anthony J Leggett and Anupam Garg. Quantum mechanics versus macroscopic realism: Is the flux there when nobody looks? *Physical Review Letters*, 54(9):857, 1985.
- [95] Stuart J Freedman and John F Clauser. Experimental test of local hidden-variable theories. *Physical Review Letters*, 28(14):938, 1972.
- [96] Gregor Weihs, Thomas Jennewein, Christoph Simon, Harald Weinfurter, and Anton Zeilinger. Violation of Bell’s inequality under strict Einstein locality conditions. *Physical Review Letters*, 81(23):5039, 1998.
- [97] Mary A Rowe, David Kielpinski, Volker Meyer, Charles A Sackett, Wayne M Itano, Christopher Monroe, and David J Wineland. Experimental violation of a Bell’s inequality with efficient detection. *Nature*, 409(6822):791, 2001.
- [98] B. Hensen, H. Bernien, A. E. Dréau, A. Reiserer, N. Kalb, M. S. Blok, J. Ruitenberg, R. F. L. Vermeulen, R. N. Schouten, C. Abellán, W. Amaya, V. Pruneri, M. W. Mitchell, M. Markham, D. J. Twitchen, D. Elkouss, S. Wehner, T. H. Taminiau, and R. Hanson. Loophole-free Bell inequality violation using electron spins separated by 1.3 kilometres. *Nature*, 526(7575):682–686, 2015.
- [99] Agustin Palacios-Laloy, François Mallet, François Nguyen, Patrice Bertet, Denis Vion, Daniel Esteve, and Alexander N Korotkov. Experimental violation of a Bell’s inequality in time with weak measurement. *Nature Physics*, 6(6):442, 2010.